



Universiteit Gent
Faculteit Wetenschappen
Vakgroep Fysica en Sterrenkunde

² No title yet

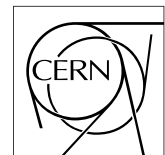
³ No sub-title neither, obviously...

⁴ Alexis Fagot

5



Thesis to obtain the degree of
Doctor of Philosophy in Physics
Academic years 2012-2017



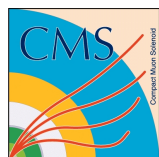


Universiteit Gent
Faculteit Wetenschappen
Vakgroep Fysica en Sterrenkunde

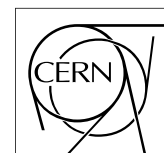
Promotoren: Dr. Michael Tytgat
Prof. Dr. Dirk Ryckbosch

Universiteit Gent
Faculteit Wetenschappen
Vakgroep Fysica en Sterrenkunde
Proeftuinstraat 86, B-9000 Gent, België
Tel.: +32 9 264.65.28
Fax.: +32 9 264.66.97

17



Thesis to obtain the degree of
Doctor of Philosophy in Physics
Academic years 2012-2017



Acknowledgements

¹⁹ Ici on remerciera tous les gens que j'ai pu croiser durant cette aventure et qui m'ont permis de passer
²⁰ un bon moment

²¹ *Gent, ici la super date de la mort qui tue de la fin d'écriture*
²² *Alexis Fagot*

Table of Contents

23

24	Acknowledgements	i
25	Nederlandse samenvatting	vii
26	English summary	ix
27	1 Introduction	1-1
28	1.1 A story of High Energy Physics	1-1
29	1.2 Organisation of this study	1-1
30	2 Investigating the TeV scale	2-1
31	2.1 The Standard Model of Particle Physics	2-2
32	2.1.1 A history of particle physics	2-2
33	2.1.2 Construction and test of the model	2-11
34	2.1.3 Investigating the TeV scale	2-12
35	2.2 The Large Hadron Collider & the Compact Muon Solenoid	2-14
36	2.2.1 LHC, the most powerful particle accelerator	2-14
37	2.2.1.1 Particle acceleration	2-15
38	2.2.2 CMS, a multipurpose experiment	2-18
39	2.2.2.1 The silicon tracker, core of CMS	2-20
40	2.2.2.2 The calorimeters, measurement of particle's energy	2-20
41	2.2.2.3 The muon system, corner stone of CMS	2-22
42	3 Muon Phase-II Upgrade	3-1
43	3.1 High Luminosity LHC and muon system requirements	3-2
44	3.2 Necessity for improved electronics	3-5
45	3.3 New detectors and increased acceptance	3-8
46	3.3.1 Improved forward resistive plate chambers	3-9
47	3.3.2 Gas electron multipliers	3-12
48	3.3.3 Installation schedule	3-19
49	3.4 Implications of the different upgrades on the Level-1 Trigger. Improvement of	
50	physics performance.	3-20
51	3.5 Ecofriendly gas studies	3-24
52	4 Physics of Resistive plate chambers	4-1
53	4.1 Principle	4-1
54	4.2 Rate capability and time resolution of Resistive Plate Chambers	4-3
55	4.2.1 Operation modes	4-3
56	4.2.2 Standard gas mixture for RPCs operated in collider experiments	4-5
57	4.2.3 Detector designs and performance	4-9
58	4.2.3.1 Double gap RPC	4-11

59	4.2.3.2 Multigap RPC (MRPC)	4-13
60	4.2.3.3 Charge distribution and performance limitations	4-16
61	4.3 Signal formation	4-18
62	4.3.1 Energy loss at intermediate energies	4-19
63	4.3.2 Primary ionization	4-23
64	4.3.3 Development and propagation of avalanches	4-26
65	4.3.4 Drift and diffusion of the electron cloud	4-30
66	4.3.5 Space charge effect & streamers	4-32
67	4.4 Effect of atmospherical conditions on the detector's performance	4-35
68	5 Longevity studies and Consolidation of the present CMS RPC subsystem	5-1
69	5.1 Testing detectors under extreme conditions	5-1
70	5.1.1 The Gamma Irradiation Facilities	5-3
71	5.1.1.1 GIF	5-3
72	5.1.1.2 GIF++	5-5
73	5.2 Preliminary tests at GIF	5-7
74	5.2.1 Resistive Plate Chamber test setup	5-7
75	5.2.2 Data Acquisition	5-10
76	5.2.3 Geometrical acceptance of the setup layout to cosmic muons	5-10
77	5.2.3.1 Description of the simulation layout	5-10
78	5.2.3.2 Simulation procedure	5-12
79	5.2.3.3 Results	5-13
80	5.2.4 Photon flux at GIF	5-13
81	5.2.4.1 Expectations from simulations	5-13
82	5.2.4.2 Dose measurements	5-18
83	5.2.5 Results and discussions	5-19
84	5.3 Longevity tests at GIF++	5-19
85	5.3.1 Description of the Data Acquisition	5-23
86	5.3.2 RPC current, environmental and operation parameter monitoring	5-24
87	5.3.3 Measurement procedure	5-24
88	5.3.4 Longevity studies results	5-24
89	6 Conclusions and outlooks	6-1
90	6.1 Conclusions	6-1
91	6.2 Outlooks	6-1
92	A A data acquisition software for CAEN VME TDCs	A-1
93	A.1 GIF++ DAQ file tree	A-1
94	A.2 Usage of the DAQ	A-2
95	A.3 Description of the readout setup	A-3
96	A.4 Data read-out	A-3
97	A.4.1 V1190A TDCs	A-4
98	A.4.2 DataReader	A-6
99	A.4.3 Data quality flag	A-10
100	A.5 Communications	A-12
101	A.5.1 V1718 USB Bridge	A-13
102	A.5.2 Configuration file	A-13
103	A.5.3 WebDCS/DAQ intercommunication	A-17
104	A.5.4 Example of inter-process communication cycle	A-18
105	A.6 Software export	A-18

106	B Details on the offline analysis package	B-1
107	B.1 GIF++ Offline Analysis file tree	B-1
108	B.2 Usage of the Offline Analysis	B-2
109	B.2.1 Output of the offline tool	B-3
110	B.2.1.1 ROOT file	B-3
111	B.2.1.2 CSV files	B-5
112	B.3 Analysis inputs and information handling	B-6
113	B.3.1 Dimensions file and IniFile parser	B-6
114	B.3.2 TDC to RPC link file and Mapping	B-7
115	B.4 Description of GIF++ setup within the Offline Analysis tool	B-9
116	B.4.1 RPC objects	B-9
117	B.4.2 Trolley objects	B-10
118	B.4.3 Infrastructure object	B-11
119	B.5 Handeling of data	B-12
120	B.5.1 RPC hits	B-13
121	B.5.2 Clusters of hits	B-14
122	B.6 DAQ data Analysis	B-15
123	B.6.1 Determination of the run type	B-16
124	B.6.2 Beam time window calculation for efficiency runs	B-17
125	B.6.3 Data loop and histogram filling	B-18
126	B.6.4 Results calculation	B-19
127	B.6.4.1 Rate normalisation	B-19
128	B.6.4.2 Rate and activity	B-21
129	B.6.4.3 Strip masking tool	B-23
130	B.6.4.4 Output CSV files filling	B-25
131	B.7 Current data Analysis	B-29

¹³²

¹³³

Nederlandse samenvatting –Summary in Dutch–

¹³⁴ Le resume en Neerlandais (j'aurais peut-être pu apprendre la langue juste pour ça...).

English summary

¹³⁶ Le meme résume mais en Anglais (on commencera par la hein!).

List of Figures

137

138	2.1	Through the gold foil experiment Rutherford could show that most of the mass of atoms was contained in a positively charged nucleus and could then propose a more accurate atomic model than that of Thomson.	2-3
140	2.2	Figure 2.2a: Meson octet. Figure 2.2b: Baryon octet. Figure 2.2c: Baryon decuplet.	2-8
141	2.3	The elementary particles of the Standard Model are showed along with their names and properties. Their interactions with the strong, weak and electromagnetic forces have been explicated using color squares. In the left column, the scalar higgs boson is depicted, while the central is focused on the matter particles, the fermions, and the right on the force carriers, the gauge bosons. The role of the Higgs boson in electroweak symmetry breaking is highlighted, and the corresponding way properties of the various particles differ in the (high-energy) symmetric phase (top) and the (low-energy) broken-symmetry phase (bottom) are showed.	2-11
142	2.4	CERN accelerator complex.	2-15
143	2.5	Pictures of the different accelerators. From top to bottom: first the LINAC 2 and the <i>Pb</i> source of LINAC 3. Then the Booster and the LEIR. Finally, the PS, the SPS and the LHC.	2-16
144	2.6	Figure 2.6a: schematics of the LHC cryodipoles. 1: Superconducting Coils, 2: Beam pipe, 3: Heat exchanger Pipe, 4: Helium-II Vessel, 5: Superconducting Bus-bar, 6: Iron Yoke, 7: Non-Magnetic Collars, 8: Vacuum Vessel, 9: Radiation Screen, 10: Thermal Shield, 11: Auxiliary Bus-bar Tube, 12: Instrumentation Feed Throughs, 13: Protection Diode, 14: Quadrupole Bus-bars, 15: Spool Piece Bus-bars. Figure 2.6b: magnetic field and resulting motion force applied on the beam particles.	2-17
145	2.7	Figure 2.7a: picture of the LHC quadrupoles. Figure 2.7b: magnetic fields and resulting focussing force applied on the beam by 2 consecutive quadrupoles.	2-18
146	2.8	Picture of the CMS barrel. The red outer layer is the muon system hosted into the red iron return yokes. The calorimeters are the blue cylinder inside in magnet solenoid and the tracker is the inner yellow cylinder built around the beam pipe.	2-19
147	2.9	View of the CMS apparatus and of its different components.	2-19
148	2.10	Slice showing CMS sub-detectors and how particles interact with them.	2-20
149	2.11	CMS tracker.	2-20
150	2.12	Figure 2.12a: picture of the ECAL. Figure 2.12b: picture of the lead tungstate crystals composing the ECAL.	2-21
151	2.13	CMS hadron calorimeter barrel.	2-21
152	2.14	A quadrant of the muon system, showing DTs (yellow), RPCs (blue), and CSCs (green).	2-22
153	2.15	Figure 2.15a: Barrel wheel with its detector rings and return yokes. Figure 2.15b: CSC endcap disk with the 2 CSC stations. The outer station is made of 10 deg detectors while the inner station is made of 20 deg detectors. Figure 2.15c: RPC endcap disk. The inner station is not equipped and the inner CSC station can be seen.	2-23
154			
155			
156			
157			
158			
159			
160			
161			
162			
163			
164			
165			
166			
167			
168			
169			
170			
171			
172			
173			
174			
175			
176			

- 177 2.16 Figure 2.16a: Cross section of a DT module showing the two superlayers measur-
 178 ing the ϕ coordinate, perpendicular to the cross section plane, and the superlayer
 179 measuring the η coordinate, placed in between the two others with honeycomb and
 180 parallel to the cross section plane. The DT detector is sandwiched in between 2
 181 RPCs whose readout strips are perpendicular to the cross section plane, measuring
 182 the ϕ coordinate. Figure 2.16b: A DT cell is shown together with its electric field.
 183 The path of a muon through a superlayer is shown. 2-23
- 184 2.17 Figure 2.17a: cathode strips and anode wire layout of a CSC panel. Figure 2.17b
 185 avalanche development and charge collection by anode wires and induction on cath-
 186 ode strips inside of a CSC panel. 2-24
- 187 2.18 Muon track reconstruction through the 6 panels of a CMS CSC using the infor-
 188 mation of anode wire groups and cathode strip charge distribution combined with
 189 comparator bits to decide on which half strip the muon is more likely to have passed. 2-24
- 190 2.19 Double gap layout of CMS RPCs. Muons passing through the gas volumes will cre-
 191 ate electron-ions pairs by ionising the gas. this ionisation will immediately translate
 192 into a developing avalanche. 2-25
- 193 3.1 Detailed timeline projection of for LHC and HL-LHC operation until 2039 show-
 194 ing the evolution of the instantaneous and integrated luminosity as designed (Fig-
 195 ure 3.1a) and in the ultimate case where the instantaneous luminosity is increased to
 196 $7.5 \times 10^{34} \text{ cm}^{-2}\text{s}^{-1}$ (Figure 3.1b) [20, 22]. 3-2
- 197 3.2 Absorbed dose in the CMS cavern after an integrated luminosity of 3000 fb. Using
 198 the interaction point as reference, R is the transverse distance from the beamline and
 199 Z is the distance along the beamline. 3-3
- 200 3.3 A quadrant of the muon system, showing DTs (yellow), RPCs (blue), and CSCs
 201 (green). The locations of new forward muon detectors for Phase-II are contained
 202 within the dashed box and indicated in red for GEM stations (ME0, GE1/1, and
 203 GE2/1) and dark blue for improved RPC (iRPC) stations (RE3/1 and RE4/1). 3-4
- 204 3.4 Figure 3.4a: Extrapolated fraction of failing channels of the present DT MiC1 elec-
 205 tronics as a function of the integrated luminosity for different scenari until LS4. Fig-
 206 ure 3.4b: Comparison of the current (left) and upgraded (right) DT data processing.
 207 So far, the data is sent to service cavern of CMS facility via copper-to-optical-fiber
 208 translators (CuOF) by each MiC1. There, data including RPCs and outer hadron
 209 calorimeter is combined into trigger primitives (TPG) and transmitted by the Twin-
 210 Mux system to CMS Track Finder. The time-to-digital converter (TDC) data is col-
 211 lected and sent to the CMS data acquisition system (DAQ) by the micro read-out
 212 server (μ ROS). After the upgrade, the TDC data will be sent via optical links to
 213 a patch panel inside the experimental cavern by each MiC2, and transferred to the
 214 back-end, where triggering and event building will be performed. 3-6
- 215 3.5 Figure 3.5a: The event loss fractions as a function of the instantaneous luminosity is
 216 compared for CFEBs (Phase-1) and DCFEBs (Phase-II) at different CSC locations.
 217 HL-LHC luminosity is marked with the dashed brown line. Figure 3.5b: Comparison
 218 of the current (left) and upgraded (right) CSC data processing. A part of the con-
 219 nections in between ALCTs and DCFEBs, and the trigger mother boards (TMBs)
 220 and data acquisition mother boards (DMBs) will be upgraded toward optical data
 221 transfer. The detector dependent units (DDUs) used as interface in between CSCs'
 222 front-end electronics and the CMS DAQ will be replaced by new FED boards. 3-7
- 223 3.6 Comparison of the simulated time residuals in between reconstructed and true muon
 224 times without (blue) and with (red) the upgraded RPC link system. 3-8

225	3.7	RMS of the multiple scattering displacement as a function of muon p_T for the proposed forward muon stations. All of the electromagnetic processes such as bremsstrahlung and magnetic field effect are included in the simulation.	3-9
228	3.8	Simulation of the impact of RPC hit inclusion onto the local trigger primitive efficiency in station 3 (left) and station 4 (right). The contribution of iRPC starts above $ \eta = 1.8$	3-9
231	3.9	Expected hit rate due to neutrons, photons, electrons and positrons at HL-HLC instantaneous luminosity of $5 \times 10^{34} \text{ cm}^{-2}\text{s}^{-1}$ in RE3/1 and RE4/1 chambers. The sensitivities of iRPCs used in the simulation for each particle are reported and differ from one endcap disk to another as the energies of the considered particles varies with the increasing distance from the interaction point.	3-10
236	3.10	Measured average charge per avalanche as a function of the effective electric field for different gas gap thickness in double gap RPCs using HPL electrodes.	3-11
238	3.11	The PETIROC time jitter as a function of the input signal amplitude, measured with and without internal clocks.	3-12
240	3.12	Schematics of a GEM showing the cathode on top, the GEM foil separating the gas volume into the drift region, in between the cathode and foil, and the induction region, in between the GEM foil and the anode, and the anode on which a 2D readout is installed. A negative voltage is applied on the cathode while the anode is connected to the ground.	3-13
245	3.13	Left: Picture of a CMS GEM foil provided by a scanning electron microscope. Right: Representation of the electric field lines in a GEM hole and of the amplification that electrons and ions undergo in the hole's volume due to the very intense electric field.	3-14
248	3.14	Schematic representation of CMS triple GEMs. The gas volume is divided into 4 areas. The drift area is the region where the primary electrons are created before being amplified a first time while passing through the first GEM foil. Then the process of drift and amplification is repeated twice in following two transfer areas and GEM foils. Finally, the charges have been amplified enough to induce current in the read-out strips while in the last drift area. The dimensions, potentials and electric fields are provided.	3-14
255	3.15	Simulated efficiency and rate of the standalone Level-1 muon trigger using tracks reconstructed in CSCs and all GEM stations compared with Phase-I values in the case where only CSCs are used or CSCs+GE1/1. The zones of inefficiency of the CSC subsystem are compensated by the addition of GEMs during Phase-II and the trigger rates is kept from increasing due to the high luminosity.	3-15
260	3.16	Figure 3.16a: Simulated resolution of the muon direction measurement $\Delta\phi$ with Phase-II conditions. In the second endcap station, the resolution is compared in the case of CSCs (ME2/1) alone and CSCs+GEMs (GE2/1+ME2/1) while a similar resolution measurement is given in the case of the first station (GE1/1+ME1/1). Figure 3.16b: The addition of GEM detectors on stations 1 and 2 (ME0 is considered to contribute to station station 1) as redundant system to CSCs allows to improve the muon momentum improvement through a more accurate measurement of the local bending angles ϕ_1 and ϕ_2	3-16
268	3.17	Schematics of the data communication chain for DAQ of the GEM subsystems. The sending of trigger data via optical links to the CSC OTMBs is only done for GE1/1 and GE2/1 to match the data with ME1/1 and ME2/1.	3-16

271 3.18 Figure 3.18a: Energy spectrum of GIF++ ^{137}Cs source as measured by the GE1/1
 272 detector installed in GIF++. Figure 3.18b: Evolution of the normalized gain of the
 273 GE1/1 detector installed at in GIF++ as a function of the integrated charge per unit
 274 area. The first part of the study, up to a charge of 55 mC/cm^2 had been done in the
 275 former Gamma Irradiation Facility (GIF) that has now been dismantled following
 276 the construction of GIF++. No variation of the normalized gain can be observed
 277 after an accumulation of 110 mC/cm^2 3-17

278 3.19 Figure 3.19a: Comparison of the gas gain as a function of the divider voltage before
 279 and after the irradiation of a triple-GEM by neutrons in CHARM. Figure 3.19b:
 280 Comparison of the gas gain as a function of the divider voltage before and after the
 281 irradiation of a triple-GEM by alpha particles. 3-18

282 3.20 Data flow of the Level-1 Trigger during Phase-II operations. 3-20

283 3.21 Comparison of Phase-II DT trigger primitives algorithmic efficiency for segments
 284 obtained with 2 super-layers (quality $\geq 6/8$) and 1 super-layer only (quality = 4/4).
 285 The simulation was done by generating 2×10^6 muons. The candidate tracks with
 286 correct time identification is showed with open symbols. 3-21

287 3.22 Simulated spatial (3.22a) and angular (3.22b) resolution of the algorithm using 8
 288 aligned hits in both super-layers (quality = 8/8) and 4 aligned hits in only one super-
 289 layer (quality = 4/4). The contribution of intermediate quality tracks (6 aligned hits)
 290 is negligible in the angular range shown. [Be careful to update this caption as it
 291 uses a text to close to the published one.] 3-21

292 3.23 Efficiency of the L1 trigger in the endcap region after Phase-II upgrade in the case
 293 CSC/GEM/RPC hits are requested in at least 2 stations out of four (3.23a) and in all
 294 four stations (3.23b). 3-22

295 3.24 Resolution of the LCT ambiguous events thanks to the combination of CSC and
 296 iRPC readout data. Using CSCs only, 2 pairs of hits are possible. 3-23

297 3.25 The angular resolution on reconstructed muon tracks in the GEM overlap region
 298 $2.0 < |\eta| < 2.15$ is compared for Phase-II conditions in the case CSC are alone
 299 (Figure 3.25a) and in the case the GEMs' data, including ME0, is combined to which
 300 of CSCs (Figure 3.25b). 3-23

301 3.26 Comparison of L1 trigger performances for prompt muons with and without the
 302 addition of GEMs in the region $2.1 < |\eta| < 2.4$ at Phase-II conditions. GEMs would
 303 allow a reduction of the trigger accept rate by an order of magnitude (Figure 3.26a)
 304 while increasing the trigger efficiency (Figure 3.26b). 3-24

305 3.27 The efficiency (solid lines) and streamer probability (dashed lines) of HFO/CO_2
 306 (Figure 3.27a) and CF_3I/CO_2 (Figure 3.27b) based gas mixtures as a function of
 307 the effective high-voltage are compared with the present CMS RPC gas mixture
 308 represented in black. The detector used for the study is a single gap RPC with similar
 309 properties than CMS RPCs. The streamer probability is defined as the proportion of
 310 events with a deposited charge greater than 20 pC 3-25

311 4.1 Different phases of the avalanche development in the RPC gas volume subjected to
 312 a constant electric field E_0 . a) An avalanche is initiated by the primary ionisation
 313 caused by the passage of a charged particle through the gas volume. b) Due to
 314 its growing size, the avalanche starts to locally influence the electric field. c) The
 315 electrons, lighter than the cations reach the anode first. d) The ions reach the cathode.
 316 While the charges have not recombined, the electric field in the small region around
 317 the avalanche stays affected and locally blinds the detector. 4-2

- 318 4.2 Movement of the charge carriers in an RPC. Figure 4.2a: Voltage across an RPC
 319 whose electrode have a relative permittivity of 5 at the moment the tension s applied.
 320 Figure 4.2b: After the charge carriers moved, the electrodes are charged and there
 321 is no voltage drop over the electrodes anymore. The full potential is applied on the
 322 gas gap only. Figure 4.2c: The streamer discharge initiated by a charged particle
 323 transports electrons and cations towards the anode and cathode respectively. 4-4
- 324 4.3 Typical oscilloscope pulses in streamer mode (Figure 4.3a) and avalanche mode(Figure 4.3b).
 325 In the case of streamer mode, the very small avalanche signal is visible. 4-4
- 326 4.4 Rate capability comparison for the streamer and avalanche mode of operation. An
 327 order of magnitude in rate capability for a maximal efficiency drop of 10% is gained
 328 by using the avalanche mode over the streamer mode. 4-5
- 329 4.5 Comparison of the charge distribution of signals induced by cosmic muons in an
 330 RPC operated with a gas mixture of argon, butane and bromotrifluoromethane (CF_3Br).
 331 The Ar/C_4H_{10} is kept constant at 60/40 in volume while the total amount of CF_3Br
 332 in the mixture is varied: 0% (Figure 4.5a), 4% (Figure 4.5b) and 8% (Figure 4.5c) [39]. 4-6
- 333 4.6 Comparison of the efficiency and streamer probability, defined as the fraction of
 334 events with an induced charge 10 times larger than that of the average avalanche,
 335 with and without irradiation by a 24 GBq ^{137}Cs source of an RPC successively
 336 operated with a 90/10 mixture $C_2H_2F_4/i-C_4H_{10}$ (Figure 4.6a) and a 70/5/10/15
 337 mixture of $Ar/i-C_4H_{10}/CO_2/C_2H_2F_4$ (Figure 4.6b) [40]. 4-6
- 338 4.7 Comparison of the fast charge ratio with and without irradiation by a 24 GBq ^{137}Cs
 339 source of an RPC successively operated with a 90/10 mixture $C_2H_2F_4/i-C_4H_{10}$
 340 (Figure 4.7a) and a 70/5/10/15 mixture of $Ar/i-C_4H_{10}/CO_2/C_2H_2F_4$ (Figure 4.7b).
 341 The results are provided for both single gap and double gap operation [40]. 4-7
- 342 4.8 Efficiency (circles and stars with 30 mV and 100 mV thresholds respectively) and
 343 streamer probability (opened circles) as function of the operating voltatge of a 2 mm
 344 single gap HPL RPC flushed with a gas mixture containing (a) 5%, (b) 2%, (c) 1%
 345 and (d) no SF_6 [42]. 4-8
- 346 4.9 Evolution of the efficiency, working voltage, and voltage at 50% of maximum ef-
 347 ficiency for CMS Barrel (Figure 4.9a) and Endcap (Figure 4.9b) RPCs obtained
 348 through yearly voltage scans since 2011. The working voltage of each RPC is up-
 349 dated after each voltage scan to ensure optimal operation [57]. 4-9
- 350 4.10 Comparison of the rate capability of 8 mm and 2 mm wide RPCs. The lines are
 351 linear fits on the data [59]. 4-10
- 352 4.11 Distributions of the induced charge of fast signals on 2 mm (Figure 4.11a) and 8 mm
 353 (Figure 4.11b) RPCs exposed to a radiation rate of 100 Hz/cm². Average induced
 354 charge of fast signals as a function of the high voltage applied on 2 mm and 8 mm
 355 RPCs (Figure 4.11c). In the case of the 2 mm RPC, a saturation of the pre-amplifier
 356 was observed. The average of the distribution is underestimated and the median is
 357 showed together with the average to account for this bias [59]. 4-10
- 358 4.12 Time distributions of the leading, trailing, and average of both leading and traling
 359 edges for 2 mm (top row) and 8 mm (bottom row) RPCs exposed to a 100 Hz/cm²
 360 radiation rate. The data was collected with RPCs operated at the voltage correspond-
 361 ing to the knee of the efficiency distribution, defined as the point where 95% of the
 362 maximum efficiency is obtained [59]. 4-11

- 363 4.13 Possible double-gap RPC layouts: a) "standard" 1D double-gap RPC, as used in
364 CMS experiment, where the anodes are facing each other and a 1D read-out plane
365 is sandwiched in between them, b) double read-out double-gap RPC as used in AT-
366 LAS experiment, where the cathodes are facing each other and 2 read-out planes are
367 used on the outer surfaces. This last layout can offer the possibility to use a 2D
368 reconstruction by using orthogonal read-out planes. 4-12
- 369 4.14 Comparison of performance of CMS double and single gap RPCs using cosmic
370 muons [55]. Figure 4.14a: Comparison of efficiency sigmoids. Figure 4.14b: Volt-
371 age distribution at 95% of maximum efficiency. Figure 4.14c: $\Delta_{10\%}^{90\%}$ distribution. . . 4-12
- 372 4.15 Representation of different RPC layouts (wide gap on Figure (a), double gap on
373 Figure (b) and multigap on Figure (c)), of the corresponding sensitive volume in
374 gray, and of the associated avalanche size [45]. 4-13
- 375 4.16 Time distributions of the leading, trailing, and average of both leading and trailing
376 edges for multigap RPCs consisting in two 4 mm (Figure 4.16a) and four 2 mm
377 (Figure 4.16b) exposed to a 100 Hz/cm² radiation rate. The data was collected with
378 RPCs operated at the voltage corresponding to the knee of the efficiency distribution,
379 defined as the point where 95% of the maximum efficiency is obtained [45]. 4-14
- 380 4.17 Presentation of a study of a possible ALICE MRPC cell using 250 μm gas gaps,
381 620 μm outer glass electrodes, and 550 μm inner floating electrodes (Figure 4.17a),
382 and of its time resolution performance as a function of the applied high voltage for
383 different radiation levels referred through different filter settings of the 740 GBq
384 ^{137}Cs source the former CERN GIF facility [60]. 4-14
- 385 4.18 Particle identification applied to electrons in the STAR experiment. The identifica-
386 tion is performed combining ToF and dE/dx measurements [65]. 4-15
- 387 4.19 Comparison of the detector performance of ALICE ToF MRPC [66] at fixed applied
388 voltage (in blue) and at fixed effective voltage (in red). The effective voltage is kept
389 fixed by increasing the applied voltage accordingly to the current drawn by the detector. 4-16
- 390 4.20 Ratio between total induced and drifting charge have been simulated for single gap,
391 double-gap and multigap layouts [67]. The total induced charge for a double-gap
392 RPC is a factor 2 higher than for a multigap. 4-17
- 393 4.21 Charge spectra have been simulated for single gap, double-gap and multigap lay-
394 outs [67]. It appears that when single gap shows a decreasing spectrum, double and
395 multigap layouts exhibit a spectrum whose peak is detached from the origin. The
396 detachment gets stronger as the number of gaps increases. 4-17
- 397 4.22 The maximal theoretical efficiency is simulated for single gap, double-gap and multi-
398 gap layouts [67] at a constant gap thickness of 2 mm and using an effective Townsend
399 coefficient of 9 mm⁻¹. 4-18
- 400 4.23 Mass stopping power as a function of $\beta\gamma = p/Mc$ for positive muons in copper [68].
401 The total stopping power is indicated with solid line and local components with
402 dashed lines. the vertical bands are used to indicate boundaries between different
403 approximations used at different energy range. 4-18
- 404 4.24 Mean mass stopping power for liquid hydrogen, as used in bubble chambers, gaseous
405 helium, carbon, aluminum, iron, tin, and lead without the inclusion of radiative effect
406 at higher $\beta\gamma$ necessary for pions and muons in denser materials [68]. 4-20
- 407 4.25 Mean excitation energies normalized to the atomic number as adopted by the ICRU [68,
408 72, 73]. 4-21
- 409 4.26 Mean mass stopping power at minimum ionization as a function of the atomic num-
410 ber [68]. 4-21

411	4.27 Example of straggling function $f(\Delta)$ of particles passing through 1.2 cm of Argon gas with a $\beta\gamma$ of 3.6 and represented with a solid line. The original Landau distribu- tion is showed with a dashed line [74].	4-22
412		
413		
414	4.28 Evolution of straggling functions $f(\Delta)$ of particles passing through a volume of Argon gas with a $\beta\gamma$ of 3.6 with increasing thickness x [74].	4-22
415		
416	4.29 Photo-absorption cross section as computed by HEED for nobles gases with different electric shell numbers [70].	4-24
417		
418	4.30 Photo-absorption cross section as computed by HEED for typical RPC gas mix- tures [70]. The RPC mixture with CO_2 corresponds to the mixture used by CALICE SDHCAL [78] while the other one was foreseen for the experiment ATLAS [79] but has been changed since then.	4-24
419		
420		
421		
422	4.31 Distributions of number of electrons (left) and energy loss (right) for a 5 GeV/c muon passing through 1.2 mm of Helium (Figure 4.31a), Argon (Figure 4.31b) or a typical RPC gas mixture (Figure 4.31c) [70].	4-25
423		
424		
425	4.32 Figure 4.32a: Mean cluster density for muons through different gas volumes [70]. Figure 4.32b: Distribution of the number of electrons per cluster for a 5 GeV/c muon traveling through a mixture of 96.7% $C_2H_2F_4$, 3% i- C_4H_{10} and 0.3% SF_6 [70, 79].	4-26
426		
427		
428		
429	4.33 Townsend and attachment coefficient for a typical 96.7/3/0.3 mixture of $C_2H_2F_4$ /i- C_4H_{10} / SF_6 , at a temperature $T = 296.15$ K and a pressure $P = 1013$ hPa [70, 79]. .	4-27
430		
431	4.34 Comparison of the distribution law of Furry and the Poisson law for $\bar{n} = 5$ [82]. . .	4-28
432		
433	4.35 Single-electron avalanche size distribution in a proportionnal counter filled with methylal at different E/p values. (a) 70, (b) 76.5, (c) 105, (d) 186.5, (e) 426V/cm torr [83].	4-28
434		
435	4.36 Figure 4.36a: Comparison of avalanche size distributions for different values of Townsend and attachment coefficients. The effective Townsend coefficient is the same for both distributions. Figure 4.36b: Fluctuation in avalanche size for avalanche started by a single electron with $\alpha = 13 \text{ mm}^{-1}$ and $\eta = 3.5 \text{ mm}^{-1}$ [79].	4-30
436		
437		
438	4.37 Figure 4.37a: Electron mean drift velocity v_D in pure $C_2H_2F_4$ and typical RPC gas mixtures. Figure 4.37b: Transverse diffusion coefficient in pure $C_2H_2F_4$ and a typical RPC gas mixture. Figure 4.37c: Longitudinal diffusion coefficient in pure $C_2H_2F_4$ and a typical RPC gas mixture. All results are given with a pressure $P =$ 760 Torr and a temperature $T = 296.15$ K [70].	4-31
439		
440		
441		
442		
443	4.38 Comparison of the free charge carriers in the gas after a time $t = 7.90$ ns in the case where no diffusion is taken into account to simulate the avalanche (Figure 4.38a) and in the case where the diffusion is implemented (Figure 4.38b) [70].	4-31
444		
445		
446	4.39 Schematic representation of an avalanche and of the electric field deformation it causes due to the local concentration of charge carriers [51].	4-33
447		
448	4.40 Evolution of the charge induced by an avalanche started by a single electron in a 1.2 mm thick RPC with an applied electric field of 54 kV/cm in the case space charge is not taken into account (Figure 4.40a) and in the case it is implemented into the simulation (Figure 4.40b). The total induced charge is correlated to the size of the avalanche [70].	4-34
449		
450		
451		
452		
453	4.41 Distributions of charge carriers within the gas volume of a 1.2 mm thick RPC and the corresponding deformation of the electric field at different time steps with an applied electric field of 55.5 kV/cm [70].	4-34
454		
455		
456	4.42 Representation of the weighting field in the volume of a RPC and the resulting in- duced current in the strip placed at 1 V and its neighbour connected to the ground. The induced current corresponds, as can be understood from Formula 4.22 [51]. . .	4-35
457		
458		
459	4.43 Schematics of CMS RPC FEE logic.	4-36

460	4.44	Equivalence in between the charge of the induced signal in input of the CMS FEE and the signal strength on the output of the pre-amplifier.	4-36
461			
462	4.45	Description of the principle of a CFD. A comparison of threshold triggering (left) and constant fraction triggering (right) is shown in Figure 4.45a. Constant frac- tion triggering is obtained thanks to zero-crossing technique as explained in Fig- ure 4.45b. The signal arriving at the input of the CFD is split into three components. A first one is delayed and connected to the inverting input of a first comparator. A second component is connected to the noninverting input of this first comparator. A third component is connected to the noninverting input of another comparator along with a threshold value connected to the inverting input. Finally, the output of both comparators is fed through an AND gate.	4-37
463			
464			
465			
466			
467			
468			
469			
470			
471	5.1	Figure 5.1a: The integrated charge per region (Barrel, Endcap) is extrapolated to HL-LHC integrated luminosity (3000 fb^{-1}) using the data accumulated in 2016 in every HV channels. Figure 5.1b: The hit rate per region (Barrel, Endcap) is linearly extrapolated to HL-LHC highest instantaneous luminosity ($5 \times 10^{34} \text{ cm}^{-2}\text{s}^{-1}$) using the rate as a function of instantaneous luminosity recorded by RPCs in 2017 showing a linear dependence.	5-2
472			
473			
474			
475			
476			
477	5.2	Background Fluka simulation compared to 2016 Data at $L = 10^{34} \text{ cm}^{-2}\text{s}^{-1}$ in the fourth endcap disk region. A mismatch in between simulation and data can be ob- served.	5-3
478			
479			
480	5.3	Layout of the test beam zone called X5c GIF at CERN. Photons from the radioactive source produce a sustained high rate of random hits over the whole area. The zone is surrounded by 8 m high and 80 cm thick concrete walls. Access is possible through three entry points. Two access doors for personnel and one large gate for material. A crane allows installation of heavy equipment in the area.	5-4
481			
482			
483			
484			
485	5.4	^{137}Cs decays by β^- emission to the ground state of ^{137}Ba (BR = 5.64%) and via the 662 keV isomeric level of ^{137}Ba (BR = 94.36%) whose half-life is 2.55min.	5-5
486			
487	5.5	Floor plan of the GIF++ facility. When the facility downstream of the GIF++ takes electron beam, a beam pipe is installed along the beam line (z-axis). The irradiator can be displaced laterally (its center moves from $x = 0.65 \text{ m}$ to 2.15 m), to increase the distance to the beam pipe.	5-5
488			
489			
490			
491	5.6	Simulated unattenuated current of photons in the xz plane (Figure 5.6a) and yz plane (Figure 5.6b) through the source at $x = 0.65 \text{ m}$ and $y = 0 \text{ m}$. With angular correction filters, the current of 662 keV photons is made uniform in xy planes.	5-6
492			
493			
494	5.7	Signals from the RPC strips are shaped by the FEE described on Figure 5.7a. Out- put LVDS signals are then read-out by a TDC module connected to a computer or converted into NIM and sent to scalers. Figure 5.7b describes how these converted signals are put in coincidence with the trigger.	5-7
495			
496			
497			
498	5.8	Description of the RPC setup. Dimensions are given in mm. A tent containing RPCs is placed at 1720 mm from the source container. The source is situated in the center of the container. RE-4-2-BARC-161 chamber is 160 mm inside the tent. This way, the distance between the source and the chambers plan is 2060 mm. Figure 5.8a provides a side view of the setup in the xz plane while Figure 5.8b shows a top view in the yz plane.	5-8
499			
500			
501			
502			
503			
504	5.9	RE-4-2-BARC-161 chamber is inside the tent as described in Figure 5.8. In the top right, the two scintillators used as trigger can be seen. This trigger system has an inclination of 10° relative to horizontal and is placed above half-partition B2 of the RPCs. PMT electronics are shielded thanks to lead blocks placed in order to protect them without stopping photons from going through the scintillators and the chamber.	5-8
505			
506			
507			
508			

509	5.10 Hit distributions over all 3 partitions of RE-4-2-BARC-161 chamber is showed on these plots. Top, middle and bottom figures respectively correspond to partitions A, B, and C. These plots show that some events still occur in other half-partitions than B2, which corresponds to strips 49 to 64, in front of which the trigger is placed, contributing to the inefficiency of detection of cosmic muons. In the case of partitions A and C, the very low amount of data can be interpreted as noise. On the other hand, it is clear that a little portion of muons reach the half-partition B1, corresponding to strips 33 to 48.	5-9
510		
511		
512		
513		
514		
515		
516		
517	5.11 Results are derived from data taken on half-partition B2 only. On the 18 th of June 2014, data has been taken on chamber RE-2-BARC-161 at building 904 (Prevessin Site) with cosmic muons providing us a reference efficiency plateau of $(97.54 \pm 0.15)\%$ represented by a black curve. A similar measurement has been done at GIF on the 21 st of July with the same chamber giving a plateau of $(78.52 \pm 0.94)\%$ represented by a red curve.	5-10
518		
519		
520		
521		
522		
523	5.12 Representation of the layout used for the simulations of the test setup. The RPC is represented as a yellow trapezoid while the two scintillators as blue cuboids looking at the sky. A green plane corresponds to the muon generation plane within the simulation. Figure 5.8a shows a global view of the simulated setup. Figure 5.8b shows a zommed view that allows to see the 2 scintillators as well as the full RPC plane.	5-11
524		
525		
526		
527		
528	5.13 γ flux $F(D)$ is plot using values from table 5.1. As expected, the plot shows similar attenuation behaviours with increasing distance for each absorption factors.	5-14
529		
530	5.14 Figure 5.14a shows the linear approximation fit done via formulae 5.7 on data from table 5.2. Figure 5.14b shows a comparison of this model with the simulated flux using a and b given in figure 5.14a in formulae 5.4 and the reference value $D_0 = 50$ cm and the associated flux for each absorption factor F_0^{ABS} from table 5.1	5-16
531		
532		
533		
534	5.15 Dose measurements has been done in a plane corresponding to the tents front side. This plan is 1900 mm away from the source. As explained in the first chapter, a lens-shaped lead filter provides a uniform photon flux in the vertical plan orthogonal to the beam direction. If the second line of measured fluxes is not taken into account because of lower values due to experimental equipments in the way between the source and the tent, the uniformity of the flux is well showed by the results.	5-18
535		
536		
537		
538		
539		
540	5.16	5-19
541	5.17 Evolution of the maximum efficiency for RE2 (5.17a) and RE4 (5.17b) chambers with increasing extrapolated γ rate per unit area at working point. Both irradiated (blue) and non irradiated (red) chambers are shown.	5-20
542		
543		
544	5.18 Evolution of the working point for RE2 (5.18a) and RE4 (5.18b) with increasing extrapolated γ rate per unit area at working point. Both irradiated (blue) and non irradiated (red) chambers are shown.	5-21
545		
546		
547	5.19 Evolution of the maximum efficiency at HL-LHC conditions, i.e. a background hit rate per unit area of 300 Hz/cm ² , with increasing integrated charge for RE2 (5.19a) and RE4 (5.19b) detectors. Both irradiated (blue) and non irradiated (red) chambers are shown. The integrated charge for non irradiated detectors is recorded during test beam periods and stays small with respect to the charge accumulated in irradiated chambers.	5-21
548		
549		
550		
551		
552		
553	5.20 Comparison of the efficiency sigmoid before (triangles) and after (circles) irradiation for RE2 (5.20a) and RE4 (5.20b) detectors. Both irradiated (blue) and non irradiated (red) chambers are shown.	5-22
554		
555		
556	5.21 Evolution of the Bakelite resistivity for RE2 (5.21a) and RE4 (5.21b) detectors. Both irradiated (blue) and non irradiated (red) chambers are shown.	5-22
557		

558	5.22 Evolution of the noise rate per unit area for the irradiated chamber RE2-2-BARC-9 only.	5-23
560	A.1 (A.1a) View of the front panel of a V1190A TDC module [89]. (A.1b) View of the 561 front panel of a V1718 Bridge module [90]. (A.1c) View of the front panel of a 6U 562 6021 VME crate [91].	A-3
563	A.2 Module V1190A <i>Trigger Matching Mode</i> timing diagram [89].	A-4
564	A.3 Structure of the ROOT output file generated by the DAQ. The 5 branches (<code>EventNumber</code> , 565 <code>number_of_hits</code> , <code>Quality_flag</code> , <code>TDC_channel</code> and <code>TDC_TimeStamp</code>) are visible on 566 the left panel of the ROOT browser. On the right panel is visible the histogram cor- 567 responding to the variable <code>nHits</code> . In this specific example, there were approximately 568 50k events recorded to measure the gamma irradiation rate on the detectors. Each 569 event is stored as a single entry in the <code>TTree</code>	A-10
570	A.4 The effect of the quality flag is explained by presenting the content of <code>TBranch</code> 571 <code>number_of_hits</code> of a data file without <code>Quality_flag</code> in Figure A.4a and the con- 572 tent of the same <code>TBranch</code> for data corresponding to a <code>Quality_flag</code> where all TDCs 573 were labelled as <code>GOOD</code> in Figure A.4b taken with similar conditions. It can be noted 574 that the number of entries in Figure A.4b is slightly lower then in Figure A.4a due 575 to the excluded events.	A-12
576	A.5 Using the same data as previously showed in Figure A.4, the effect of the quality 577 flag is explained by presenting the reconstructed hit multiplicity of a data file with- 578 out <code>Quality_flag</code> in Figure A.5a and the reconstructed content of the same RPC 579 partition for data corresponding to a <code>Quality_flag</code> where all TDCs were labelled as 580 <code>GOOD</code> in Figure A.5b taken with similar conditions. The artificial high content of bin 581 0 is completely suppressed.	A-12
582	A.6 WebDCS DAQ scan page. On this page, shifters need to choose the type of scan 583 (Rate, Efficiency or Noise Reference scan), the gamma source configuration at the 584 moment of data taking, the beam configuration, and the trigger mode. These in- 585 formation will be stored in the DAQ ROOT output. Are also given the minimal 586 measurement time and waiting time after ramping up of the detectors is over before 587 starting the data acquisition. Then, the list of HV points to scan and the number of 588 triggers for each run of the scan are given in the table underneath.	A-14
589	B.1 Example of expected hit time distributions in the cases of efficiency (Figure B.1a) 590 and noise/gamma rate per unit area (Figure B.1b) measurements as extracted from 591 the raw ROOT files. The unit along the x-axis corresponds to ns. The fact that 592 "the" muon peak is not well defined in Figure B.1a is due to the contribution of all 593 the RPCs being tested at the same time that don't necessarily have the same signal 594 arrival time. Each individual peak can have an offset with the ones of other detectors. 595 The inconsistancy in the first 100 ns of both time distributions is an artefact of the 596 TDCs and are systematically rejected during the analysis.	B-16
597	B.2 The effect of the quality flag is explained by presenting the reconstructed hit multi- 598 plicity of a data file without <code>Quality_flag</code> . The artificial high content of bin 0 is the 599 effect of corrupted data.	B-19

List of Tables

608

609	3.1	Details of the greenhouse fluorinated gases used in CMS and of their GWP [23].	3-24
610	4.1	Properties of the most used electrode materials for RPCs.	4-3
611	5.1	Total photon flux ($E\gamma \leq 662$ keV) with statistical error predicted considering a 612 ^{137}Cs activity of 740 GBq at different values of the distance D to the source along 613 the x-axis of irradiation field [86].	5-13
614	5.2	Correction factor c is computed thanks to formulae 5.5 taking as reference $D_0 =$ 615 50 cm and the associated flux F_0^{ABS} for each absorption factor available in table 5.1.	5-15
616	5.3	The data at D_0 in 1997 is taken from [86]. In a second step, using Equations 5.8 617 and 5.9, the flux at D can be estimated in 1997. Then, taking into account the 618 attenuation of the source activity, the flux at D can be estimated at the time of the 619 tests in GIF in 2014. Finally, assuming a sensitivity of the RPC to γ $s = 2 \times 10^{-3}$, 620 an estimation of the hit rate per unit area is obtained.	5-17
621	A.1	Inter-process communication cycles in between the webDCS and the DAQ through 622 file string signals.	A-19

623

List of Acronyms

624

List of Acronyms

625

626

A

628

629 AFL
630 ALCTs

Almost Full Level
anode local charged track boards

631

632

B

633

635 BARC
636 BLT
637 BMTF
638 BNL
639 BR

Bhabha Atomic Research Centre
Block Transfer
Barrel Muon Track Finder
Brookhaven National Laboratory
Branching Ratio

640

641

C

642

644 CAEN
645 CERN
646 CFD
647 CFEBs
648 CMB
649 CMS
650 CSC
651 CuOF

Costruzioni Apparecchiature Elettroniche Nucleari S.p.A.
European Organization for Nuclear Research
Constant Fraction Discriminator
cathode front-end boards
Cosmic Microwave Background
Compact Muon Solenoid
Cathode Strip Chamber
copper-to-optical-fiber translators

652

653

D

654

656 DAQ
657 DCS
658 DQM

Data Acquisition
Detector Control Software
Data Quality Monitoring

659	DT	Drift Tube
660		
661		
662	E	
663		
664	ECAL	electromagnetic calorimeter
665	EMTF	Endcap Muon Track Finder
666		
667		
668	F	
669		
670	FCC	Future Circular Collider
671	FEE	Front-End Electronics
672	FEB	Front-End Board
673	FWHM	full-width-at-half-maximum
674		
675		
676	G	
677		
678	GE-/-	Find a good description
679	GE1/1	Find a good description
680	GE2/1	Find a good description
681	GEANT	GEometry ANd Tracking - a series of software toolkit platforms developed by CERN
682		
683	GEB	GEM Electronics board
684	GEM	Gas Electron Multiplier
685	GIF	Gamma Irradiation Facility
686	GIF++	new Gamma Irradiation Facility
687	GWP	Global Warming Potential
688		
689		
690	H	
691		
692	HCAL	hadron calorimeter
693	HL-LHC	High Luminosity LHC
694	HPL	High-pressure laminate
695	HV	High Voltage
696		
697		
698	I	
699		
700	ICRU	International Commission on Radiation Units & Measurements
701	iRPC	improved RPC

702	IRQ	Interrupt Request
703	ISR	Intersecting Storage Rings
704		
705		
706	L	
707		
708	LEIR	Low Energy Ion Ring
709	LEP	Large Electron-Positron
710	LHC	Large Hadron Collider
711	LS1	First Long Shutdown
712	LS2	Second Long Shutdown
713	LS3	Third Long Shutdown
714	LV	Low Voltage
715	LVDS	Low-Voltage Differential Signaling
716		
717		
718	M	
719		
720	MiC1	first version of Minicrate electronics
721	mip's	minimum ionizing particles
722	MC	Monte Carlo
723	MCNP	Monte Carlo N-Particle
724	ME-/	Find good description
725	ME0	Find good description
726	MRPC	Multigap RPC
727		
728		
729	N	
730		
731	NIM	Nuclear Instrumentation Module logic signals
732		
733		
734	O	
735		
736	OH	Optohybrid Board
737	OMTF	Overlap Muon Track Finder
738		
739		
740	P	
741		
742	PAI	Photo-Absorption Ionisation
743	PAIR	Photo-Absorption Ionisation with Relaxation
744	PMT	PhotoMultiplier Tube

745	PS	Proton Synchrotron
746	PU	pile-up
747		
748	Q	
749		
750		
751	QCD	Quantum Chromodynamics
752	QED	Quantum Electrodynamics
753		
754	R	
755		
756		
757	RE/-	Find a good description
758	RE2/2	Find a good description
759	RE3/1	Find a good description
760	RE3/2	Find a good description
761	RE4/1	Find a good description
762	RE4/2	Find a good description
763	RE4/3	Find a good description
764	RMS	Root Mean Square
765	ROOT	a framework for data processing born at CERN
766	RPC	Resistive Plate Chamber
767		
768	S	
769		
770		
771	SC	Synchrocyclotron
772	SLAC	Stanford Linear Accelerator Center
773	SM	Standard Model
774	SPS	Super Proton Synchrotron
775	SUSY	supersymmetry
776		
777	T	
778		
779		
780	TDC	Time-to-Digital Converter
781	TDR	Technical Design Report
782	ToF	Time-of-flight
783	TPG	trigger primitives
784		
785	W	
786		
787		
788	webDCS	Web Detector Control System

789

790

791

792

793 YETS Year End Technical Stop

1

Introduction

794

795

⁷⁹⁶ **1.1 A story of High Energy Physics**

⁷⁹⁷ **1.2 Organisation of this study**

2

798

799

Investigating the TeV scale

800 „We may regard the present state of the universe as the effect of the
801 past and the cause of the future. An intellect which at any given mo-
802 ment knew all of the forces that animate nature and the mutual posi-
803 tions of the beings that compose it, if this intellect were vast enough
804 to submit the data to analysis, could condense into a single formula
805 the movement of the greatest bodies of the universe and that of the
806 lightest atom; for such an intellect nothing could be uncertain and
807 the future just like the past would be present before its eyes.”

808

809 - Pierre Simon de Laplace, *A Philosophical Essay on Probabilities*, 1814

Throughout history, physics experiment became more and more powerful in order to investigate finer details of nature and helped understanding the elementary blocks of matter and the fundamental interactions that bond them in the microscopic world. Nowadays, the Standard Model (SM) of particle physics is the most accurate theory designed to explain the behaviour of particles and was able to make very precise predictions that are constantly verified, although some hints of new physics are visible as bricks are still missing to have a global comprehension of the Universe.

To highlight the limits of the SM and test the different alternative theories, ever more powerful machines are needed. This is in this context that the Large Hadron Collider (LHC) has been thought and built to accelerate and collide particles at energies exceeding anything that had been done before. Higher collision energies and high pile-up imply the use of enormous detectors to measure the properties of the interaction products. The Compact Muon Solenoid (CMS) is a multipurpose experiment that have been designed to study the proton-proton collisions of the LHC and give answers on various high energy physics scenari. Nevertheless, the luminosity delivered by the collider will in the future be increased to levels beyond the original plans to improve its discovery potential giving no choice to experiments such as CMS to upgrade their technologies to cope with the increased radiation levels and detection rates.

2.1 The Standard Model of Particle Physics

In this early 21st century it is now widely accepted that matter is made of elementary blocks referred to as *elementary particles*. The physics theory that classifies and describes the best the behaviour and interaction of such elementary particles is the so called Standard Model that formalizes 3 of the 4 fundamental interactions (electromagnetic, weak and strong interactions). It's development took place during the 20th century thanks to a strong collaboration in between the theoretical and experimental physicists.

2.1.1 A history of particle physics

The idea that nature is composed of elementary bricks, called *atomism*, is not contemporary as it was already discussed by Indian or Greek philosophers during antiquity. In Greece, atomism has been rejected by Aristotelianism as the existance of *atoms* would imply the existance of a void that would violate the physical principles of Aristotle philosophy. Aristotelianism has been considered as a reference in the european area until the 15th century and the italian *Rinascimento* where antic text and history started to be more deeply studied. The re-discovery of Platon's philosophy would allow to open the door to alternative theories and give a new approach to natural sciences where experimentation would become central. A new era of knowledge was starting. By the begining of the 17th century, atomism was re-discovered by philosophers and the very first attempt to estimate an *atom* size would be provided by Magnetus in 1646. Although his *atoms* correspond to what would nowadays be called *molecules*, Magnetus achieved feats by calculating that the number of molecules in a grain of incense would be of the order of 10^{18} simply by considering the time necessary to smell it everywhere in a large church after the stick was lit on. It is now known that this number only falls short by 1 order of magnitude.

An alternative philosophy to atomism popularized by Descartes was corpuscularianism. Built on ever divisible corpuscles, contrary to atoms, it's principles would be mainly used by alchemists like Newton who would later develop a corpuscular theory of light. Boyle would combine together ideas of both atomism or corpuscularianism leading to mechanical philosophy. The 18th century have

seen the development of engineering providing philosophical thought experiments with repeatable demonstration and a new point of view to explain the composition of matter and Lavoisier would greatly contribute to chemistry and atomism by publishing in 1789 a list of 33 chemical elements corresponding to what is now called *atoms*. In the early 19th century Dalton would summarize the knowledge on composition of matter and Fraunhofer would invent the spectrometer and discover the spectral lines. The rise of atomic physics, chemistry and mathematical formalism would unravel the different atomic elements and ultimately, the 20th century would see the very first sub-atomic particles.

Discovery of the inner structure of the atom

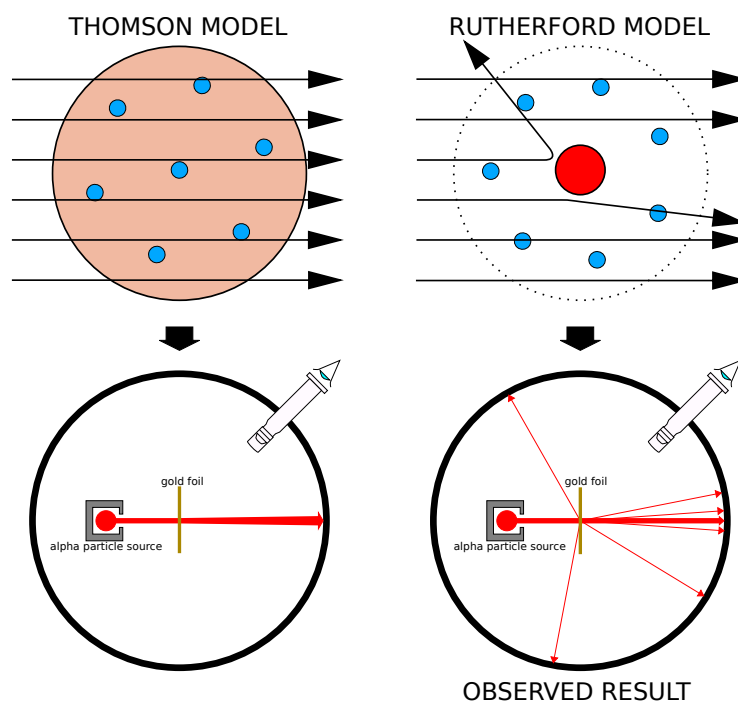


Figure 2.1: Through the gold foil experiment Rutherford could show that most of the mass of atoms was contained in a positively charged nucleus and could then propose a more accurate atomic model than that of Thomson.

The negative *electron* would be the first to be discovered in 1897 by Thomson after 3 decades of research on cathode rays by proving that the electrification observed in an electroscope, as reported by Perrin, was due to the rays themselves and that they had to be composed of electrically charged particles. In 1900, Becquerel would show the *beta rays* emitted by radium had the same charge over mass ratio than what measured by Thomson for cathode rays, pointing to electrons as a constituent of atoms. In 1907, Rutherford and Royds showed that *alpha* particles, once captured in a tube and subjected to an electric spark causing an electron avalanche, where helium ions as they could combine with 2 electrons to form a ${}^4\text{He}$. This discovery was directly followed by the constraint of the atom structure in 1909 through the gold foil experiment in which the deflection angle of alpha particles fired at a very thin gold foil was measured and highlighted atoms where mainly empty with

871 nearly all its mass contained into a tiny positively charged *nucleus*. With these two observations,
 872 he could formulate the Rutherford model of the atom in 1911, shown together with the Thomson
 873 plum pudding model in Figure 2.1. The link in between atomic number and number of positive and
 874 negative charges contained into the atoms would fast be understood and the different kind of element
 875 transmutation appeared to be purely nuclear processes making clear that the electromagnetic nature
 876 of chemical transformation could not possibly change nuclei. Thus a new branch in physics appeared
 877 to study nuclei exclusively: the nuclear physics.

878 Moreover, in 1913 quantum physics would be introduced into the atomic model by Bohr based
 879 on the assumptions of Plank to explain spectral lines, and other observed quantum effects. The same
 880 year, Moseley would confirm Bohr's model and Debye would extend it by introducing elliptical
 881 orbits.

882 By studying alpha emission and the product of their interaction with nitrogen gas, Rutherford
 883 reported in 1919 the very first nuclear reaction leading to the discovery that the hydrogen nucleus was
 884 composed of a single positively charged particle that was later baptised *proton*. This idea came from
 885 1815 Prout's hypothesis proposing that all atoms are composed of "*protyles*" (i.e. hydrogen atoms).
 886 By using scintillation detectors, Rutherford could highlight typical hydrogen nuclei signature and
 887 understand that the impact of alpha particles with nitrogen would knock out an hydrogen nucleus
 888 and produce an oxygen 17, as explicated in Formula 2.1 and would then postulate that protons are
 889 building bricks of all elements.



890 With this assumption and the discovery of isotopes together with Aston, elements with identical
 891 atomic number but different masses, Rutherford would propose that all elements' nuclei but hydrogen's are composed of both charged particles, protons, and of chargeless particles, which he called
 892 *neutrons*, and that these neutral particles would help maintaining nuclei as one, as charged protons
 893 were likely to electrostatically repulse each other, and introduced the idea of a new force, a *nuclear*
 894 force. Though the first idea concerning neutrons was a bond state of protons and electrons as it was
 895 known that the beta decay, emitting electrons, was taking place in the nucleus, it was then showed
 896 that such a model would hardly be possible due to Heisenberg's uncertainty principle and by the
 897 recently measured *spin* of both protons and electrons. The spin, discovered through the study of
 898 the emission spectrum of alkali metals, would be understood as a "two-valued quantum degree of
 899 freedom" and formalized by Pauli and extended by Dirac, to take the relativist case into account.
 900 Measured to be $\frac{1}{2}\hbar$ for both, it was impossible to arrange an odd number of half integer spins and
 901 obtain a global nucleus spin that would be integer. Finally, in 1932, following the discovery of a new
 902 neutral radiation, Chadwick could discover the neutron as an uncharged particle with a mass similar
 903 to that of the proton whose half integer spin would reveal to be the solution to explain the nuclear
 904 spin.

906 Development of the Quantum Electrodynamics

907 Historically, the development of the quantum theory revolved around the question of emission and
 908 absorption of discrete amount of energy through light. Einstein used the initial intuition of Plank
 909 about the black-body radiation to develop in 1905 a model to explain the photoelectric effect in
 910 which light was described by discrete quanta now called *photons*. For this model, Einstein introduced
 911 the concept of wave-particle duality as classical theory was not able to describe the phenomenon.
 912 With the new understanding of atoms and of their structure, classical theories also proved unable

913 to explain atoms stability. Indeed, using classical mechanics, electrons orbiting around a nucleus
 914 should radiate an energy proportional to their angular momentum and thus lose energy through
 915 time and the spectrum of energy emission should then be continuous, but it was known since the
 916 19th century and the discovery of spectral lines that the emission spectrum of material was discrete.

917 This was Bohr who first suggested that a quantum description of the atom was necessary in 1913.
 918 Using the correspondence principle stating that at large enough numbers the quantum calculations
 919 should give the same results than the classical theory, he proposed the very first quantum model
 920 of the hydrogen atom explaining the line spectrum by introducing the principal quantum number
 921 n describing the electron shell. This model would then be improved by Sommerfeld that would
 922 quantize the z-component of the angular momentum, leading to the second and third quantum
 923 numbers, or azimuthal and magnetic quantum number, l and m defining for the second the orbital
 924 angular momentum of the electrons on their shells and thus, the shape of the orbital, and for the third
 925 the available orbital on the subshell for each electron. Nevertheless, although the model was not only
 926 limited to spherical orbitals anymore, making the atom more realistic, the Zeeman effect couldn't be
 927 completely explained by just using n , l and m . A solution would be brought after the discovery of
 928 Pauli in 1924, as Uhlenbeck, Goudsmit, and Kramers proposed in 1925 the idea of intrinsic rotation
 929 of the electron, introducing a new angular momentum vector associated to the particle itself, and
 930 not to the orbital, and associated to a new quantic number s , the *spin* projection quantum number
 931 explaining the lift of degeneracy to an even number of energy levels.

932 The introduction of the *spin* happened 1 year after another attempt of improvement of the theory
 933 was made by De Broglie in his PhD thesis. The original formulation of the quantum theory only
 934 considered photons as energy quanta behaving as both waves and particles. De Broglie proposed
 935 that all matter are described by waves and that their momentum is proportional to the oscillation of
 936 quantized electromagnetic field oscillators. This interpretation was able to reproduce the previous
 937 version of the quantum energy levels by showing that the quantum condition involves an integer
 938 multiple of 2π , as shown by Formula 2.2.

$$p = \hbar k \Leftrightarrow \int pdx = \hbar \int kdx = 2\pi\hbar n \quad (2.2)$$

939 Although the intuition of De Broglie about the wave-particle duality of all matter, his interpreta-
 940 tion was semiclassical and it's in 1926 that the first fully quantum mechanical wave-equation would
 941 be introduced by Schrödinger to describe electron-like particles, reproducing the previous semiclas-
 942 sical formulation without inconsistencies. This complexe equation describes the evolution of the
 943 wave function Ψ of the quantum system, defined by its position vector \mathbf{r} and time t as an energy
 944 conservation law, in which the hamiltonian of the system \hat{H} is explicit, by solving the Equation 2.3.

$$i\hbar \frac{\partial}{\partial t} |\Psi(\mathbf{r}, t)\rangle = \hat{H} |\Psi(\mathbf{r}, t)\rangle \quad (2.3)$$

945 In 1927, Dirac would go further in his paper about emission and absorption of radiation by
 946 proposing a second quantization not only of the physical process at play but also of the electromag-
 947 netic field, providing the ingredients to the first formulation of *Quantum Electrodynamics (QED)*
 948 and the description of photon emission by electrons dropping into a lower energy state in which the
 949 final number of particles is different than the initial one. To complete this model to the many-body
 950 wave functions of identical particles, Jordan included creation and annihilation operators for fields
 951 obeying Fermi-Dirac statistics leading to a model describing particles that would be referred to as
 952 *fermions*. Nevertheless, in order to properly treat electromagnetism, the incorporation of the relativ-

ity theory developed by Einstein. Including gravity into quantum physics still is a challenge nowadays, but in 1928 Pauli and Jordan would show that special relativity's coordinate transformations could be applied to quantum fields as the field commutators were Lorentz invariant. Finally derived the same year, the Dirac equation, shown as Equation 2.4, similarly to Schrödinger's equation, is a single-particle equation but it incorporates special relativity in addition to quantum mechanics rules. It features the 4×4 gamma matrices γ^μ built using 2×2 Pauli matrices and unitary matrix, the 4-gradient ∂_μ , the rest mass m of any half integer spin massive particle described by the wave function $\psi(x, t)$, also called a Dirac spinor, and the speed of light c . In addition to perfectly reproduce the results obtained with quantum mechanics so far, it also provided with *negative-energy solutions* that would later be interpreted as a new form of matter, *antimatter* and give a theoretical justification to the Pauli equation that was phenomenologically constructed to account for the spin as in the non-relativistic limit, the Dirac equation is similar.

$$i\hbar\gamma^\mu\partial_\mu\psi - mc\psi = 0 \quad (2.4)$$

The successes of the QED was soon followed with theoretical problems as computations of any physical process involving photons and charged particles were showed to be only reliable at the first order of perturbation theory. At higher order of the theory, divergent contributions were appearing giving nonsensical results. Only two effects were contributing to these infinities.

- The self-energy of the electron (or positron), the energy that the particle has due its own interaction with its environment.
- The vacuum polarization, virtual electron–positron pairs produced by a background electromagnetic field in the vacuum which is not an "empty" space. These virtual pairs affect the charge and current distributions generated by the original electromagnetic field.

Solving this apparent problem was done by carefully defining the concepts of each observables, for example mass or charge, as these quantities are understood within the context of a non-interacting field equation, and that from the experiment point of view, they are abstractions as what is measured are "renormalized observables" shifted from there "bare" value by the interaction taking place in the measuring process. The infinities needed to be connected to corrections of mass and charge as those are fixed to finite values by experiment. This was the intuition of Bethe in 1947 who successfully computed the effect of such *renormalization* in the non-relativist case. Fully covariant formulations of QED including renormalization was achieved by 1949 by Tomonaga, Schwinger, Feynman and Dyson and Feynman is now famous for his association of diagrams to the term of the scattering matrix, greatly simplifying the representation and computation of interactions as the diagrams directly corresponded the measurable physical processes and would then be used in every quantum field theories. With the resolution of infinities, QED had mostly reached its final form, being still today the most accurate physical theory and would serve as a model to build all other quantum field theories.

Development of the quark model and Quantum Chromodynamics

To explain the nuclear force that holds *nucleons* (protons and neutrons) together, Yukawa theoretically proposed in 1934 the existence of a force carrier called *meson* due to it's predicted mass in the range in between the electron and nucleon masses. Discovered in 1936 by Anderson and Neddermeyer, and confirmed using bubble chambers in 1937 by Street and Stevenson, a first meson

993 candidate was observed in the decay products of cosmic rays. Assuming it had the same electric
 994 charge than electrons and protons, this particle was observed to have a curvature due to magnetic
 995 field that was sharper than protons but smoother than electrons resulting in a mass in between that
 996 of electrons and protons. But its properties were not compatible with Yukawa's theory, which was
 997 emphasized by the discovery of a new candidate in 1947, again in cosmic ray products using photo-
 998 graphic emulsions.

999 This new candidate, although it had a similar mass than the already believed *meson*, would rather
 1000 decay into it. For distinction, the first candidate would then be renamed "*mu meson*" when the second
 1001 would be the "*pi meson*". The *mu meson* was behaving like a heavy electron and didn't participate
 1002 in the strong interaction whereas the pion was believed to be the carrier of the nuclear interaction.
 1003 This lead to classify the *mu* in a new category of particles called *leptons* together with the electron
 1004 that shared similar properties and *the neutrino*, and be renamed *muon*. The *pi meson* was finally
 1005 found to be a triplet of particles: a positively charged, a negatively charged, and a neutral particle.
 1006 The neutral *pi meson* has been more difficult to identify as it wouldn't leave tracks on emulsions nor
 1007 on bubble chambers and needed to be studied via it's decay products. It was ultimately identified in
 1008 University of California's cyclotron in 1950 through the observation of its decay into 2 photons.

1009 Also discovered in 1947 but in cloud chamber photographs, the *K meson* as also been an im-
 1010 portant step towards the establishment of the Standard Model. A triplet of particle, 2 charged and a
 1011 neutral, with a mass roughly half that of a proton, were reported. These particles were baptised *K*
 1012 *meson* in contrast to the "light" *pi* and *mu* "L-mesons". The particularity of the *K* were there very
 1013 slow decays with a typical lifetime of the order of 10^{-10} s much greater than the 10^{-23} s of *pi*-proton
 1014 reactions. The concept of *strangeness*, a new quantum number was then introduced by Pais as an
 1015 attempt to explain this phenomenon as *strange* particles appeared as a pair production of a strange
 1016 and anti-strange particle.

1017 With the development of synchrotrons, the particle *zoo* would grow to several dozens during the
 1018 1950s as higher energies were reachable through acceleration. In 1961, a first classification system,
 1019 called Eightfold Way, was proposed by Gell-Mann and finding its roots in the Gell-Mann–Nishijima
 1020 formula, which relates the electric charge Q , the third component of the isospin I_3 , the *baryon*
 1021 number B and the strangeness S , as explicitated in Formula 2.5. The isospin was a quantum number
 1022 introduced in 1932 to explain symmetries of the newly discovered neutron using representation
 1023 theory of SU(2). The baryon number, was introduced by Nishijima as a quantum number for baryons,
 1024 i.e. particles of the same family as nucleons. The mesons were classified in an octet and baryons of
 1025 spin $\pm \frac{1}{2}$ and $\pm \frac{3}{2}$ were respectively classified into an octet and a decuplet, as shown in Figure 2.2. To
 1026 complete the baryon decuplet, Gell-Mann predicted the existance of baryon Ω^- which would later
 1027 be discovered in 1964.

$$Q = I_3 + \frac{1}{2}(B + S) \quad (2.5)$$

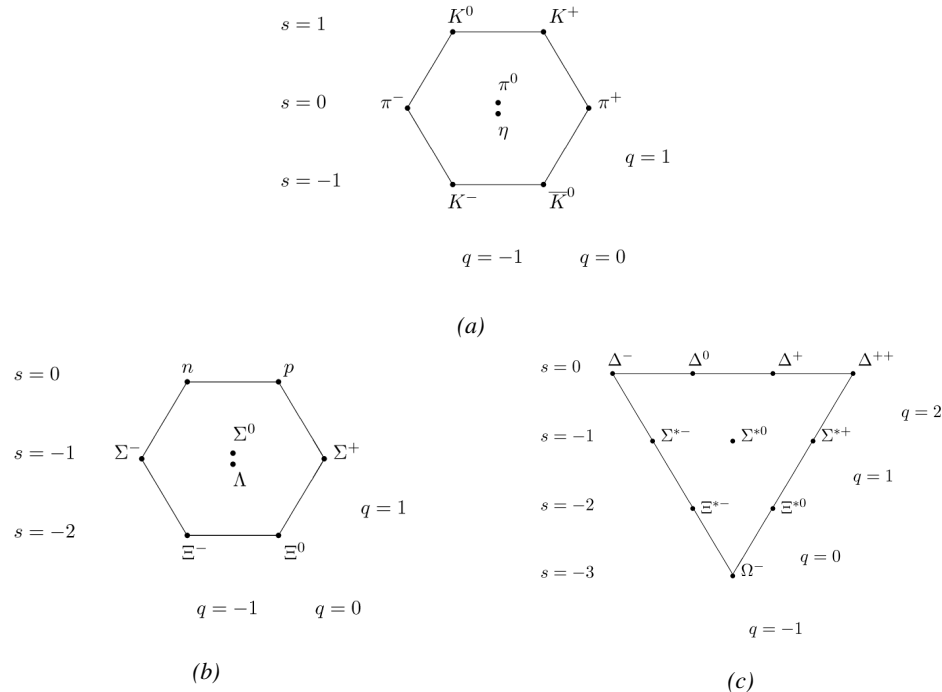


Figure 2.2: Figure 2.2a: Meson octet. Figure 2.2b: Baryon octet. Figure 2.2c: Baryon decuplet.

Strong of this classification using an SU(3) flavor symmetry, Gell-Mann, and independently Zweig, would propose a full theoretical model in which *hadrons* (strongly interacting particles, i.e. mesons and baryons) were not elementary particles anymore. They would rather be composed with 3 flavors of particles called *quarks* and there anti-particles. The 3 flavors were called *up*, *down* and *strange*. *Up* and *down* would be used to explain the nucleons and non-strange mesons, while *strange* would come into the composition of hadrons showing strangeness. *Up* and *down* flavors would be discovered in 1968 thanks to the deep inelastic scattering experiments conducted at the Stanford Linear Accelerator Center (SLAC), and *strange* could only be indirectly validated even though it provided a robust explanation to *kaon* (K) and *pion* (π). However, in the decade following the Gell-Mann-Zweig quark model proposition, several improvement to the model were brought, first by Glashow and Bjorken the same year that predicted the existence of a fourth quark flavor, the *charm*, that would equalize the then known number of quarks and leptons and finally in 1973 by Kobayashi and Maskawa that would increase the number of quarks to 6 to explain the experimental observation of CP violation. These two quarks would be referred to as *top* and *bottom* for the first time in 1975. It's only after these additions to the quark model that finally the *charm* would be discovered in 1974 at both SLAC and Brookhaven National Laboratory (BNL). A meson where the *charm* was bound with an *anti-charm*, called J/ψ , would help convince the physics community of the validity of the model. The *top* would be discovered soon after in 1977 in Fermilab and indicate the existence of the *bottom* that would resist to discovery until Fermilab's experiments CDF and D \emptyset in 1995 due to its very large mass and the energy needed to produce it.

As remarked by Struminsky, the original quark model proposal composed of 3 quarks should possess an additional quantum number due to mesons such as Ω^- or Δ^{++} . Indeed, these mesons are composed of 3 identical quarks, respectively 3 *strange* and *up* quark, with parallel spins, which

should be forbidden by the exclusion principle. Independentle, Greenberg and Han-Nambu proposed an additional SU(3) degree of freedom possessed by the quarks, that would later be refered to as *color charge gauge*, that could interact through *gluons*, the gauge boson octet corresponding to this degree of freedom. Nevertheless, as observing free quarks proved to be impossible, two visions of the quarks were argued mainly due to the failures to observe these particles free to prove their existence. On one side, Gell-Mann proposed to see quarks as mathematical construct instead of real particles, as they are always confined, implying that quantum field theory would not describe entirely the strong interaction. Opposed to this vision, Feynman on the contrary argued that quarks were real particles, that he would call *partons*, that should be described as all other particles by a distribution of position and momentum. The implications of quarks as point-like particles would be verified at SLAC and the concept of *color* would be added to the quark model in 1973 by Fritzsch and Leutwyler together with Gell-Mann to propose a description of the strong interaction through the theory of Quantum Chromodynamics (QCD). The discovery the same year of asymptotic freedom within the QCD by Groos, Politzer and Wilczek, allowed for very precise predictions thanks to the perturbation theory. Nowadays, the confinement of quarks is studied in experiments such as ALICE, through exploration of the quark-gluon plasma.

1067 The Weak interaction, spontaneous symmetry breaking, the Higgs mechanism and the Elec- 1068 troweak unification

1069 The weak interaction is the process that causes radioactive decays. Thanks to the neutron discovery,
1070 Fermi could explain in 1934 the beta radiations through the beta decay process in which the neutron
1071 decays into a proton by emitting an electron. Though the missing energy observed during this
1072 process triggered a huge debate about the apparent non conservation of energy, momentum and spin
1073 of the process, Fermi, as Pauli before him, proposed that the missing energy was due to a neutral
1074 not yet discovered particle that would then be baptised *neutrino*. The impossibility to detect such
1075 a particle would leave some members of the scientific community sceptical, but hints of energy
1076 conservation and of the existence of the neutrino were provided by measuring the energy spectrum
1077 of electrons emitted through beta decay, as there was a strict limit on their energy. It's only 30 years
1078 later in 1953 that it would be discovered by the team of Cowan and Reines using the principle of
1079 inverse beta decay described through Formula 2.6. The experiment consisted in placing water tanks
1080 sandwiched in between liquid scintillators near a nuclear reactor with an estimated neutrino flux of
1081 $5 \times 10^{13} \text{ cm}^{-2} \text{s}^{-1}$. However, in order to explain the absence of some reactions in the experiment
1082 of Cowan and Reines, and constraint the beta decay theory of Fermi and extend it to the case of
1083 the muon, Konopinski and Mahmoud proposed in 1953 that the muon decay would eject a particle
1084 similar to the neutrino and thus predicted the existence of a muon neutrino that would be different
1085 than the one involved in the beta decay, related to the electron. With this, the idea of lepton number
1086 would arise. The muon neutrino would successfully be detected in 1962 by Lederman, Schwartz and
1087 Steinberger.

$$\bar{\nu} + p \rightarrow n + e^+ \quad (2.6)$$

1088 The theory could not be valid though as the probability of interaction, called cross-section, would
1089 have been increasing without bond with the square of the energy. Fermi assumed in a two vector
1090 current coupling but Lee and Yang noted that an axial current could appear and would violate parity.
1091 The experiment of Wu in 1956 would confirm the parity violation and Gamow and Teller would try to
1092 account for it by describing Fermi's interaction through allowed (parity-violating) and superallowed

1093 (parity-conserving) decays. But the success of QED as a quantum field theory would spark the
1094 development of such a theory to describe the weak interaction.

1095 As previously discussed, the great success of QED was built on an underlying symmetry, inter-
1096 preted as a gauge invariance so that the effect of the force is the same in all space-time coordinates,
1097 and of the possibility to renormalize it in order to absorb the infinities. Independently in 1958,
1098 Glashow, and Salam and Ward used 1957 Schwinger ideas about vector intermediary for the decay
1099 processes, could find a way to unite both the electromagnetic and weak interaction into a gauge
1100 theory involving 4 gauge bosons, 3 of which were massive and carried out the weak interaction and
1101 a massless boson carrying the electromagnetic interaction. Among the 3 massive bosons, 2 were
1102 charged and 1 was neutral, similarly to the previously theorized *pi meson* vector of the Yukawa
1103 model and all have a mass much greater than nucleons and thus a very short life time implying a
1104 finite very short range contrary to the contact interaction originally proposed by Fermi.

1105 Breakthrough in other fields of physics contributed in giving theoretical support and interpreta-
1106 tion to the unified electroweak theory. The stepping stone would be the use of spontaneous symmetry
1107 breaking that was inspired to Nambu at the end of the 1950s following the development of the BCS
1108 superconductivity mechanism in 1957. Cooper had shown that BCS pairs, pairs of electrons bound
1109 together at low temperature, could have lower energy than the Fermi energy and where responsi-
1110 ble for superconductivity. This lead to the discovery of Goldstone-Nambu bosons as a result of the
1111 spontaneous breaking of the chiral symmetry in a theory describing nucleons and mesons devel-
1112 opped by Nambu and Jona-Lasinio in 1961, and now understood as a low-energy approximation of
1113 QCD. Similarly to mechanism of energy gap appearance in superconductivity, the nucleon mass
1114 is suggested to the result of a self-energy of a fermion field and is studied through a four-fermion
1115 interaction in which, as a consequence of the symmetry, bound states of nucleon-antinucleon pairs
1116 appear and can be regarded as virtual pions. Though the symmetry is maintained in the equations,
1117 the ground state is not preserved. Goldstone would later the same year show that the bound states
1118 corresponds to spinless bosons with zero mass.

1119 Although the model in itself didn't revolutionize particle physics, spontaneous symmetry break-
1120 ing would be generalized to quantum field theories. As all fundamental interactions are described
1121 using gauge theories based on underlying symmetries, processes such as the chiral symmetry break-
1122 ing would be introduced soon after the publication of Nambu and Jona-Lasinio. In 1962, Anderson,
1123 following an idea of Schwinger who suggested that zero-mass vector bosons were not necessarily
1124 required to describe the conservation of baryons contrary to the bosons emerging from chiral sym-
1125 metry breaking, discussed the implications of spontaneous symmetry breaking in particles physics.
1126 A model was finally independently built in 1964 by Brout and Englert, Higgs, and Guralnik, Hagen,
1127 and Kibble, who discovered that combining an additional field into a gauge theory in order to break
1128 the symmetry, the resulting gauge bosons acquire a nonzero mass. Moreover, Higgs stated that this
1129 implied the existence of at least one new massive, i.e. self-interacting, scalar boson, that are now
1130 known as *Higgs bosons* corresponding to this additional field. The Higgs mechanism today specific-
1131 ally refers to the process through which the gauge bosons of the weak interaction acquire mass. In
1132 1968, Weinberg could point to the Higgs mechanism to integrate a Higgs field into a new version
1133 of the electroweak theory in which the spontaneous symmetry breaking mechanism of the Higgs
1134 field would explicitly explain the masses of the weak interaction gauge bosons and the zero-mass
1135 of photons.

2.1.2 Construction and test of the model

The Standard Model of particle physics was built in the middle of the 1970s after the experimental confirmation of the existence of quarks. It is based on the assembly of the models previously introduced and describing the fundamental interactions, except for gravitation, and their gauge bosons as well as the way elementary "matter" particles interact with the fields associated with these force carriers. In this sense, the development of QED and the unification of the electroweak interaction, of the Yukawa interaction and of QCD, and of the Higgs mechanism made it possible to explain most of contemporary physics.

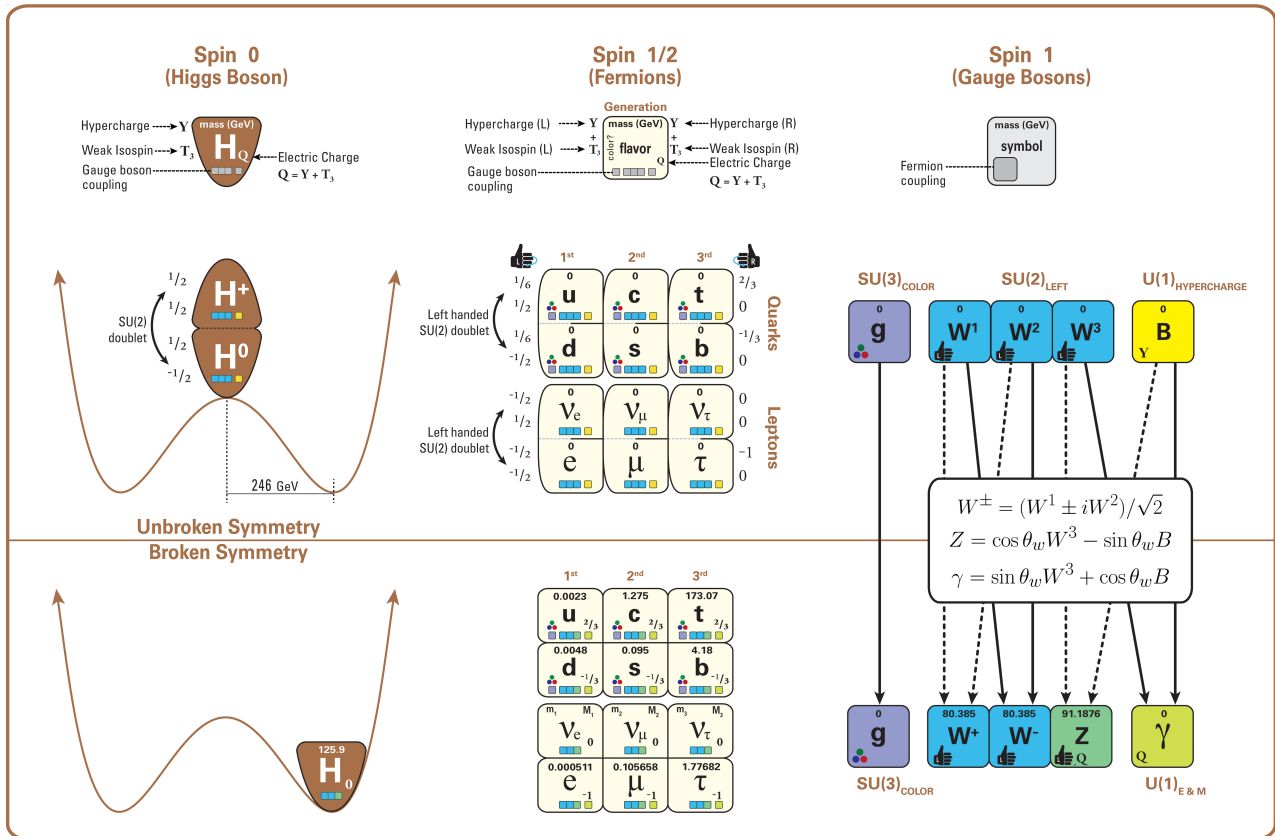


Figure 2.3: The elementary particles of the Standard Model are showed along with their names and properties. Their interactions with the strong, weak and electromagnetic forces have been explicited using color squares. In the left column, the scalar higgs boson is depicted, while the central is focused on the matter particles, the fermions, and the right on the force carriers, the gauge bosons. The role of the Higgs boson in electroweak symmetry breaking is highlighted, and the corresponding way properties of the various particles differ in the (high-energy) symmetric phase (top) and the (low-energy) broken-symmetry phase (bottom) are showed.

In the SM, "matter" particles, are described by 12 fermion fields of spin $\frac{1}{2}$ obeying the Fermi-Dirac statistics, i.e. subjected to the Pauli exclusion principle. To each fermion is associated its corresponding antiparticle. The fermions are classified according to the way they interact and, thus, according to the charges they carry. 6 of them are classified as quarks (u, d, c, s, t , and b) and are subjected to all interactions and the 6 others as leptons ($e^-, \mu^-, \tau^-, \nu_e, \nu_\mu$, and ν_τ). Leptons

1149 are not subjected to the strong interaction and among them, the 3 neutrinos only interact weakly as
 1150 they are neutral particles, which explains why they are so difficult to detect. The gauge boson fields
 1151 are the gluons g for the strong interaction, the photon γ for the electromagnetic interaction and the
 1152 weak bosons W^+ , W^- , and Z^0 for the weak interaction. Finally, the Higgs field H^0 is responsible,
 1153 through the spontaneous symmetry breaking, of the mixing of the massless electroweak boson fields
 1154 W_1 , W_2 , W_3 , and B leading to the observable states γ , W^+ , W^- , and Z^0 that can gain mass while
 1155 interacting with the Higgs field. This picture of the SM is summarized through Figure 2.3 where the
 1156 antifermions are not showed.

1157 When the model was first finalized, the existence of the weak gauge bosons, of the charm, of the
 1158 third quark generation composed of top and bottom quarks to explain the observed CP violation was
 1159 not proven but the predictions were measured with good precision in the years following. First, the
 1160 charm quark would be discovered in 1974, followed by the bottom quark in 1977. The weak bosons
 1161 would be discovered during the next decade in 1983. The top quark would resist until 1995 due to
 1162 its very large mass but would offer the last piece of the elementary QCD particles. The very last
 1163 predicted elementary particle of the model that was not observed yet would prove to be very difficult
 1164 to observe. the Higgs boson needed the start of the LHC to finally be observed in 2012. A few years
 1165 more of tests were necessary to measure its properties to confirm the observation of a scalar boson
 1166 compatible with the predicted Higgs boson H^0 . Eventhough only quark-antiquark (mesons) and 3
 1167 quark states (baryons) were observed, exotic hadrons were not forbidden by QCD and no limit of
 1168 quark is imposed by the theory. Moreover, gluons could form bond states by themselves and with
 1169 quarks. These two types of states are called *glueballs* and *hybrid hadrons*. For decades, experi-
 1170 ments have been conducted without confirmation of such possible states existing. Nevertheless, in
 1171 2014, tetraquarks were observed by LHCb, one of LHC's main experiments, and in 2015, the same
 1172 experiment reported the discovery of pentaquarks making the SM one of the best tested theories of
 1173 physics.

1174 2.1.3 Investigating the TeV scale

1175 Even though the SM is a well tested theory, several hints of physics going beyond its scope have
 1176 been observed. First of all, gravity is not explained through this model and huge difficulties are en-
 1177 countered when trying to include gravitation. The strength of gravitational interaction is expected to
 1178 be negligible at the scale of elementary particles, nevertheless, adding gravitation in the perspective
 1179 of developing a "theory of everything" leads to divergent integrals that could not be fixed through
 1180 renormalization.

1181 Moreover, the SM considers neutrinos to be massless but it was shown in the late 1960s by the
 1182 Homestake experiment that the flux of solar neutrinos (i.e. ν_e) measured didn't match the predicted
 1183 values due to neutrino oscillations, confirmed in the early 2000s by the Sudbury Neutrino Obser-
 1184 vatory. This oscillation implies that neutrinos that can be observed are a superposition of massive
 1185 neutrino states. The research on neutrino oscillation is already quite advanced with experiments
 1186 looking at atmospheric, reactor or beam neutrinos in order to determine the elements of the mixing
 1187 matrix similar to the CKM matrix describing the mixing of quarks. Nevertheless, no answer to the
 1188 origin of neutrino mass is provided.

1189 Another intriguing fact is that the universe is dominated by matter. However, the SM predicted
 1190 that matter and antimatter should have been created in equal amounts and no mechanism is able to
 1191 explain this matter-antimatter asymmetry. Although this asymmetry is seen from the visible uni-
 1192 verse, it may be possible that other unknown regions of the Universe are dominated by antimatter.

1193 Another possibility to explain the apparent asymmetry would be the existence of a electric dipole
1194 in any fundamental particle that would permit matter and antimatter particles to decay at different
1195 rates.

1196 The discrepancy of velocity dispersion of stars in galaxies with respect to the visible mass they
1197 contain is known since the end of the 19th century where Kelvin proposed that this problem could
1198 be solved if a "*great majority of [the stars] would be dark bodies*". Throughout the 20th century,
1199 physicists like Kapteyn, Zwicky, showed the first hints of a "*dark matter*" by studying star veloc-
1200 ities and galactic clusters, followed by robust measurements of galaxy rotation curves by Babcock
1201 which suggested that the mass-to-luminosity ratio was different from what would be expected from
1202 watching the visible light. Later in the 1970s, Rubin and Ford from direct light observations and
1203 Rogstad and Shostak from radio measurements showed that the radial velocity of visible objects in
1204 galaxies was increasing with increasing distance to the center of the galaxy. Finally observation of
1205 lensing effect by galaxy clusters, temperature distribution of hot gas in galaxies and clusters, and
1206 the anisotropies in the Cosmic Microwave Background (CMB) kept on pointing to a "*dark matter*".
1207 From all the data accumulated, the visible matter would only account to no more than 5% of the total
1208 content on the visible universe. Alternative theories have tried to investigate modified versions of
1209 the General Relativity as this theory is only well tested at the scale of the solar system but is not suf-
1210 ficiently tested on wider ranges or even theories in which gravitation is not a fundamental force but
1211 rather an emergent one, but so far, such theories have difficulties to reproduce all the experimental
1212 observations as easily as through dark matter.

1213 A possible theory to offer dark matter candidates would be supersymmetry (SUSY) which pro-
1214 poses a relationship in between bosons and fermions. In this model, each elementary particle,
1215 through a spontaneous spacetime symmetry breaking mechanism would have a *super partner* from
1216 the other family of particles. On top of providing heavy dark matter candidates, supersymmetry
1217 could also help solving the *Hierarchy problem*, the very large scale difference in between the weak
1218 interaction and gravity, although, as mentioned before, in the case gravity is found not to be a funda-
1219 mental force, this problem would automatically fade.

1220
1221 All these different aspects of physics beyond the Standard Model of particle physics and the
1222 Standard model itself can be tested through the use of very energetic and intense hadron and ion col-
1223 liders. The LHC at CERN is a perfect tool to seek answers to these open questions except maybe for
1224 the gravity as gravity is extremely weak at particles level. For example, one of LHCb experiment's
1225 goal is to investigate CP-violation and thus baryonic asymmetry. In 2017, the collaboration has an-
1226 nounced to have so far a 3.3σ statistical significance over a CP-violation through the study of the
1227 decays of Λ_b^0 and $\overline{\Lambda}_b^0$ into a proton (or antiproton) and 3 pions. Many analysis teams are also working
1228 hard on supersymmetry both in ATLAS and CMS collaborations, the two multipurpose experiments
1229 of LHC, even though no evidence of a supersymmetrical theory was seen, the few hint having the
1230 tendency to confirm the standard model. These experiments also have the possibility to investigate
1231 ways to explain Majorana neutrino mass through Yukawa interactions of scalar particles.

1232 The higher the center-of-mass energy, the smaller details the experiments will be able to see, the
1233 heavier the potential particle creation barrier will be, the stronger the cross-section of certain rare
1234 decay channels will be. As a comparison, with collisions happening at 14 TeV, the LHC is approxi-
1235 mately 2 orders of magnitude more sensitive to the Higgs than the Tevatron was with its already very
1236 powerful 2 TeV. All these advantages eventually lead to new discoveries and deeper understanding
1237 of the models describing our Universe. But the LHC only is a step forward to gather more precise
1238 tests of the Standard Model and new knowledge about the physics beyond it. A successful physics

1239 campaign will probably serve to justify the building of new accelerators with even greater discovery
1240 potential like for example the Future Circular Collider (FCC) that would push even further the study
1241 of the unanswered questions of contemporary physics.

1242 2.2 The Large Hadron Collider & the Compact Muon Solenoid

1243 Throughout its history, CERN has played a leading role in high energy particle physics. Large re-
1244 gional facilities such as CERN were thought after the second world war in an attempt to increase
1245 international scientific collaboration and allows scientists to share the forever increasing costs of
1246 experiment facilities required due to the need for increasing the energy in the center of mass to
1247 deeper probe matter. The construction of the first accelerators at the end of the 50s, the Synchro-
1248 cyclotron (SC) and the Proton Synchrotron (PS), was directly followed by the first observation of
1249 antinuclei in 1965 [1]. Strong from the experience of the Intersecting Storage Rings (ISR), the very
1250 first proton-proton collider that showed hints that protons are not elementary particles, the Super
1251 Proton Synchrotron (SPS) was built in the 70s to investigate the structure of protons, the preference
1252 for matter over antimatter, the state of matter in the early universe or exotic particles, and lead to
1253 the discovery in 1983 of the W and Z bosons [2–5]. These newly discovered particles and the elec-
1254 troweak interaction would then be studied in details by the Large Electron-Positron (LEP) collider
1255 that will help to prove in 1989 that there only are three generations of elementary particles [6]. The
1256 LEP would then be dismantled in 2000 to allow for the LHC to be constructed in the existing tunnel.

1257 2.2.1 LHC, the most powerful particle accelerator

1258 The LHC has always been considered as an option to the future of CERN. At the moment of the
1259 construction of the LEP beneath the border between France and Switzerland, the tunnel was built in
1260 order to accomodate what would be a Large Hadron Collider with a dipole field of 10 T and a beam
1261 energy in between 8 and 9 TeV [7] directly followed in 1985 with the creation of a 'Working Group
1262 on the Scientific and Technological Future of CERN' to investigate such a collider [8]. The decision
1263 was finally taken almost 10 years later, in 1994, to construct the LHC in the LEP tunnel [9] and the
1264 approval of the 4 main experiments that would take place at the 4 interaction points would come in
1265 1997 [10] and 1998 [11]:

- 1266 • ALICE [12] has been designed in the purpose of studying quark-gluon plasma that is believed
1267 to have been a state of matter that existed in the very first moment of the universe.
- 1268 • ATLAS [13] and CMS [14] are general purpose experiments that have been designed with
1269 the goal of continuing the exploration of the Standard Model and investigate new physics.
- 1270 • LHCb [15] has been designed to investigate the preference of matter over antimatter in the
1271 universe through the CP violation.

1272 These large scale experiments, as well as the full CERN accelerator complex, are displayed on
1273 Figure 2.4. The LHC is a 27 km long hadron collider and the most powerful accelerator used for
1274 particle physics since 2008 [16]. The LHC was originally designed to collide protons at a center-
1275 of-mass energy of 14 TeV and luminosity of $10^{34} \text{ cm}^{-2}\text{s}^{-1}$, as well as Pb ions at a center-of-mass
1276 energy of 2.8 TeV/A with a peak luminosity of $10^{27} \text{ cm}^{-2}\text{s}^{-1}$. Run 1 of LHC, when the center-of-
1277 mass energy only was half of the nominal LHC energy, was enough for both CMS and ATLAS to

discover the Higgs boson [17] and for LHCb to discover pentaquarks [18] and confirm the existance of tetraquarks [19]. Nevertheless, after the Third Long Shutdown (LS3) (2024-2026), the accelerator will be in the so called High Luminosity LHC (HL-LHC) configuration [20], increasing its instantaneous luminosity to $10^{35} \text{ cm}^{-2}\text{s}^{-1}$ for pp collisions and to $4.5 \times 10^{27} \text{ cm}^{-2}\text{s}^{-1}$, boosting the discovery potential of the LHC. The HL-LHC phase should last at least another 10 years depending on the breakthrough this machine would lead to. Already a new accelerating device, the FCC, as been proposed to prepare the future of high energy physics after the LHC.

CERN's Accelerator Complex

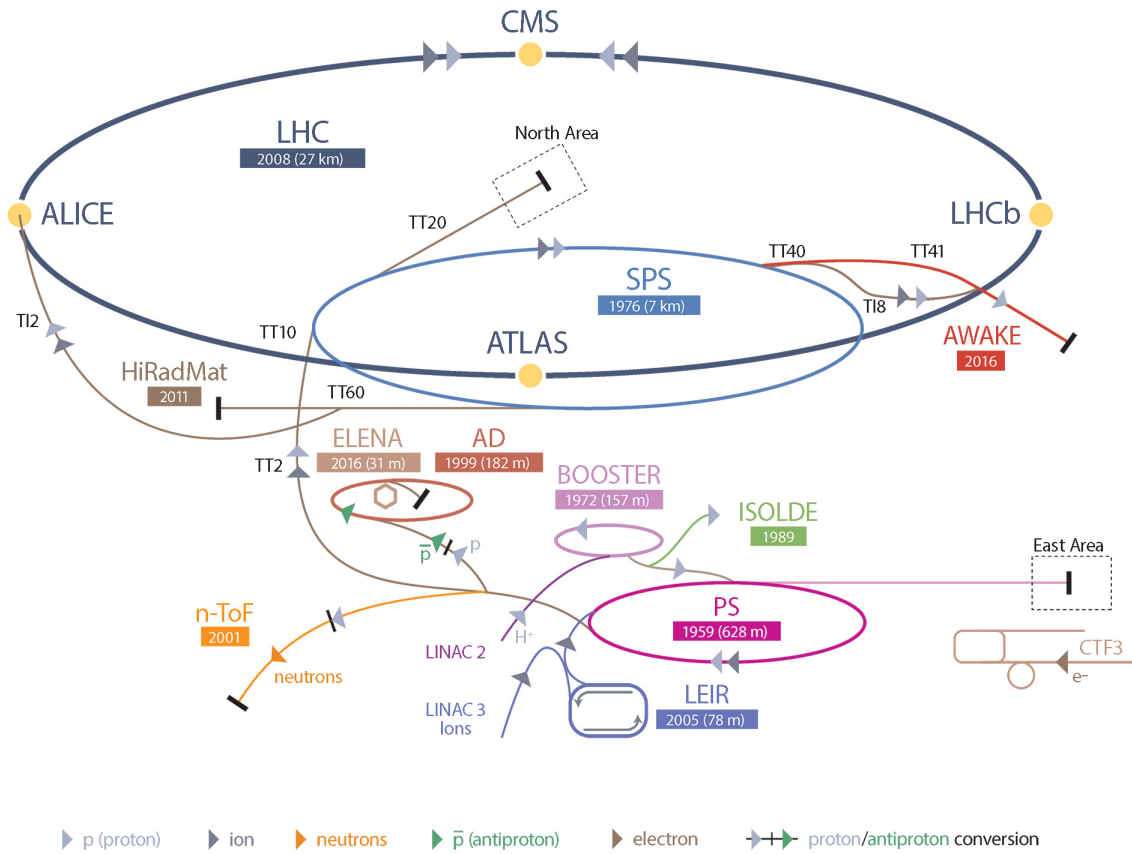


Figure 2.4: CERN accelerator complex.

2.2.1.1 Particle acceleration

The LHC is the last of a long series of accelerating devices. Before being accelerated by the LHC, the particles need to pass through different acceleration stages. All these acceleration stages are visible on Figure 2.4 and pictures of the accelerators are showed in Figure 2.5.

The story of accelerated protons at CERN starts with a bottle of hydrogen gas injected into the source chamber of the linear particle accelerator *LINAC 2* in which a strong electric field strips the

1292 electron off the hydrogen molecules only to keep their nuclei, the protons. The cylindrical conductors,
 1293 alternatively positively or negatively charged by radiofrequency cavities, accelerate protons by
 1294 pushing them from behind and pulling them from the front and ultimately give them an energy of
 1295 50 MeV, increasing their mass by 5% in the process.

1296

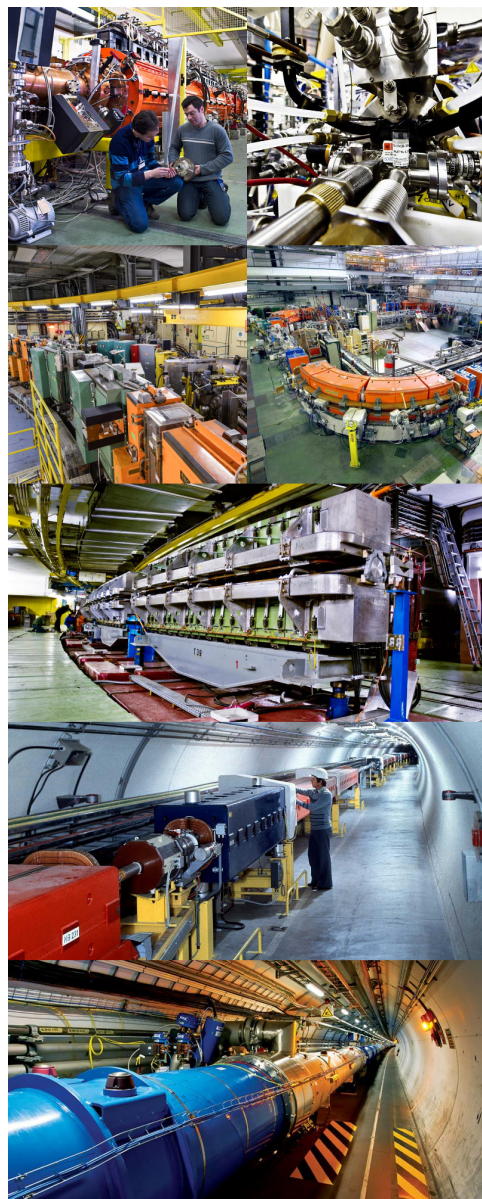


Figure 2.5: Pictures of the different accelerators. From top to bottom: first the LINAC 2 and the Pb source of LINAC 3. Then the Booster and the LEIR. Finally, the PS, the SPS and the LHC.

1297 When exiting the LINAC 2, the protons are divided into 4 bunches and injected into the 4 su-
 1298 perimposed synchrotron rings of the *Booster* where they are then accelerated to reach an energy of

1299 1.4 GeV before being injected into the PS. Before the Booster was operational in 1972, the protons
 1300 were directly injected into the PS from the LINAC 2 but the low injection energy limited the amount
 1301 of protons that could be accelerated at once by the PS. With the Booster, the PS accepts approxi-
 1302 mately 100 times more particles.

1303

1304 The 4 proton bunches are thus sent as one to the PS where their energy eventually reaches
 1305 26 GeV. Since the 70s, the main goal of this 628 m circumference synchrotron has been to sup-
 1306 ply other machines with accelerated particles. Nowadays, not only the PS accelerates protons, it also
 1307 accelerates heavy ions from the *Low Energy Ion Ring (LEIR)*. Indeed, the LHC experiments are not
 1308 only designed to study *pp*-collisions but also *Pb*-collisions. Lead is first injected into the dedicated
 1309 linear collider *LINAC 3*, that accelerate the ions using the same principle than LINAC 2. Electrons
 1310 are striped off the lead ions all along the acceleration process and eventually, only bare nuclei are
 1311 injected in the LEIR whose goal is to transform the long ion pulses received into short dense bunches
 1312 for LHC. Ions injected and stored in the PS were aceelerated by the LEIR from 4.2 MeV to 72 MeV.

1313

1314 Directly following the PS, is finally the last acceleration stage before the LHC, the 7 km long
 1315 *SPS*. The SPS accelerates the protons to 450 GeV and inject proton in both LHC accelerator rings
 1316 that will increase their energy up to 7 TeV. When the LHC runs with heavy lead ions for ALICE
 1317 and LHCb, ions are injected and accelerated to reach the energy of 2.8 TeV/A.

1318

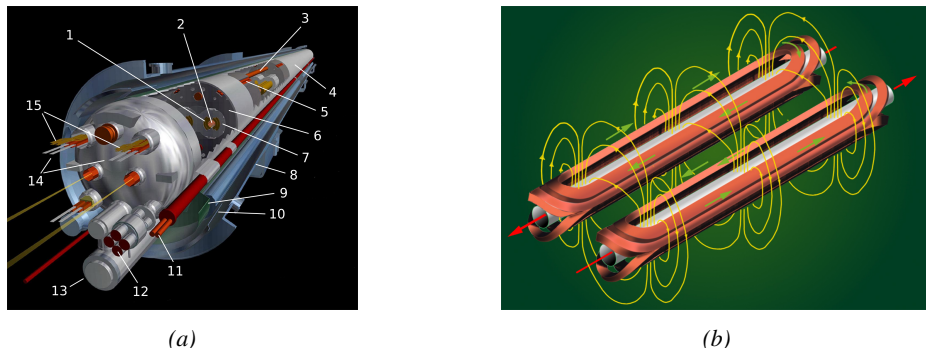


Figure 2.6: Figure 2.6a: schematics of the LHC cryodipoles. 1: Superconducting Coils, 2: Beam pipe, 3: Heat exchanger Pipe, 4: Helium-II Vessel, 5: Superconducting Bus-bar, 6: Iron Yoke, 7: Non-Magnetic Collars, 8: Vacuum Vessel, 9: Radiation Screen, 10: Thermal Shield, 11: Auxiliary Bus-bar Tube, 12: Instrumentation Feed Throughs, 13: Protection Diode, 14: Quadrupole Bus-bars, 15: Spool Piece Bus-bars. Figure 2.6b: magnetic field and resulting motion force applied on the beam particles.

1319

1320 The LHC beams are not continuous and are rather organised in bunch of paticles. When in *pp*-
 1321 collision mode, the beams are composed of 2808 bunches of 1.15×10^{11} protons separated by 25 ns.
 1322 When in *Pb* collision mode, the 592 *Pb* bunches are on the contrary composed of 2.2×10^8 ions
 1323 separated by 100 ns. The two parrallel proton beams of the LHC are contained in a single twin-
 1324 bore magnet due to the space restriction in the LEP tunnel. Indeed, building 2 completely separate
 1325 accelerator rings next to each other was impossible. The dipoles of the 1232 twin-bore magnets are
 1326 showed in Figure 2.6 alongside the magnetic field generated along the dipole section to accelerate the
 1327 particles. The dipoles generate a nominal field of 8.33 T, needed to give protons and lead nucleons
 their nominal energy. Some 392 quadrupoles, presented in Figure 2.7, are also used to focus to the

1328 beams, as well as other multipoles to correct smaller imperfections.

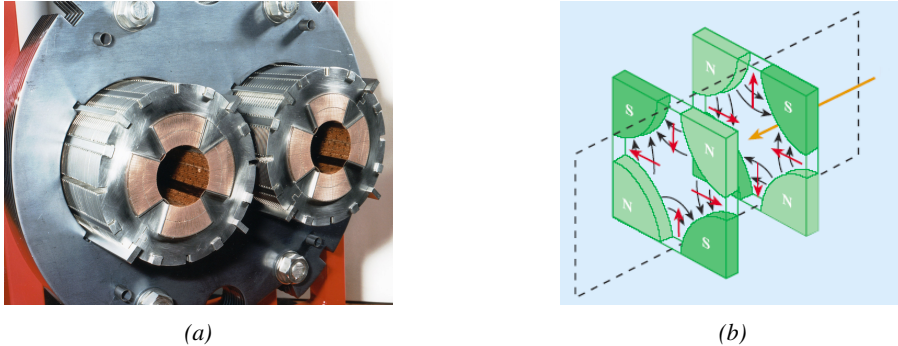


Figure 2.7: Figure 2.7a: picture of the LHC quadrupoles. Figure 2.7b: magnetic fields and resulting focussing force applied on the beam by 2 consecutive quadrupoles.

1329 2.2.2 CMS, a multipurpose experiment

1330 Among the four main LHC experiments is the Compact Muon Solenoid used as a multipurpose tool to
1331 investigate the SM and physics beyond its scope. Proposed through a letter of intention in 1992 [14],
1332 and as its name suggests, this very compact detector's uses the muons as a clear tag of most of SM
1333 and new physics interesting channels. In the original 1997 Technical Design Report (TDR) [21], the
1334 very first sentences were stating that "*Muons are an unmistakable signature of most of the physics*
1335 *LHC is designed to explore. The ability to trigger on and reconstruct muons at the highest lumi-*
1336 *nosities is central to the concept of CMS, the Compact Muon Solenoid.*" CMS participated in the
1337 discovery of the Higgs boson and the measurement of its properties and couplings together with
1338 ATLAS and is also actively involved in the search for SUSY and heavy ion collisions. Other exotic
1339 physics are also being investigated using the data collected by CMS.

1340 The CMS apparatus in itself is the heaviest detector ever built starring a SI15m diameter and a
1341 29 m length for a total weight of 14 kT. A thick 4 T solenoid magnet located at the beam interaction
1342 point hosts trackers and calorimeters. Extending in all directions around the magnet, heavy iron
1343 return yokes are installed to extend the magnetic field and support a muon system. The apparatus
1344 consists of a barrel, referring to the magnet and the detectors contained in it and the part of the muon
1345 system built directly in the cylinder around the magnet, and of 2 endcaps in the forward and back-
1346 ward region of the detector that closes the apparatus and complete the detection coverage along the
1347 beam line. A front view on the barrel is provided in Figure 2.8 while a detailed view of the apparatus
1348 is given in Figure 2.9.

1349
1350 In order to efficiently detect all long leaving particles and measure their properties with good
1351 precision, the CMS detector uses an onion like layout around of the interaction point in order to
1352 maximize the covered solid angle. As detailed in Figure 2.10, in the innermost region of the detector,
1353 closest to the interaction point, the silicon tracker records the trajectory of charged particles. Around
1354 it, the electromagnetic calorimeter (ECAL) stops and measure the energy deposition of electrons
1355 and photons. In the next layer, the hadron calorimeter (HCAL), hadrons are stopped and their energy
1356 measured. These layers are contained inside of the magnet of CMS, the superconducting solenoid.
1357 Outside of the magnet are the muon chambers embedded into iron return yokes used to control the

1358 magnetic field and gives muons, the only particles traveling completely through the whole detector, a
 1359 double bending helping in reconstructing their energy and trajectory. Note that photons and neutral
 1360 hadrons are differentiated from electrons and charged hadrons in the calorimeters by the fact that
 1361 don't interact with the silicon tracker and that they are not influenced by the magnetic field.

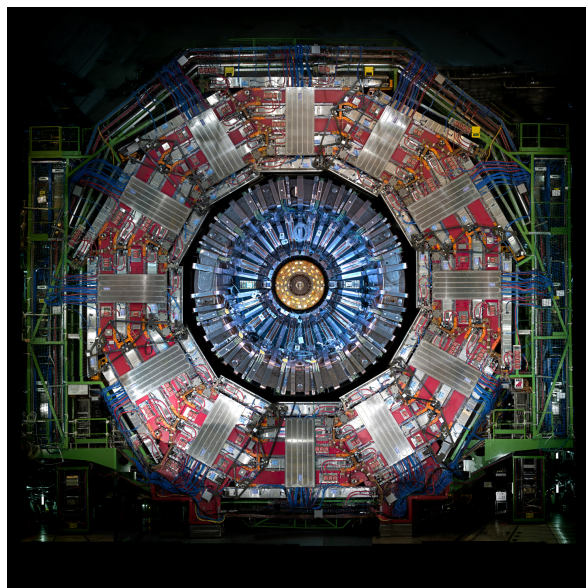


Figure 2.8: Picture of the CMS barrel. The red outer layer is the muon system hosted into the red iron return yokes. The calorimeters are the blue cylinder inside in magnet solenoid and the tracker is the inner yellow cylinder built around the beam pipe.

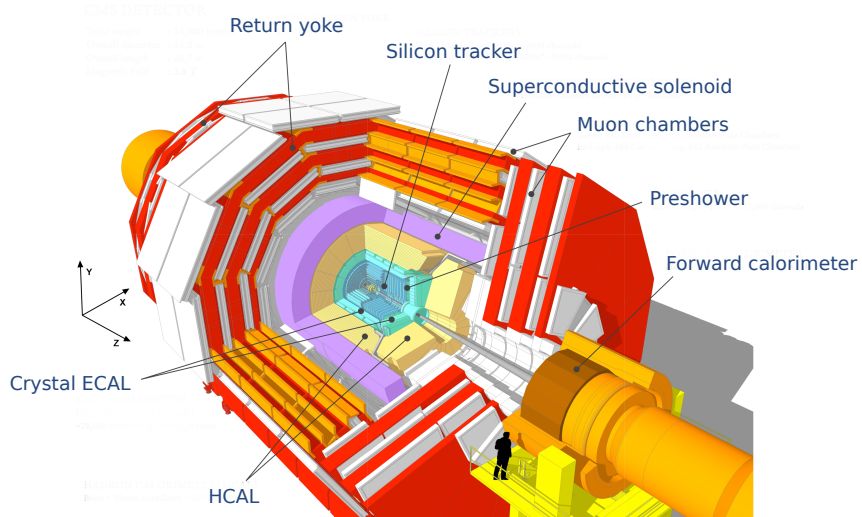


Figure 2.9: View of the CMS apparatus and of its different components.

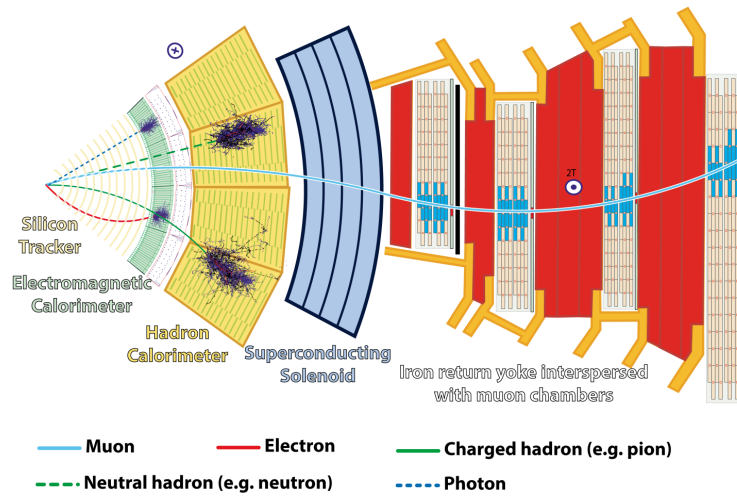


Figure 2.10: Slice showing CMS sub-detectors and how particles interact with them.

2.2.2.1 The silicon tracker, core of CMS

The silicon tracker visible on Figure 2.11 is divided into 2 different sub-systems: the *pixel detector* at the very core and the *microstrip detector* around it. This system is composed of 75 million individual readout channels with up to 6000 channels per squared centimeter for the pixels making it the world's biggest silicon detector. This density allows for measurements of the particle tracks with a precision of the order of $10\ \mu\text{m}$. This is necessary to reconstruct all the different interaction vertices with precision and have a precise measure of the curvature of the charged particles traveling through the magnetic field to estimate their charge and momentum.

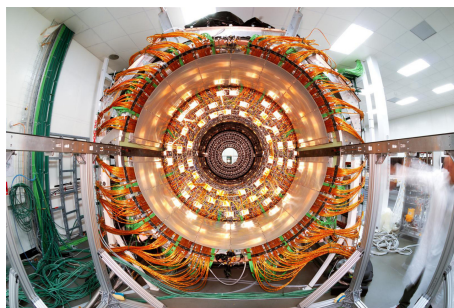


Figure 2.11: CMS tracker.

2.2.2.2 The calorimeters, measurement of particle's energy

The ECAL directly surrounding the tracker is composed of crystals of lead tungstate, PbWO_4 , a very dense but optically transparent material used to stop high energy electrons and photons. These crystal blocks basically are extremely dense scintillators which scintillate in fast, short light bursts proportionally to the energy deposition. The light is yielded rapidly and contained at 80% in the corresponding 25 ns lasting bunch crossing. Each crystal is isolated from the other by the carbon fiber matrix they are embedded in. It is composed of a barrel containing more than 60,000 crystals

1377 and of closing endcaps containing another 15,000 crystals. In front of the ECAL endcap is installed
 1378 a preshower detector made out of two layers of lead and silicon strip detectors to increase the spatial
 1379 resolution close to the beam line for pion-photon and single-double photon discrimination purposes.
 1380 Figure 2.12 shows the calorimeter inside of the magnet and the crystals.

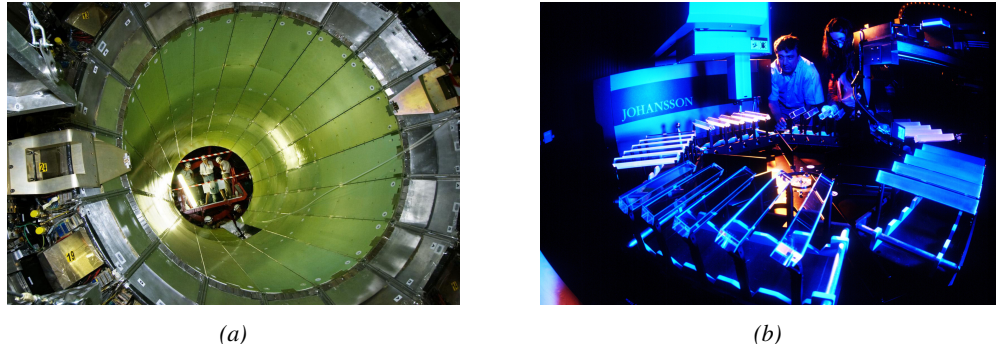


Figure 2.12: Figure 2.12a: picture of the ECAL. Figure 2.12b: picture of the lead tungstate crystals composing the ECAL.

1381 The next layer is the HCAL measuring the hadrons momentum and providing indirect hints of
 1382 non interacting neutral particles, such as neutrinos, as missing transverse momentum. Several layers
 1383 of brass or steel are interleaved with plastic scintillators readout by photodiodes using wavelength-
 1384 shifting fibers. The HCAL is also composed of a barrel, showed in Figure 2.13 and of endcaps. It
 1385 also features forward calorimeters on both sides of CMS in the region very close to the beam line at
 1386 high pseudorapidity ($3.0 < |\eta| < 5.0$). The role of these forward calorimeters, made using steel and
 1387 quartz fibers, is to measure very energetic hadrons.



Figure 2.13: CMS hadron calorimeter barrel.

1388 Finally, in the outer region of the apparatus, a muon system is used to trigger on potentially
 1389 interesting event by identifying muons. Indeed, the muon system is a very important part of the
 1390 CMS trigger infrastructure designed to efficiently select data from the enormous data flow received
 1391 by the detectors as the LHC delivers collisions at a rate of 40 MHz with a pile-ip of 20 to 30 collisions
 1392 per bunch crossing during Phase-I and up to 200 during Phase-II, representing billions of interactions
 1393 per second among which a large quantity are low energy collisions that are not likely to produce new
 1394 reactions, and which is physically impossible for nowadays technologies to cope with. Working at
 1395 a maximum rate of 100 kHz, the trigger system is able to select the 100,000 more interesting events

1396 by looking at the energy distribution of the interaction products and clear signatures like muons
 1397 reconstructed by the muon system. the vast majority of these events will not finally be stored after
 1398 physics tests are applied.

1399 **2.2.2.3 The muon system, corner stone of CMS**

1400 The challenge for the muon system is to provide a robust and fast measurement of muons. Three
 1401 different subsystems, and soon 4 after LS2, compose the muon system as showed in Figure 2.14 in
 1402 which a quadrant of the CMS detector focused on muon system. Drift Tube (DT) are found in the
 1403 barrel region covering the low pseudorapidity region where particles transverse momentum is lower
 1404 and Cathode Strip Chamber (CSC) are found in the endcap region covering higher pseudorapidity
 1405 region closer to beam line where particles have a stronger momentum. The redundancy of the system
 1406 is insured by Resistive Plate Chamber (RPC) in both the barrel and endcap region. Nevertheless, the
 1407 region closest to the beam line ($|\eta| > 1.8$) was not equipped with RPCs. This lack of redundancy
 1408 in the high pseudo rapidity region will be solved during LS2, the following Year End Technical
 1409 Stop (YETS) in 2021 and 2022, and LS3 where the necessary services, detectors and Link System,
 1410 that collects the data and synchronizes them, will be installed.

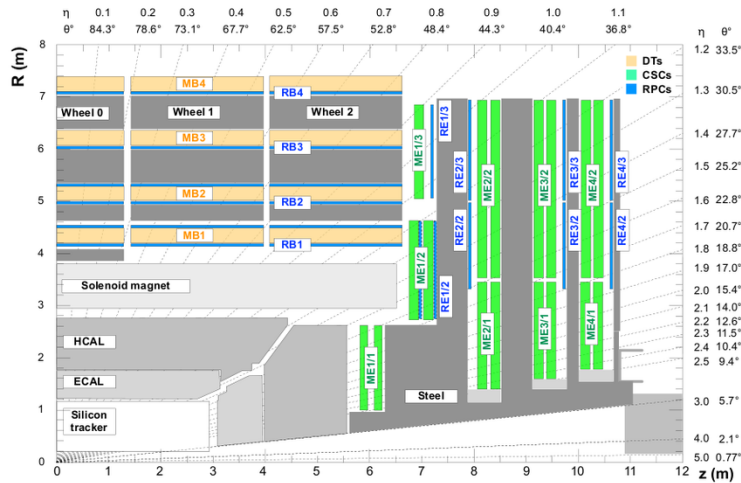


Figure 2.14: A quadrant of the muon system, showing DTs (yellow), RPCs (blue), and CSCs (green).

1411 The barrel region is divided into 5 *wheels* made out of 4 *rings* of detectors with iron return yokes
 1412 in between them whereas the endcaps are made out of 4 disks, each divided into pseudorapidity
 1413 stations, 2 for CSCs (except for the first disk where 3 stations are equipped) and 3 for RPCs, although
 1414 only 2 RPCs stations are equipped at present. The wheels and disks are showed in Figure 2.15. So
 1415 far, each subsystem was dedicated to a particular task. DTs, in the barrel, and CSCs, in the endcaps,
 1416 are used mainly for their spatial resolution. Indeed, DTs' resolution is of the order of 100 μm along
 1417 both the $(r - \phi)$ and $(r - z)$ components while the resolution of CSCs is similar but varies in a range
 1418 from 50 μm to 140 μm depending on the distance to the beamline. On the other hand, RPCs are used
 1419 for their time resolution as they can deliver an information on the muon tracks within 1.5 ns.

1420 The 250 CMS DTs, found in the barrel covering the pseudorapidity region $0 < |\eta| < 1.2$
 1421 and whose structure is shown in Figure 2.16, are composed of 3 *superlayers* of DT cells. Two of
 1422 these superlayers are dedicated to measuring the ϕ coordinate of the muons and while the last one

measures the η (or z) coordinate. Each superlayer consists on 4 layers of 60 to 70 DT cells arranged in quincunx to allow for a precise reconstruction of the muon path through the DT layers. Each DT cell is a rectangular aluminium gas volume with a central anode wire. Cathode strips are placed on the narrow surface of the cells and electrode strips are placed on the wide surface to help shaping the electric field to ensure a consistent drift velocity of electrons in the drift volume. These detectors are operated using a 85/15 mixture of Ar and CO_2 .

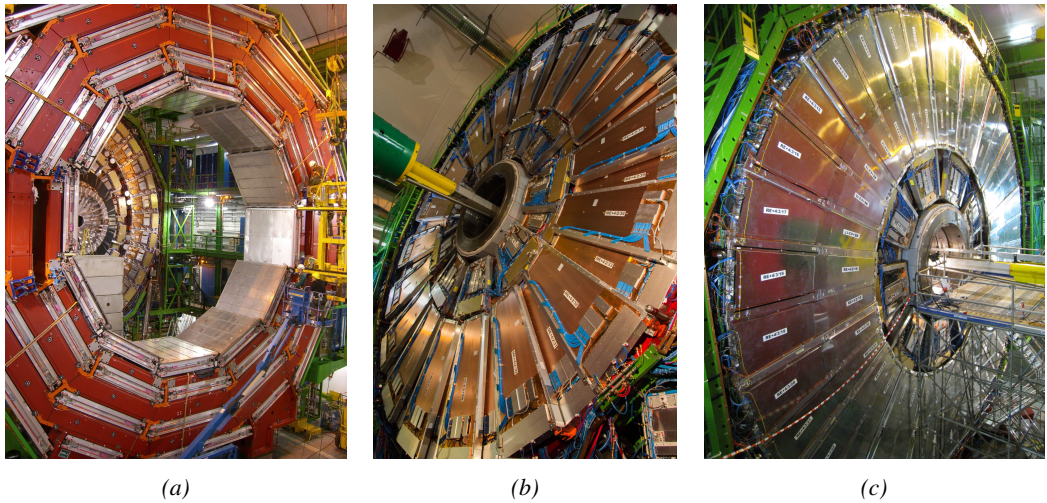


Figure 2.15: Figure 2.15a: Barrel wheel with its detector rings and return yokes. Figure 2.15b: CSC endcap disk with the 2 CSC stations. The outer station is made of 10 deg detectors while the inner station is made of 20 deg detectors. Figure 2.15c: RPC endcap disk. The inner station is not equipped and the inner CSC station can be seen.

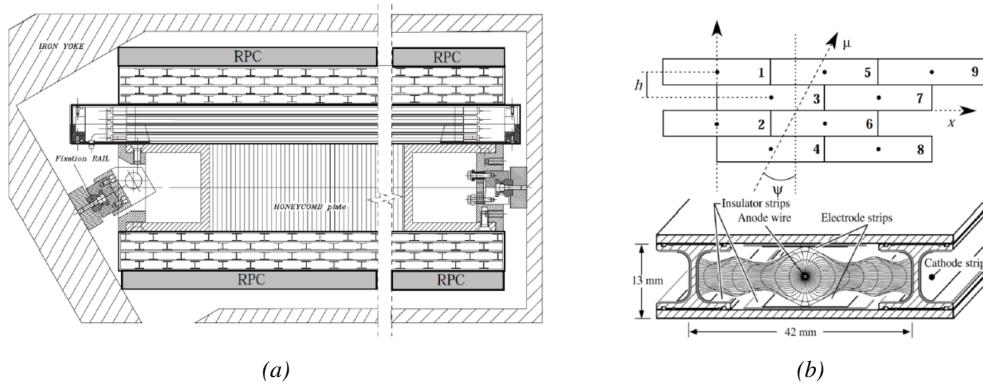


Figure 2.16: Figure 2.16a: Cross section of a DT module showing the two superlayers measuring the ϕ coordinate, perpendicular to the cross section plane, and the superlayer measuring the η coordinate, placed in between the two others with honeycomb and parallel to the cross section plane. The DT detector is sandwiched in between 2 RPCs whose readout strips are perpendicular to the cross section plane, measuring the ϕ coordinate. Figure 2.16b: A DT cell is shown together with its electric field. The path of a muon through a superlayer is shown.

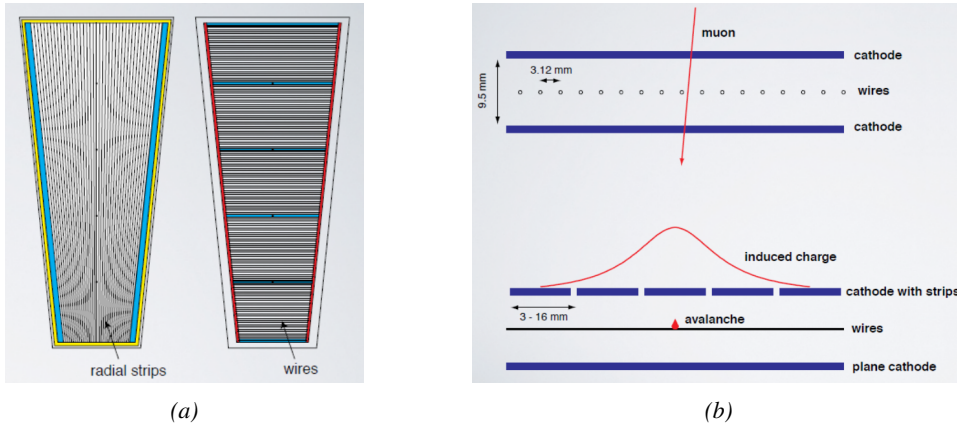


Figure 2.17: Figure 2.17a: cathode strips and anode wire layout of a CSC panel. Figure 2.17b avalanche development and charge collection by anode wires and induction on cathode strips inside of a CSC panel.

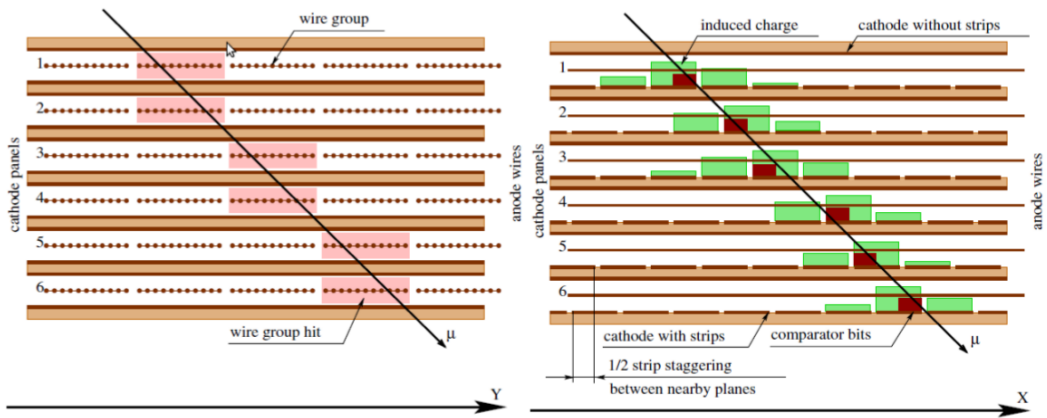


Figure 2.18: Muon track reconstruction through the 6 panels of a CMS CSC using the information of anode wire groups and cathode strip charge distribution combined with comparator bits to decide on which half strip the muon is more likely to have passed.

The 540 CMS CSCs, found in the endcaps covering the pseudorapidity region $0.9 < |\eta| < 2.5$ and described through Figure 2.17, are composed of 6 panels of CSC, each panel consisting in a wide gas volume of 9.5 mm (7 mm in the case of ME1/1 station) containing anode wires and whose surfaces are cathodes. The top cathode is a wide copper plane of the size of the gas volume. The bottom cathode is divided into thin trapezoidal copper strips radially arranged to measure the azimuthal coordinate ϕ with a pitch ranging from 8 to 16 mm. The $0.50 \mu\text{m}$ anode wires are placed perpendicularly to the strips to measure radial coordinate r and are grouped by 10 to 15 with a wire to wire space of 3.2 mm. In the specific case of ME1/1 placed against the HCAL endcap, the $0.30 \mu\text{m}$ anode wires have a wire to wire distance of 2.5 mm and are not disposed perpendicularly to the strips but slightly tilted by an angle of 29 deg to compensate for the lorentz force due to the very strong local magnetic field of 4 T. These detectors are operated with a 40/50/10 mixture of Ar, CO₂ and CF₄. Combining the information of the multiple CSC panels, the detectors achieve a very precise measurement of the muon track.

Despite their excellent spatial resolution, the wire chambers (DTs and CSCs) are limited in terms of time resolution by the fact that the charge needs to drift towards the anode wire and be collected before having the confirmation that a particle was detected as the drift volume is not used to develop avalanches. Indeed, the stronger electric field close to the anode wire triggers the avalanche and the gain of the detector. Due to the drift, the time resolution is thus limited at best to approximately 2 to 3 ns. In addition, even though the intrinsic time resolution of the tracking chambers is rather good compared to the 25 ns in between successive collisions, the processing time of the trigger system doesn't allow for very fast triggering as it provides a time precision of only 12.5 ns. Thus, detectors fully dedicated to timing measurement have been installed as a redundant system. These detectors are RPCs, also gaseous detectors but that use current induction instead of charge collection allowing for a time resolution of the order of 1.5 ns only. Theoretically, depending on the design used, RPCs could reach a time resolution of the order of 10 ps but in the context of LHC where bunch crossing happen every 25 ns, a time resolution of 1.5 ns is sufficient to accurately assign the right bunch crossing to each detected muon.

The 1056 RPCs equipping the CMS muon system both in the barrel and endcap regions and covering the pseudorapidity region $0 < |\eta| < 1.6$ are composed of two layers of RPC *gaps* as described in Figure 2.19. Each gap consists in two resistive electrodes made out of 2 mm thick Bakelite enclosing a 2 mm thick gas volume containing a 95.2/4.5/0.3 mixture of $C_2H_2F_4$, $i - C_4H_{10}$ and SF_6 . Due to this geometry, the electric field inside of a gap is homogeneous and linear at every point in the gas translating into a uniform development of avalanches in the gas volume as soon as a passing muon ionises the gas. The two gaps sandwich a readout copper strip plane. A negative voltage is applied on the outer electrodes, used as cathodes, and the inner electrodes, the anodes, are simply connected to the ground as well as the readout panel that picks up the current induced by the accumulated charge of the growing avalanches in one or both of the gas gaps. This OR system allows for a lower gain (i.e. a lower electric field) on both gaps to reach the maximal efficiency of such a detector.

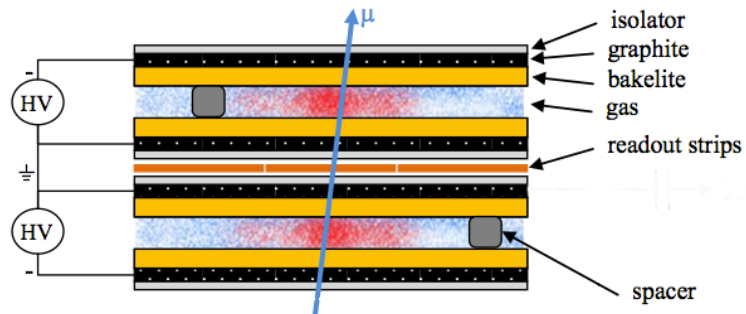


Figure 2.19: Double gap layout of CMS RPCs. Muons passing through the gas volumes will create electron-ion pairs by ionising the gas. this ionisation will immediately translate into a developing avalanche.

3

1468

1469

Muon Phase-II Upgrade

1470 The very first proton beam successfully circulated in the LHC in September 2008 directly followed
1471 by an incident leading to mechanical damage that would delay the LHC program for a year until
1472 November 2009, the very first collisions at a center-of-mass energy of 7 TeV taking place in March
1473 2010. The energy of the beam would be increased after a First Long Shutdown (LS1) starting early
1474 2013 after less than 3 years of data taking. Nevertheless, this first data taking period at only 7 TeV
1475 was sufficient to claim the discovery of a new particle compatible with the Higgs boson in July 2012.
1476 During the 2 years of shutdown, the upgrade of the accelerator allowed for several maintainances
1477 along the beam pipes, repair and consolidation of magnet connection and high-current splices. But
1478 not only the LHC was upgraded. Indeed, the experiments at the 4 collision points also took the
1479 advantage of this time to upgrade their system in prevision of the next LHC run (Run-II) until
1480 2018 and the Second Long Shutdown (LS2) as the luminosity and energy of the beam would be
1481 continuously increasing. By the end of Run-II, the luminosity will have reached twice its nominal
1482 value when the center-of-mass energy has already got close to its nominal value by reaching an
1483 historical 13 TeV for the first time in 2017.

1484 The next long shutdown will occur at the end of this year and will again be the occasion for sim-
1485 ilar maintenance and consolidation in prevision of Run-III and the future upgrade of LS3. Still, the
1486 main occupation of LS2 on LHC side will be the upgrade of LHC injectors. On the experiments side,
1487 LHCb and ALICE will, in a very tight schedule, implement major upgrades while ATLAS and CMS
1488 will wait until LS3 to upgrade their detectors in prevision of high luminosity *LHC-Phase-II*. ALICE
1489 main challenge is an upgrade of their apparatus to cope with the 50 kHz $Pb - Pb$ collisions. Simi-
1490 larly, LHCb will upgrade their frontend readout electronics to cope with the full 40 MHz collisions
1491 delivered by LHC. ATLAS will perform standard maintenance and CMS will focus on the urgent up-
1492 grade of the pixel detector and on the installation of new muon detectors in order to take profit of LS2
1493 time to mitigate the upgrade of detectors foreseen during LS3. Run-III will start in 2021 with the LHC
1494 at its nominal center-of-mass energy and will bring LHC-Phase-I to an end at the end of 2023. By
1495 then the luminosity will only increase to reach 2.5 times the nominal luminosity but during these 3
1496 years of run, the LHC will deliver as much integrated luminosity as what what brought during the al-

most 7 years of both Run-I and II of data taking. Phase-I will end with an overall 300 fb^{-1} delivered.

1498

1499 3.1 High Luminosity LHC and muon system requirements

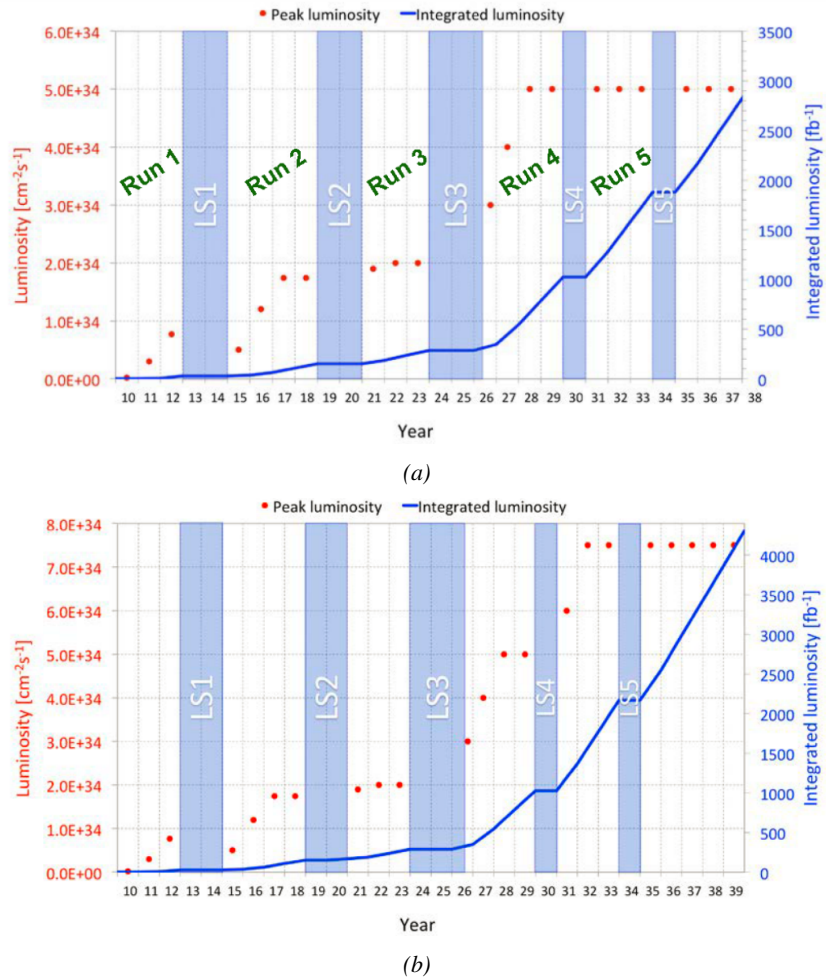


Figure 3.1: Detailed timeline projection of for LHC and HL-LHC operation until 2039 showing the evolution of the instantaneous and integrated luminosity as designed (Figure 3.1a) and in the ultimate case where the instantaneous luminosity is increased to $7.5 \times 10^{34} \text{ cm}^{-2}\text{s}^{-1}$ (Figure 3.1b) [20, 22].

After approximately 15 years of operation, the LHC will undergo a new series of upgrade during the LS3 in order to boost its discovery potential as showed in Figure 3.1. This moment onward is what is referred to HL-LHC or Phase-II. The goal is to aim for a luminosity 5 to 7 times stronger than the nominal one trying to reach even 10 times this value if possible. Increasing the luminosity means that the beam size at the collision points needs to be reduced to boost the number of collisions per bunch crossing. For this purpose, new focusing and bending magnets, and collimators will be installed at the collision points as well as newly developed "crab cavities" that will tilt the particle

1500

1501

1502

1503

1504

1505

1506

1507 bunched just prior to the collisions by giving them transverse momentum and thus increasing their
 1508 meeting area. In addition, the full proton injection line will be upgraded.

1509 Over its full lifetime, the HL-LHC is expected to deliver an outstanding integrated luminosity of
 1510 3000 fb^{-1} leading, in the case of Higgs studies to measuring the couplings of the boson to a precision
 1511 of 2 to 5% thanks to the estimated 15 millions of Higgs created every year providing a more precise
 1512 measurement of potential deviations from the theoretical predictions. SUSY and heavy gauge boson
 1513 studies would also see their mass range limits pushed away by at least 1 TeV and could lead to a new
 1514 breakthrough. SUSY is a particularly important topic as it could give an answer to why the Higgs
 1515 boson can stay so light while coupled to heavy particles by introducing the contributions of the super
 1516 partners on top of providing dark matter candidates. Finally, the increase of luminosity will give the
 1517 possibility to investigate "exotic" mode like for example the models introducing extra dimensions to
 1518 explain the hierarchy problem.

1519 On the experiments side, the pile-up (PU) will be increased up to 150 to 200 interactions per
 1520 bunch crossing in ATLAS and CMS, making necessary an strong upgrade of the trigger system and
 1521 of the inner trackers and of the calorimeters. Both ATLAS and CMS will also need to upgrade
 1522 the muon trigger at the level of the endcaps mainly focusing on the coverage near the beam line in
 1523 order to increase the detection acceptance and event selection. Moreover, the increased luminosity
 1524 will also lead to an increased background rate and a faster ageing of the detectors. This PhD work
 1525 takes place into this very specific context of muon detector consolidation and certification for the
 1526 HL-LHC period in order to provide the CMS experiment with robust new detectors and confirm that
 1527 the present system will survive through the next 20 years of HL-LHC.

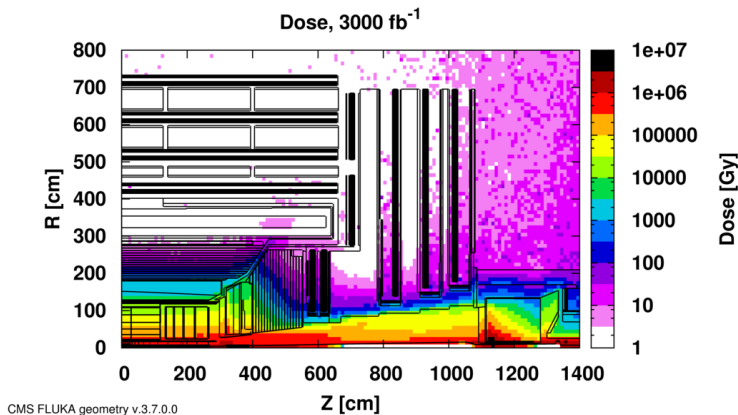


Figure 3.2: Absorbed dose in the CMS cavern after an integrated luminosity of 3000 fb . Using the interaction point as reference, R is the transverse distance from the beamline and Z is the distance along the beamline.

1528 The end of 2018 will mark the beginning of LS2 and the start of Phase-II upgrade activities.
 1529 From the HL-LHC period onwards, i.e. past LS3, the performance degradation due to integrated
 1530 radiation as well as the average number of inelastic collisions per bunch crossing, seen as pile-up
 1531 into the detectors' readout that far exceeds this of the original LHC plans, will rise substantially and
 1532 become a major challenge for all of the LHC experiments, like CMS, that were forced to address
 1533 an upgrade program for Phase-II [23]. Dealing with the data from the muon detectors will force
 1534 to upgrade the detectors and electronics towards the most recent technologies. Simultaneously, this
 1535 will push new latency requirements onto the Level-1 trigger and the Data Acquisition (DAQ) that

will only be fulfilled by upgrading the system with electronics having deeper buffering and faster processing. Simulations of the expected distribution of absorbed dose in the CMS detector under HL-LHC conditions show, in Figure 3.2, that detectors placed close to the beam line will have to withstand high irradiation, the radiation dose being of the order of a few tens of Gy.

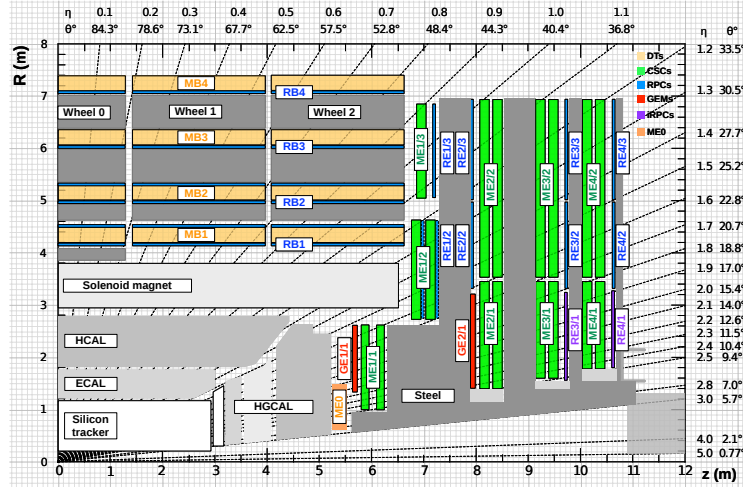


Figure 3.3: A quadrant of the muon system, showing DTs (yellow), RPCs (blue), and CSCs (green). The locations of new forward muon detectors for Phase-II are contained within the dashed box and indicated in red for GEM stations (ME0, GE1/1, and GE2/1) and dark blue for improved RPC (iRPC) stations (RE3/I and RE4/1).

The increase of irradiation close to the beam line will affect the background rate seen by the muon detectors in this area and tracking muons will prove to be difficult as this region is not yet equipped with all the detectors that were already foreseen for Phase-I. Improving this situation will come with the increase of hit numbers recorded along the particle track to reduce the ambiguity on muon versus background detection. Moreover, the measurement of small production cross-section and/or decay branching ratio processes, such as the Higgs boson coupling to charge leptons, and in particular to muons, or the $B_s \rightarrow \mu^+ \mu^-$ decay, is of major interest and specific upgrades in the forward regions of the detector will be required to maximize the physics acceptance to the largest possible solid angle.

To ensure proper trigger performance within the present coverage, the muon system will be completed with new chambers and the electronics of the present system will need to be upgraded to ensure an efficient triggering. Figure 3.3 shows the addition of Gas Electron Multiplier (GEM) and improved RPC (iRPC) in the pseudo-rapidity region $1.6 < |\eta| < 2.4$ to complete the redundancy of the already existing CSCs as originally scheduled in the CMS Technical Proposal [24]. A first step into this direction will be taken by installing GEMs on the first endcap disk in position GE1/1 during LS2, during which preparations for the future installation of more GEMs and RPCs will take place by installing the needed services. During the YETS following LS2, iRPCs will be installed on the third and fourth endcap disks in position RE3/1 and RE4/1, and more GEMs will equip the second endcap in position GE2/1 and the inner layer, closest to the HCAL endcap called ME0 during LS3, finally completing the redundant coverage of the muon system and extending it a little by extending the reach to $|\eta| = 2.8$, the redundancy in the region $2.4 < |\eta| < 2.8$ being maintained by the 6 GEM layers contained in each ME0 detector that provide enough tracking points to efficiently reject

1562 neutron-induced background.

1563 Nevertheless, the region beyond $|\eta| > 2.8$ and extending to $|\eta| = 5.0$ only is covered by the
 1564 forward HCAL detectors and lack redundant muon detector coverage. Extensions of the tracker in
 1565 the context of HL-LHC will increase its coverage up to $|\eta| = 4.0$ but the identification of muons and
 1566 measurement of their energy with reasonable precision only using the tracker is nearly impossible.
 1567 Thus, this increased tracker coverage range needs to be put in parallel with a matching muon detector
 1568 and will open doors to multi-lepton final states in which leptons are likely to have a low transverse
 1569 momentum and to be found near the beam line.

1570

1571 Finally, as the muon system is composed only of gaseous detectors, strong environmental con-
 1572 cerns have risen over the last years as the European directives will restrict the use of fluorine based
 1573 gas mixtures. Both the CSC and RPC subsystems, using CF_4 , $C_2H_2F_4$, or SF_6 , will need to adapt
 1574 their working gas in order to strongly reduce the greenhouse potential of the mixtures released into
 1575 the atmosphere due to gas leaks.

1576 3.2 Necessity for improved electronics

1577 Drift Tubes and Cathode Strip Chambers are important components used to identify and measure
 1578 muons, especially thanks to their spatial resolution of the order of $100\text{ }\mu\text{m}$. Nevertheless, the lumi-
 1579 nosity and irradiation during HL-LHC will cause serious event loss and ageing on the electronics of
 1580 these subsystems that will comprise the triggering and data transferring needs of CMS. Thus, elec-
 1581 tronics upgrade are foreseen to address these expected problems. While only the RPCs' electronic
 1582 system is able to operate under Phase-II requirements, DTs and CSCs will need to improve their
 1583 trigger accept rate and latency to ensure that Level-1 trigger threshold stays at the same level [25],
 1584 and DAQ data transfer rate, that respectively need to achieve a minimum of 500 kHz , get down to
 1585 $12.5\text{ }\mu\text{s}$ [26], and increase to 1082 Gbit/s DTs and to 1026 Gbit/s for CSCs. As of today, the Level-
 1586 1 trigger accept rate of DTs doesn't reach 300 kHz while this of CSCs is below 250 kHz but the
 1587 foreseen upgrades are expected to increase the rate way beyond the requirement in the of DTs and
 1588 up to 4 MHz for CSCs [23].

1589 The first version of Minicrate electronics (MiC1) used by DTs don't allow for high enough
 1590 trigger rate. In addition to this problem, it was showed that these electronics contain components
 1591 that are not radiation hard enough to sustain HL-LHC conditions and thus, a too large number of
 1592 channels may fail due to radiations. Considering the most optimistic scenario, at least 19% of the
 1593 channels could have failed by LS4, as explicitated in Figure 3.4, far before the end of the HL-LHC
 1594 campain. The MiC1 will be replaced on each detector by an improved version referred to as MiC2
 1595 while front-end electronics and high-voltage modules will not need any replacement. On the other
 1596 hand, CSCs showed that there electronics would be able to live through the 10 years of Phase-II but
 1597 the limited buffer depth might cause memory overflows and readout inefficiencies with a fraction
 1598 of event loss ranging from 5 to more than 10% at an instantaneous luminosity similar to which of
 1599 HL-LHC depending on the expected background, as showed on Figure 3.5 through the different
 1600 detector positions. Thus the replacement of CSCs' cathode front-end boards (CFEBs) by digital
 1601 ones, DCFEBS, with deeper buffer would permit to make event loss negligible and satisfy HL-LHC
 1602 requirements [23].

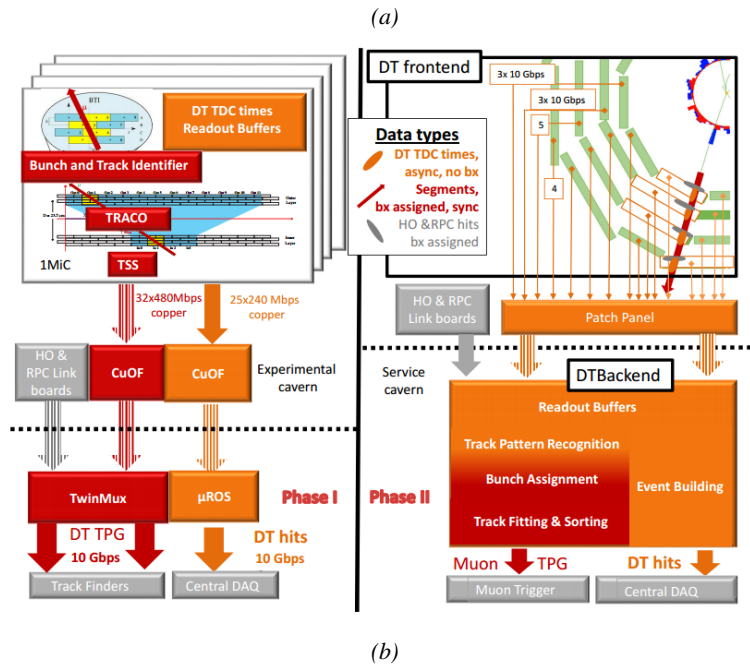
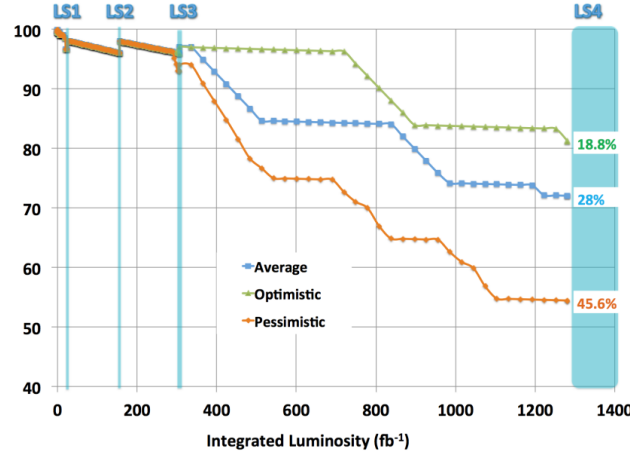


Figure 3.4: Figure 3.4a: Extrapolated fraction of failing channels of the present DT MiC1 electronics as a function of the integrated luminosity for different scenari until LS4. Figure 3.4b: Comparison of the current (left) and upgraded (right) DT data processing. So far, the data is sent to service cavern of CMS facility via copper-to-optical-fiber translators (CuOF) by each MiC1. There, data including RPCs and outer hadron calorimeter is combined into trigger primitives (TPG) and transmitted by the TwinMux system to CMS Track Finder. The time-to-digital converter (TDC) data is collected and sent to the CMS data acquisition system (DAQ) by the micro read-out server (μ ROS). After the upgrade, the TDC data will be sent via optical links to a patch panel inside the experimental cavern by each MiC2, and transferred to the back-end, where triggering and event building will be performed.

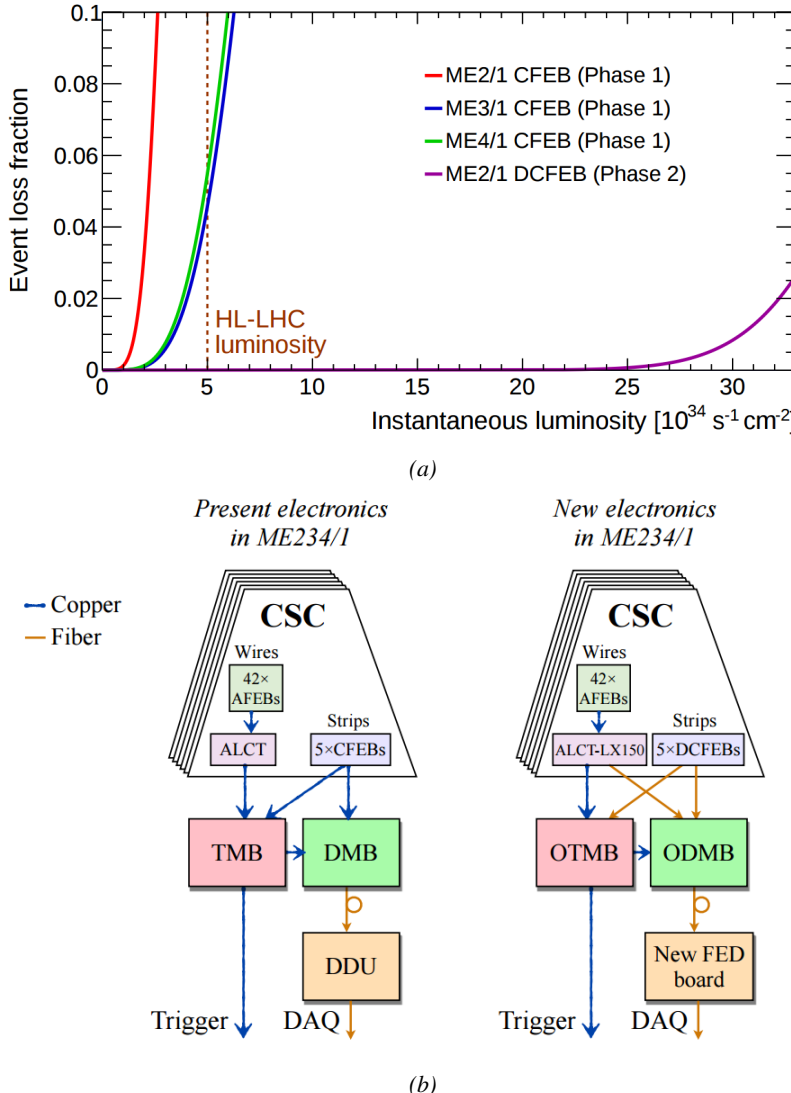


Figure 3.5: Figure 3.5a: The event loss fractions as a function of the instantaneous luminosity is compared for CFEBs (Phase-1) and DCFEBs (Phase-II) at different CSC locations. HL-LHC luminosity is marked with the dashed brown line. Figure 3.5b: Comparison of the current (left) and upgraded (right) CSC data processing. A part of the connections in between ALCTs and DCFEBs, and the trigger mother boards (TMBs) and data acquisition mother boards (DMBs) will be upgraded toward optical data transfer. The detector dependent units (DDUs) used as interface in between CSCs' front-end electronics and the CMS DAQ will be replaced by new FED boards.

All these new DT and CSC electronics will be connected to the trigger electronics via optical links to ensure a faster communication. The main change will come from the new DT minicrate modules which will not anymore be responsible for trigger and event building logic which will be transferred to the back-end electronics instead located in the service cavern via the patch pannels to which the Time-to-Digital Converter (TDC) data will be sent. The trigger and data transfer logic will barely change for CSCs. The existing copper cable connections of cathode and anode FEBs (CFEBs,

1609 and AFEBs which data is transmitted through the ALCTs) toward the trigger and data mother boards
 1610 (TMBs and DMBs) will simply be replaced by optical fibers and the TMBs and DMBs upgraded with
 1611 optical versions (OTMBS and ODMBs). As a new feature, the full anode wire data from ALCTs
 1612 will be sent to the ODMBs causing a lack of FPGA memory resources in these ALCT boards that
 1613 will thus need replacement.

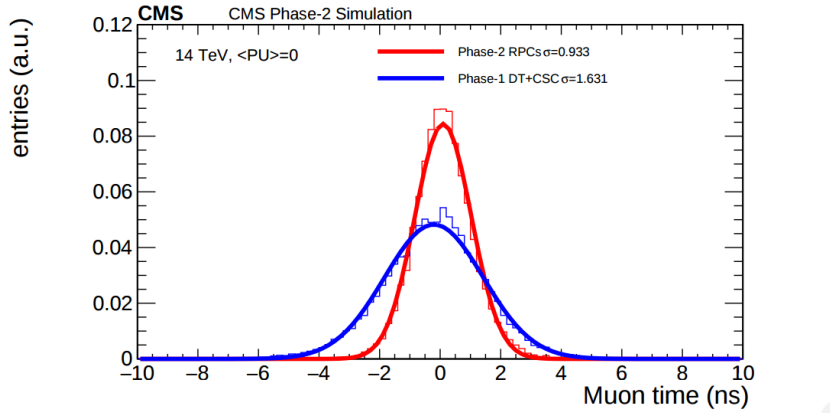


Figure 3.6: Comparison of the simulated time residuals in between reconstructed and true muon times without (blue) and with (red) the upgraded RPC link system.

1614 The upgrade on the side of Resistive Plate Chambers will then not come from their on-board
 1615 electronics but from the Link System located in the service cavern of CMS and that connects the
 1616 front-end electronics data of RPCs into CMS trigger processors. The main motivation for such an
 1617 upgrade is that the electronic board composing the link system are built using obsolete components
 1618 and weak components that can easily suffer from the electromagnetic noise. These components may
 1619 be the source of failing channels throughout Phase-II. Moreover, these link boards were originally
 1620 designed only to match RPC digitized signals with the corresponding bunch crossing. Due to this
 1621 feature, the time resolution of the full RPC chain is thus limited to 25 ns and does not exploit the full
 1622 time resolution of the detectors. This would make the synchronization of the RPC system easier and
 1623 allow to have a finer offline background removal within the 25 ns in between bunch crossings thanks
 1624 to the order of magnitude gained in terms of time resolution.

1625 Upgrading RPC link system will require the installation of 1376 new link boards and 216 control
 1626 boards. The new boards will make use of the recent progress made with fast FPGAs and will be a
 1627 great improvement to the ASICs formerly used as they will be able to process signals from several
 1628 detectors in parallel. The benefit from using the full RPC time resolution thanks to the upgraded
 1629 link system can be seen through Figure 3.6 where the resolution of the RPC system itself is better
 1630 than that of DTs and CSCs that was used until now.

1631 3.3 New detectors and increased acceptance

1632 In the present muon system, the redundancy was assured by RPCs used for their good timing per-
 1633 formances. The extension of the muon system towards higher pseudo-rapidity in order to complete
 1634 the redundancy in this very region and to contribute to the precision of muon momentum measure-
 1635 ments will require muon chambers with a spatial resolution less or comparable to the contribution

¹⁶³⁶ muon of multiple scattering through the detector volume [21]. Most of the plausible physics is
¹⁶³⁷ covered only considering muons with $p_T < 100$ GeV thus, in order to match CMS requirements,
¹⁶³⁸ a spatial resolution of $\mathcal{O}(\text{few mm})$ will be necessary for the proposed new RPC stations while the
¹⁶³⁹ GEMs will need a resolution better than 1 mm, as showed by the simulation in Figure 3.7.

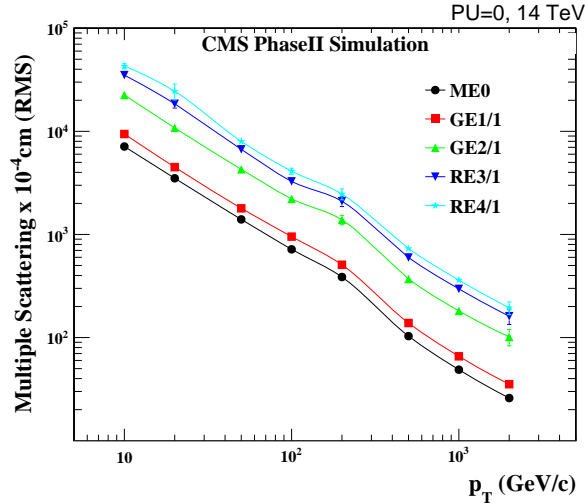


Figure 3.7: RMS of the multiple scattering displacement as a function of muon p_T for the proposed forward muon stations. All of the electromagnetic processes such as bremsstrahlung and magnetic field effect are included in the simulation.

¹⁶⁴⁰ 3.3.1 Improved forward resistive plate chambers

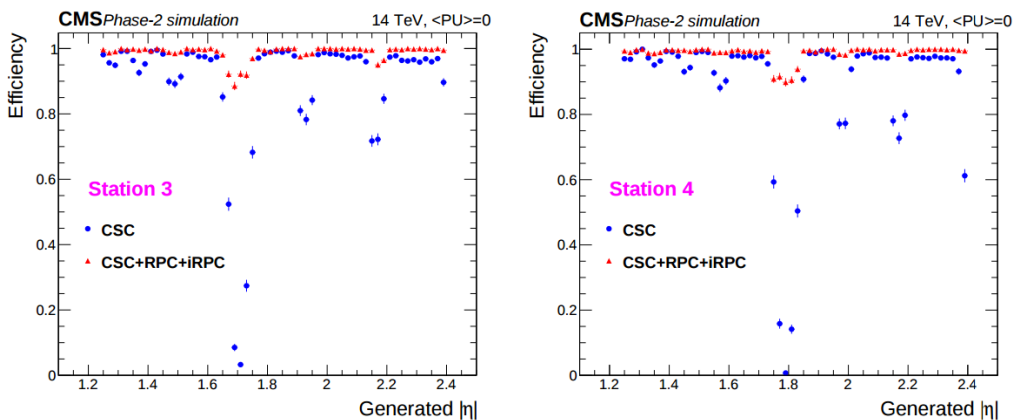


Figure 3.8: Simulation of the impact of RPC hit inclusion onto the local trigger primitive efficiency in station 3 (left) and station 4 (right). The contribution of iRPC starts above $|\eta| = 1.8$.

¹⁶⁴¹ Figure 3.3 shows that the iRPCs that will equip the third and fourth endcap disks in position RE3/1
¹⁶⁴² and RE4/1 will finally be the partners of the CSCs in position ME3/1 and ME4/1 and complete
¹⁶⁴³ Phase-I plans but bringing the needed upgrades in the scope of Phase-II as the older chambers are

not suitable to equip the forward region of CMS due to HL-LHC rates and charge deposition. By completing the redundancy, more track along the muon trajectory will be available and the lever arm will be improved. The benefits from extending the redundancy of the muon system with iRPCs to the forward most region is showed in Figure 3.8 in which the trigger efficiency is showed with and without RPCs in which it is possible to see that the efficiency of CMS trigger with the complete redundancy is improved is above 95% in the region $|\eta| > 1.8$ as the iRPCs help filling the holes in the CSC system.

1651

The detectors that will be installed in the coming years will be similar to the already existing RPC system. 18 of the new chambers, each spanning 20° in φ around the beam axis with 96 radially oriented trapezoidal read-out strips, will cover each muon endcap disk leading to the production of 72 iRPCs. The main difference with the old RPC chambers is that these detectors will not have readout strips segmented in η as by using fast front-end electronics the strips will be read-out on both sides allowing for a radial spatial resolution of the order of 2 cm in order to contribute to the better reconstruction of muon in the forward region where the bending of muons by the magnetic field is low. This is motivated by the fact that, in the case a η segmentation was used, at least 5 pseudorapidity partitions would have been necessary to reach the minimal radial spatial resolution (≈ 20 cm). Having only one strip read-out from both along the chamber reduces by 60% the total number of channels and the necessary cabling and allows for a better spatial resolution. The strip pitch will range from 6.0 mm (5.9 mm) on the high pseudo-rapidity end to 12.3 mm (10.9 mm) on the low one on position RE3/1 (RE4/1). The spatial resolution in the direction perpendicular to the strips should reach approximately 3 mm, better than the minimal needed resolution (Figure 3.7), and the overall time resolution of the new installation will be equally 1.5 ns, as for the present due to the same link system being used.

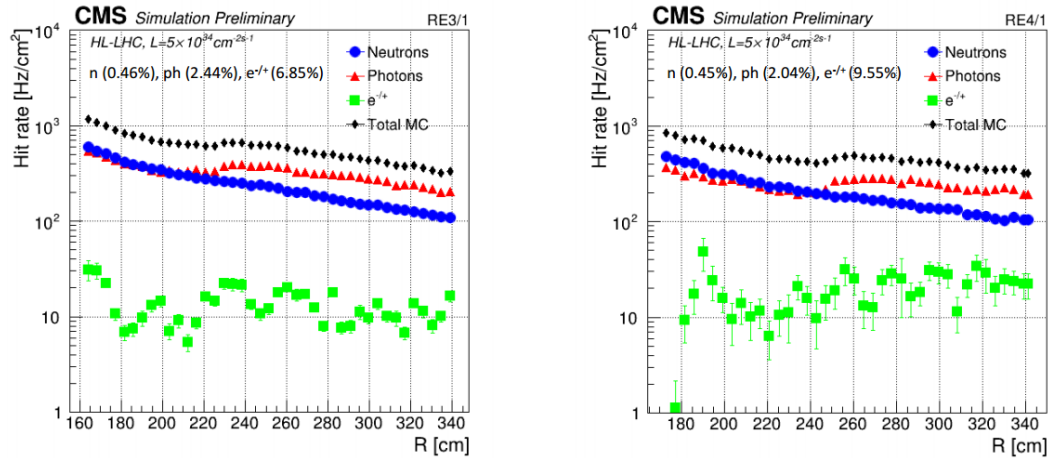


Figure 3.9: Expected hit rate due to neutrons, photons, electrons and positrons at HL-HLC instantaneous luminosity of $5 \times 10^{34} \text{ cm}^{-2}\text{s}^{-1}$ in RE3/1 and RE4/1 chambers. The sensitivities of iRPCs used in the simulation for each particle are reported and differ from one endcap disk to another as the energies of the considered particles varies with the increasing distance from the interaction point.

Nevertheless, having only a single strip instead of pseudo-rapidity segmentation will increase the probability of double hits in the same channel. This probability was estimated to be low enough

as it shouldn't exceed 0.7%. This estimation was made assuming an average hit rate per unit area of 600 Hz/cm² in the iRPCs (see Figure 3.9), a cluster size (average number of strips fired per muon) of 2, a strip active area of 158.4 × 0.87 cm² and a safety factor 3 leading to an estimated rate per strip of 380 kHz corresponding to an average time interval of 2600 ns in between 2 consecutive hits. The time for a signal to go through the full strip length is about 10 ns to which can be added 1 ns of dead time and 2 TDC clock cycles of 2.5 ns for a minimal time interval of 16 ns necessary to avoid ambiguities. The probability of having ambiguous double hits in a strip is then the ratio in between this minimal time interval in between 2 consecutive hits and the average time interval estimated from the rate the detectors are subjected to.

The instantaneous luminosity at HL-LHC being very high, the rates at the level of the new chambers needed to be simulated in order to understand the necessary requirements for these detectors. The simulated results for different background components (neutrons, photons, electrons and positrons) are showed in Figure 3.9 assuming known sensitivities to these particles. It is showed that on average over the iRPC areas the rates would be of the order of 600 Hz/cm² (600 Hz/cm² seen in RE3/1 and 480 Hz/cm² in RE4/1) [27]. Thus, taking into account a safety factor of about 3, it was decided that improved RPCs should at least be certified for rates reaching 2 kHz/cm² which would be achieved thanks to several improvements on the design and on the electronics. The detectors design will be based on the existing RPC design as they will be double gaps. Similarly to the existing RPC system, the electrode material will be HPL although the thickness of the electrodes and of the gas gap will be reduced to 1.4 mm as a thinner gas gap leads to a decrease of deposited charge per avalanche as showed in Figure 3.10. The smaller the gas gap, the more the detector becomes sensitive to gap non-uniformities across the electrode planes making a gap of 1.4 mm a good compromise in between these two competing factors.

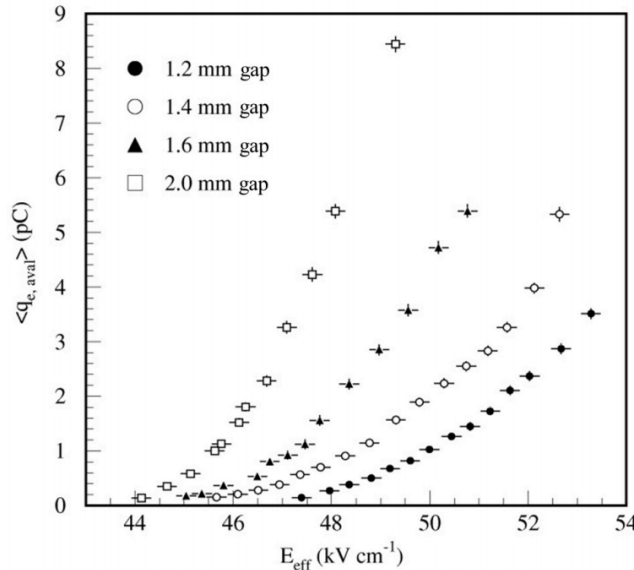


Figure 3.10: Measured average charge per avalanche as a function of the effective electric field for different gas gap thickness in double gap RPCs using HPL electrodes.

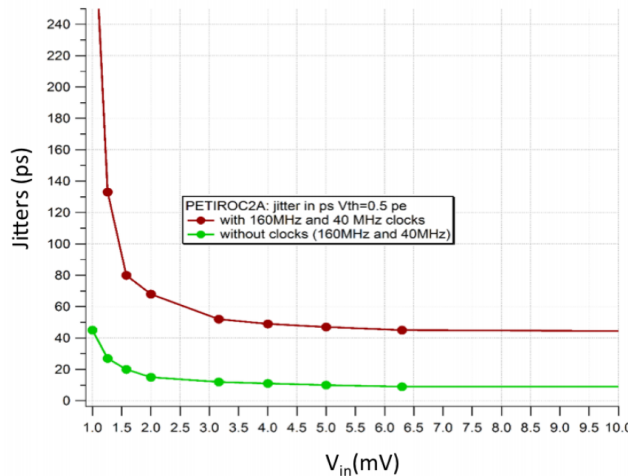


Figure 3.11: The PETIROC time jitter as a function of the input signal amplitude, measured with and without internal clocks.

1693 A lower charge deposition inside of the detector volume means a slower ageing and a longer life-
 1694 time for detectors subjected to high irradiation. But, in order to take advantage of the lower detector
 1695 gain, more sensitive electronics are required so that the part of gain that was formerly done in the gas
 1696 volume can be moved to the electronics. Achieving this with the technology developed more than
 1697 10 years ago for the present system is not possible as the signal over noise ratio of such electronics
 1698 doesn't allow to detect charges as low as 10 fC. Moreover, the new front-end electronics will need
 1699 to be radiation hard to survive to more than 10 years of HL-LHC conditions. The new technology
 1700 that has been chosen is based on the PETIROC ASIC manufactured by OMEGA and is a 64-channel
 1701 ASIC called CMS RPCROC on which the original SiGe technology will be replaced by CMOS to
 1702 increase its radiation hardness while keeping fast pre-amplification and discrimination with a very
 1703 low jitter that can reach less than 20 ps if no internal clock is used, as can be seen from Figure 3.11.
 1704 The ASIC is associated with an FPGA which purpose is to measure time thanks to a TDC with a
 1705 time resolution of 50-100 ps developed by Tsinghua University and that will provide a measurement
 1706 of the signal position along the strip with a precision of a few cm by measuring the signal timing
 1707 on both ends of the strips. In order to read-out all 96 strips, 3 ASICs and 3 TDCs, each having 64
 1708 channels, are hosted on a front-end board attached to the chamber.

1709
 1710 [Wait for the analysis of 2018 GIF++ data to add interesting information about the time and
 1711 spatial resolution measured during test beam periods.]
 1712

1713 3.3.2 Gas electron multipliers

1714 In the region closer to the interaction point where the spatial resolution is requested to be better
 1715 than 1 mm for the new detectors (at least for GE1/1 and ME0, GE2/1 being in the same order of
 1716 requested spatial resolution than the new iRPCs that will equip the third and fourth endcaps), the
 1717 choice has been made to use triple GEMs, micro pattern gaseous detectors, in the place of RPCs.
 1718 The GE1/1 project had been the first to be approved and demonstrators had been installed in CMS

¹⁷¹⁹ already during LS1. The rest of the detectors will be installed during LS2 while the GE2/1 and ME0
¹⁷²⁰ projects are still under development. ME0, GE1/1 and GE2/1 will be installed respectively next to
¹⁷²¹ the HCAL endcap, on the first and on the second muon endcap disks as can be seen from Figure 3.3.

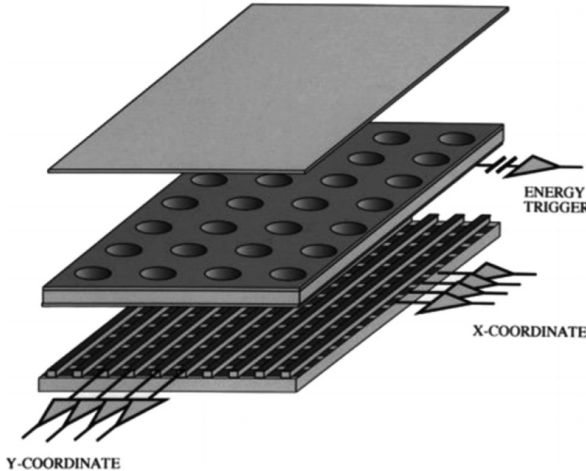


Figure 3.12: Schematics of a GEM showing the cathode on top, the GEM foil separating the gas volume into the drift region, in between the cathode and foil, and the induction region, in between the GEM foil and the anode, and the anode on which a 2D read-out is installed. A negative voltage is applied on the cathode while the anode is connected to the ground.

¹⁷²² Gas Electron multipliers are gaseous detectors [28] which gas volume is confined in between
¹⁷²³ 2 planar electrodes, the anode serving as read-out panel. The gas volume is divided in 2 or more
¹⁷²⁴ regions by a single or multiple *GEM foils* as showed in Figure 3.12. These foils are very thin, of
¹⁷²⁵ the order of a few tens of μm , and are pierced with holes as can be seen in Figure 3.13. Both
¹⁷²⁶ surfaces of the GEM foils are clad with copper in order to apply a strong electric field in between
¹⁷²⁷ each side that will generate very strong potentials in the holes. The gas region contained in between
¹⁷²⁸ the cathode and the GEM foil is called the drift region as the electric field is not strong enough to
¹⁷²⁹ cause avalanches and thus start an amplification. The primary electrons drift toward the foil and are
¹⁷³⁰ accelerated and amplify by the very high potential within the holes, as showed in Figure 3.13. Then
¹⁷³¹ the electrons reach the second drift region in which they will induce signal on the read-out located
¹⁷³² on the anode. By restraining the amplification process at the level of the holes, the electrons can stay
¹⁷³³ in a very confined space and thus induce a very localized current, providing the GEMs with a very
¹⁷³⁴ good spatial resolution.

¹⁷³⁵ In order to achieve a stronger amplification, the amplification process can be repeated several
¹⁷³⁶ times in a row. The GEMs that will be used in CMS are triple GEM detectors operated with a 70/30
¹⁷³⁷ gas mixture of Ar/CO_2 . They contain 3 GEM foils and thus 3 electron amplifications, as can be
¹⁷³⁸ seen in Figure 3.14. The GEM foils used in CMS are 50 μm foils clad with 5 μm of copper on
¹⁷³⁹ each side. The foils are pierced with double-canonical holes which inner and outer diameters are
¹⁷⁴⁰ respectively 50 and 70 μm which are placed 140 μm from each other in an hexagonal pattern, as
¹⁷⁴¹ showed in Figure 3.13. These detectors have a time resolution better than 10 ns and reach very good
¹⁷⁴² spatial resolutions of less than 200 μrad as indeed the position of the hits is not measured along the
¹⁷⁴³ strips but following the azimuthal angle granularity of the radially organized trapezoidal strips.

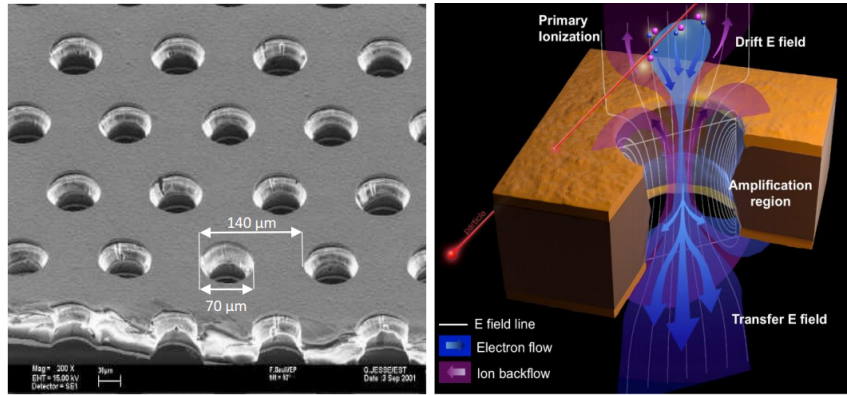


Figure 3.13: Left: Picture of a CMS GEM foil provided by a scanning electron microscope. Right: Representation of the electric field lines in a GEM hole and of the amplification that electrons and ions undergo in the hole's volume due to the very intense electric field.

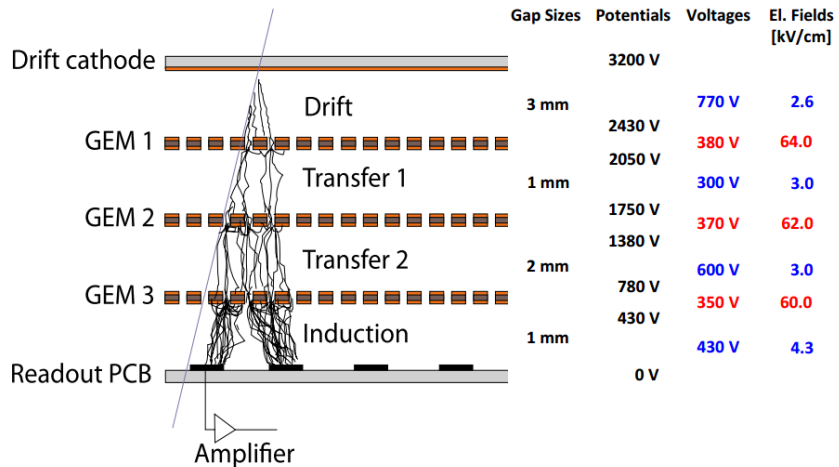


Figure 3.14: Schematic representation of CMS triple GEMs. The gas volume is divided into 4 areas. The drift area is the region where the primary electrons are created before being amplified a first time while passing through the first GEM foil. Then the process of drift and amplification is repeated twice in following two transfer areas and GEM foils. Finally, the charges have been amplified enough to induce current in the read-out strips while in the last drift area. The dimensions, potentials and electric fields are provided.

1744 The GEM Upgrade is divided into 3 subsystems as GE1/1 was the first approved project [29]
 1745 and that the detectors will already be installed during LS2. GE2/1 and ME0, on the other hand,
 1746 will profit of the R&D knowledge and skills developed for GE1/1 while the requirements for each
 1747 subsystem are different as they are not placed at the same distance from the interaction point. In this
 1748 very forward region, a different position with respect to the center of the detector can change dra-
 1749 matically the conditions in which the detectors will have to be operated. In terms of rate capability,
 1750 GE2/1, which is the furthest, is required to withstand 2.1 kHz/cm² while GE1/1 needs to be better
 1751 than 10 kHz/cm² and ME0, better than 150 kHz/cm². In terms of ageing with respect to charge
 1752 deposition, ME0 needs to be certified to 840 mC/cm², GE1/1 to 200 mC/cm² and GE2/1 only to

1753 9 mC/cm². All 3 detectors need to have a time resolution better than 10 ns and an angular resolution
 1754 better than 500 µrad.

1755 On each GE1/1 ring, 36 super chambers, consisting of 2 single GEM layers and spanning 10°,
 1756 will be installed covering the pseudo-rapidity region $1.6 < |\eta| < 2.2$ together with ME1/1 CSCs and
 1757 the reach of the muon system will be improved thanks to the GE2/1 that will overlap with the GE1/1
 1758 and cover a region from $|\eta| > 1.6$ to $|\eta| < 2.4$ and complete the redundancy of ME2/1. The super
 1759 chambers, built with 2 triple GEM layers each consisting of 4 single GEM modules due to the rather
 1760 large surface of the GE2/1 chambers, that will be installed on the first ring of the second endcap will
 1761 span 20° each, hence, a total of 72 chambers will be assembled to equip the muon system. Finally,
 1762 the ME0 installed near the HCAL endcap will cover the region $2.0 < |\eta| < 2.8$ and this subsystem
 1763 will consist in super modules of 6 layers of triple GEM detectors covering an azimuthal angle of 20°
 1764 leading to the construction of 216 single detectors.

1765 All these new GEM detectors will be using a similar internal layout which is described in Fig-
 1766 ure 3.14. The incoming muons will create detectable electron-ion pairs in the 3 mm thick drift
 1767 volume in which an electric field of 2.6 kV/cm is applied for the electrons to drift to the first GEM
 1768 foil on which a very intense field of 64 kV/cm is applied over a distance of only 60 µm which allows
 1769 for an average electronic gain of 20 to 25. After the first amplification stage, the electrons drift over
 1770 the 1 mm separating the 2 first GEM foils thanks to an electric field of 3.0 kV/cm and are again
 1771 amplified by a factor 20 to 25 while going through the second GEM foil to which is applied an elec-
 1772 tric field of 62 kV/cm. The electron drift another 2 mm towards the last GEM foil through a field of
 1773 3.0 kV/cm and are multiplied one last time from a similar factor passing through the 60 kV/cm
 1774 of the last GEM foil holes. Finally, they drift along the 1 mm of the induction volume in a field of
 1775 4.3 kV/cm to reach the trapezoidal strips on the read-out PCB used as anode. The total detector
 1776 gain is approximately of the order of 10^4 and the resulting output signal is both due to the induction
 1777 of moving charges in the induction volume and of charge pic-up once they read the read-out strips.

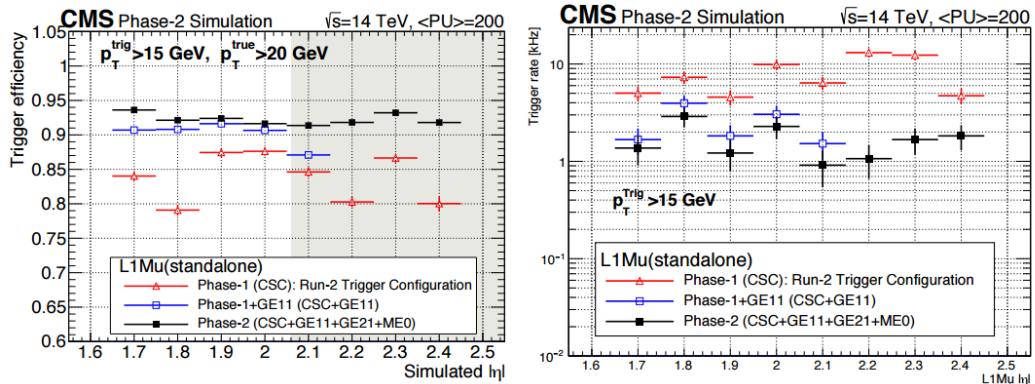


Figure 3.15: Simulated efficiency and rate of the standalone Level-1 muon trigger using tracks reconstructed in CSCs and all GEM stations compared with Phase-I values in the case where only CSCs are used or CSCs+GE1/1. The zones of inefficiency of the CSC subsystem are compensated by the addition of GEMs during Phase-II and the trigger rates is kept from increasing due to the high luminosity.

1778 Adding the GEMs into the forward region of the muon system will allow to strongly enhance
 1779 the Level-1 Trigger performance by reducing the inefficiency regions and the trigger rate as showed
 1780 in Figure 3.15. Moreover, benefiting from the good spatial and angular resolution of the GEMs, the

¹⁷⁸¹ precision into the muon measurement will also be greatly improved by the addition of GEMs as can
¹⁷⁸² be seen from the simulation presented in Figure 3.16.

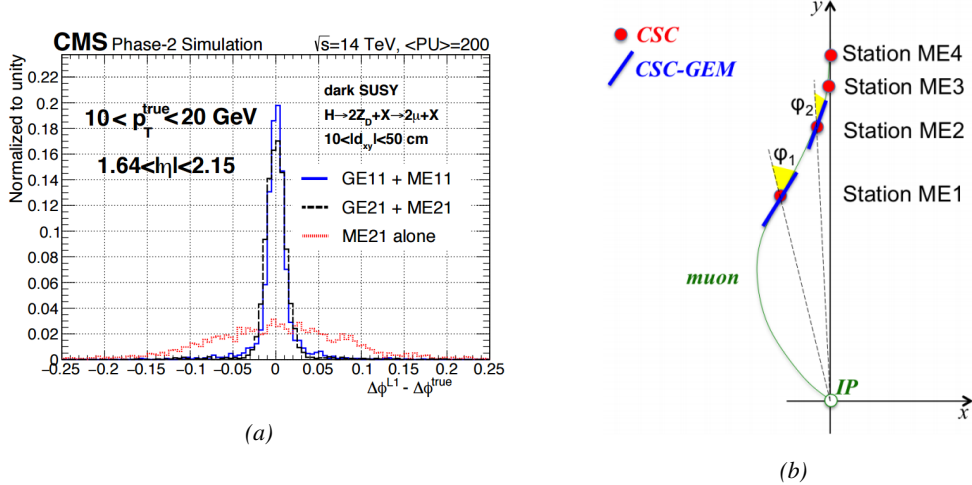


Figure 3.16: Figure 3.16a: Simulated resolution of the muon direction measurement $\Delta\phi$ with Phase-II conditions. In the second endcap station, the resolution is compared in the case of CSCs (ME2/I) alone and CSCs+GEMs (GE2/I+ME2/I) while a similar resolution measurement is given in the case of the first station (GE1/I+ME1/I). Figure 3.16b: The addition of GEM detectors on stations 1 and 2 (ME0 is considered to contribute to station station 1) as redundant system to CSCs allows to improve the muon momentum improvement through a more accurate measurement of the local bending angles ϕ_1 and ϕ_2 .

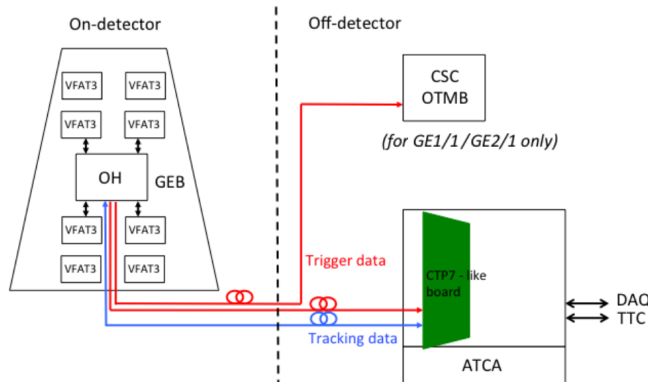


Figure 3.17: Schematics of the data communication chain for DAQ of the GEM subsystems. The sending of trigger data via optical links to the CSC OTMBs is only done for GE1/I and GE2/I to match the data with ME1/I and ME2/I.

¹⁷⁸³ The read-out of GEMs will use the same technology. The anode planes used as read-out PCBs
¹⁷⁸⁴ and referred to as GEM Electronics board (GEB) host on their outer surface VFAT3 ASICs that
¹⁷⁸⁵ connect to a total of 128 strips for a very fine angular granularity. Along the endcap radius, the strips are
¹⁷⁸⁶ divided into 8 pseudo-rapidity partitions. In the case of GE1/I and ME0, each η -partition consist in
¹⁷⁸⁷ 384 read-out strips connected into 3 VFAT3 ASICs and offering a while the large GE2/I partitions

1788 contain twice as many channels. Both GE1/1 and GE2/1 strips have an angular pitch of $474\text{ }\mu\text{m}$
 1789 while this of ME0 is twice larger due to its proximity with the interaction point. The VFAT3 ASICs
 1790 allow for a latency better than the $12.5\text{ }\mu\text{s}$ required by CMS Level-1 Trigger and there frequencies
 1791 goes up to 1 MHz. They are connected into the Optohybrid Board (OH) and this full ensemble
 1792 (GEB+VAT3+OH) constitute the on-chamber electronics. The OH is then sending the data to the
 1793 modules constituting the DAQ of the GEM system via optical fibers. These back-end electronics
 1794 modules are located in the service cavern of CMS and host CMS communication devices, used to
 1795 have a common clock, and control and links to the Endcap Muon Track Finder (EMTF) system.
 1796 Moreover, GE1/1 and GE2/1 also have links with the CSC OTMBs as the OH of these 2 subsystems
 1797 send data into these boards. This communication chain can be seen in Figure 3.17.

1798
 1799 The detectors that will placed in CMS will have to live through Phase-II without significant
 1800 performance degradation to ensure an efficient data taking and the possibility to investigate more
 1801 exotic physics. As the 3 GEM subsystems will be using the same detector technology, the choice
 1802 was made to certify the GEMs in the worst of the 3 environments, i.e. the ME0 station located right
 1803 behind the HCAL. According to FLUKA simulation, including all the latest foreseen upgrades into
 1804 the CMS detector geometry, it was shown that the maximal hit rate expected in ME0 would be of
 1805 the order of 50 kHz/cm^2 with contributions of neutrons (6 kHz/cm^2), photons (35 kHz/cm^2), and
 1806 electrons and positrons (8 kHz/cm^2) resulting in a charge deposition a little lower than 300 mC/cm^2
 1807 after 10 years of HL-LHC [23]. It is necessary to understand the classical ageing effects on the GEMs
 1808 but also premature ageing due to contaminants in the gas mixture leading to polymerization on the
 1809 surface of the GEM foils during operation and the effect of discharges on the detector operations if
 1810 they have to happen during their lifetime.

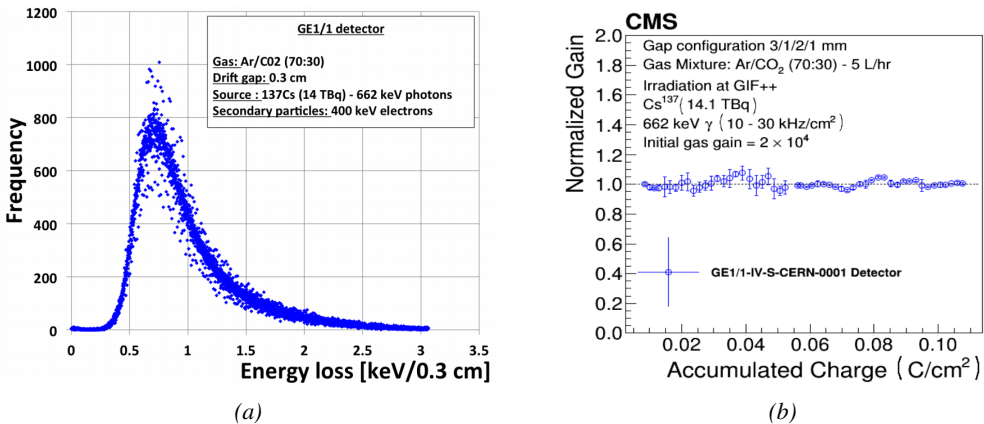


Figure 3.18: Figure 3.18a: Energy spectrum of GIF^{++} ^{137}Cs source as measured by the GE1/1 detector installed in GIF^{++} . Figure 3.18b: Evolution of the normalized gain of the GE1/1 detector installed at in GIF^{++} as a function of the integrated charge per unit area. The first part of the study, up to a charge of 55 mC/cm^2 had been done in the former Gamma Irradiation Facility (GIF) that has now been dismantled following the construction of GIF^{++} . No variation of the normalized gain can be observed after an accumulation of 110 mC/cm^2 .

1811 To characterize the classical ageing effects, a campaign is being conducted in the new Gamma
 1812 Irradiation Facility (GIF^{++}) of CERN where a GE1/1 detector operated at its nominal gain is placed
 1813 50 cm from the facility's 14 TBq ^{137}Cs source which emits gammas at an energy of 662 keV. In

order to spot any ageing of the detector, the effective gain is kept monitored, as can be seen in Figure 3.18b, as its variations gives clues about different aspects of the detector such as the geometry of the holes, the electric field configuration or the gas composition. The monitoring of the gamma energy distribution, showed on Figure 3.18a, can give an idea on the evolution of the performance of the chamber and finally, the evolution of the currents through time also is a good indicator of the appearance of dark current in the detector that would be due to the emission of electrons by thin insulating layers of the detector subjected to a long lasting irradiation known as Malter effect. At the time the Technical Design Report (TDR) for the Phase-II upgrade of the muon system was written [23], the GEM group had reported a total integrated charge of 110 mC/cm^2 which, if compared with 10 years of HL-LHC operation, represents a safety factor of 18 for the GE1/1 subsystem and a factor 37 for the GE2/1 subsystem but only 39% of the total expected ME0 integrated charge. It is estimated that reaching the total integrated charge necessary to certify the detectors for Phase-II operation will take another 2 to 3 years. Nevertheless, the present status of the longevity study shows no degradation of the performance of the detector installed in GIF++ as can be seen through Figure 3.18.

Aside of the classical ageing tests, outgassing of the different materials composing the GEMs have been conducted by placing the different materials to be tested into an outgassing box that consists in a stainless steel cylinder through which the CMS GEM 70/30 gas mixture of Ar/CO_2 with the possible contaminants is flowed while the detector is exposed to the continuous irradiation of a radioactive source and the heat is raised to enhance the outgassing. From the detector that was placed into this outgassing box, only one component was identified to cause loss of performance due to outgassing. This component was the polyurethane *Cell-Pack* used to coat the internal frame of the GEMs and the polymerization on its surface caused a 20% decrease of the gas gain. this polyurethane was replaced with a new one for which no outgassing effect causing a loss of performance was reported.

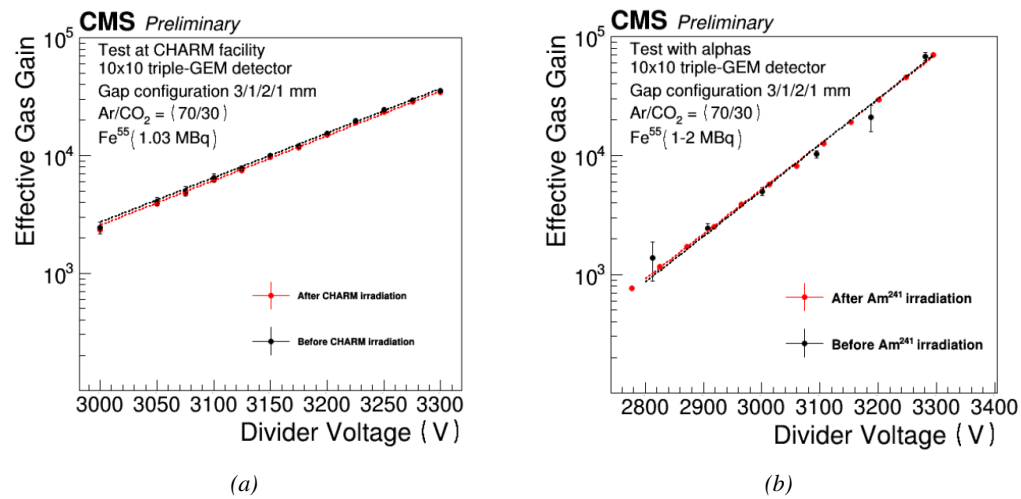


Figure 3.19: Figure 3.19a: Comparison of the gas gain as a function of the divider voltage before and after the irradiation of a triple-GEM by neutrons in CHARM. Figure 3.19b: Comparison of the gas gain as a function of the divider voltage before and after the irradiation of a triple-GEM by alpha particles.

Finally, even though the triple-GEM technology makes the detectors safe of discharges thanks to

its several amplification stages that allow to reach high gas gain using a relatively low electric field applied on the foils and to the distance separating the last foil from the read-out panel that is high enough to prevent discharging from developing all the way to the read-out, and hence, be stopped before it can cause any harm, it is important to have a good understanding of the discharge probability to ensure a safe operation over long periods. In order to further prevent discharges to develop in the detector volume, the GEM foils' power supply have been sectorized and protection resistors have been installed to limit the energy available for the discharge development. To reproduce the high-energy neutron background conditions of CMS, a GE1/1 detector have been placed in the CHARM facility of CERN. This facility allows to irradiate the detectors with a neutron fluence as high as $2.5 \times 10^8 / \text{cm}^2$. The detectors were operated with a slightly higher gain of 3.5×10^4 . It was measured that the discharge probability for a GEM operated under CMS conditions was of 2.85×10^{-9} per heavily ionizing particle with a 95% confidence level that would correspond to 225 discharges per cm^2 in ME0, 17 in GE1/1 and 12 in GE2/1 during the full HL-LHC period. According to Figure 3.19a, no degradation of the performance was observed after the irradiation at CHARM were 24 discharges per unit area were reported. Nevertheless, another test were the detector was exposed to a 5.5 MeV alpha source and were 450 discharges per unit area were reported didn't show any drop of performances either, as can be seen in Figure 3.19b.

3.3.3 Installation schedule

The previous discussion on the different upgrade projects makes it clear that a lot of work is scheduled for CMS to be ready at the end of LS3 for HL-LHC. Conducting all the upgrades of the muon system together with upgrades of the other subsystems like the replacement of the Tracker and of part of the ECAL, will prove to be very difficult as the opening of CMS to access the Barrel will be done by fully opening the endcaps leaving only the first disk to be accessible. Thus, most subsystems have planned early installation over LS2, and the following YETS until LS3 in order to give more space to LS3 schedule.

First of all, LS2 will see the installation of GE1/1 detectors, all the on-detector schedule of CSCs and the installation of the necessary services for the improved RPCs to be installed later, such as the HV and LV power supply lines, the gas and cooling lines or signal cables. CSCs will have a huge work to do during LS2 as they will need to extract all of their detectors to refurbish them with upgraded DCFEB and ALCT mezzanine boards. The GE1/1 services were installed during LS1 together with a few demonstrator and only the detectors needs to be integrated into the first endcap disk. The detectors are presently being built and tested at the different assembly site to prepare for a smooth LS2 work.

The work of GEMs will be continued during the following YETS during which is planned the installation of the GE2/1 stations to only leave the ME0 to be installed during LS3. The iRPC program will follow a similar path as the new detectors will be installed during the YETS preceding LS3 in prevision of the fact that the endcap disks will not be accessible during LS3. This way, all the subsystems, but DTs, made great effort on planning their installation and integration within CMS only to have to deal with off-detector issues during the LS3 period, such as the replacement of ODMBs and HV system in the case of CSCs or the upgrade of the RPC Link System. Finally, during LS3 are scheduled the replacement of DT minicrates electronics and the installation and integration of ME0 GEMs together with the HGCAL.

3.4 Implications of the different upgrades on the Level-1 Trigger. Improvement of physics performance.

The upgrades of the different subsystems will have a subsequent impact on the Level-1 Trigger. Indeed, although its main scheme will not be affected, the efficiency of the trigger in identifying muons and provide the DAQ with good and fast trigger that can cope with HL-LHC instantaneous luminosity is a major improvement. In addition to the upgrade of the muon system in terms of trigger accept rate and latency, the Level-1 Trigger will get extra information in including the Tracker Trigger into its Muon Track Finder logic and combine the L1 Muon Trigger with Tracker and Calorimeter Triggers to generate a Global L1 Trigger with a much better momentum resolution, as showed in Figure 3.20.

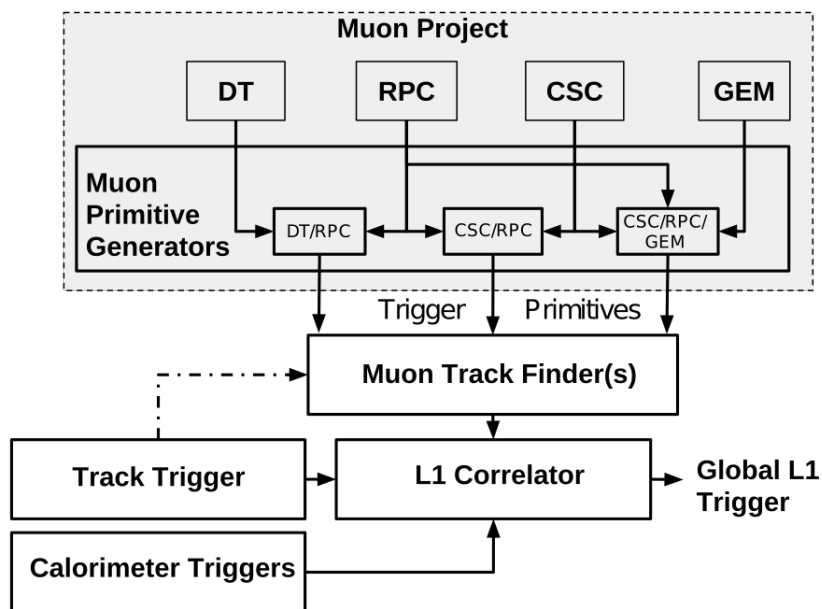


Figure 3.20: Data flow of the Level-1 Trigger during Phase-II operations.

In terms of muon trigger, 3 regions are considered due to their different track finding logic: the Barrel Muon Track Finder (BMTF), the Endcap Muon Track Finder (EMTF) for both the barrel and endcap regions, and finally the Overlap Muon Track Finder (OMTF) which concerns the pseudo-rapidity region in which there is a common coverage by both the barrel and endcap muon systems. This region can be seen in Figure 3.3 for $0.9 < |\eta| < 1.2$ and requires a specific more complex logic to provide with an efficient reconstruction of the muons due to the different orientation of the detectors and of the more complex magnetic field of this region that needs to be taken into account. The benefits of the upgrade for each of these track finders will be coming from different improvements and will be detailed sector by sector.

The main contribution to the improvement of the BMTF is the time resolution improvement of RPC link systems that will allow to take profit of the full 1.5 ns resolution of the detectors. From the perspective of RPCs only, this improvement will help reducing the neutron induced background and

slightly improve the bunch crossing assignment. The upgrade of DT electronics is also to take into account as the trigger primitive generator will be renewed through the use of TDCs that will send the digitized signals directly to the back-end electronics instead of having an on-detector trigger logic as it will be the case until the end of Phase-I. The front data of both DTs and RPCs will be sent to the same back-end electronics. These upgrades were detailed in section 3.2 and will lead to a more robust operation of the trigger in the barrel region. Indeed, the combination of RPC hits together with DT primitives will bring improvement in the bunch crossing assignment and improve the efficiency of the trigger in between the wheels where the quality of DT primitives is the poorest. Moreover, having a redundant information is important in the case of failure and loss of efficiency of one of either subsystems.

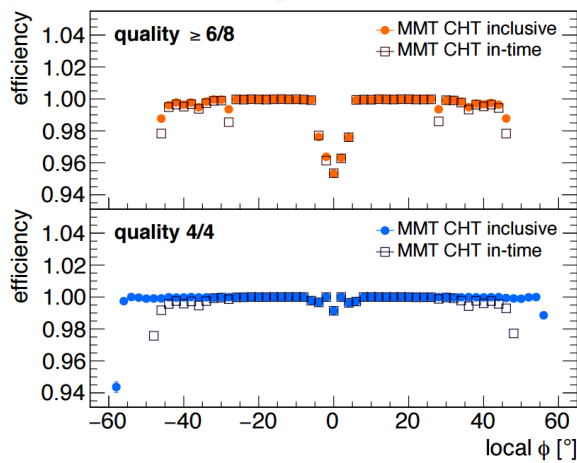


Figure 3.21: Comparison of Phase-II DT trigger primitives algorithmic efficiency for segments obtained with 2 super-layers ($\text{quality} \geq 6/8$) and 1 super-layer only ($\text{quality} = 4/4$). The simulation was done by generating 2×10^6 muons. The candidate tracks with correct time identification is showed with open symbols.

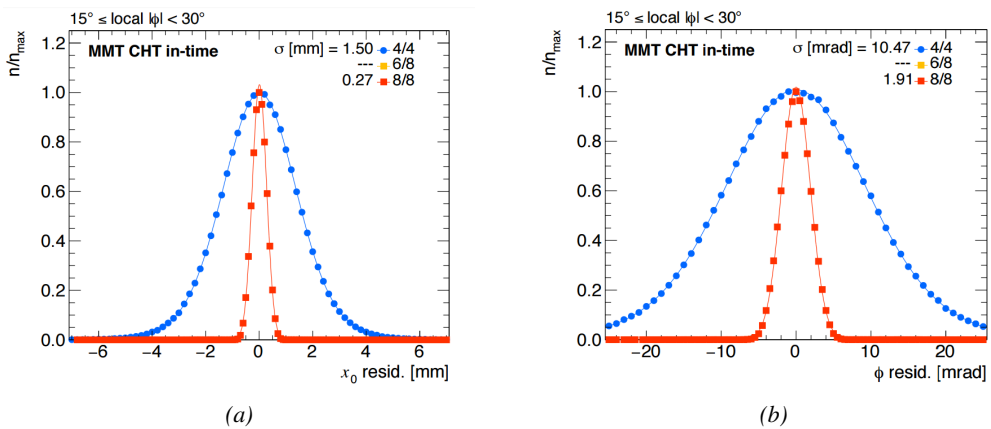


Figure 3.22: Simulated spatial (3.22a) and angular (3.22b) resolution of the algorithm using 8 aligned hits in both super-layers (quality = 8/8) and 4 aligned hits in only one super-layer (quality = 4/4). The contribution of intermediate quality tracks (6 aligned hits) is negligible in the angular range shown. [Be careful to update this caption as it uses a text to close to the published one.]

The loss of single hit efficiency of DTs due to ageing will also force the DT to change the algorithm use to identify tracks. So far, the identification was only performed at the level of a single DT super-layer, which is composed of 4 single DT layers. In the perspective the single efficiency drops, this will require to be upgraded to try to combine the data of more than a single super-layer to keep a high muon track identification efficiency. In addition to this change in trigger primitive candidate quality, new algorithms with higher efficiency are being developed. According to Figure 3.21, the efficiency of the new algorithm, both in the cases using 1 or 2 super-layers, is higher than with the current system [30]. Moreover, the overall efficiency of an algorithm requesting at least a muon detected in 6 DT layers out of the 8 composing the 2 super-layers of a DT module would stay comparable to the 4 DT layers out of 4 algorithm within the local bending angle range. On the other hand, despite the slight loss of efficiency in the low angle range, the algorithm using more DT layers achieves both higher spatial and angular resolution according to Figure 3.22.

1928

With new detectors to cover the very forward region and the upgrade of RPC Link System, the EMTF will be greatly improved. The current EMTF already use more sophisticated algorithms by combining together RPC hits and CSC primitives and will also benefit from the improved time resolution of the RPC system. The GEMs, in stations 1 and 2, and the iRPCs, in stations 3 and 4, will be added into the EMTF algorithm. Both these contributions will help increasing the efficiency of the L1 trigger in the endcap region in one hand, and help lowering the L1 trigger rate in the other hand, especially in the most forward region. The improvement of the efficiency will come both from the better time resolution of RPC link boards and from the addition of more hits along the muon tracks and also a contribution from the GEMs to the lever arm of each track thanks to their high angular resolution.

1939

The rate will be partly reduced in the forward region thanks to the better spatial resolution of iRPCs, with respect to the current RPC system, that will reduce the ambiguity brought by multiple local charged tracks in CSCs, as explained through Figure 3.24. Indeed, as the rates will increase, the probability to record more than a single local charged track will greatly increase. This is due to the fact that the trigger algorithm uses information from 3 consecutive bunch crossings to find muon tracks. It is estimated that with iRPCs operated at 95% efficiency the resolution of ambiguous events would be of the order of 99.7%.

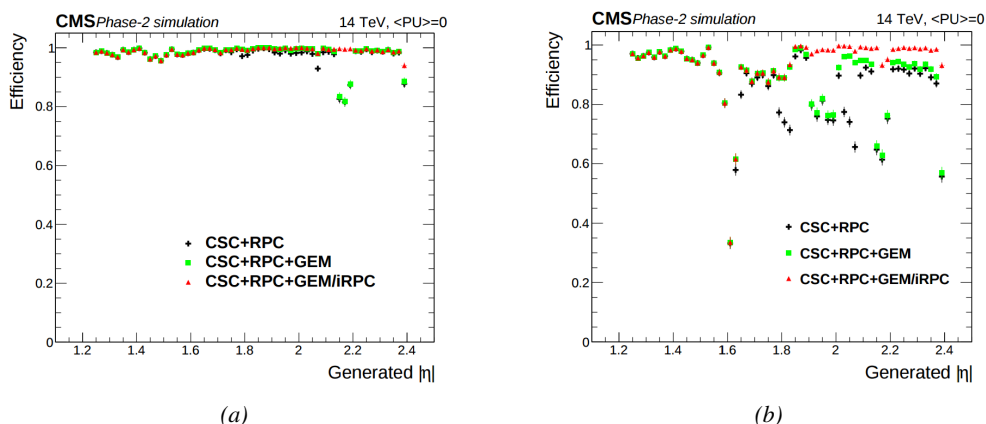


Figure 3.23: Efficiency of the L1 trigger in the endcap region after Phase-II upgrade in the case CSC/GEM/RPC hits are requested in at least 2 stations out of four (3.23a) and in all four stations (3.23b).

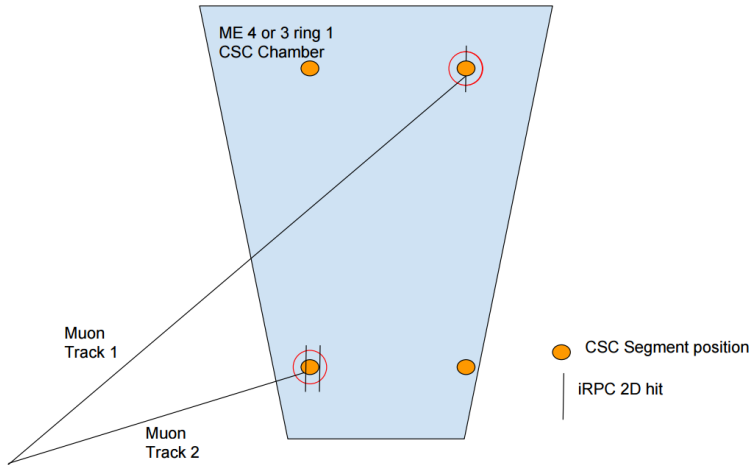


Figure 3.24: Resolution of the LCT ambiguous events thanks to the combination of CSC and iRPC readout data. Using CSCs only, 2 pairs of hits are possible.

1946 The addition of GEMs will improve greatly the measured muon momentum resolution by im-
 1947 proving the global resolution of the direction of muon tracks, as can be seen in Figure 3.25, which
 1948 will contribute to lowering the trigger rate and increase the efficiency, as can be seen from Figure 3.26
 1949 that focuses especially in the most challenging pseudo-rapidity region. Data from both CSCs and
 1950 GEMs are combined into the OTMB to build on each station, GEM/CSC primitives matching space
 1951 and time information from both subsystems.

1952 Finally, the development of a track finder specific to the overlap region was already achieved
 1953 during the Phase-I upgrade of the L1-Trigger [31]. Nevertheless, the improvements of DT spatial
 1954 resolution and RPC timing will be carried and implemented into the OMTF.

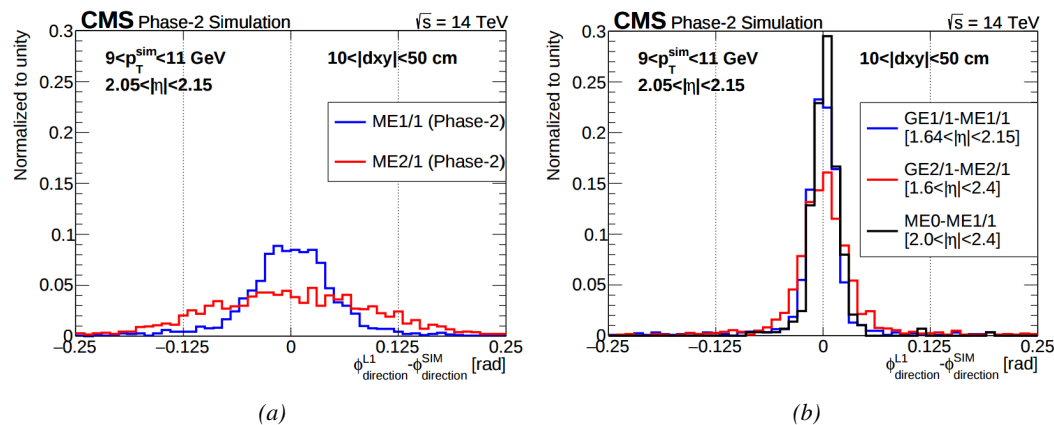


Figure 3.25: The angular resolution on reconstructed muon tracks in the GEM overlap region $2.0 < |\eta| < 2.15$ is compared for Phase-II conditions in the case CSC are alone (Figure 3.25a) and in the case the GEMs' data, including ME0, is combined to which of CSCs (Figure 3.25b).

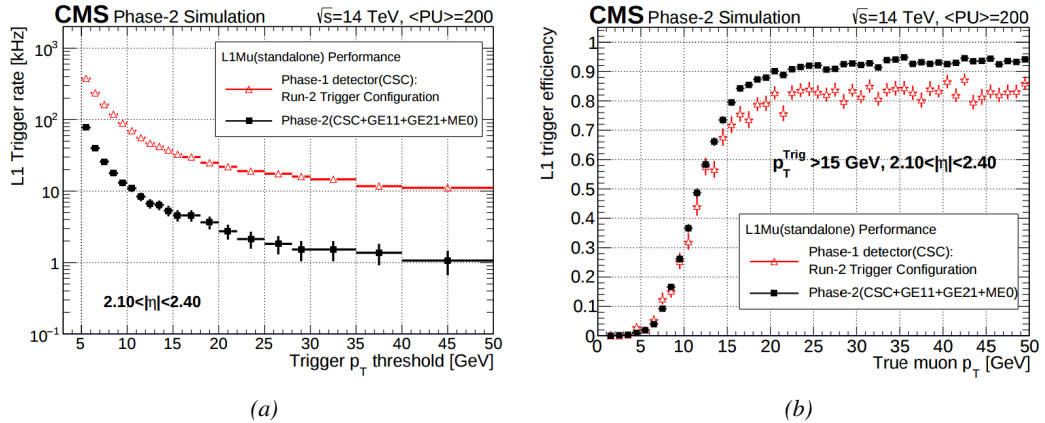


Figure 3.26: Comparison of L1 trigger performances for prompt muons with and without the addition of GEMs in the region $2.1 < |\eta| < 2.4$ at Phase-II conditions. GEMs would allow a reduction of the trigger accept rate by an order of magnitude (Figure 3.26a) while increasing the trigger efficiency (Figure 3.26b).

3.5 Ecofriendly gas studies

Future strict restrictions in the use of certain gases will affect the gaseous detectors of several experiment, including CMS. The European Commission adopted a new "F-gas regulation" in 2014 [32] with the goal to strongly control and reduce the use of fluorinated gases with high Global Warming Potential (GWP). Using CF_4 , $C_2H_2F_4$ and SF_6 , both CSC and RPC subsystems will need to address this problem by finding new gas mixture for the operation of their detectors. Finding a replacement for these gas component that were used for very specific reasons will be a great challenge. Indeed, CSCs use CF_4 in order to enhance the longevity of the detectors, increase the drift velocity of electrons and quench photons with a non-flammable gas mixture. RPCs use a mixture mainly composed of $C_2H_2F_4$, or $R134a$, that features a high effective Townsend coefficient and the great average fast charge allowing for operations with a high threshold, and contains a small fraction of SF_6 that is used for its electronegative properties that prevents the development of delta-rays in the gas volume that might trigger multiple ionization and avalanches.

	CSC	RPC
Greenhouse gases used	CF_4	$C_2H_2F_4$ and SF_6
Greenhouse gases fraction in the gas mixture	10%	95.2% and 0.3%
Global Warming Potential (relative to CO_2)	6500	1300 and 23900
Gas mixture re-circulation	Yes, 90%	Yes, 85%
Gas mixture replenishing rate (l/hr)	700	1100
F-gas recuperation	Yes, $\approx 40\%$	No
F-gas venting rate (l/hr)	42	1047 and 3.3
CO_2 -equivalent rate (m^3/h)	273	1440
Relative impact (entire muon system = 100%)	16%	84%

Table 3.1: Details of the greenhouse fluorinated gases used in CMS and of their GWP [23].

Nevertheless, all these gases have a very high GWP, as reported in Table 3.1, and only few options are left. The subsystems need to work on strongly decrease the loss of these gases due to leaks in the

gas system or completely change their gas mixture for more ecofriendly ones. Reducing the amount of F-gas released in the atmosphere due to leaks on the current gas system will require installation of a F-gas recuperation system on RPCs side and an upgrade of CSCs existing one in addition to the repair of existing leaks. With such measures, it is expected that the total rate of greenhouses gas vented in the atmosphere would represent only 1.6% of the current levels [23]. In the most critical case the F-gas were to be banned, it would be necessary to have replacement mixtures to operate CMS. CSC is presently investigating replacement for CF_4 such as CF_3I , C_4F_6 , IC_3F_6 , C_3F_8 or CHF_3 while RPCs, in collaboration with the ATLAS RPC group which uses the same gas mixture and, hence, faces similar restrictions, have identified CF_3I ($GWP \leq 1$) and $C_3H_2F_4$ ($GWP \leq 1$), referred to as HFO-1234ze, as potential candidates with mixtures containing CO_2 but more R&D needs to be conducted for both subsystems before concluding on the best alternative. No good alternative to the present mixtures will require very efficient abatement system in CMS to burn and convert the greenhouse gases into less harmful ones. This way, the air pollution would be strongly reduced.

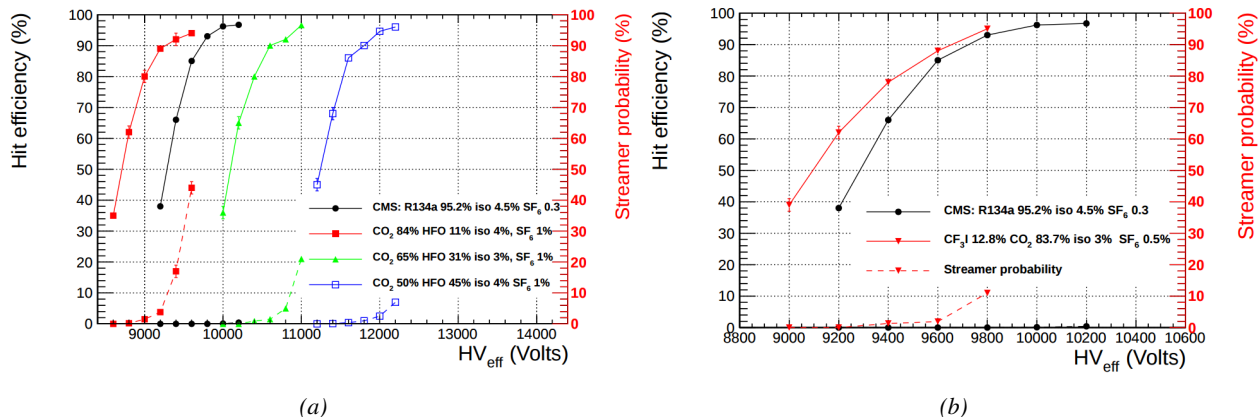


Figure 3.27: The efficiency (solid lines) and streamer probability (dashed lines) of HFO/CO₂ (Figure 3.27a) and CF₃I/CO₂ (Figure 3.27b) based gas mixtures as a function of the effective high-voltage are compared with the present CMS RPC gas mixture represented in black. The detector used for the study is a single gap RPC with similar properties than CMS RPCs. The streamer probability is defined as the proportion of events with a deposited charge greater than 20 pC.

The status of RPC studies are presented in Figure 3.27 in which the performance (efficiency and streamer probability) of an RPC operated with alternative gas mixtures is compared to the present CMS RPC mixture. Although the efficiency of detectors operated with mixtures containing CO₂/CF₃I or CO₂/HFO as a replacement for C₂H₂F₄ seem to reach similar levels than which of the detectors operated with the present mixture, the new gas mixtures feature a streamer probability (probability to have very large avalanches whose induced charge is greater than 20 pC) that far exceeds which of the present fluorinated mixture. The SF₆, being a component of the mixture added in order to reduce the probability of large avalanches thanks to its electronegativity, doesn't seem to prevent streamers as efficiently even when used at levels more than 3 times higher than with the standard CMS RPC mixture. Nevertheless, it is important to note that these results were obtained with a single gap RPC while the use of a double gap RPC would reduce the operation voltage by 200 to 300 V, lowering the induced charge. A compromise in between good efficiency and acceptable level of streamer probability and the fine tuned composition of potential replacement gas mixtures

¹⁹⁹⁷ will be studied using a standard double-gap CMS RPC.

4

1998

1999

Physics of Resistive plate chambers

2000 A Resistive Plate Chamber (RPC) is a gaseous detector used in high-energy physics experiments as
2001 described in Chapter 3. It has been developed in 1981 by Santonico and Cardarelli [33], under the
2002 name of *Resistive Plate Counter*, as an alternative to the local-discharge spark counters proposed in
2003 1978 by Pestov and Fedotovich [34, 35]. Working with spark chambers implied using high-pressure
2004 gas and high mechanical precision which the RPC simplified by formerly using a gas mixture of
2005 argon and butane flowed at atmospheric pressure and a constant and uniform electric field propagated
2006 in between two parallel electrode plates. Moreover, a significant increase in rate capability was
2007 introduced by the use of electrode plate material with high bulk resistivity, preventing the discharge
2008 from growing throughout the whole gas gap. Indeed, the effect of using resistive electrodes is that
2009 the constant electric field is locally canceled out by the development of the discharge, limiting its
2010 growth.

2011 Through its development history, different operating modes [36–38], gas mixtures [33, 38–43]
2012 and new detector designs [44–46] have been discovered, leading to further improvement of the rate
2013 capability of such a detector. The low developing costs and easily achievable large detection ar-
2014 eas offered by RPCs, as well as the wide range of possible designs, made them a natural choice to
2015 as muon chambers and/or trigger detectors in multipurpose experiments such as CMS [21] or AT-
2016 LAS [47], time-of-flight detectors in ALICE [48], calorimeter with CALICE [49] or even detectors
2017 for volcanic muography with ToMuVol [50].

2018 4.1 Principle

2019 RPCs are ionisation detectors composed of two parallel resistive plate electrodes in between which
2020 a constant electric field is set. The space in between the electrodes, referred to as *gap*, is filled with
2021 a dense gas that is used to generate primary ionization into the gas volume. The free charge carriers
2022 (electrons and cations) created by the ionization of the gas molecules are then accelerated towards the
2023 electrodes by the electric field, as shown in Figure 4.1 [51]. RPCs being passive detectors, a current
2024 on pick-up copper read-out placed outside of the gas volume is induced by the charge accumulation

2025 during the growth of the avalanche resulting from the acceleration of the charge carriers. As a
 2026 consequence, the time resolution of the detector is substantially increased as the output signal is
 2027 generated while the electrons are still in movement. The advantage of a constant electric field, over
 2028 multi-wire proportional chambers, is that the electrons are being fully accelerated from the moment
 2029 charge carriers are freed and feel the full strength of the electric field that doesn't depend on the
 2030 distance to the readout and that the output signal doesn't need for the electrons to be physically
 2031 collected.

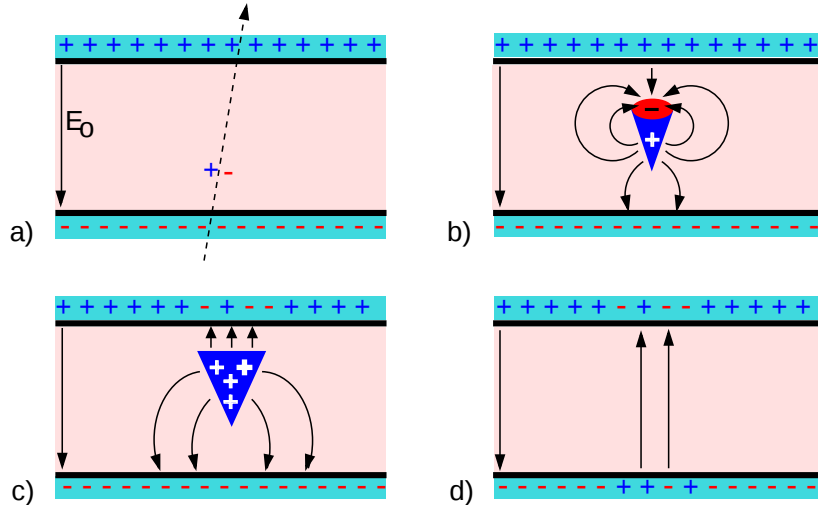


Figure 4.1: Different phases of the avalanche development in the RPC gas volume subjected to a constant electric field E_0 . a) An avalanche is initiated by the primary ionisation caused by the passage of a charged particle through the gas volume. b) Due to its growing size, the avalanche starts to locally influence the electric field. c) The electrons, lighter than the cations reach the anode first. d) The ions reach the cathode. While the charges have not recombined, the electric field in the small region around the avalanche stays affected and locally blinds the detector.

2032 After an avalanche developed in the gas, a time long compared to the development of a discharge
 2033 is needed to recombine the charge carriers in the electrode material due to their resistivity. This
 2034 property has the advantage of affecting the local electric field and avoiding sparks in the detector
 2035 but, on the other hand, the rate capability is intrinsically limited by the time constant τ_{RPC} of the
 2036 detector. Using a quasi-static approximation of Maxwell's equations for weakly conducting media,
 2037 it can be shown that the time constant τ_{RPC} necessary to the charge recombination at the interface
 2038 in between the electrode and the gas volume is given by the Formula 4.1 [52].

$$\tau_{RPC} = \frac{\epsilon_{electrode} + \epsilon_{gas}}{\sigma_{electrode} + \sigma_{gas}} \quad (4.1)$$

2039 A gas can be assimilated to vacuum, leading to $\epsilon_{gas} = \epsilon_0$ and $\sigma_{gas} = 0$, and the electrodes
 2040 permittivity and conductivity can be written as $\epsilon_{electrode} = \epsilon_r \epsilon_0$ and $\sigma_{electrode} = 1/\rho_{electrode}$,
 2041 showing the strong dependence of the time constant to the electrodes resistivity in Formula 4.2.

$$\tau_{RPC} = (\epsilon_r + 1)\epsilon_0 \times \rho_{electrode} \quad (4.2)$$

2042 Very few materials with a low enough resistivity exist in nature. The resistivity targeted to build

2043 RPCs ranges from 10^9 to $10^{12} \Omega \cdot \text{cm}$. The most common RPC electrode materials are displayed in
 2044 Table 4.1. When the doped glass and ceramics can offer short time constants of the order of 1 ms,
 2045 the developing cost of such materials is quite high due to the very low demand. Thus, High-pressure
 2046 laminate (HPL) is often the choice for high rate experiments using very large RPC detection areas.
 2047 Other experiments working at cosmic muon fluxes can safely operate with ordinary float glass.

Material	$\rho_{\text{electrode}} (\Omega \cdot \text{cm})$	ϵ_r	$\tau_{\text{RPC}} (\text{ms})$
Float glass	10^{12}	~ 7	~ 700
High-pressure laminate	10^{10} to 10^{12}	~ 6	~ 6 to 600
Doped glass (LR S)	10^9 to 10^{11}	~ 10	~ 1 to 100
Doped ceramics (SiN/SiC)	10^9	~ 8.5	~ 1
Doped ceramics (Ferrite)	10^8 to 10^{12}	~ 20	~ 0.2 to 2000

Table 4.1: Properties of the most used electrode materials for RPCs.

2048 4.2 Rate capability and time resolution of Resistive Plate Cham- 2049 bers

2050 The electrode material plays a key role in the maximum intrinsic rate capability of RPCs. R&D is
 2051 continuously being done to develop at always cheaper costs material with lower resistivity. Never-
 2052 theless, the amount of charge released, i.e. the size of the discharge, if reduced leads to a smaller
 2053 blind area in the detector, increasing the rate capability of the detector. On the other hand, the drift
 2054 velocity of electrons in the gas volume being quite stable with the applied electric field, the design of
 2055 a detector and the associated read-out and pulse-processing electronics will be a major component of
 2056 the time resolution of RPCs. Moreover, the sensitivity of the electronics will also help increasing the
 2057 rate capability by lowering the gain the gas volume needs to be operated at, increasingly lowering
 2058 the gas volume in which the signals will develop.

2059 4.2.1 Operation modes

2060 Being a gaseous detector using an accelerating electric field to amplify the signal of primary charge
 2061 carriers, the RPC can be operated into different modes as the electric field intensity varies. Each
 2062 mode offers different performances for such a detector, and it will be showed that the operating mode
 2063 corresponding to the lowest electric field possible is best suited for high rate detectors working in
 2064 collider experiments.

2065 RPCs where developed early 1980s. At that time it was using an operating mode now referred to
 2066 as *streamer mode*. Streamers are large discharges that develop in between the 2 electrodes enough to
 2067 locally discharge the electrodes. If the electric field inside of the gas volume is strong enough, with
 2068 electrons being fast compared to ions, a large and dense cloud of positive ions will develop nearby
 2069 the anode and extend toward the cathode while the electrons are being collected, eventually leading
 2070 to a streamer discharge due to the increase of field seen at the cathode. The field is then strong
 2071 enough so that electrons are pulled out of the cathode. Electrodes, though they are a unique volume
 2072 of resistive material, can be assimilated to capacitors. At the moment an electric field is applied in
 2073 between their outer surfaces, the charge carriers inside of the volume will start moving leading to
 2074 a situation where there is no voltage across the electrodes and a higher density of negative charges,
 2075 i.e. electrons, on the inner surface of the cathode. Finally, when a streamer discharge occurs, these

2076 electrons are partially released in the gas volume contributing to increase the discharge strength until
 2077 the formation of a conductive plasma, the streamer. This can be understood through Figure 4.2 [36].
 2078 Streamer signals are very convenient in terms of read-out as no further amplification is required
 2079 with output pulses amplitudes of the order of a few tens to few hundreds of mV as can be seen on
 2080 Figure 4.3.

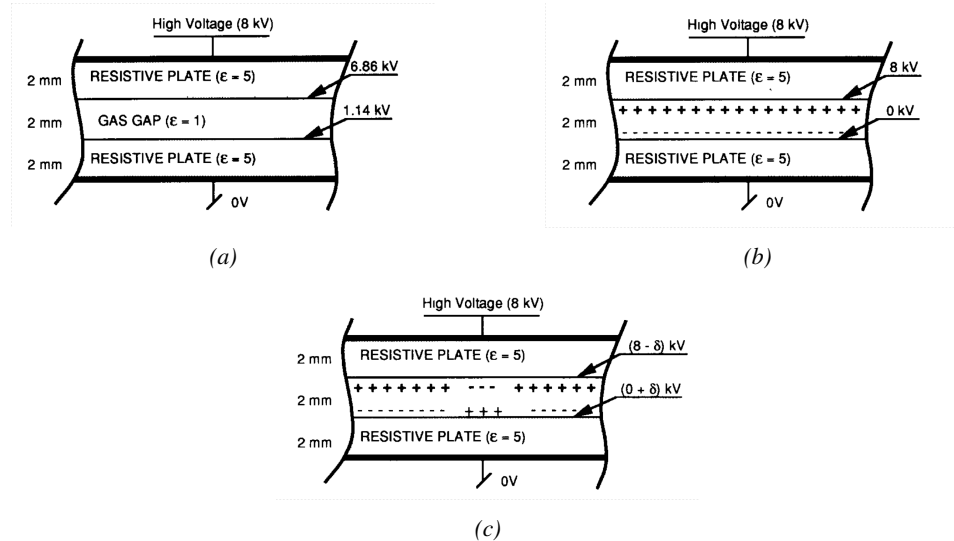


Figure 4.2: Movement of the charge carriers in an RPC. Figure 4.2a: Voltage across an RPC whose electrode have a relative permittivity of 5 at the moment the tension is applied. Figure 4.2b: After the charge carriers moved, the electrodes are charged and there is no voltage drop over the electrodes anymore. The full potential is applied on the gas gap only. Figure 4.2c: The streamer discharge initiated by a charged particle transports electrons and cations towards the anode and cathode respectively.

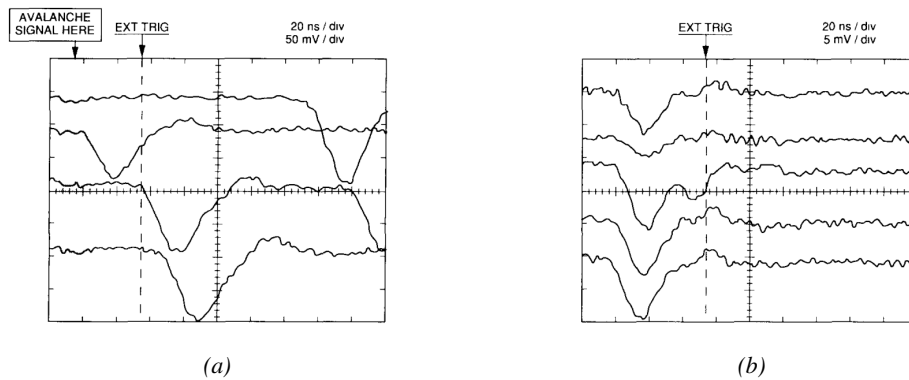


Figure 4.3: Typical oscilloscope pulses in streamer mode (Figure 4.3a) and avalanche mode (Figure 4.3b). In the case of streamer mode, the very small avalanche signal is visible.

2081 When the electric field is reduced though, the electronic gain is small until the electrons get close
 2082 enough to the anode and the positive ion cloud is much smaller. The electric field cannot rise to the
 2083 point a field emission of electrons on the cathode is possible. The resulting signal is weak, of the

order of a few mv as shown on Figure 4.3, and requires amplification. This is the *avalanche mode* of RPC operation. This mode offers a higher rate capability by providing smaller discharges that don't affect the electrodes charge and are more locally contained in the gas volume as was demonstrated by Crotty with Figure 4.4 [36]. The detector only stays locally blind the time the charge carriers are recombined and there is no need for electrode recharge which is a long process affecting a large portion of the detector. Another advantage of avalanche signals over streamer is the great time consistency. Figure 4.3 shows very clearly that avalanche signals have a very small time jitter. Thus, using such a mode is a natural choice for experiments in which the detectors are required to have a high detection rate.

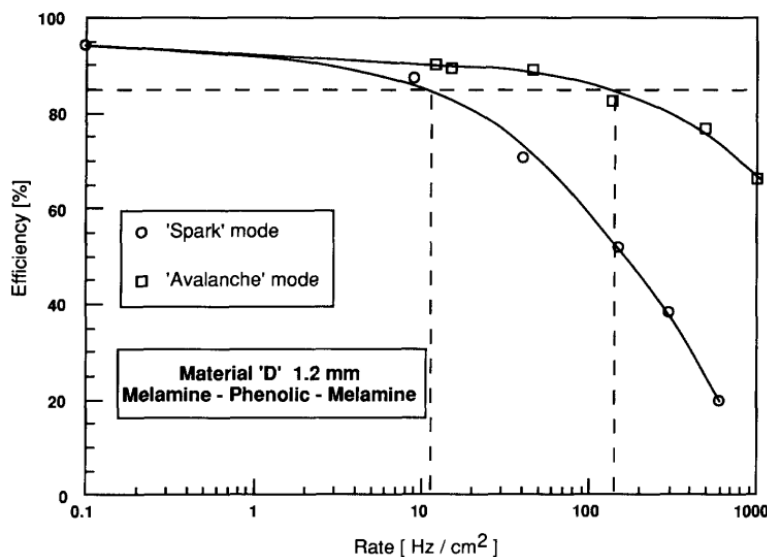


Figure 4.4: Rate capability comparison for the streamer and avalanche mode of operation. An order of magnitude in rate capability for a maximal efficiency drop of 10% is gained by using the avalanche mode over the streamer mode.

4.2.2 Standard gas mixture for RPCs operated in collider experiments

The first RPC working in streamer mode was operated with a 50/50 mixture of argon and butane [33], a standard mixture used at that time in multi-wire proportional chambers, taking profit of the good effective Townsend coefficient of argon to maximize the number of primary charge carriers freed in the gas by ionizing particles and of the quenching properties of butane. Before the discovery of the avalanche mode of RPC operation and concerned about the rate capability of RPCs operated in streamer mode, the performance improvement of the detectors through the increase of fast charge ratio in the signal development ,decreasing the charge induced per avalanche as can be seen through Figure 4.5, was studied by adding Freon based gases, such as CF_3Br , into the typical Ar/C_4H_{10} gas mixture was studied and showed that a lower induced charge could lead to an improvement the rate capability [39]. This consideration lead to the discovery of the avalanche mode which confirmed that the smaller the induced charge, the better the rate capability of the RPCs [36]. This discovery could happen thanks to the increased number of lower induced charge events allowed by adding a fraction of strong quencher in the gas mixture.

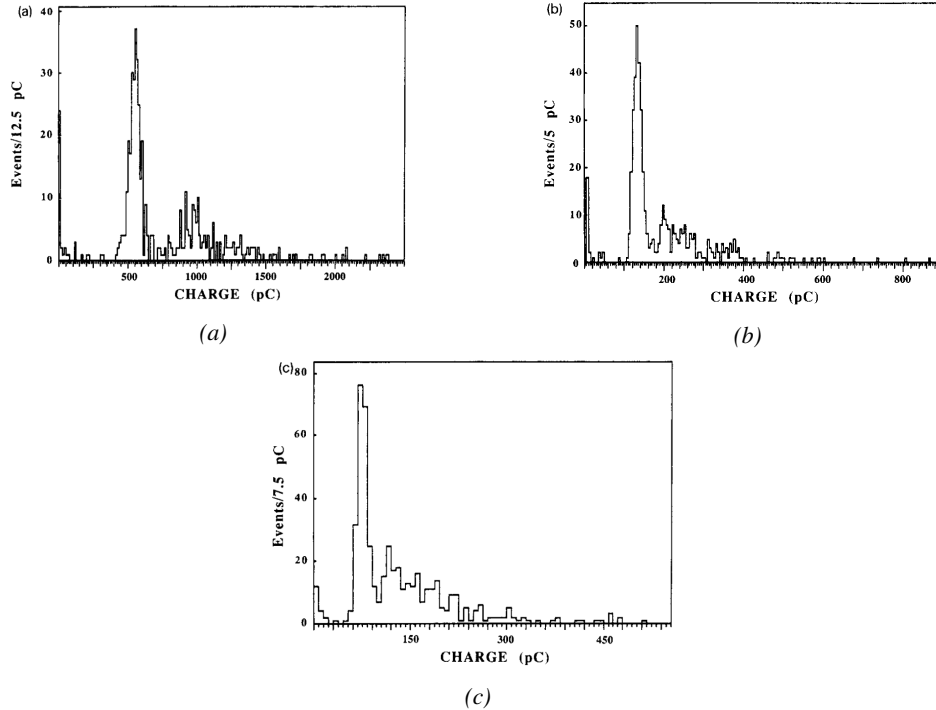


Figure 4.5: Comparison of the charge distribution of signals induced by cosmic muons in an RPC operated with a gas mixture of argon, butane and bromotrifluoromethane (CF_3Br). The Ar/C_4H_{10} is kept constant at 60/40 in volume while the total amount of CF_3Br in the mixture is varied: 0% (Figure 4.5a), 4% (Figure 4.5b) and 8% (Figure 4.5c) [39].

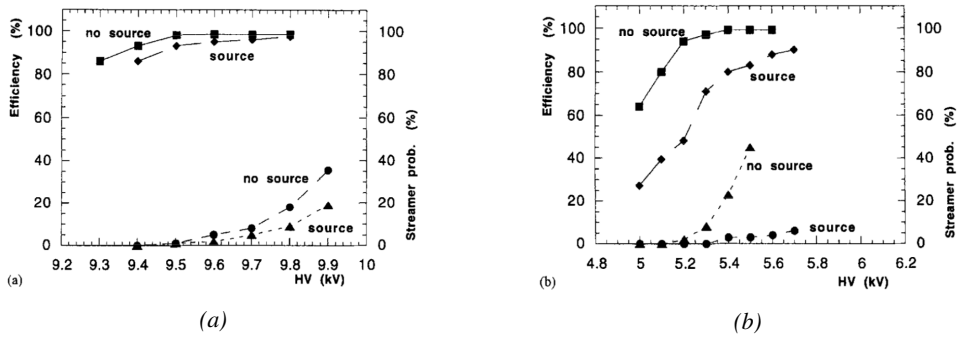


Figure 4.6: Comparison of the efficiency and streamer probability, defined as the fraction of events with an induced charge 10 times larger than that of the average avalanche, with and without irradiation by a 24 GBq ^{137}Cs source of an RPC successively operated with a 90/10 mixture $C_2H_2F_4/i-C_4H_{10}$ (Figure 4.6a) and a 70/5/10/15 mixture of $Ar/i-C_4H_{10}/CO_2/C_2H_2F_4$ (Figure 4.6b) [40].

From this moment onward, more and more studies were conducted in order to find a gas mixture that would allow for the best suppression of streamers for the benefit of low charge avalanches. Most R&D groups working with narrow gaps started using freon-based gas mixtures while users of wide gap RPCs kept using Ar/CO_2 based mixtures. The differences in between narrow and wide gaps will

be later discussed in Section 4.2.3. The CF_3Br having a high GWP, tetrafluoroethane ($C_2H_2F_4$) was preferred to it as more suitable ecofriendly gas in the middle of the 90s. An advantage of this new freon component is that it featured a high primary ionization and a low operating voltage, as reported by Cardarelli [38]. Thus, the new gas mixtures used were mainly composed of tetrafluoroethane alone with lower content of isobutane in order to reduce the flammability of the mixtures in the case it were to be used in accelerator experiments for safety reasons. Performance and models about such mixtures were discussed in papers of Abbrescia [40, 41] and showed a better suitability of such a gas mixture, with respect to argon based ones, for operations with high radiation backgrounds leading to a need for high rate capability of the detectors, as can be seen from Figures 4.6 and 4.7. Indeed, although the operating voltage of a tetrafluoroethane based mixture is higher than which of an argon based mixture but the efficiency under irradiation is more stable, the voltage range with negligible streamer probability is much wider, and the fast charge ratio available is much greater, providing with more stable operation of the detector.

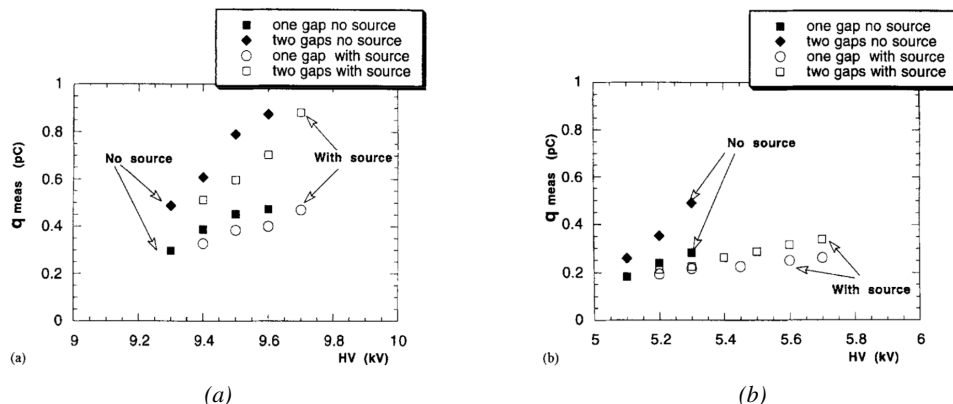


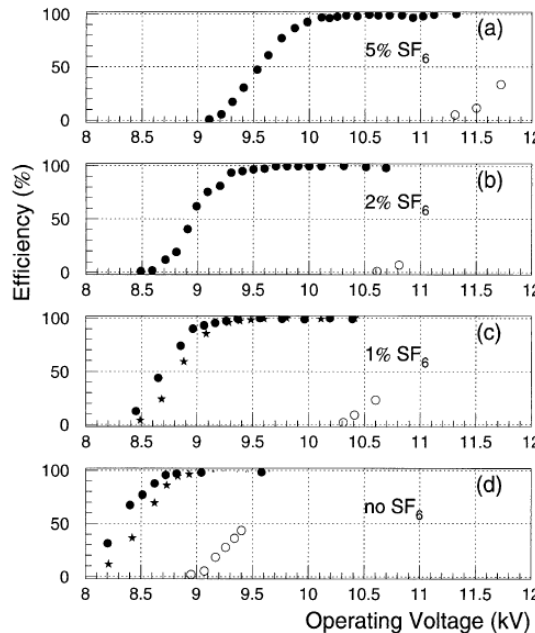
Figure 4.7: Comparison of the fast charge ratio with and without irradiation by a 24 GBq ^{137}Cs source of an RPC successively operated with a 90/10 mixture $C_2H_2F_4/i-C_4H_{10}$ (Figure 4.7a) and a 70/5/10/15 mixture of $Ar/i-C_4H_{10}/CO_2/C_2H_2F_4$ (Figure 4.7b). The results are provided for both single gap and double gap operation [40].

Aside of the improvement of the rate capability through linseed oil surface treatment of HPL electrodes, which allowed for a lower intrinsic noise rate and dark current of the detectors by improving the smoothness of the electrodes surface [53], it was later found that the streamers could be further suppressed by adding an electronegative compound into the gas mixture. The benefits of adding SF_6 in order to push the transitions from avalanche to streamers towards high voltages has been discussed in 1998 [42, 43] and eventually the high rate RPC destined to be used in accelerator physics would unanimously start using this compound into RPC gas mixtures. Being able to control the creation of streamers allows for slower ageing of the detector and lower power consumption as the currents driven by the electrodes consecutively to the induced charges would be smaller. In summary, the typical gas mixture RPCs are operated with is generally composed of the following 3 gas compounds, although, as mentioned in Chapter 3.5, research is being conducted into new more ecofriendly gas mixture using gases with a much lower Global Warming Potential:

- Tetrafluoroethane ($C_2F_4H_2$), also referred to as *Freon* or *R134a*, is the principal compound of the RPC gas mixtures, with a typical fraction above 90%. It is used for its high effective

2138 Townsend coefficient and the great average fast charge that allows to operate the detector
 2139 with a high threshold with respect to argon, for example, that has similar effective Townsend
 2140 coefficient but suffers from a lower fast charge. To operate with similar conditions, argon
 2141 would require a higher electric field leading to a higher fraction of streamers, thus limiting the
 2142 rate capability of the detector [40, 41].

- 2143 • Isobutane ($i\text{-C}_4\text{H}_{10}$), only present in a few percent in the gas mixtures, is used for its UV
 2144 quenching properties [54] helping to prevent streamers due to UV photon emission during the
 2145 avalanche growth.
- 2146 • Sulfur hexafluoride, (SF_6), simply referred to as SF_6 , is used in very little quantities for its
 2147 high electronegativity. Excess of electrons are being absorbed by the compound and streamers
 2148 are suppressed [42, 43]. Nevertheless, a fraction of SF_6 higher than 1% will not bring
 2149 any extra benefice in terms of streamer cancelation power but will lead to higher operating
 2150 voltage [42], as can be understood through Figure 4.8.



2151 *Figure 4.8: Efficiency (circles and stars with 30 mV and 100 mV thresholds respectively) and streamer prob-
 2152 ability (opened circles) as function of the operating voltatge of a 2 mm single gap HPL RPC flushed with a gas
 2153 mixture containing (a) 5%, (b) 2%, (c) 1% and (d) no SF_6 [42].*

2154 In the last steps of R&D, the gas mixture of CMS RPCs was forseen to be a 96.2/3.5/0.3 compo-
 2155 sition of $\text{C}_2\text{H}_2\text{F}_4/\text{i-C}_4\text{H}_{10}/\text{SF}_6$ [55] but finally it was slightly changed into a 95.2/4.5/0.3 mixture
 2156 of the same gases [56]. A summary of the operation performance of the RPCs since the start of LHC
 and of CMS data taking is given in Figure 4.9 [57]. The performance of the detectors is regularly
 monitored and the operating voltages updated in order to obtain a very stable performance through
 time. Nevertheless, the detectors will face new challenges during Phase-II during which they will

exposed to more extreme radiation conditions. Description of the longevity tests with extreme irradiation and the conclusions regarding the operation of the present RPC system will be given in Chapter 5.

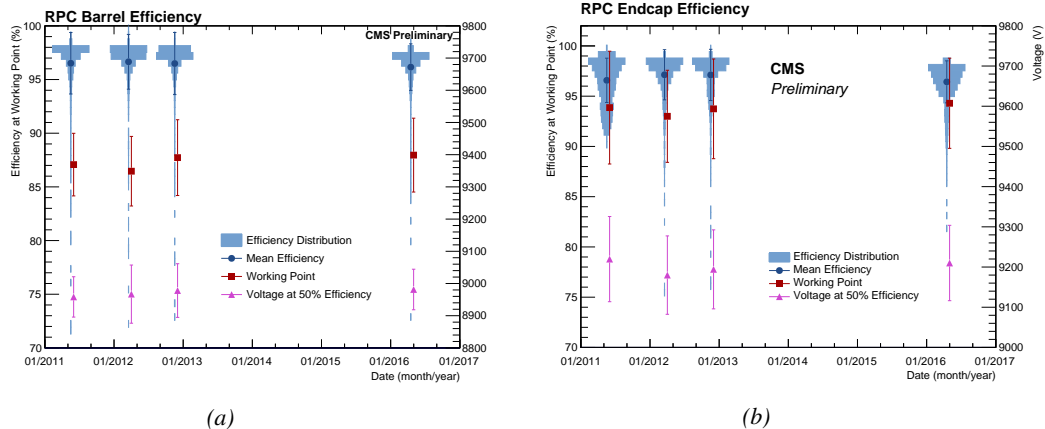


Figure 4.9: Evolution of the efficiency, working voltage, and voltage at 50% of maximum efficiency for CMS Barrel (Figure 4.9a) and Endcap (Figure 4.9b) RPCs obtained through yearly voltage scans since 2011. The working voltage of each RPC is updated after each voltage scan to ensure optimal operation [57].

It was already discussed that in the future, it is likely that the use of freon gases could be banned.
 As potential replacement for tetrafluoroethane was proposed the trifluoriodomethane (CF_3I), a molecule with similar properties than CF_3Br which was replaced by the tetrafluoroethane, and the 1,3,3,3-tetrafluoropropene ($C_3H_2F_4$ or HFO-1234re), a molecule with similar properties than the actual tetrafluoroethane and proposed as a replacement in refrigerating and air conditioning systems [58]. These 2 gases have stronger quenching properties than $C_2H_2F_4$ which means a much stronger electric field needs to be applied on the parallel electrodes of the RPCs in order to reach full efficiency. But the power supply system of CMS RPC is limited to 15 kV and so is ATLAS power supply system which is participating in a joined R&D. As can be seen from Figure 3.27, reducing the working voltage was achieved by mixing the potential replacements together with CO_2 . Introducing carbon dioxide into the mixture while keeping similar levels of isobutane and SF_6 increases the streamer probability and the best candidate identified for a compromise in between low enough working voltage and acceptable levels of streamers corresponds to a mixture containing 50% of CO_2 , 45% of HFO, 4% of isobutane and 1% of SF_6 but is not yet considered satisfactory. On the other hand, no good replacement for SF_6 has yet been identified. With its very high Global Warming Potential (23900), even small fraction of this gas in the mixture (it only represents 0.3% of CMS standard mixture but more than 5% of its overall GWP) substantially increase the danger for the environment. Although finding a replacement for this gas is less critical than for the tetrafluoroethane composing more than 90% of usual RPC standard mixtures, the problem will need to be addressed.

4.2.3 Detector designs and performance

Different RPC design have been used and each of them present its own advantages. Historically, the first type of RPC to have been developed is what is now referred to as *narrow gap* RPC [33, 59].

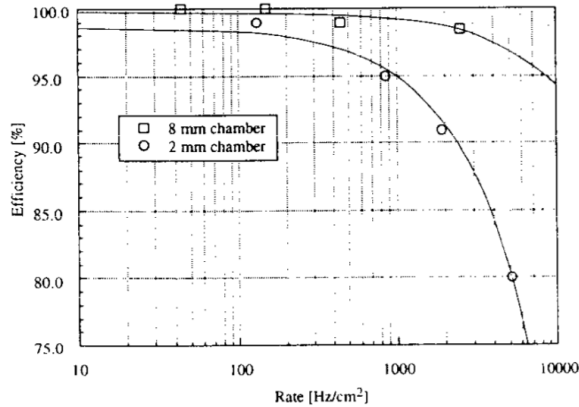


Figure 4.10: Comparison of the rate capability of 8 mm and 2 mm wide RPCs. The lines are linear fits on the data [59].

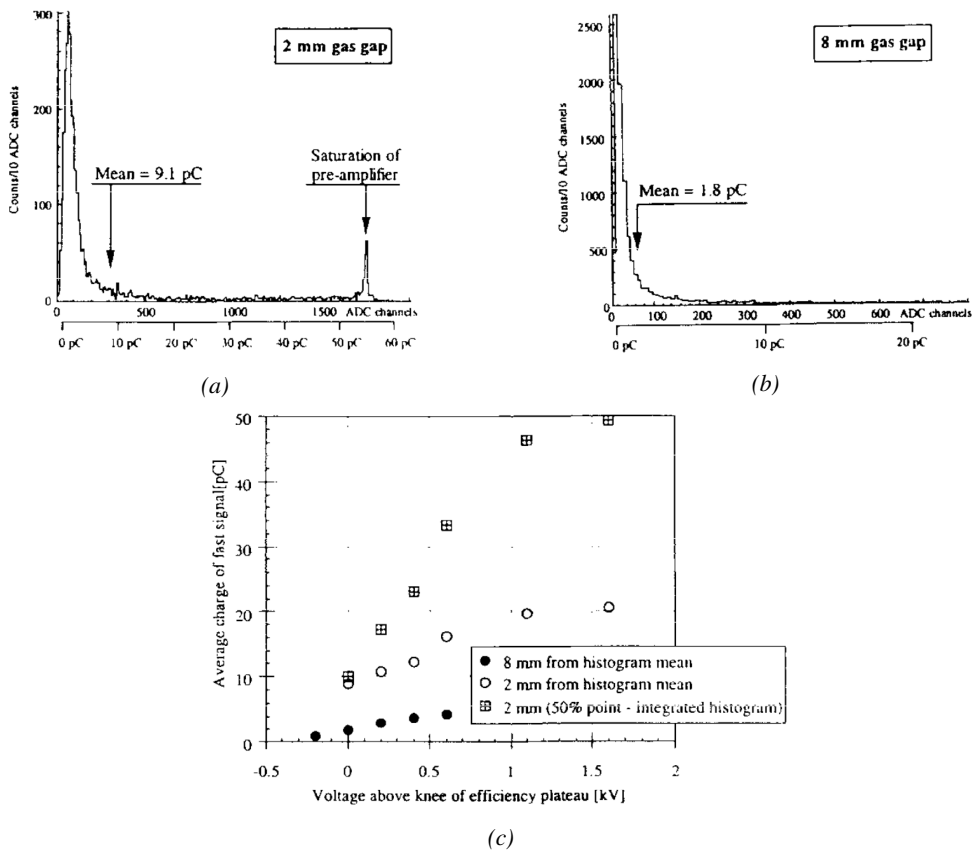


Figure 4.11: Distributions of the induced charge of fast signals on 2 mm (Figure 4.11a) and 8 mm (Figure 4.11b) RPCs exposed to a radiation rate of 100 Hz/cm^2 . Average induced charge of fast signals as a function of the high voltage applied on 2 mm and 8 mm RPCs (Figure 4.11c). In the case of the 2 mm RPC, a saturation of the pre-amplifier was observed. The average of the distribution is underestimated and the median is showed together with the average to account for this bias [59].

After the avalanche mode has been discovered [36], it has been showed that increasing the width of the gas gap lead to higher rate capability, due to lower charge deposition per avalanche, and lower power dissipation [59], as is showed in Figures 4.10 and 4.11. The distance in between the electrode being greater, a weaker electric field can be applied and a lower gain used as a longer gas volume will contribute to the signal induction on the read-out circuit. Nevertheless, by increasing the gas gap width, the time resolution of the detector decreases. This is a natural result if the increase of active gas volume in the detector is taken into account. Indeed, for a given detection threshold on the induced charge per signal, only the small fraction of gas closest to the cathode will provide enough gain to have a detectable signal. In the case of a wider gas volume, the active region is then larger and a larger time jitter is introduced with the variation of starting position of the avalanche, as discussed in [44] and showed in Figure 4.12.

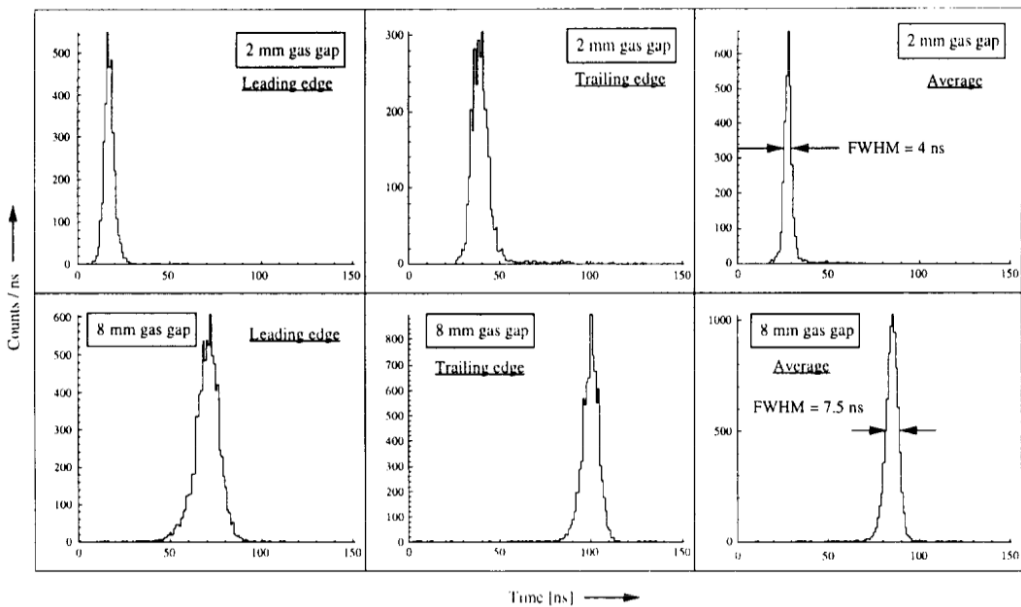


Figure 4.12: Time distributions of the leading, trailing, and average of both leading and trailing edges for 2 mm (top row) and 8 mm (bottom row) RPCs exposed to a 100 Hz/cm² radiation rate. The data was collected with RPCs operated at the voltage corresponding to the knee of the efficiency distribution, defined as the point where 95% of the maximum efficiency is obtained [59].

To improve both the time resolution and the rate capability, different methods were used trying to take advantage of both narrow and wide gap RPCs into a single design. Thus, double gap RPCs, combining two narrow gaps into a single detector to increase the effective sensitive volume, and multigap RPCs, which divided the large volume of a wide gap RPC into thinner sub-gaps by adding intermediate electrodes in between the cathode and anode to improve the time resolution by mimicking narrow gap RPCs, were developed starting from the middle of the 90s.

4.2.3.1 Double gap RPC

Made out of 2 narrow RPC detectors stacked on top of each other as shown in Figure 4.13, this detector layout, popularized by the two multipurpose experiments CMS [21] and ATLAS [47] at LHC, can be used as an OR system in which each individual chamber participates in the output signal

and increases the overall sensitive volume of the detector apparatus. Keeping the copper strip read-out system at the ground, CMS and ATLAS, due to different goals, have chosen different designs as CMS RPCs possess a 1D read-out while ATLAS RPCs offer a 2D read-out. The difference comes from placing the read-out in between the gaps, the anodes facing each other, or to have both RPC gaps in between 2 layers of read-out panels, one along the X-axis and one along the Y-axis, the cathodes facing each other.

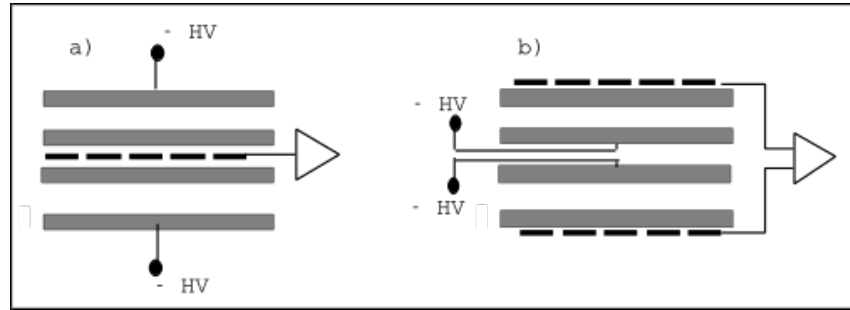


Figure 4.13: Possible double-gap RPC layouts: a) "standard" 1D double-gap RPC, as used in CMS experiment, where the anodes are facing each other and a 1D read-out plane is sandwiched in between them, b) double read-out double-gap RPC as used in ATLAS experiment, where the cathodes are facing each other and 2 read-out planes are used on the outer surfaces. This last layout can offer the possibility to use a 2D reconstruction by using orthogonal read-out planes.

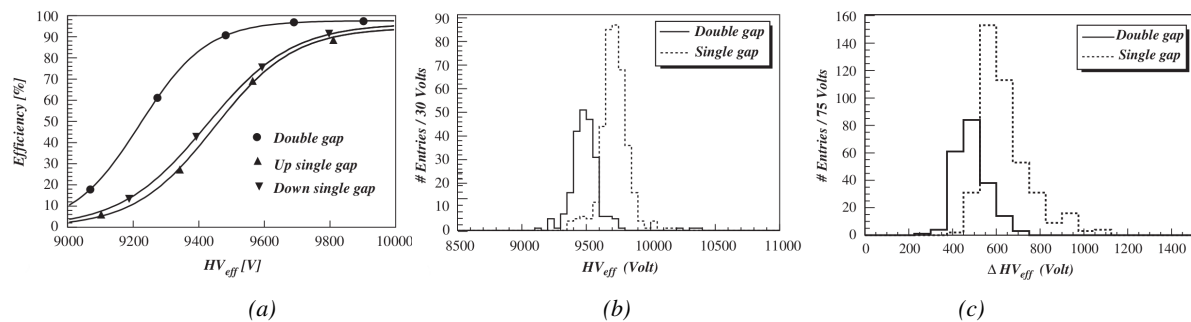


Figure 4.14: Comparison of performance of CMS double and single gap RPCs using cosmic muons [55]. Figure 4.14a: Comparison of efficiency sigmoids. Figure 4.14b: Voltage distribution at 95% of maximum efficiency. Figure 4.14c: $\Delta_{10\%}^{90\%}$ distribution.

The gain of such a detector is reduced by a factor 2 with respect to single-gap RPCs with an efficiency plateau reached at lower voltage, as visible on Figure 4.14, due to the two gas gaps contributing to the signal formation and offering a dynamic range closer to that of a wide gap RPC. A double gap is then fully efficient while the individual RPC gaps composing it are only 70 to 80% efficient. Naturally, by operating the double gap at a lower voltage, the rate capability is found to be increased as the induced charge per gap is then lower than in the case of a single gap detector also leading to a reduction of the streamer probability and a better extraction of the fast charge of the total signal as could be seen through previously presented Figure 4.7.

2218 **4.2.3.2 Multigap RPC (MRPC)**

2219 MRPCs are layouts in which floating sub electrode plates are placed into a wide gap RPC to divide
 2220 the gas volume and create a sum of narrow gaps [44, 45]. Similarly to the double gap RPC for which
 2221 the gain could be reduced by increasing the dynamic range, the multigap reduces the gain while
 2222 keeping a total dynamic range similar to which of a wide gap RPC by reducing the size of each
 2223 individual sub-gap composing the detector. The dynamic range, associated to the sensitive volume,
 2224 and the comparison of each detector layout to the wide gap RPC is showed in Figure 4.15.

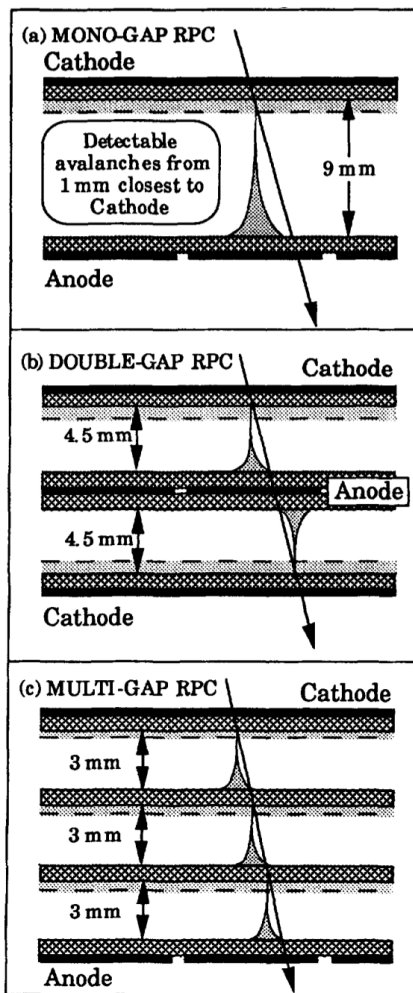


Figure 4.15: Representation of different RPC layouts (wide gap on Figure (a), double gap on Figure (b) and multigap on Figure (c)), of the corresponding sensitive volume in gray, and of the associated avalanche size [45].

2225 By operating the detector with thinner gaps, the time resolution is improved. Comparatively to
 2226 the time resolution presented in Figure 4.12 for the wide gap RPC of 8 mm, a complementary study
 2227 was conducted on multigaps using two 4 mm and four 2 mm subgaps and showed, via Figure 4.16,
 2228 an improvement of the time resolution with the reduction of the gap width and of the number of gaps

while the same sensitive volume was kept [45].

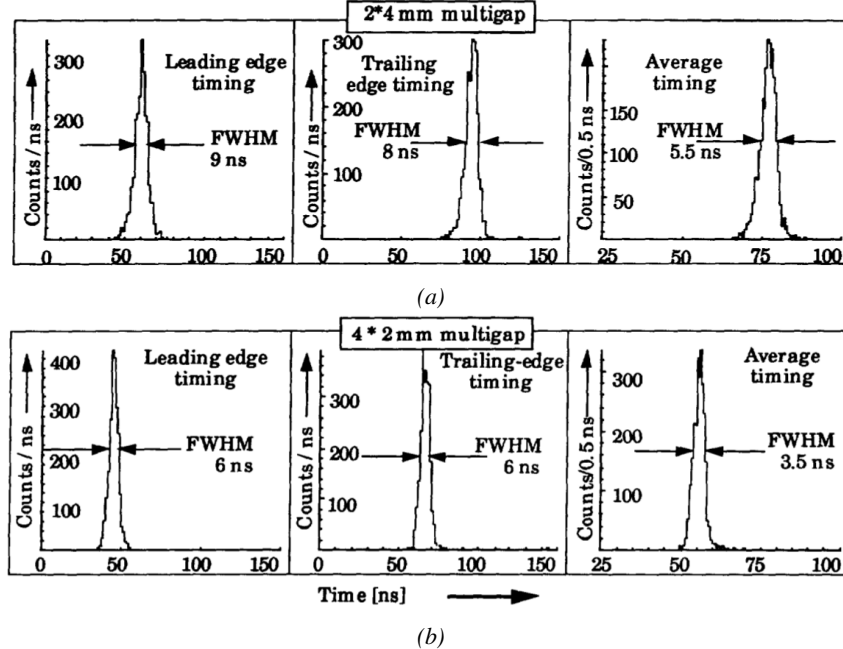


Figure 4.16: Time distributions of the leading, trailing, and average of both leading and trailing edges for multigap RPCs consisting in two 4 mm (Figure 4.16a) and four 2 mm (Figure 4.16b) exposed to a 100 Hz/cm^2 radiation rate. The data was collected with RPCs operated at the voltage corresponding to the knee of the efficiency distribution, defined as the point where 95% of the maximum efficiency is obtained [45].

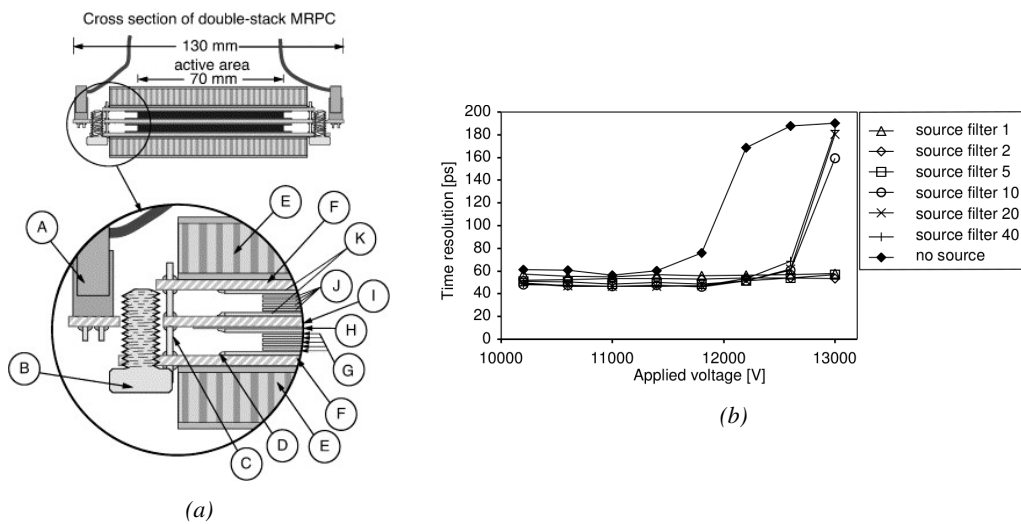


Figure 4.17: Presentation of a study of a possible ALICE MRPC cell using $250 \mu\text{m}$ gas gaps, $620 \mu\text{m}$ outer glass electrodes, and $550 \mu\text{m}$ inner floating electrodes (Figure 4.17a), and of its time resolution performance as a function of the applied high voltage for different radiation levels referred through different filter settings of the $740 \text{ GBq } ^{137}\text{Cs}$ source the former CERN GIF facility [60].

After the problem of streamers was solved by adding SF_6 into the gas mixture, the size of the MRPCs decreased as the research groups started applying the concept of dividing the gas volume into subvolumes to the narrow gap RPCs leading to the now widely used micro gap MRPCs. The time resolution of such a detector can reach of few tens of ps, with gas gaps of the order of a few hundred μm as showed in Figure 4.17 representing a single cell of ALICE Time-of-flight (ToF) system consisting of double MRPCs, as it was studied in the early 2000s [60].

Sometimes used as a double multigap RPC, taking advantage of the OR of double gap RPCs to both be able to operate a higher number of gaps while keeping a reasonable high voltage applied in between the cathode and anode and to further reduce the gain, the MRPC is mainly used as ToF detector [60–64] due to its excellent timing properties that allow to perform particle identification as explained by Williams in [65]. The principle of particle identification using ToF is simply the measurement of the velocity of a particle. Indeed, particles are defined by their mass (for the parameter of interest here, their electric charge being measured using the bending angle of the particles traveling through a magnetic field) and this mass can be calculated by measuring the velocity β and momentum of the particle:

$$\beta = \frac{p}{\sqrt{p^2 + m^2}} \quad (4.3)$$

Intuitively, it is trivial to understand that 2 different particles having the same momentum will have a different velocity due to the mass difference and thus a different flight time T_1 and T_2 through the detector and this is used to separate and identify particles. The better the time resolution of the ToF system used, the stronger will the separation be:

$$T = \frac{L}{v} = \frac{L}{c \cdot \beta}, \quad \Delta T = T_1 - T_2 = \frac{L}{c} \left(\sqrt{1 + m_1^2/p^2} - \sqrt{1 + m_2^2/p^2} \right) \cong (m_1^2 - m_2^2) \frac{L}{2cp^2} \quad (4.4)$$

An example of particle identification is given for the case of STAR experiment in Figure 4.18.

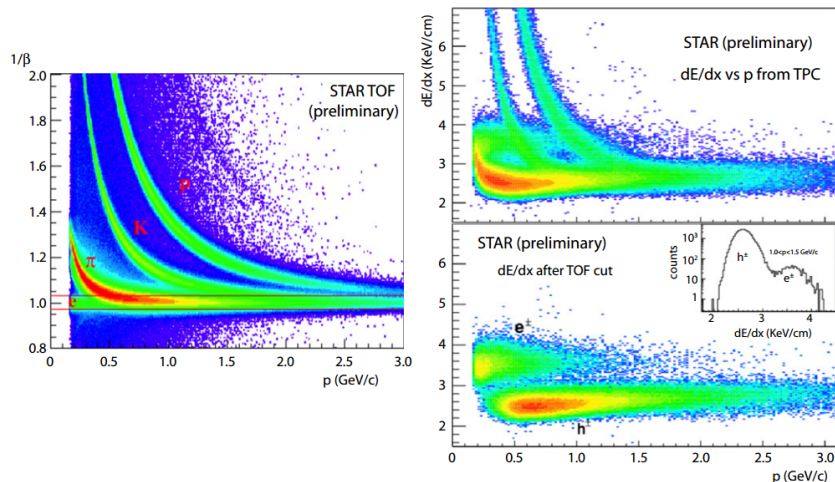


Figure 4.18: Particle identification applied to electrons in the STAR experiment. The identification is performed combining ToF and dE/dx measurements [65].

2250 Taking into account the distortion effect on the electric field inside of a MRPC built using micro
 2251 gaps due to the exposition to irradiation, distortion that can be understood by monitoring the current
 2252 drawn by the detector which should stay constant at constant electric field, another benefice of using
 2253 such small gas gaps is the strong reduction of the average avalanche volume and thus of the blind
 2254 spot on MRPCs leading to an improved rate capability. Multigaps can sustain backgrounds of several
 2255 kHz/cm² as demonstrated in Figure 4.19.

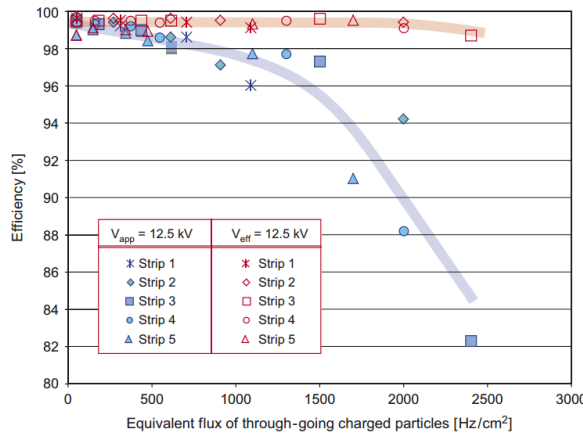


Figure 4.19: Comparison of the detector performance of ALICE ToF MRPC [66] at fixed applied voltage (in blue) and at fixed effective voltage (in red). The effective voltage is kept fixed by increasing the applied voltage accordingly to the current drawn by the detector.

2256 4.2.3.3 Charge distribution and performance limitations

2257 [This part could be moved in the next section of the chapter and deepened using the perspective
 2258 of the avalanche physics.]

2259 The direct consequence of the different RPC layouts is a variation of intrinsic time resolution of
 2260 the RPC as the gap size decreases and of the rate capability when the deposited charge per event is
 2261 spread over a larger number of amplification volumes, allowing for a reduction of the overall gain of
 2262 the detectors which is replaced by an on-electronics pre-amplification of the signals. in this sense,
 2263 an advantage is given to multigaps whose design use sub-millimeter gas volumes providing very
 2264 consistent signals.

2265 From the charge spectrum point of view, each layout has its own advantages. When the double-
 2266 gap has the highest induced over drifting charge ratio, as seen in Figure 4.20, the multigap has a
 2267 charge spectrum strongly detached from the origin, as visible in Figure 4.21. A high induced over
 2268 drifting charge ratio means that the double gap can be safely operated at high threshold or that at
 2269 similar threshold it can be operated with a twice smaller drifting charge, meaning a higher rate
 2270 capability if operated with sensitive enough electronics. On the other hand, the strong detachment
 2271 of the charge spectrum from the origin in the MRPC case allows to reach a higher efficiency with
 2272 increasing threshold as most of the induced charge is not low due to the convolution of several
 2273 single gap spectra. The range of stable efficiency increases with the number of gap, as presented in
 2274 Figure 4.22.

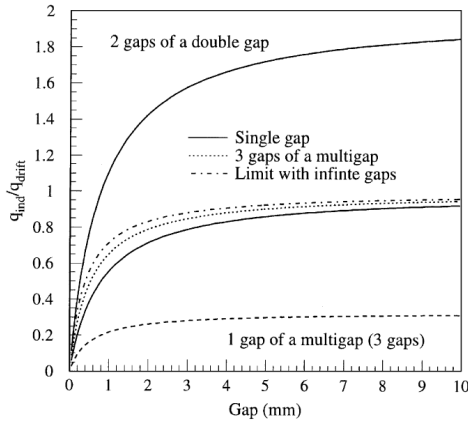


Figure 4.20: Ratio between total induced and drifting charge have been simulated for single gap, double-gap and multigap layouts [67]. The total induced charge for a double-gap RPC is a factor 2 higher than for a multigap.

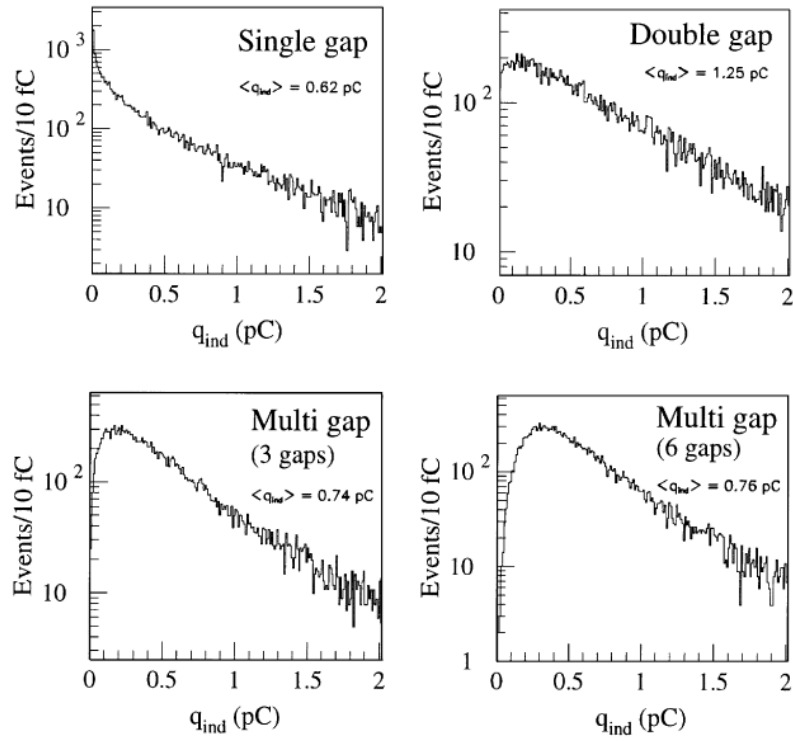


Figure 4.21: Charge spectra have been simulated for single gap, double-gap and multigap layouts [67]. It appears that when single gap shows a decreasing spectrum, double and multigap layouts exhibit a spectrum whose peak is detached from the origin. The detachment gets stronger as the number of gaps increases.

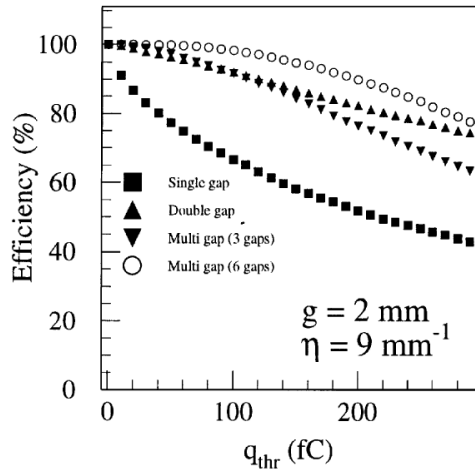


Figure 4.22: The maximal theoretical efficiency is simulated for single gap, double-gap and multigap layouts [67] at a constant gap thickness of 2 mm and using an effective Townsend coefficient of 9 mm^{-1} .

4.3 Signal formation

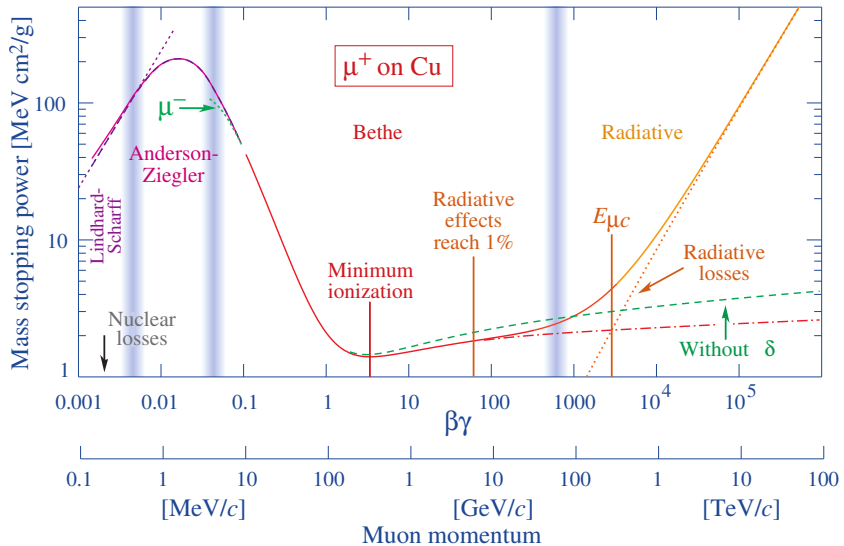


Figure 4.23: Mass stopping power as a function of $\beta\gamma = p/Mc$ for positive muons in copper [68]. The total stopping power is indicated with solid line and local components with dashed lines. The vertical bands are used to indicate boundaries between different approximations used at different energy range.

The physics of Resistive Plate Chambers still is far from being fully understood and work is regularly being accomplished in trying to model these detectors the best way possible by phenomenological models using well-defined physics [51, 69, 70]. These theoretical works have nevertheless lead to a better understanding of the key principles that account for RPCs signal formation. As previously

discussed, the typical mixture of such a detector is in great majority composed by a ionizing gas with some quenching properties and a low ionization potential to easily produce electrons, with the addition of UV quencher and electronegative compounds. The electronic avalanche formation will be triggered by a charged particle passing through the gas, typically a muon in the case of most uses of RPCs. The production of electrons in the gas of a detector is related to the energy lost by the incoming particle traveling through a material medium. The example of the mass stopping power of copper on muons is given in Figure 4.23 on which the different energy loss mechanisms at different energy ranges are visible. Once primary electrons have been freed in the gas volume, the electric field applied in between the electrodes of the RPC will make the charges move and there will be a competition in the gas in between the Townsend and attachment coefficient which describe the evolution of the number of electrons in an avalanche. While drifting through the gas, the electrons are also subjected to diffusion that will affect the evolution of the avalanches. Finally, when the avalanche is big enough, the accumulation of negative (electrons) and positive (ions) charges in the gas volume will start affecting the local electric field. This effect is known as space charge effect.

4.3.1 Energy loss at intermediate energies

Intuitively, a particle traveling through a medium will interact with its components, losing energy. When a muon travels through the gas of a gaseous detector, at the energy range usually observed, it interacts with the molecules of the gas leading to dissipation of the transferred energy in the form of inelastic diffusion or ionization. The photons and electron-ion pairs resulting from these interaction can trigger avalanches in the gas which will contribute to feed the avalanche growth thanks to the strong electric field applied in between the 2 electrodes of a RPC.

The mass stopping power of moderately relativistic ($0.1 \lesssim \beta\gamma \lesssim 1000$) heavy particles ($M \gg m_e$) traveling through a medium via excitation and ionization processes was studied by Bethe in 1930 [71] and is well described by the so called the Bethe Formula given in Equation 4.5.

$$\left\langle -\frac{dE}{dx} \right\rangle = K z^2 \frac{Z}{A} \frac{1}{\beta^2} \left(\frac{1}{2} \ln \frac{2m_e c^2 \beta^2 \gamma^2 W_{max}}{I^2} - \beta^2 - \delta(\beta\gamma) \right) \quad (4.5)$$

The different parameters used in this equation are

E	- incident particle energy γMc^2	MeV
x	- mass per unit area	g cm^{-2}
N_A	- Avogadro's number	$6.022\ 140\ 857(74) \times 10^{23} \text{ mol}^{-1}$
c	- speed of light in vacuum	$299\ 792\ 458 \text{ m s}^{-1}$
μ_0	- permeability of free space	$4\pi \times 10^{-7} \text{ N A}^{-2}$
ϵ_0	- permittivity of free space $\epsilon_0 = 1/\mu_0 c^2$	$8.854\ 187\ 817 \dots \times 10^{-12} \text{ F m}^{-1}$
α	- fine structure constant $\alpha = e^2/4\pi\epsilon_0\hbar c$	$1/137.035\ 999\ 139(31)$
r_e	- classical electron radius $r_e = e^2/4\pi\epsilon_0 m_e c^2$	$2.817\ 940\ 3227(19) \text{ fm}$
e	- elementary charge of the electron	$-1.6021766208(98) \times 10^{-19} \text{ C}$
$m_e c^2$	- electron mass $\times c^2$	$0.510\ 998\ 9461(31) \text{ MeV}$
K	- constant defined as $K = 4\pi N_A r_e^2 m_e c^2$	$0.307\ 075 \text{ MeV mol}^{-1} \text{ cm}^2$
z	- charge number of incident particle	
Z	- atomic number of absorbing medium	
A	- atomic mass of absorbing medium	g mol^{-1}
β	- velocity of particle $\beta = v/c$	
γ	- Lorentz factor $\gamma = (1 - \beta^2)^{-1/2}$	
W_{max}	- maximum energy transfer through a single collision	MeV

I - mean excitation energy of absorbing medium eV
 $\delta(\beta\gamma)$ - density effect correction to ionization energy loss

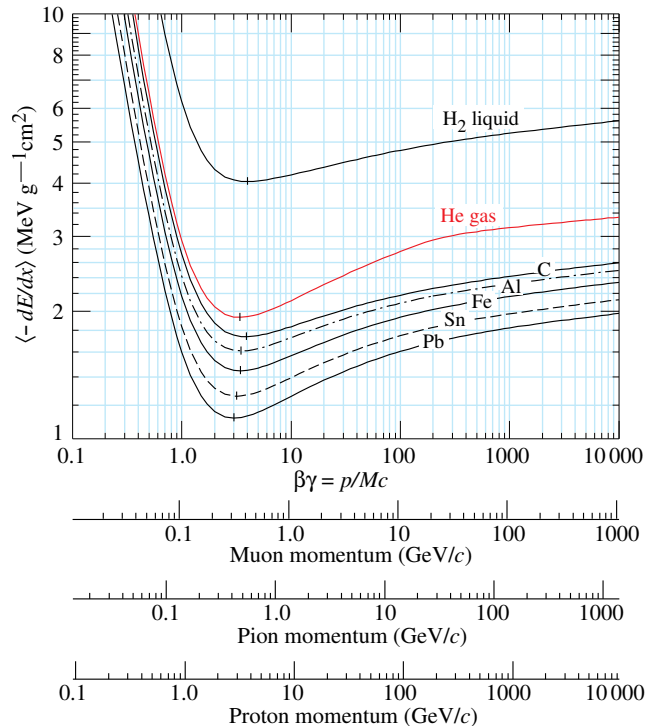


Figure 4.24: Mean mass stopping power for liquid hydrogen, as used in bubble chambers, gaseous helium, carbon, aluminum, iron, tin, and lead without the inclusion of radiative effect at higher $\beta\gamma$ necessary for pions and muons in denser materials [68].

In this equation, the maximum energy transfer W_{max} is defined as function of the incident particle mass M , expressed in MeV/c^2

$$W_{max} = \frac{2m_e c^2 \beta^2 \gamma^2}{1 + 2\gamma m_e/M + (m_e/M)^2} \quad (4.6)$$

and the mean excitation energy I depends on the absorber and its determination is non-trivial but recommendation are given by the International Commission on Radiation Units & Measurements (ICRU) based on experimental measurements and interpolations as showed in Figure 4.25.

For the case of copper, the mean stopping power is visible in Figure 4.23. The mean stopping power corresponding only to the Bethe range for other materials is given in Figure 4.24 and shows that $\langle -dE/dx \rangle$ is similar for each material with a slow decrease with Z . The factor affecting the most is β as the dependence on M is introduced at higher energies in the logarithm via the max transfer energy per single collision but in most practice cases, only the dependence on β is considered as most of the relativistic particles are closed to the lowest mean energy loss rate and are referred to as minimum ionizing particles (mip's). The almost logarithmic relation in between the mean energy loss rate for minimum ionizing particles and Z is showed in Figure 4.26.

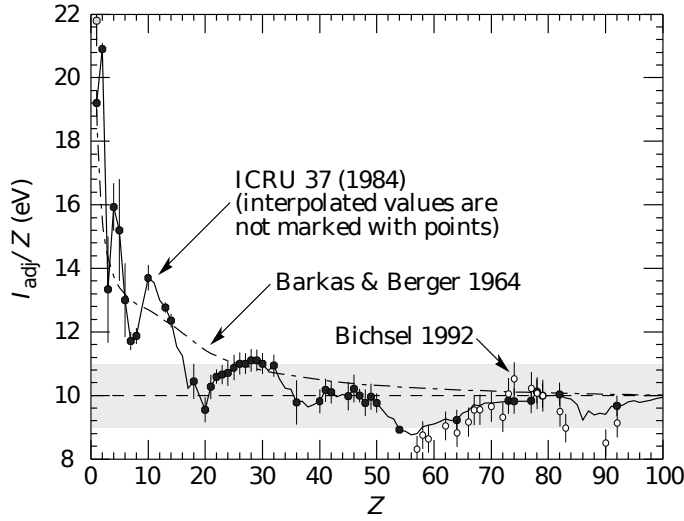


Figure 4.25: Mean excitation energies normalized to the atomic number as adopted by the ICRU [68, 72, 73].

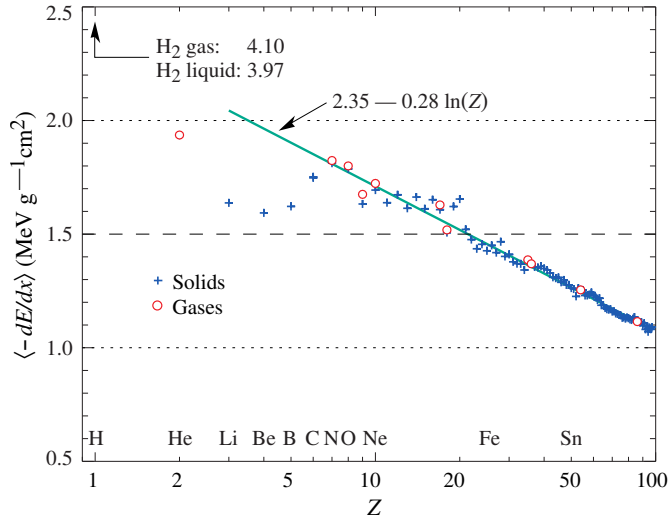


Figure 4.26: Mean mass stopping power at minimum ionization as a function of the atomic number [68].

Finally, the term $\delta(\beta\gamma)/2$ corresponds to the density effect correction introduced to account for the polarization of a real media that limits the spatial extension of the electric field of relativistic particles. Indeed, as the energy of a particle increases, the associated electric field will flatten and extend. Due to this effect, the distant collision contribution to Equation 4.5 will increase as $\ln(\beta\gamma)$ but the polarization of the media trunc this rise. At high energies, the correction is given by Equation 4.7

$$\delta/2 \longrightarrow \ln(\hbar\omega_p/I) + \ln(\beta\gamma) - 1/2 \quad (4.7)$$

where $\hbar\omega_p$ represents the plasma energy that depends on the electron density of the media and

the electron mass and can be calculated as $\sqrt{\rho \langle Z/A \rangle} \times 28.816$ eV. The introduction of this correction term reduces the increase of the mean stopping power at higher energies as can be seen in Figure 4.23. Moreover, due to poorer electron density, the effect is less visible on gases than on liquids and solids has van be seen from Figure 4.24.

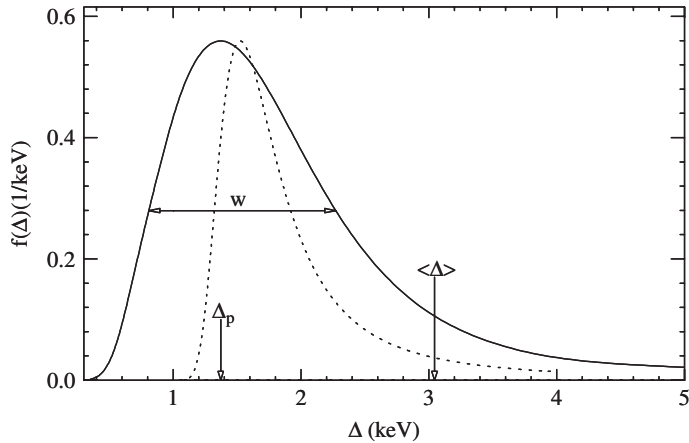


Figure 4.27: Example of straggling function $f(\Delta)$ of particles passing through 1.2 cm of Argon gas with a $\beta\gamma$ of 3.6 and represented with a solid line. The original Landau distribution is showed with a dashed line [74].

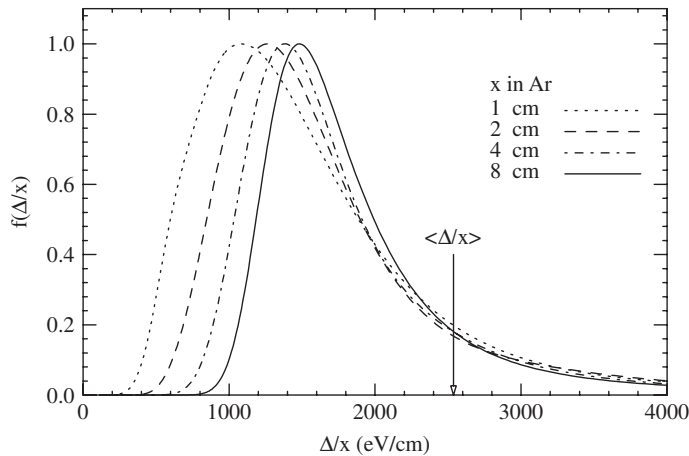


Figure 4.28: Evolution of straggling functions $f(\Delta)$ of particles passing through a volume of Argon gas with a $\beta\gamma$ of 3.6 with increasing thickness x [74].

The mean energy loss per collision can be difficult to measure for low data samples and is not always representative of the energy loss distribution for a given incident particle energy. Hence, it is easier to access the most probable energy loss which is a lower value than than the average loss due to the distribution of the energy transfer. This value is well described by a highly skewed Landau distribution for detectors with "moderate" thickness x , expressed in g mol⁻¹. But for gas volumes, a Landau distribution greatly underestimates the width w of the distribution and only succeeds to provide with a correct value for the most probable energy loss, as showed in Figure 4.27. Thus, the energy loss distribution is better represented by its most probable energy loss Δ_p and its full-

width-at-half-maximum (FWHM) w . As showed by Figure 4.28, the distribution is affected by the thickness of the gas volume and the most probable energy loss normalized to the thickness is increased and the width decreased, converging towards the Landau distribution, whereas the mean energy loss is unchanged. Correction are brought to the original Landau equation in order to account better for the number of collisions leading to an increased width of the energy loss distribution [74].

In the case of gas mixtures, composed of several elements, using Bragg additivity it can be understood that the mean energy loss of the mixture is the sum of the mean energy losses in each individual element j layer of weight w_j .

$$\left\langle \frac{dE}{dx} \right\rangle = \sum w_j \left\langle \frac{dE}{dx} \right\rangle_j \quad (4.8)$$

4.3.2 Primary ionization

Using Bethe formula to understand the mean energy transfer of charged particle when traveling through a gas volume give an intuition of the physics that affect the particle but doesn't provide a detailed enough information about the individual ionizations along its tracks at a microscopic level. In order to simulate efficiently an RPC and hence understand the processes governing avalanches creation and growth, knowledge on the ionization process is necessary.

To convert the energy loss rate into a number of primary ionizations was developed in 1980 the Photo-Absorption Ionisation (PAI) model [75] based on the cross section of ionization of gas atoms to real photons and the dielectric constant of the medium through which the charged particles are going. Indeed, the interaction of charged particles with the gas molecules being of electromagnetic nature, it is mediated by quasi-real photons and, hence, the cross section to photon ionization is important to understand. This approach is nevertheless semi-classical as it relies on classical electrodynamics and it only gives access to the energy transfer to the gas atoms and no information on the energy dissipation and secondary emissions is available on the output of the model. The energy transferred to the medium is not all used for ionization. For an energy deposition Δ , the number of electron-ion pairs produced is:

$$\Delta = n_i W \quad (4.9)$$

W corresponds to the mean work per pair production that depends on the medium and is greater than the ionization potential leading to the conclusion that part of the transferred energy is dissipated through other processes [70, 76]. In order to understand the energy dissipation and the secondary emissions, the fine structure of each atom is taken into account. Through the PAI model, the incident charged particle interacts is assumed to interact with the full atom rather than with a single electron.

Although, considering that the particle interacts with a single electron, leads to the possibility to study the excited state of the atom once the photo-electron has been emitted with an energy corresponding to the transferred energy minus the binding energy of the electronic shell. The resulting vacancies in the electronic shell will be filled through emission of photons or Auger electrons and can contribute to further ionization or excitation in the gas volume. Fluorescence photons are usually not considered as they only constitute a very small fraction of secondary emissions [77]. Assuming that the transferred energy is absorbed in its totality by a single electronic shell, the PAI model was modified to include relaxations and constitute the new Photo-Absorption Ionisation with Relaxation (PAIR) model [77]. In this model, the cross section corresponding to the whole atom is re-expressed using a sum of partial cross sections corresponding to the different electronic shells. When one or

more electrons are knocked out of the atom, the vacancies are filled by electrons of the shell above with relaxation by Auger electron emission. These processes happen in cascade from the inner shell to the outer one until all the vacancies are filled and the energy has been released.

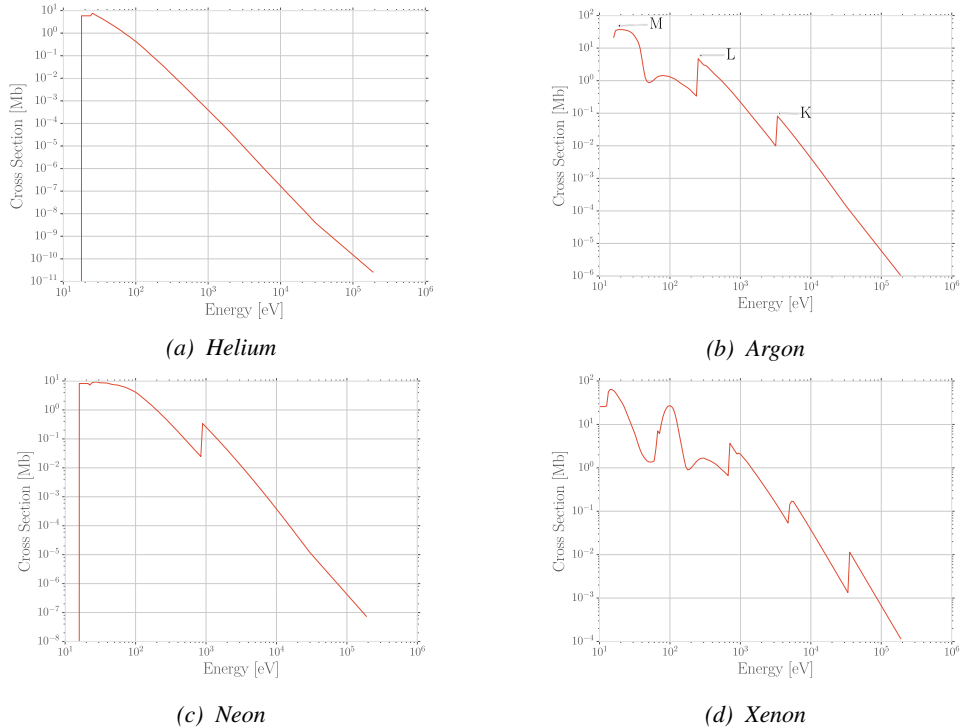


Figure 4.29: Photo-absorption cross section as computed by HEED for noble gases with different electric shell numbers [70].

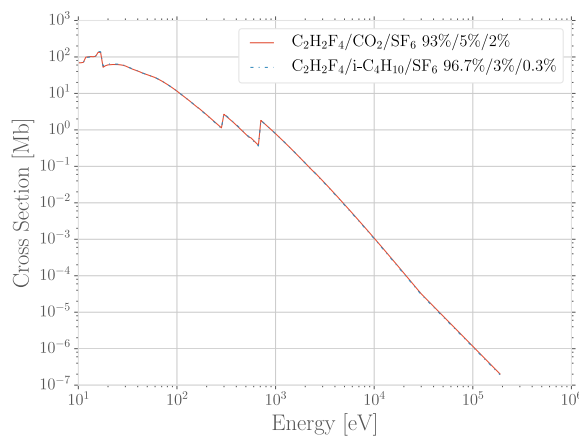


Figure 4.30: Photo-absorption cross section as computed by HEED for typical RPC gas mixtures [70]. The RPC mixture with CO_2 corresponds to the mixture used by CALICE SDHCAL [78] while the other one was foreseen for the experiment ATLAS [79] but has been changed since then.

This model is included in the program HEED developed at CERN [80] and called by Garfield, a program developed for the simulation of gaseous detectors. The results for the cross section for a few noble gases are given in Figure 4.29. It can be seen that for each shell, the cross section is increased. More complex patterns are seen with bigger atoms such as Xenon on Figure 4.29d. For gas mixtures, like the typical RPC mixtures, the cross section is showed in Figure 4.30. Both mixtures being mainly composed of $C_2H_2F_4$, the variations in between the 2 cross section profiles are very subtle and depends on the concentration of the other compounds.

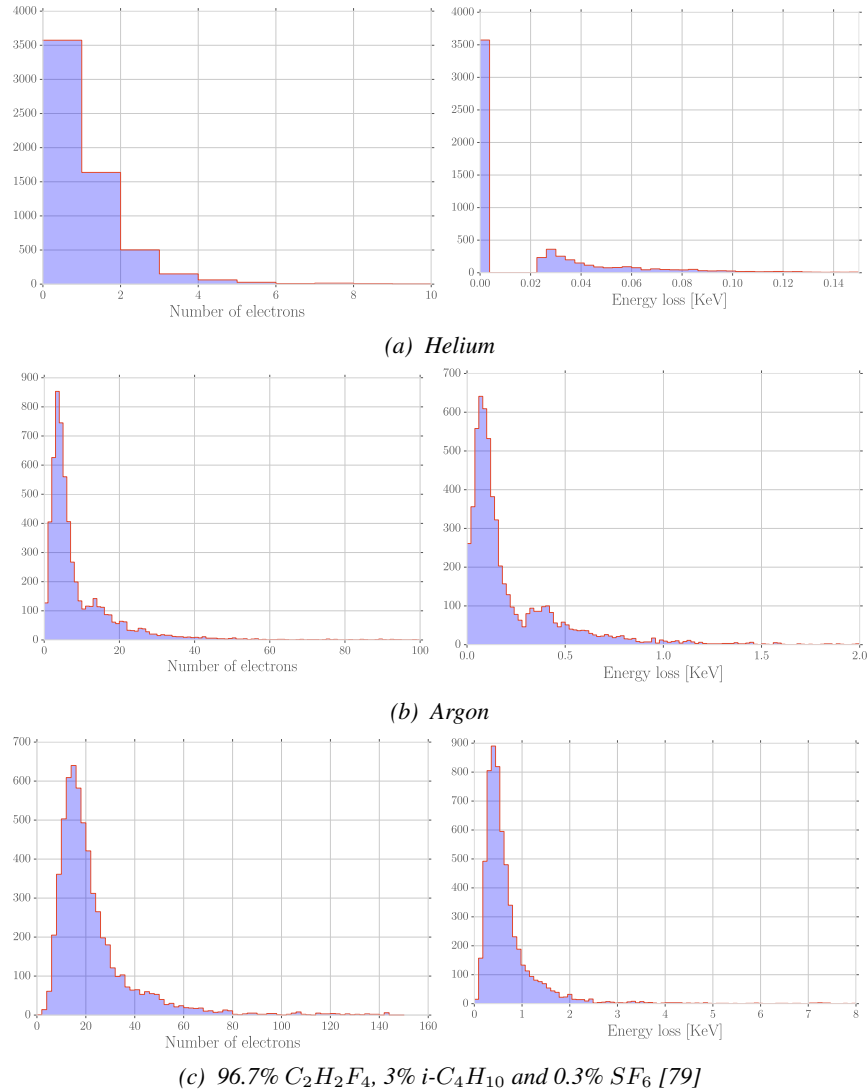


Figure 4.31: Distributions of number of electrons (left) and energy loss (right) for a 5 GeV/c muon passing through 1.2 mm of Helium (Figure 4.31a), Argon (Figure 4.31b) or a typical RPC gas mixture (Figure 4.31c) [70].

Once the cross section of interaction is known, it is possible to extract the distribution of energy loss and of the number of electron produced, as showed in Figure 4.31 for Helium, Argon, which is

used in gaseous detectors, and for a typical RPC mixture [70]. The distributions are computed using HEED and show typical straggling function profiles with some complex structures that can be related to interaction of the incoming particle with the different electronic shells. Helium does not have a great photo-absorption cross-section according to Figure 4.29a and a muon will not be likely to lose a lot of energy and to create a lot of electrons whereas in a more complex atom like Argon, the cross-section is greater and will lead to a greater energy loss of muons and more electron produced. Finally, a complex gas mixture used in RPCs will offer an even greater cross-section, a wider energy loss distribution and will be able to produce more electrons. The same information is seen by looking at the evolution of the mean number of cluster as a function of the lorentz factor associated to muons showed in Figure 4.32a. Indeed, the greater photo-absorption cross-section of RPC mixtures allow for a much greater amount of clusters to be created by charged particles. The size of these clusters is studied through Figure 4.32b which shows that, in most of the cases ($\approx 80\%$), the clusters only are composed of a single electron which is consistent with minimum ionizing particles.

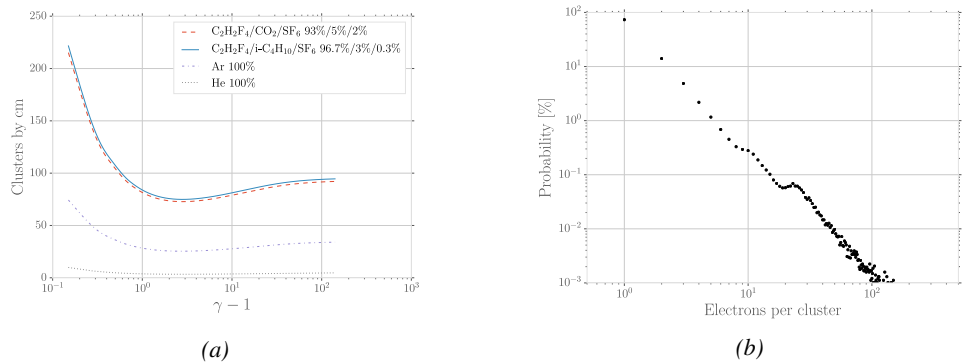


Figure 4.32: Figure 4.32a: Mean cluster density for muons through different gas volumes [70]. Figure 4.32b: Distribution of the number of electrons per cluster for a 5 GeV/c muon traveling through a mixture of 96.7% $C_2H_2F_4$, 3% $i-C_4H_{10}$ and 0.3% SF_6 [70, 79].

4.3.3 Development and propagation of avalanches

From the clusters released in the gas volume by the charged particles, free electrons will start drifting due to the electric applied in between the electrodes of the RPC. Gaining velocity and energy, these electrons in their turn will be able to ionize the gas. This process being repeated by all the produced electrons will trigger an avalanche to develop.

The growth of the avalanche can be intuitively understood as a competition between 2 effects. Due to their increasing energy, electrons have a probability to trigger new ionizations by interacting with gas molecules. On the other hand, before the minimal amount of energy is reached, the electrons can get attached to a gas molecule instead. These two effects can be described using a simple model in which the multiplication and attachment processes are given by the Townsend coefficient α and the attachment coefficient η , assuming that the history of previous interactions in the gas does not influence new interactions. This model simply takes into account probabilities to have at the gas depth z for a given number n of free electrons in the gas $n+1$ or $n-1$ electrons at the depth $z+dz$ (respectively $n\alpha dz$ and $n\eta dz$). Then, the mean number of electrons \bar{n} and cations \bar{p} can be written

²⁴¹⁵ for single compound gases as

$$\frac{d\bar{n}}{dz} = (\alpha - \eta)\bar{n}, \quad \frac{d\bar{p}}{dz} = \alpha\bar{n} \quad (4.10)$$

²⁴¹⁶ which, assuming the initial conditions $\bar{n}(0) = 1$ and $\bar{p}(0) = 0$, lead to the mean number of
²⁴¹⁷ electrons and cations at a depth z

$$\bar{n}(z) = e^{(\alpha-\eta)z}, \quad \bar{p}(z) = \frac{\alpha}{\alpha-\eta} \left(e^{(\alpha-\eta)z} - 1 \right) \quad (4.11)$$

²⁴¹⁸ The Townsend and attachment coefficient as a function of the applied electric field are given in
²⁴¹⁹ Figure 4.33 for a standard RPC gas mixture using Magboltz [81].

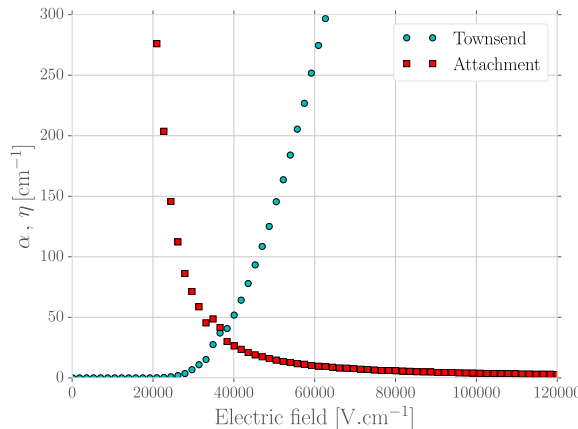


Figure 4.33: Townsend and attachment coefficient for a typical 96.7/3/0.3 mixture of $C_2H_2F_4/i-C_4H_{10}/SF_6$, at a temperature $T = 296.15$ K and a pressure $P = 1013$ hPa [70, 79].

²⁴²⁰ Nevertheless, there are more to the avalanche growth than simply these two factors. Throughout
²⁴²¹ the 20th century, models have been developed to better understand the physics of discharges in gas.
²⁴²² In 1937, Furry developed a model to describe electromagnetic cascades [82] that would be used for
²⁴²³ electron avalanches in gas during the 1950s. Furry realized that the use of a Poisson law to describe
²⁴²⁴ the distribution of shower sizes could not be accurate as he understood that the events occurring in
²⁴²⁵ the development of a cascade are not independent from each other, as a Poisson law would suggest.
²⁴²⁶ Indeed, part of the particles produce others and this process depends on both their original energy
²⁴²⁷ and energy lost. Experimental results showed excess of small showers and an under estimate of very
²⁴²⁸ large ones. To solve this problem, Furry proposed a distribution of sizes of following the likelihood
described in Equation 4.12, in which $\bar{n} = e^{\alpha z}$, compared with a Poisson law in Figure 4.34.

$$P(n, \bar{n}) = \bar{n}^{-1} (1 - \bar{n}^{-1})^{n-1} \quad (4.12)$$

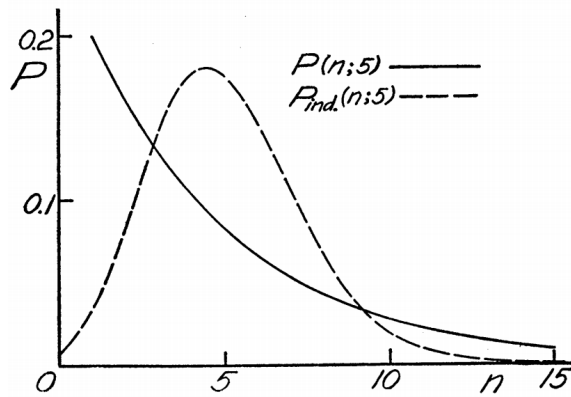


Figure 4.34: Comparison of the distribution law of Furry and the Poisson law for $\bar{n} = 5$ [82].

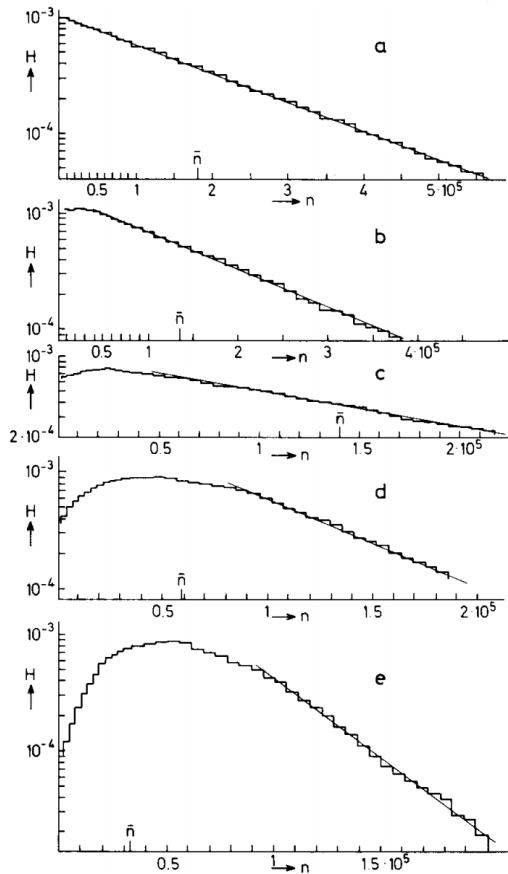


Figure 4.35: Single-electron avalanche size distribution in a proportional counter filled with methylal at different E/p values. (a) 70, (b) 76.5, (c) 105, (d) 186.5, (e) 426V/cm torr [83].

²⁴³⁰ In this model, no extra energy is brought to the electrons in the showers, contrary to the case of
²⁴³¹ a gaseous detector such as a RPC where an electric field accelerates them. Using the Furry model,

2432 Genz studied the fluctuations in electron avalanches in gaseous detectors [83]. Collisions leading to
 2433 ionizations leave electrons with an energy much smaller than the ionization energy eU_i , where U_i is
 2434 the ionization potential of a gas molecule. Hence, the electrons need to travel a distance $s = U_i/E$
 2435 along the electric field E to acquire a high enough energy to trigger a new ionization. For the
 2436 probability of a new ionization to be independent from the path followed by the electrons since the
 2437 previous ionization, the mean free path $1/\alpha$ of electrons in the gas has to be large compared to s and
 2438 thus $E/\alpha \gg U_i$. The Townsend coefficient is related to the gas pressure leading to conditions on the
 2439 value of E/p . Avalanches in gas are large compared to the showers Furry has studied in his original
 2440 paper. For very large avalanche sizes, Equation 4.12 can be written as an exponential, as showed in
 2441 Equation 4.13.

$$P(n, \bar{n}) = \bar{n}^{-1} e^{-n/\bar{n}} \quad (4.13)$$

2442 This exponential behaviour is showed through Figure 4.35. In practice, to fully understand the
 2443 avalanche growth, taking into account the path followed by electrons from one ionization to another
 2444 will become necessary. In the same paper, Genz then discusses models using Polya distributions
 2445 to estimate the multiplication by looking at the size of the avalanche it self. Indeed, the number of
 2446 charge carriers in the avalanche might become important enough to have an effect on the multipli-
 2447 cation process. To account for this, it was proposed to use a varying Townsend coefficient such as
 2448 described by Equation 4.14 depending on the position x in which θ is an empirical parameter leading
 2449 to the probability distribution of Equation 4.15. In the limit case where θ goes to 0, the formula
 2450 describes again the Furry model. But the data deviates from this model as well at large n values.
 2451 Moreover, the introduction of an empirical parameters makes the model hard to interpret physically.

$$\alpha(n, x) = \alpha(x) \left(1 + \frac{\theta}{n}\right), \quad n > 0 \quad (4.14)$$

$$P(n, x) = \frac{1 + \theta}{\bar{n}} \frac{1}{\theta!} \left(\frac{n(1 + \theta)}{\bar{n}}\right)^{\theta} e^{-\frac{n(1 + \theta)}{\bar{n}}} \quad (4.15)$$

2452 In order to have a model that describes reality better, the introduction of the attachment into the
 2453 model is an important step. Despite its limitations, the Furry model had the advantage to describe
 2454 well avalanches occurring when the attachment could be ignored. This is only natural that this model
 2455 was then extended to included attachment. This was done by Riegler, Lippmann and Veenhof [79]
 2456 which showed that was important was to consider both the Townsend coefficient describing the
 2457 multiplication *and* the attachment coefficient, not only the effective multiplication coefficient $\bar{\alpha} =$
 2458 $\alpha - \eta$. The probability to see an avalanche started by a single electron grow to a size n after having
 2459 traveled a distance z through the gas is given by Equation 4.16.

$$\begin{aligned} P(n, z) = & P(n - 1, z) (n - 1) \alpha dz (1 - (n - 1) \eta dz) \\ & + P(n, z) (1 - n \alpha dz) (1 - n \eta dz) \\ & + P(n, z) n \alpha dz n \eta dz \\ & + P(n + 1, z) (1 - (n + 1) \alpha dz) (n + 1) \eta dz \end{aligned} \quad (4.16)$$

2460 The first term of this probability that from a state with $n - 1$ electrons, only 1 multiplies while
 2461 the others don't get attached. Both the second and third terms describes the probability that from
 2462 a state with already n electrons the total number of electrons stay the same. On the second term,
 2463 no electron gets attached nor multiplies while on the third term, 1 electron gets multiplied and 1

2464 gets attached to compensate. Finally, the fourth term describes the probability to fall from a state
 2465 with $n + 1$ to a state with n electrons due to the attachment of a single electron. At the first order,
 2466 the evaluation of the previous expression leads to Equation 4.17 which general solution is given in
 2467 Equation 4.18 in which are introduced the variables $\bar{n}(z)$, defined as in Equation 4.11, and $k = \eta/\alpha$
 2468 making explicit the fact that the distribution not only depends on the effective Townsend coefficient.

$$\frac{dP(n, z)}{dz} = -P(n, z)n(\alpha + \eta) + P(n - 1, z)(n - 1)\alpha + P(n + 1, z)(n + 1)\eta \quad (4.17)$$

$$P(n, z) = \begin{cases} k \frac{\bar{n}(z)-1}{\bar{n}(z)-k}, & n = 0 \\ \bar{n}(z) \left(\frac{1-k}{\bar{n}(z)-k} \right)^2 \left(\frac{\bar{n}(z)-1}{\bar{n}(z)-k} \right)^{n-1}, & n > 0 \end{cases} \quad (4.18)$$

2469 The example given through Figure 4.36 shows the importance of each individual process in
 2470 the growth of avalanches and the fluctuation of their size. The values of α and η will influence
 2471 the probability distribution, as can be seen from Figure 4.36a. Then, Figure 4.36b shows that the
 2472 fluctuation really takes place within the very first interactions. Indeed, when the avalanche contains
 2473 a large enough amount of charge carriers (a few hundreds), its size then increases like $e^{z(\alpha-\eta)}$.

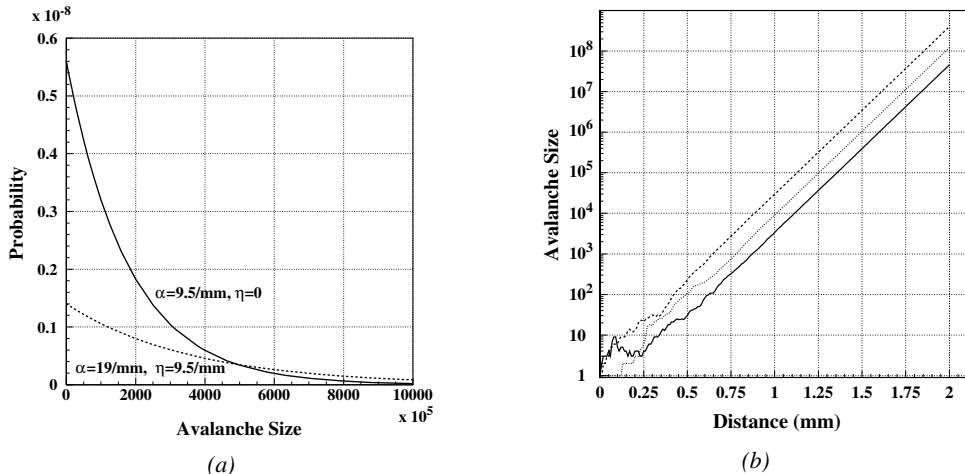


Figure 4.36: Figure 4.36a: Comparison of avalanche size distributions for different values of Townsend and attachment coefficients. The effective Townsend coefficient is the same for both distributions. Figure 4.36b: Fluctuation in avalanche size for avalanche started by a single electron with $\alpha = 13 \text{ mm}^{-1}$ and $\eta = 3.5 \text{ mm}^{-1}$ [79].

2474 4.3.4 Drift and diffusion of the electron cloud

2475 During the growth of avalanches, an electron cloud drifting along the electric field through the gas
 2476 will undergo thermal diffusion due to random collisions with the gas molecules. This phenomenon
 2477 can be studied using Maxwell-Boltzmann distribution whose mean is defined by the thermal energy
 2478 of the cloud $\langle E \rangle = 3/2kT$ with an extra component coming from the constant drift motion. The
 2479 drift of electrons along the field lines is usually observed on a macroscopic scale through which the
 2480 speed can be assimilated to a constant v_D which corresponds to the mean drift speed over a large
 2481 number of collisions in the gas.

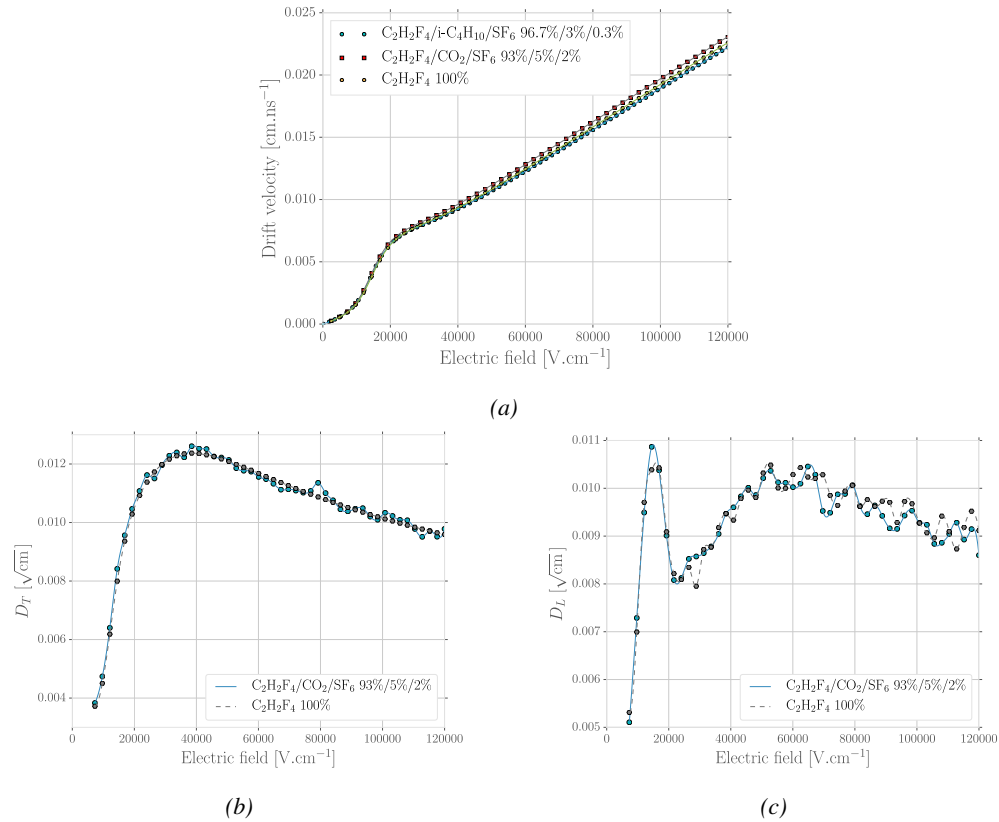


Figure 4.37: Figure 4.37a: Electron mean drift velocity v_D in pure $C_2H_2F_4$ and typical RPC gas mixtures. Figure 4.37b: Transverse diffusion coefficient in pure $C_2H_2F_4$ and a typical RPC gas mixture. Figure 4.37c: Longitudinal diffusion coefficient in pure $C_2H_2F_4$ and a typical RPC gas mixture. All results are given with a pressure $P = 760$ Torr and a temperature $T = 296.15$ K [70].

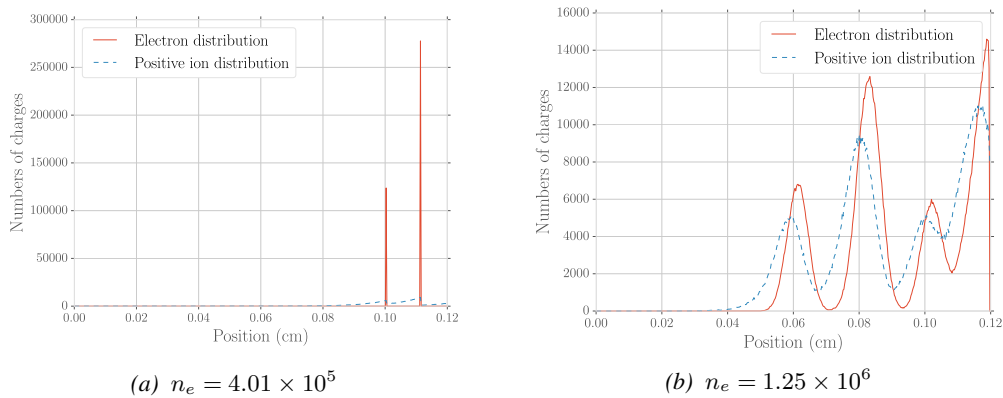


Figure 4.38: Comparison of the free charge carriers in the gas after a time $t = 7.90$ ns in the case where no diffusion is taken into account to simulate the avalanche (Figure 4.38a) and in the case where the diffusion is implemented (Figure 4.38b) [70].

Indeed, at the microscopic scale, the electrons are drifting over a distance δz while acquiring the corresponding kinetic energy $T = e_0 |\vec{E}| \delta z$ until they are slowed down by a collision in which they lose part of their energy. This process is repeated as long as electrons are free carriers. Starting from a point-like electron cloud, the Gaussian density distribution at \vec{r}_0 will be described by Formula 4.19 in which the width of the isotropic distribution is $\sigma = 2\bar{D}t$, with \bar{D} being a diffusion coefficient expressed in m^2/s [51].

$$\varphi(\vec{r}, t) = \frac{1}{(\sqrt{2\pi}\sigma(t))^3} \exp\left(-\frac{(\vec{r} - \vec{r}_0)^2}{2\sigma^2(t)}\right) \quad (4.19)$$

Now, if the constant drifting motion is added, the distribution is anisotropic and can be divided onto transversal (Formula 4.20) and longitudinal (Formula 4.21) terms, $\varphi(r, z, t) = \varphi_T(r, t)\varphi_L(z, t)$, with a cylindrical symmetry around the field axis [51]. The variables t and $\sigma_{T,L}(t)$ can be hidden to the profit of the diffusion coefficients by using the relations $v_D = l/t$ and $\sigma_{T,L}^2(t) = 2\bar{D}_{T,L}l/v_D$ and introducing new diffusion coefficients $D_{T,L} = \sqrt{2\bar{D}_{T,L}/v_D}$ in order to explicitly show the dependence of the Gaussian width in drifted distance l .

$$\varphi_T(r, t) = \frac{1}{D_T^2 l} \exp\left(-\frac{(r - r_0)^2}{2D_T^2 l}\right) \quad (4.20)$$

$$\varphi_L(z, t) = \frac{1}{\sqrt{2\pi l} D_L} \exp\left(-\frac{(z - z_0)^2}{2D_L^2 l}\right) \quad (4.21)$$

These coefficients, as well as the drift velocity of the electrons, can be calculated thanks to Magboltz as showed in Figure 4.37. The influence of the diffusion on the distribution of charge carriers throughout the gas volume is depicted in Figure 4.38. From very localised electron clusters in the gas in Figure 4.38a, a Gaussian diffusion is then visible in Figure 4.38b. Due to the interactions with gas molecules during the drift, diffusions can occur in the forward and backward direction. Electrons diffused backward will effectively drift over a longer distance and multiply more than electrons diffused forward that will see a shorter drift length. As an effect, the avalanche develops over a longer time and extends over a greater gas volume than in the case the electron cloud is considered as point like and without diffusion. Moreover, as a side effect to the longer growth of the avalanche due to backward longitudinal diffusion, the total production of electrons is increased.

4.3.5 Space charge effect & streamers

Now that have been considered the basic processes that influence the development of avalanches in a gaseous detector in the previous sections, it is now important to consider the influence of the charge carriers present in the avalanche on the electric field seen by the avalanche. Indeed, each charged particle induces an electric field and it is only natural that the increasing density of electrons and ions in the detector volume will affect the electric field. Thus, parameters such as the Townsend and attachment coefficients, drift velocity or diffusion coefficients will find themselves to be modified along the gas gap length due to this effect referred to as *space charge effect*. Figure 4.39 is a more detailed version of Figure 4.1 (b) in which three electric regions are distinguished [51]. When compared to the linear electric field of strength E_0 that is developed in between the detector's electrodes, the accumulation of negative charges (electrons) on the front of the avalanche will reinforce the effective electric field in between the anode of the avalanche front. Deeper in the gas volume, the positive charges (cations) slowly drift towards the cathode and can induce together with the avalanche front

2517 opposite electric field loops. Finally, due to the density of positive charges, the electric field seen in
 2518 between the ions tails and the cathode charged with negative charges is on average stronger than E_0
 2519 and compensate for the locally reversed field E_2 . Lippmann roughly estimated by considering that
 2520 10^6 charges were contained in a sphere of radius $r_d = 0.1$ mm that the space charge effect could
 2521 change the electric field by 3% and the Townsend and attachment coefficient up to 14% [51, 70].

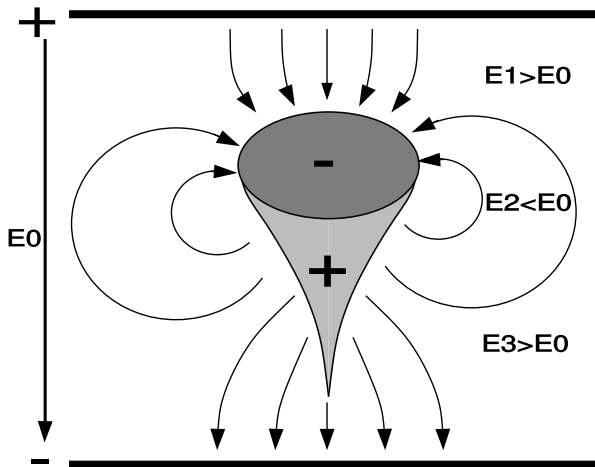


Figure 4.39: Schematic representation of an avalanche and of the electric field deformation it causes due to the local concentration of charge carriers [51].

2522 To account for the space charge effect, the electric potential and field of free charges are solved
 2523 and applied to each charges in the avalanche [51, 70]. As discussed by Fran ais who has been work-
 2524 ing on simulating RPCs similar to that used by the SDHCAL project of ILC, the computation of
 2525 these equations for each individual charge carrier to dynamically know the space charge field at ev-
 2526 ery stage of an avalanche development is a difficult task and would require far too much computation
 2527 time and a solution is to pre-compute an interpolation table keeping an adequately large number of
 2528 values of the space charge field for each positions in space thanks to which the values stored in the
 2529 interpolation table become very close to the analytic solution and allow for a much faster simulation.
 2530

2531 The study of space charge effect through simulation shows that it can lead to a saturation of
 2532 the avalanche growth due to the deformation of the electric field, as showed through Figure 4.40.
 2533 Additionnally, a more precise understanding of the space charge effect is given through Figure 4.41
 2534 which looks at the distribution of charges and the distortion of the electric field at different steps of
 2535 the evolution of an avalanche in a RPC. At the moment a 5 GeV muon ionizes the gas, electron-ion
 2536 pairs are created in the gas in different clusters (Figure 4.41a). Later, the first clusters have reached
 2537 the anode while the clusters that where created the closest to the cathode are now big enough to start
 2538 influencing the electric field in the gap (Figure 4.41b). When a cluster is big enough, the electric field
 2539 in front of it locally increases a lot and contributes to a stronger but very localised multiplication. At
 2540 the same moment, the positive ions right behind the cluster avalanche front decrease the electric field,
 2541 saturating the electron multiplication on the tail of the electron cloud (Figure 4.41c). Finally, when
 2542 all the electrons have reached the anode and are relaxing, the electric field still is very deformed
 2543 by the distribution of both positive and negative ions in the the gas volume closest to the anode
 2544 (Figure 4.41d).

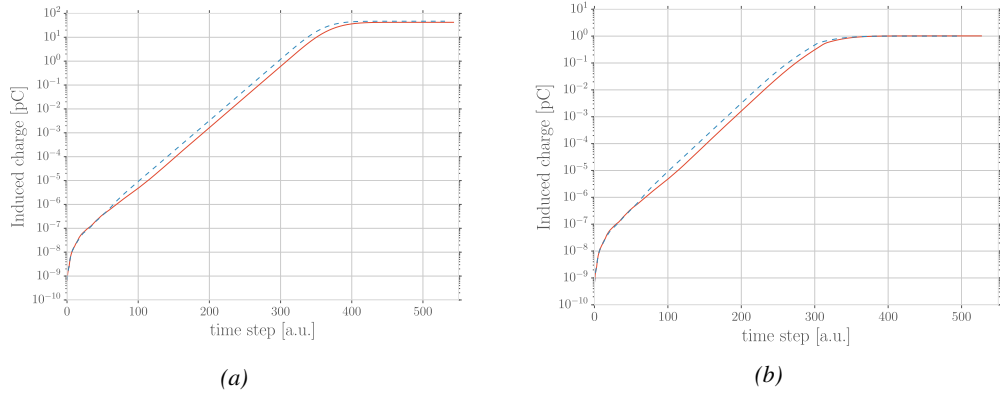


Figure 4.40: Evolution of the charge induced by an avalanche started by a single electron in a 1.2 mm thick RPC with an applied electric field of 54 kV/cm in the case space charge is not taken into account (Figure 4.40a) and in the case it is implemented into the simulation (Figure 4.40b). The total induced charge is correlated to the size of the avalanche [70].

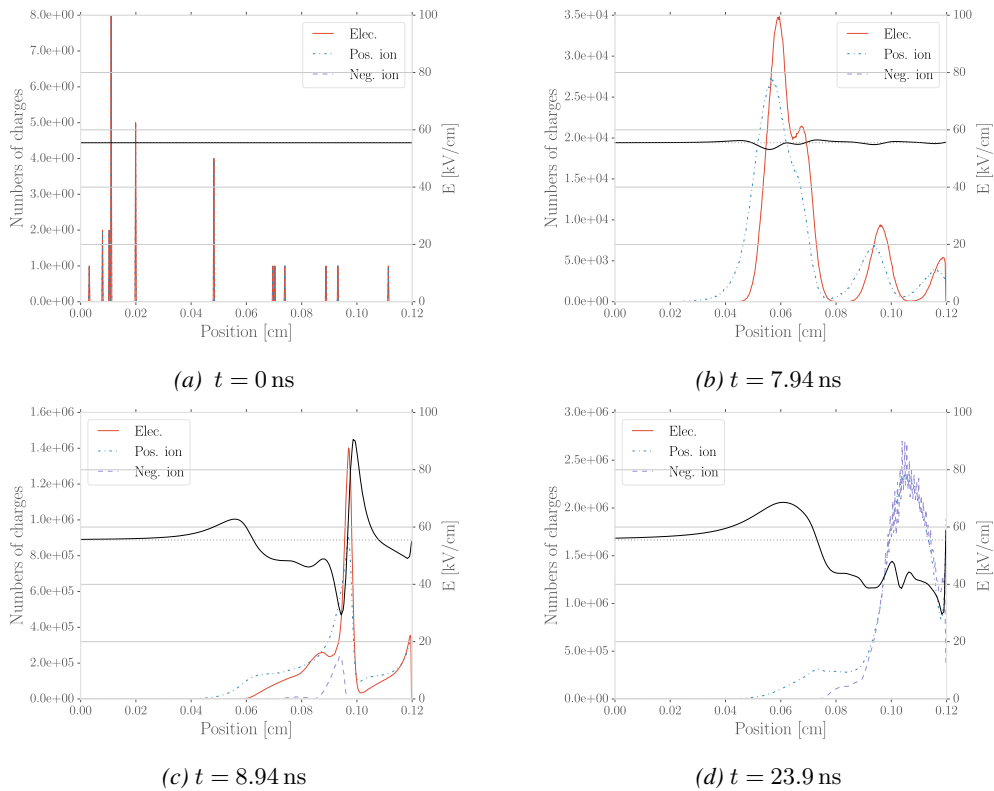


Figure 4.41: Distributions of charge carriers within the gas volume of a 1.2 mm thick RPC and the corresponding deformation of the electric field at different time steps with an applied electric field of 55.5 kV/cm [70].

2545 The electric field following the development of an avalanche can stay perturbed for a long time
 2546 with respect to the avalanche development due to the slow drift of the much heavier ions. This can

result in powerful secondary avalanches triggered by the fluctuation of the electric field together with the emission of UV-photons leading to emission of electrons at the surface of the electrode. This is a slow phenomenon compared to the development of avalanches. Experimentally, it is observed that the stronger the electric field applied over the gap, the sooner after the avalanche, referred to as *precursor signal* in this context, and the stronger will the secondary avalanche be, possibly reaching the streamer regime. This could be due to the amount of UV-photons emitted by the growing precursor. These photons will be able to trigger new avalanches in a radius of a few mm around the precursor by knocking electrons from the cathode by photoelectric effect. The strong distortions of the electric field due to a large avalanche will be more likely to emit UV-photons as the electric field at the front of the precursor avalanche will be large, providing the electrons with a larger energy. Eventually, the new avalanches can grow to form streamers.

4.4 Effect of atmospherical conditions on the detector's performance

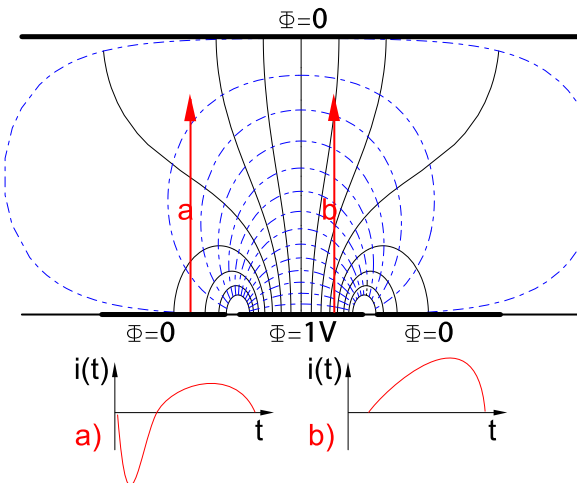


Figure 4.42: Representation of the weighting field in the volume of a RPC and the resulting induced current in the strip placed at 1 V and its neighbour connected to the ground. The induced current corresponds, as can be understood from Formula 4.22 [51].

The movement of charge carriers, and in particular, the movement of a dense electron cloud toward the anode induces a current signal on the readout electrodes (strips or pads). The ions on the other hand induce only a very small current as their movement is much slower than which of the electrons. The current induced by n_{CL} clusters of $N_j(t)$ charge carriers drifting at velocities $\vec{v}_{Dj}(t) = \dot{\vec{x}}_j(t)$ at a time t is given by Formula 4.22 in which e_0 is the unit charge and \vec{E}_w is the weighting field.

$$i(t) = \sum_{j=1}^{n_{CL}} \vec{E}_{wj}(\vec{x}_j(t)) \cdot \vec{v}_{Dj}(t) e_0 N_j(t) \quad (4.22)$$

The weighting field, that has been schematised in Figure 4.42, corresponds to the electric field that would be observed in the gas gap if a readout electrode is placed at a potential of 1 V while

keeping all the other electrodes grounded. Then the induced charge in the readout can be simply obtained by integrating Formula 4.22 over the duration T of the signal, as given by Formula 4.23.

$$Q(t) = \int_0^T \sum_{j=1}^{n_{CL}} \vec{E}_{wj}(\vec{x}_j(t)) \cdot \vec{v}_{Dj}(t) e_0 N_j(t) \quad (4.23)$$

The signal induced in the readout of RPCs operated in avalanche mode is then sent into Front-End Electronics in which they will be pre-amplified and discriminated. The discrimination and digitization of signals in CMS FEE is described through Figure 4.43. On a first stage, analogic signals are amplified, following the curve given on Figure 4.44, and then sent to the Constant Fraction Discriminator (CFD) described in Figure 4.45. At the end of the chain, 100 ns long pulses are sent in the LVDS output. The digital signals are both used as trigger for CMS and to evaluate the performance of the detectors. The performance will depend on the applied HV, i.e. on the electric field inside of the gas volume, but also on the threshold applied on the CFDs. Indeed, in order to reduce the probability to measure noise, the threshold is set to a level where the noise is strongly suppressed while the signals are not too affected. Typically, CMS FEEs are set to a threshold of 215 mV after pre-amplification, corresponding to an input charge of about 140 fC.

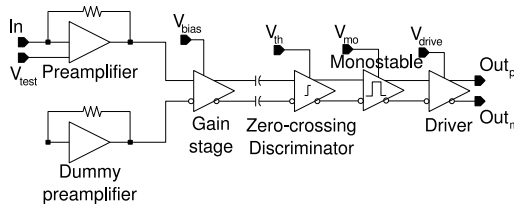


Figure 4.43: Schematics of CMS RPC FEE logic.

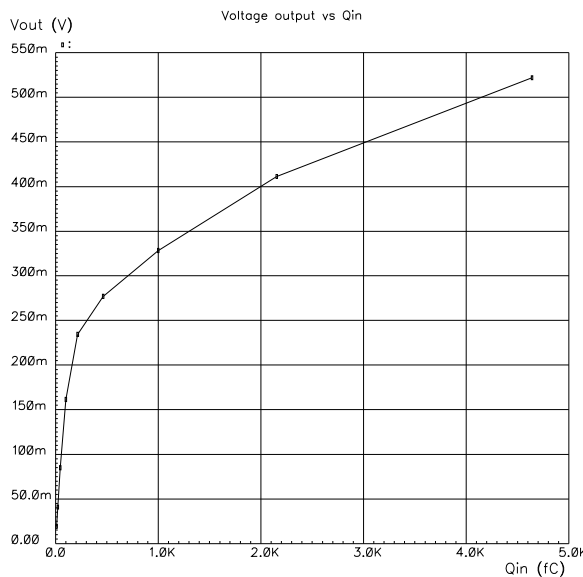


Figure 4.44: Equivalence in between the charge of the induced signal in input of the CMS FEE and the signal strength on the output of the pre-amplifier.

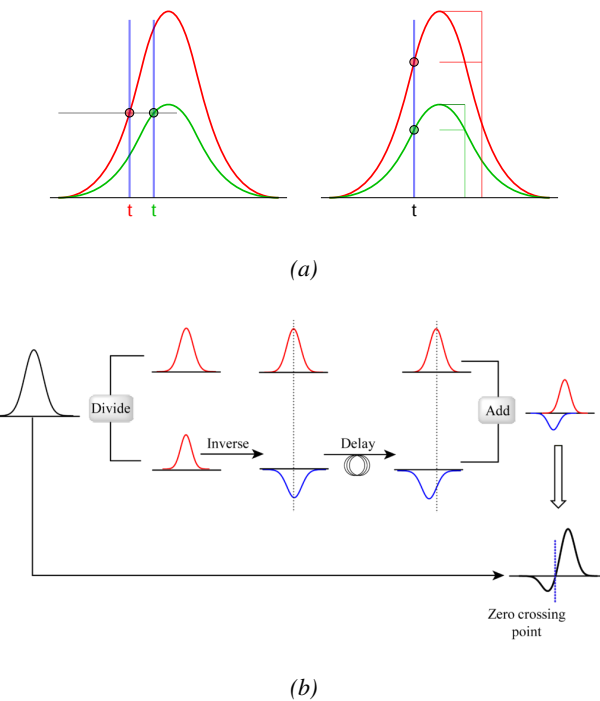


Figure 4.45: Description of the principle of a CFD. A comparison of threshold triggering (left) and constant fraction triggering (right) is shown in Figure 4.45a. Constant fraction triggering is obtained thanks to zero-crossing technique as explained in Figure 4.45b. The signal arriving at the input of the CFD is split into three components. A first one is delayed and connected to the inverting input of a first comparator. A second component is connected to the noninverting input of this first comparator. A third component is connected to the noninverting input of another comparator along with a threshold value connected to the inverting input. Finally, the output of both comparators is fed through an AND gate.

5

2580

2581

2582

Longevity studies and Consolidation of the present CMS RPC subsystem

2583 The RPC system, located in both barrel and endcap regions, provides a fast, independent muon
2584 trigger with a looser p_T threshold over a large portion of the pseudorapidity range ($|\eta| < 1.6$).
2585 During HL-LHC operations the expected conditions in terms of background and pile-up will make
2586 the identification and correct p_T assignment a challenge for the muon system. The goal of RPC
2587 upgrade is to provide additional hits to the Muon system with precise timing. All these informations
2588 will be elaborated by the trigger system in a global way enhancing the performance of the trigger in
2589 terms of efficiency and rate control. The RPC Upgrade is based on two projects: an improved Link
2590 Board System and the extension of the RPC coverage up to $|\eta| = 2.4$.

2591 The extension of the RPC system up to $|\eta| = 2.1$ was already planned in the CMS TDR and
2592 staged because of budget limitations and expected background rates higher than the rate capability
2593 of the present CMS RPCs in that region. An extensive R&D program has been done in order to
2594 develop an improved RPC that fulfills the CMS requirements. Two new RPC layers in the innermost
2595 ring of stations 3 and 4 will be added with benefits to the neutron-induced background reduction and
2596 efficiency improvement for both trigger and offline reconstruction.

2597 The Link Board system is responsible to process, synchronize and zero-suppress the signals
2598 coming from the RPC front end boards. The Link Board components have been produced between
2599 2006 and 2007 and will be subjected to ageing and failure in the long term. The upgraded Link Board
2600 system will overcome the ageing problems and will allow for a more precise timing information to
2601 the RPC hits from 25 to 1 ns.

2602 **5.1 Testing detectors under extreme conditions**

2603 The upgrade from LHC to HL-LHC will increase the peak luminosity from $10^{34} \text{ cm}^{-2} \text{ s}^{-1}$ to reach
2604 $5 \times 10^{34} \text{ cm}^{-2} \text{ s}^{-1}$, increasing in the same way the total expected background to which the RPC
2605 system will be subjected to. Composed of low energy gammas and neutrons from $p\text{-}p$ collisions,

2606 low momentum primary and secondary muons, puch-through hadrons from calorimeters, and particles produced in the interaction of the beams with collimators, the background will mostly affect
 2607 the regions of CMS that are the closest to the beam line, i.e. the RPC detectors located in the endcaps.
 2608
 2609

2610 Data collected in 2016 allowed to study the values of the background rate in all RPC system. In
 2611 Figure 5.1, the distribution of the chamber background hit rate per unit area is shown at a luminosity
 2612 of $5 \times 10^{34} \text{ cm}^{-2}\text{s}^{-1}$ linearly. The maximum rate per unit area at HL-LHC conditions is expected
 2613 to be of the order of 600 Hz cm^{-2} , including a safety factor 3. Nevertheless, Fluka simulations were
 2614 conducted in order to understand the background at HL-LHC conditions. The comparison to the data
 2615 has shown, in Figure 5.2, a discrepancy of a factor 2 even though the order of magnitude is consistent.
 2616

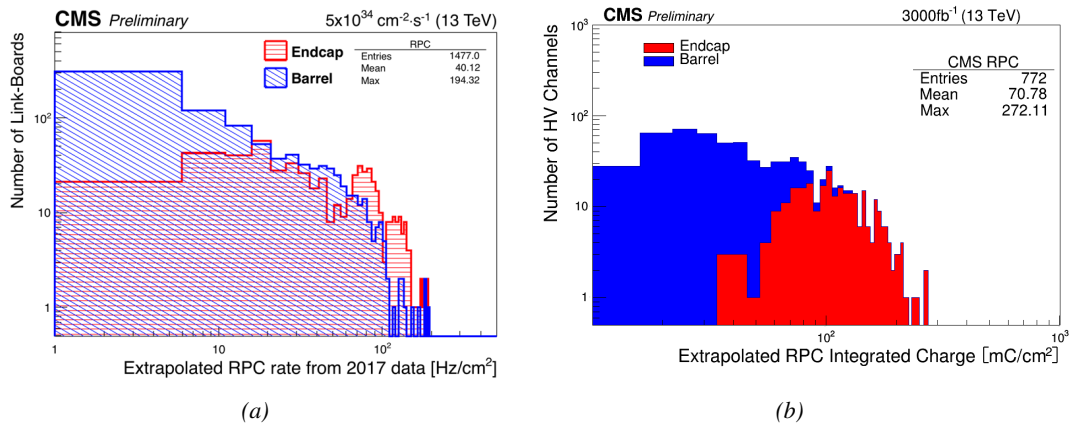


Figure 5.1: Figure 5.1a: The integrated charge per region (Barrel, Endcap) is extrapolated to HL-LHC integrated luminosity (3000 fb^{-1}) using the data accumulated in 2016 in every HV channels. Figure 5.1b: The hit rate per region (Barrel, Endcap) is linearly extrapolated to HL-LHC highest instantaneous luminosity ($5 \times 10^{34} \text{ cm}^{-2}\text{s}^{-1}$) using the rate as a function of instantaneous luminosity recorded by RPCs in 2017 showing a linear dependence.

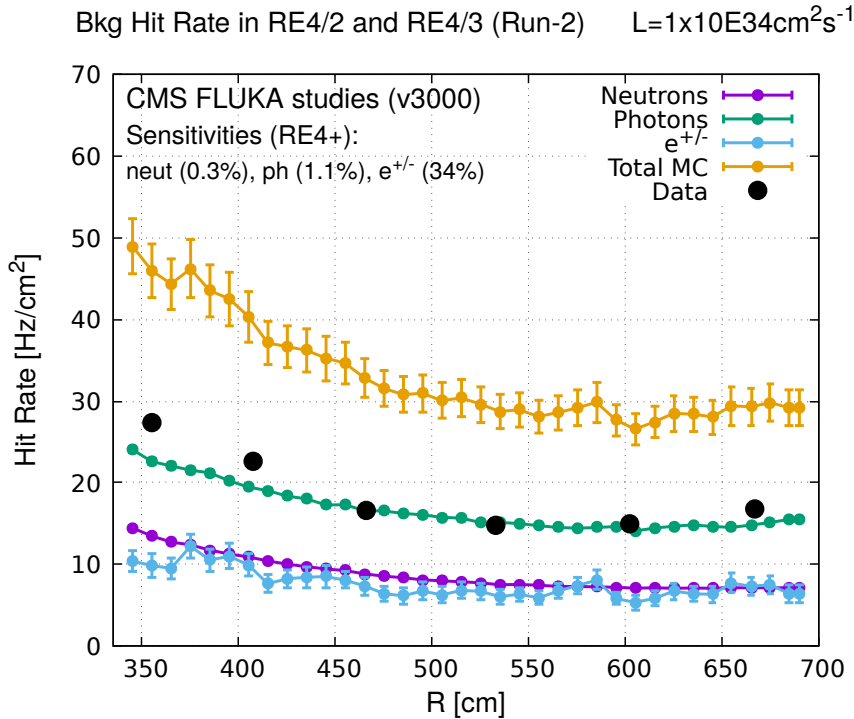


Figure 5.2: Background Fluka simulation compared to 2016 Data at $L = 10^{34} \text{ cm}^{-2}\text{s}^{-1}$ in the fourth endcap disk region. A mismatch in between simulation and data can be observed.

In the past, extensive long-term tests were carried out at several gamma and neutron facilities certifying the detector performance. Both full size and small prototype RPCs have been irradiated with photons up to an integrated charge of $\sim 0.05 \text{ C/cm}^2$ and $\sim 0.4 \text{ C/cm}^2$, respectively [84, 85]. During Run-I, the RPC system provided stable operation and excellent performance and did not show any aging effects for integrated charge of the order of 0.01 C/cm^2 . Projections on currents from 2016 Data, has allowed to determine that the total integrated charge, by the end of HL-LHC, would be of the order of 1 C/cm^2 , including a safety factor 3.

2624

2625 5.1.1 The Gamma Irradiation Facilities

2626 5.1.1.1 GIF

2627 Located in the SPS West Area at the downstream end of the X5 test beam, the Gamma Irradiation
 2628 Facility (GIF) was a test area in which particle detectors were exposed to a particle beam in presence
 2629 of an adjustable gamma background [86]. Its goal was to reproduce background conditions these
 2630 detectors would suffer in their operating environment at LHC. GIF layout is shown in Figure 5.3.
 2631 Gamma photons are produced by a strong ^{137}Cs source installed in the upstream part of the zone
 2632 inside a lead container. The source container includes a collimator, designed to irradiate a $6 \times 6 \text{ m}^2$
 2633 area at 5 m maximum to the source. A thin lens-shaped lead filter helps providing with a uniform
 2634 outcoming flux in a vertical plane, orthogonal to the beam direction. The principal collimator hole
 2635 provides a pyramidal aperture of $74^\circ \times 74^\circ$ solid angle and provides a photon flux in a pyramidal vol-

ume along the beam axis. The photon rate is controled by further lead filters allowing the maximum rate to be limited and to vary within a range of four orders of magnitude. Particle detectors under test are then placed within the pyramidal volume in front of the source, perpendicularly to the beam line in order to profit from the homogeneous photon flux. Adjusting the background flux of photons can then be done by using the filters and choosing the position of the detectors with respect to the source.

2641

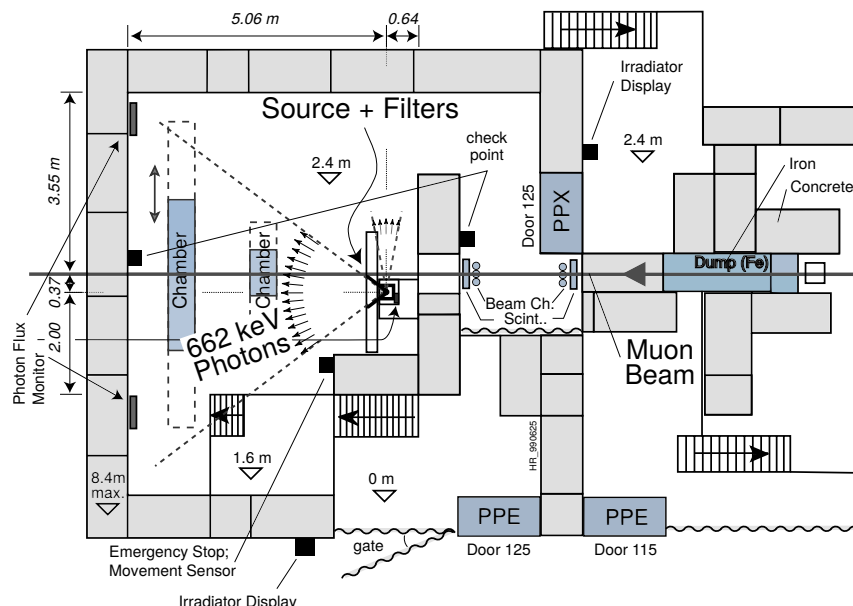


Figure 5.3: Layout of the test beam zone called X5c GIF at CERN. Photons from the radioactive source produce a sustained high rate of random hits over the whole area. The zone is surrounded by 8 m high and 80 cm thick concrete walls. Access is possible through three entry points. Two access doors for personnel and one large gate for material. A crane allows installation of heavy equipment in the area.

As described on Figure 5.4, the ^{137}Cs source emits a 662 keV photon in 85% of the decays. An activity of 740 GBq was measured on the 5th March 1997. To estimate the strength of the flux in 2014, it is necessary to consider the nuclear decay through time assiciated to the Cesium source whose half-life is well known ($t_{1/2} = (30.05 \pm 0.08)\text{y}$). The GIF tests where done in between the 20th and the 31st of August 2014, i.e. at a time $t = (17.47 \pm 0.02)\text{y}$ resulting in an attenuation of the activity from 740 GBq in 1997 to 494 GBq in 2014.

2648

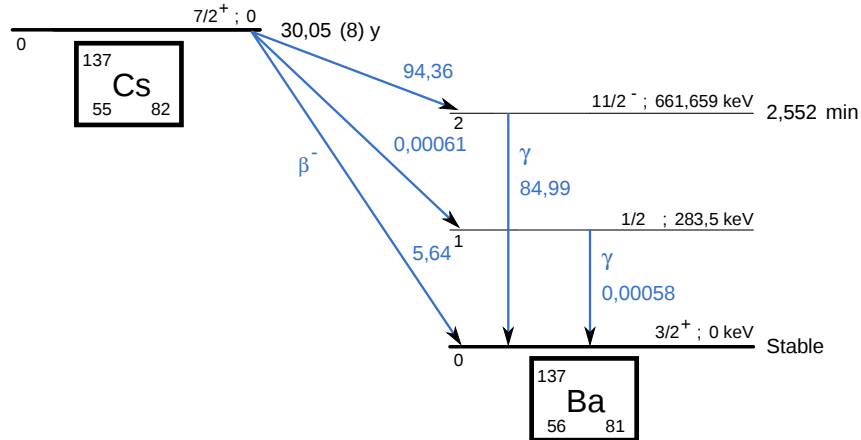


Figure 5.4: ^{137}Cs decays by β^- emission to the ground state of ^{137}Ba (BR = 5.64%) and via the 662 keV isomeric level of ^{137}Ba (BR = 94.36%) whose half-life is 2.55min.

5.1.1.2 GIF++

The new Gamma Irradiation Facility (GIF++), located in the SPS North Area at the downstream end of the H4 test beam, has replaced its predecessor during LS1 and has been operational since spring 2015 [87]. Like GIF, GIF++ features a ^{137}Cs source of 662 keV gamma photons, their fluence being controlled with a set of filters of various attenuation factors. The source provides two separated large irradiation areas for testing several full-size muon detectors with continuous homogeneous irradiation, as presented in Figure 5.5.

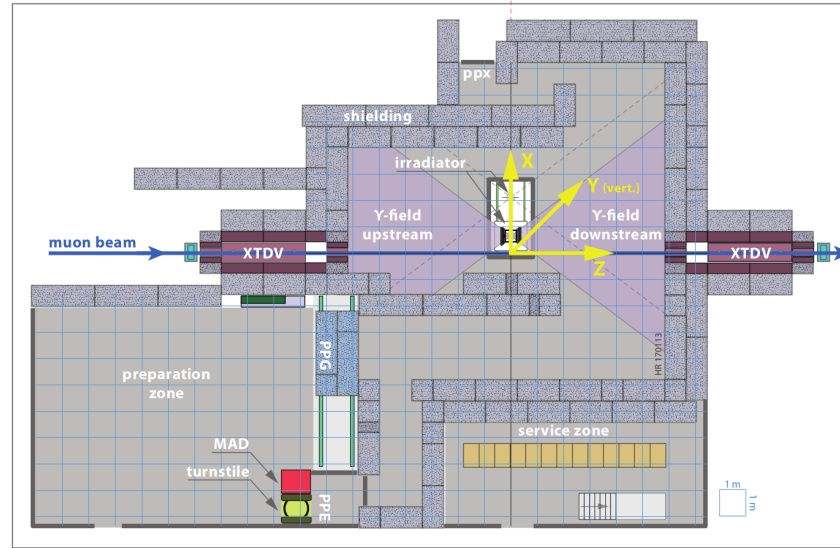


Figure 5.5: Floor plan of the GIF++ facility. When the facility downstream of the GIF++ takes electron beam, a beam pipe is installed along the beam line (z-axis). The irradiator can be displaced laterally (its center moves from $x = 0.65 \text{ m}$ to 2.15 m), to increase the distance to the beam pipe.

2657 The source activity was measured to be about 13.5 TBq in March 2016. The photon flux being
 2658 far greater than HL-LHC expectations, GIF++ provides an excellent facility for accelerated aging
 2659 tests of muon detectors.

2660

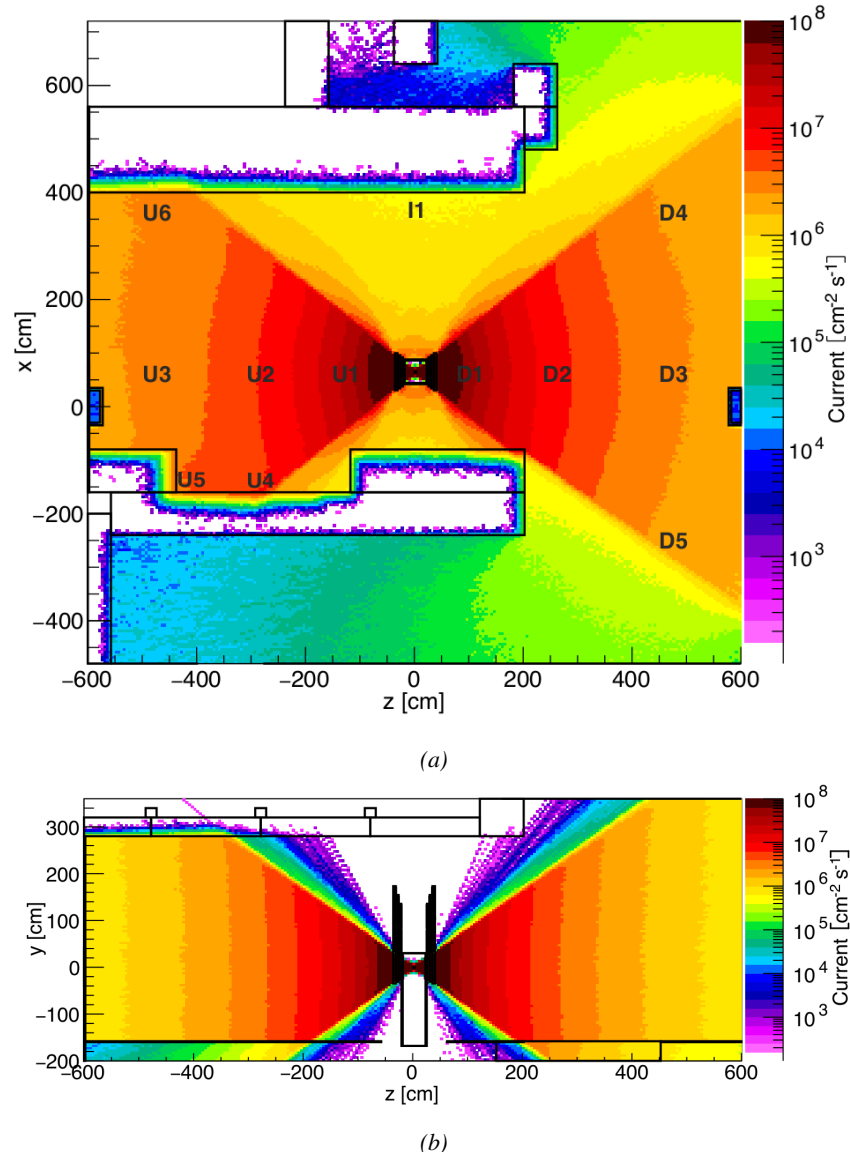


Figure 5.6: Simulated unattenuated current of photons in the xz plane (Figure 5.6a) and yz plane (Figure 5.6b) through the source at $x = 0.65 \text{ m}$ and $y = 0 \text{ m}$. With angular correction filters, the current of 662 keV photons is made uniform in xy planes.

2661 The source is situated in the muon beam line with the muon beam being available a few times a
 2662 year. The H4 beam, composed of muons with a momentum of about 150 GeV/c, passes through the
 2663 GIF++ zone and is used to study the performance of the detectors. Its flux is of 104 particles/ s cm^2

2664 focused in an area similar to $10 \times 10 \text{ cm}^2$. Therefore, with properly adjusted filters, one can imitate
 2665 the HL-LHC background and study the performance of muon detectors with their trigger/readout
 2666 electronics in HL-LHC environment.

2667

2668 5.2 Preliminary tests at GIF

2669 5.2.1 Resistive Plate Chamber test setup

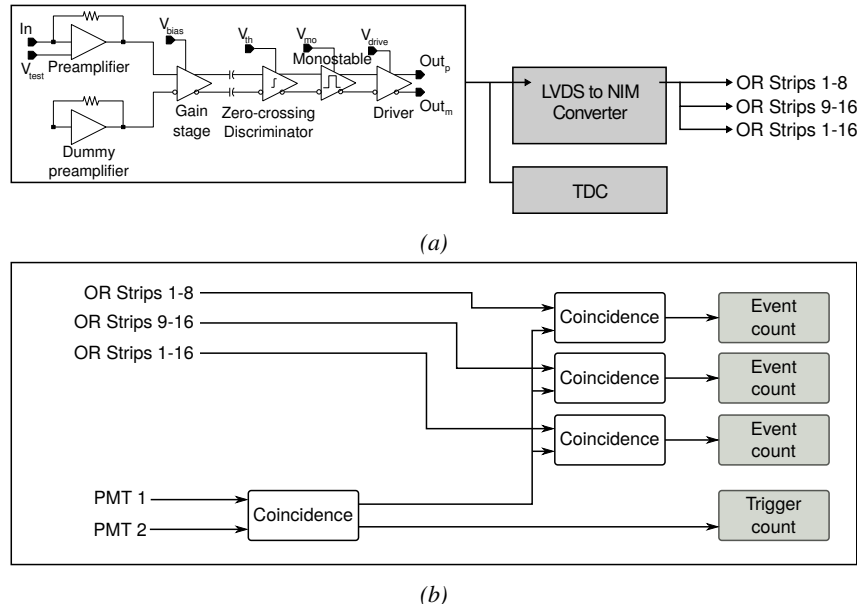


Figure 5.7: Signals from the RPC strips are shaped by the FEE described on Figure 5.7a. Output LVDS signals are then read-out by a TDC module connected to a computer or converted into NIM and sent to scalers. Figure 5.7b describes how these converted signals are put in coincidence with the trigger.

2670 During summer 2014, preliminary tests have been conducted in the GIF area on a newly produced
 2671 RE4/2 chamber labelled RE-4-2-BARC-161. This chamber has been placed into a trolley covered
 2672 with a tent. The position of the RPC inside the tent and of the tent related to the source is described
 2673 in Figure 5.8. To test this CMS RPC, three different absorber settings were used. First of all,
 2674 measurements were done with fully opened source. Then, to complete this preliminary study, the
 2675 gamma flux has been attenuated from a factor 2 and a factor 5. The expected gamma flux at the level
 2676 of our detector will be discussed in subsection ??.

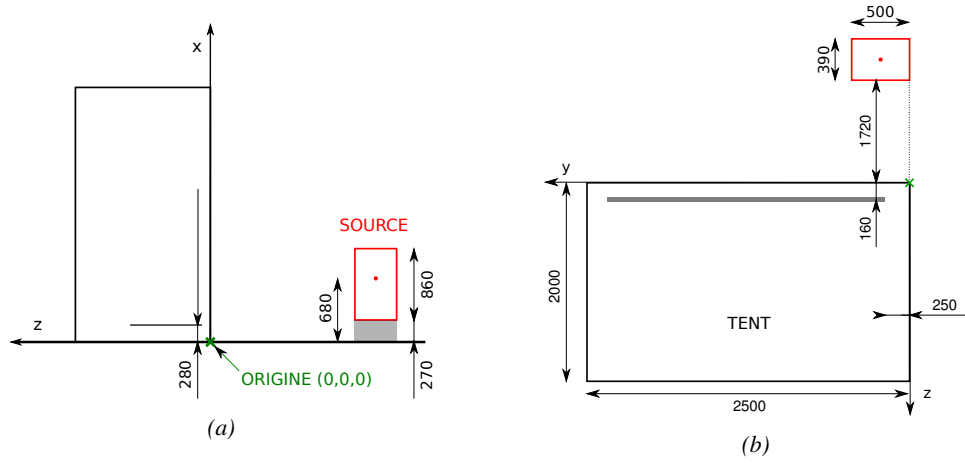


Figure 5.8: Description of the RPC setup. Dimensions are given in mm. A tent containing RPCs is placed at 1720 mm from the source container. The source is situated in the center of the container. RE-4-2-BARC-161 chamber is 160 mm inside the tent. This way, the distance between the source and the chambers plan is 2060 mm. Figure 5.8a provides a side view of the setup in the xz plane while Figure 5.8b shows a top view in the yz plane.



Figure 5.9: RE-4-2-BARC-161 chamber is inside the tent as described in Figure 5.8. In the top right, the two scintillators used as trigger can be seen. This trigger system has an inclination of 10° relative to horizontal and is placed above half-partition B2 of the RPCs. PMT electronics are shielded thanks to lead blocks placed in order to protect them without stopping photons from going through the scintillators and the chamber.

At the time of the tests, the beam not being operational anymore, a trigger composed of 2 plastic scintillators has been placed in front of the setup with an inclination of 10° with respect to the detector plane in order to look at cosmic muons. Using this particular trigger layout, shown on Figure 5.9, leads to a cosmic muon hit distribution into the chamber similar to the one in Figure 5.10.

2681 Measured without gamma irradiation, two peaks can be seen on the profil of partition B, centered on
 2682 strips 52 and 59. Section 5.2.3 will help us understand that these two peaks are due respectively to
 2683 forward and backward coming cosmic particles where forward coming particles are first detected by
 2684 the scintillators and then the RPC while the backward coming muons are first detected in the RPC.

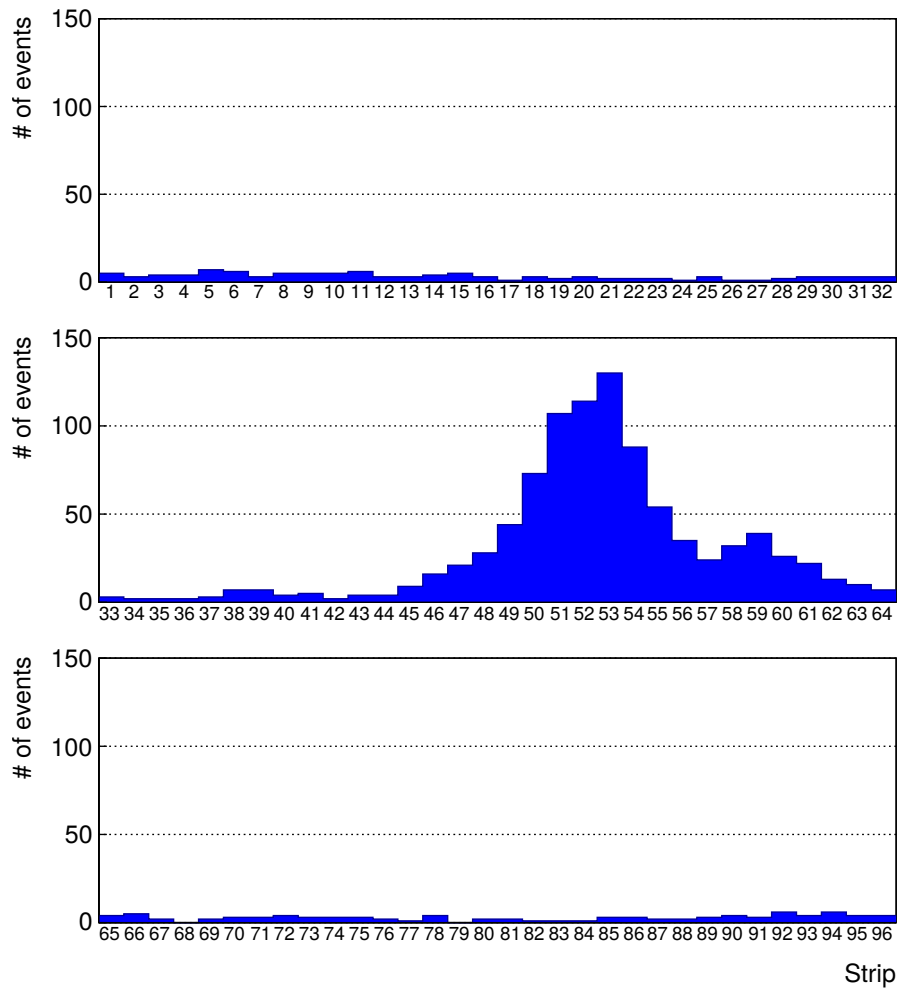


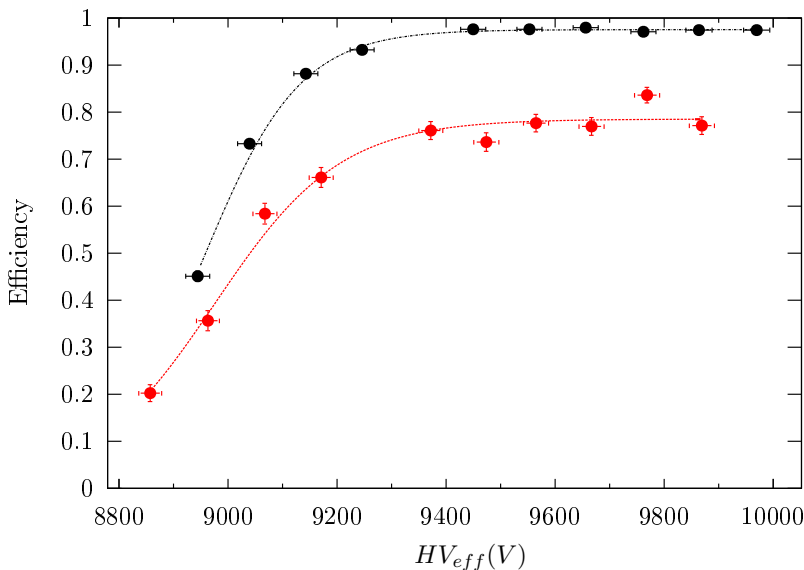
Figure 5.10: Hit distributions over all 3 partitions of RE-4-2-BARC-161 chamber is showed on these plots. Top, middle and bottom figures respectively correspond to partitions A, B, and C. These plots show that some events still occur in other half-partitions than B2, which corresponds to strips 49 to 64, in front of which the trigger is placed, contributing to the inefficiency of detection of cosmic muons. In the case of partitions A and C, the very low amount of data can be interpreted as noise. On the other hand, it is clear that a little portion of muons reach the half-partition B1, corresponding to strips 33 to 48.

2685 **5.2.2 Data Acquisition**

2686 **5.2.3 Geometrical acceptance of the setup layout to cosmic muons**

2687 In order to profit from a constant gamma irradiation, the detectors inside of the GIF bunker need
 2688 to be placed in a plane orthogonal to the beam line. The muon beam that used to be available was
 2689 meant to test the performance of detectors under test. This beam not being active anymore, another
 2690 solution to test detector performance had to be used. Thus, it has been decided to use cosmic muons
 2691 detected through a telescope composed of two scintillators. Lead blocks were used as shielding to
 2692 protect the photomultipliers from gammas as can be seen from Figure 5.9.

2693 An inclination has been given to the cosmic telescope to maximize the muon flux. A good com-
 2694 promise had to be found between good enough muon flux and narrow enough hit distribution to
 2695 be sure to contain all the events into only one half partitions as required from the limited available
 2696 readout hardware. Nevertheless, a consequence of the misplaced trigger, that can be seen as a loss
 2697 of events in half-partition B1 in Figure 5.10, is an inefficiency. Nevertheless, the inefficiency of ap-
 2698 proximately 20% highlighted in Figure 5.11 by comparing the performance of chamber BARC-161
 2699 in 904 and at GIF without irradiation seems too important to be explained only by the geometri-
 2700 cal acceptance of the setup itself. Simulations have been conducted to show how the setup brings
 2701 inefficiency.



2702 *Figure 5.11: Results are derived from data taken on half-partition B2 only. On the 18th of June 2014, data
 2703 has been taken on chamber RE-2-BARC-161 at building 904 (Preressin Site) with cosmic muons providing us a
 2704 reference efficiency plateau of $(97.54 \pm 0.15)\%$ represented by a black curve. A similar measurement has been
 2705 done at GIF on the 21st of July with the same chamber giving a plateau of $(78.52 \pm 0.94)\%$ represented by a
 2706 red curve.*

2707 **5.2.3.1 Description of the simulation layout**

2708 The layout of GIF setup has been reproduced and incorporated into a Monte Carlo (MC) simulation
 2709 to study the influence of the disposition of the telescope on the final distribution measured by the

2705 RPC. A 3D view of the simulated layout is given into Figure 5.12. Muons are generated randomly
 2706 in a horizontal plane located at a height corresponding to the lowest point of the PMTs. This way,
 2707 the needed size of the plane in order to simulate events happening at very big azimuthal angles (i.e.
 2708 $\theta \approx \pi$) can be kept relatively small. The muon flux is designed to follow the usual $\cos^2\theta$ distribution
 2709 for cosmic particle. The goal of the simulation is to look at muons that pass through the muon
 2710 telescope composed of the two scintillators and define their distribution onto the RPC plane. During
 2711 the reconstruction, the RPC plane is then divided into its strips and each muon track is assigned to a
 2712 strip.

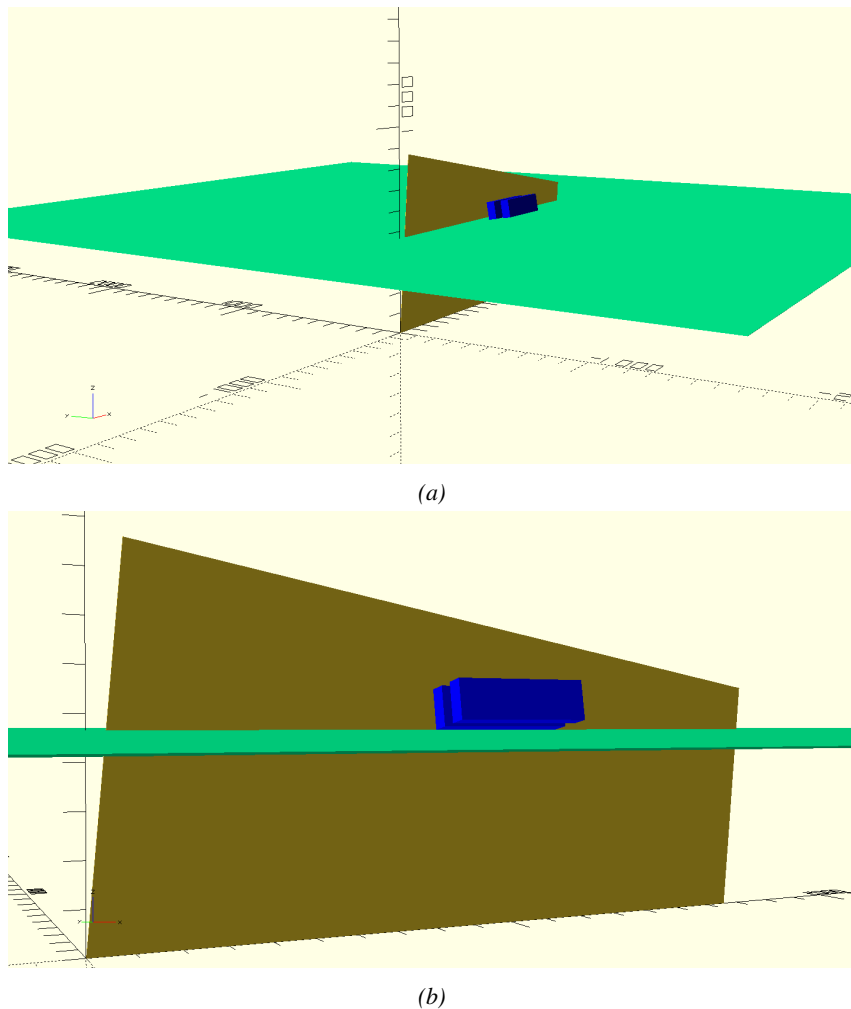


Figure 5.12: Representation of the layout used for the simulations of the test setup. The RPC is represented as a yellow trapezoid while the two scintillators as blue cuboids looking at the sky. A green plane corresponds to the muon generation plane within the simulation. Figure 5.8a shows a global view of the simulated setup. Figure 5.8b shows a zoomed view that allows to see the 2 scintillators as well as the full RPC plane.

2713 In order to further refine the quality of the simulation and understand deeper the results the
 2714 dependance of the distribution has been studied for a range of telescope inclinations. Moreover,
 2715 the threshold applied on the PMT signals has been included into the simulation in the form of a

2716 cut. In the approximation of uniform scintillators, it has been considered that the threshold can be
 2717 understood as the minimum distance particles need to travel through the scintillating material to give
 2718 a strong enough signal. Particles that travel a distance smaller than the set "threshold" are thus not
 2719 detected by the telescope and cannot trigger the data taking. Finally, the FEE threshold also has
 2720 been considered in a similar way. The mean momentum of horizontal cosmic rays is higher than
 2721 those of vertical ones but the stopping power of matter for momenta ranging from 1 GeV to 1 TeV
 2722 stays comparable. It is then possible to assume that the mean number of primary e^- /ion pairs per
 2723 unit length will stay similar and thus, depending on the applied discriminator threshold, muons with
 2724 the shortest path through the gas volume will deposit less charge and induce a smaller signal on the
 2725 pick-up strips that could eventually not be detected. These two thresholds also restrain the overall
 2726 geometrical acceptance of the system.

2727 5.2.3.2 Simulation procedure

2728 The simulation software has been designed using C++ and the output data is saved into ROOT
 2729 histograms. Simulations start for a threshold T_{scint} varying in a range from 0 to 45 mm in steps
 2730 of 5 mm, where $T_{scint} = 0$ mm corresponds to the case where there isn't any threshold apply on
 2731 the input signal while $T_{scint} = 45$ mm, which is the scintillator thickness, is the case where muons
 2732 cannot arrive orthogonally onto the scintillator surface. For a given T_{scint} , a set of RPC thresholds
 2733 are considered. The RPC threshold, T_{RPC} varies from 2 mm, the thickness of the gas volume, to
 2734 3 mm in steps of 0.25 mm. For each $(T_{scint}; T_{RPC})$ pair, $N_\mu = 10^8$ muons are randomly generated
 2735 inside the muon plane described in the previous paragraph with an azimuthal angle θ chosen to follow
 2736 a $\cos^2\theta$ distribution.

2737 Planes are associated to each surface of the scintillators. Knowing muon position into the muon
 2738 plane and its direction allows us, by assuming that muons travel in a straight line, to compute the
 2739 intersection of the muon track with these planes. Applying conditions to the limits of the surfaces
 2740 of the scintillator faces then gives us an answer to whether or not the muon passed through the
 2741 scintillators. In the case the muon has indeed passed through the telescope, the path through each
 2742 scintillator is computed and muons whose path was shorter than T_{scint} are rejected and are thus
 2743 considered as having not interacted with the setup.

2744 On the contrary, if the muon is labeled as good, its position within the RPC plane is computed
 2745 and the corresponding strip, determined by geometrical tests in the case the distance through the
 2746 gas volume was enough not to be rejected because of T_{RPC} , gets a hit and several histograms
 2747 are filled in order to keep track of the generation point on the muon plane, the intersection points
 2748 of the reconstructed muons within the telescope, or on the RPC plane, the path traveled through
 2749 each individual scintillator or the gas volume, as well as other histograms. Moreover, muons fill
 2750 different histograms whether they are forward or backward coming muons. They are discriminated
 2751 according to their direction components. When a muon is generated, an (x, y, z) position is assigned
 2752 into the muon plane as well as a $(\theta; \phi)$ pair that gives us the direction it's coming from. This way,
 2753 muons satisfying the condition $0 \leq \phi < \pi$ are designated as backward coming muons while muons
 2754 satisfying $\pi \leq \phi < 2\pi$ as forward coming muons.

2755 This simulation is then repeated for different telescope inclinations ranging in between 4 and 20°
 2756 and varying in steps of 2° . Due to this inclination and to the vertical position of the detector under
 2757 test, the muon distribution reconstructed in the detector plane is asymmetrical. The choice has been
 2758 made to chose a skew distribution formula to fit the data built as the multiplication of gaussian and
 2759 sigmoidal curves together. A typical gaussian formula is given as 5.1 and has three free parameters

2760 as A_g , its amplitude, \bar{x} , its mean value and σ , its root mean square. Sigmoidal curves as given by
 2761 formula 5.2 are functions converging to 0 and A_s as x diverges. The inflection point is given as x_i
 2762 and λ is proportional to the slope at $x = x_i$. In the limit where $\lambda \rightarrow \infty$, the sigmoid becomes a
 2763 step function.

$$g(x) = A_g e^{\frac{-(x-\bar{x})^2}{2\sigma^2}} \quad (5.1)$$

$$s(x) = \frac{A_s}{1 + e^{-\lambda(x-x_i)}} \quad (5.2)$$

2764 Finally, a possible representation of a skew distribution is given by formula 5.3 and is the product
 2765 of 5.1 and 5.2. Naturally, here $A_{sk} = A_g \times A_s$ and represents the theoretical maximum in the limit
 2766 where the skew tends to a gaussian function.

$$sk(x) = g(x) \times s(x) = A_{sk} \frac{e^{\frac{-(x-\bar{x})^2}{2\sigma^2}}}{1 + e^{-\lambda(x-x_i)}} \quad (5.3)$$

2767 5.2.3.3 Results

2768 Influence of T_{scint} on the muon distribution

2769 Influence of T_{RPC} on the muon distribution

2770 Influence of the telescope inclination on the muon distribution

2771 Comparison to data taken at GIF without irradiation

2772 5.2.4 Photon flux at GIF

2773 5.2.4.1 Expectations from simulations

2774 In order to understand and evaluate the γ flux in the GIF area, simulations had been conducted in
 2775 1999 and published by S. Agosteo et al [86]. Table 5.1 presented in this article gives us the γ flux
 2776 for different distances D to the source. This simulation was done using GEANT and a Monte Carlo
 2777 N-Particle (MCNP) transport code, and the flux F is given in number of γ per unit area and unit time
 2778 along with the estimated error from these packages expressed in %.

Nominal ABS	Photon flux F [$\text{cm}^{-2}\text{s}^{-1}$]			
	at $D = 50 \text{ cm}$	at $D = 155 \text{ cm}$	at $D = 300 \text{ cm}$	at $D = 400 \text{ cm}$
1	$0.12 \times 10^8 \pm 0.2\%$	$0.14 \times 10^7 \pm 0.5\%$	$0.45 \times 10^6 \pm 0.5\%$	$0.28 \times 10^6 \pm 0.5\%$
2	$0.68 \times 10^7 \pm 0.3\%$	$0.80 \times 10^6 \pm 0.8\%$	$0.25 \times 10^6 \pm 0.8\%$	$0.16 \times 10^6 \pm 0.6\%$
5	$0.31 \times 10^7 \pm 0.4\%$	$0.36 \times 10^6 \pm 1.2\%$	$0.11 \times 10^6 \pm 1.2\%$	$0.70 \times 10^5 \pm 0.9\%$

Table 5.1: Total photon flux ($E\gamma \leq 662 \text{ keV}$) with statistical error predicted considering a ^{137}Cs activity of 740 GBq at different values of the distance D to the source along the x -axis of irradiation field [86].

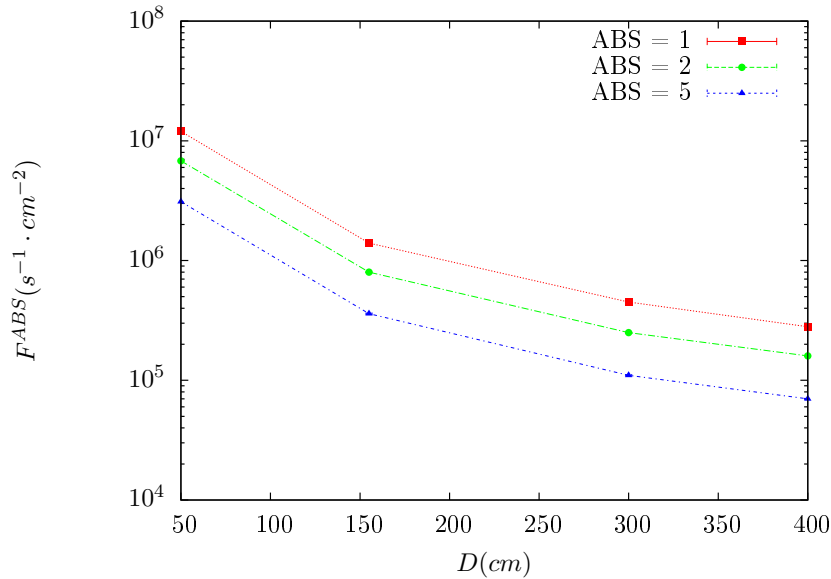


Figure 5.13: γ flux $F(D)$ is plot using values from table 5.1. As expected, the plot shows similar attenuation behaviours with increasing distance for each absorption factors.

The simulation doesn't directly provides us with an estimated flux at the level of our RPC. First of all, it is needed to extract the value of the flux from the available data contained in the original paper and then to estimate the flux in 2014 at the time the experimentation took place. Figure 5.13 that contains the data from Table 5.1. In the case of a pointlike source emitting isotropic and homogeneous gamma radiations, the gamma flux F at a distance D to the source with respect to a reference point situated at D_0 where a known flux F_0 is measured will be expressed like in Equation 5.4, assuming that the flux decreases as $1/D^2$, where c is a fitting factor.

$$F^{ABS} = F_0^{ABS} \times \left(\frac{cD_0}{D} \right)^2 \quad (5.4)$$

By rewriting Equation 5.4, it comes that :

$$c = \frac{D}{D_0} \sqrt{\frac{F^{ABS}}{F_0^{ABS}}} \quad (5.5)$$

$$\Delta c = \frac{c}{2} \left(\frac{\Delta F^{ABS}}{F^{ABS}} + \frac{\Delta F_0^{ABS}}{F_0^{ABS}} \right) \quad (5.6)$$

Finally, using Equation 5.5 and the data in Table 5.1 with $D_0 = 50$ cm as reference point, we can build Table 5.2. It is interesting to note that c for each value of D doesn't depend on the absorption factor.

Nominal ABS	Correction factor c		
	at $D = 155$ cm	at $D = 300$ cm	at $D = 400$ cm
1	$1.059 \pm 0.70\%$	$1.162 \pm 0.70\%$	$1.222 \pm 0.70\%$
2	$1.063 \pm 1.10\%$	$1.150 \pm 1.10\%$	$1.227 \pm 0.90\%$
5	$1.056 \pm 1.60\%$	$1.130 \pm 1.60\%$	$1.202 \pm 1.30\%$

Table 5.2: Correction factor c is computed thanks to formulae 5.5 taking as reference $D_0 = 50$ cm and the associated flux F_0^{ABS} for each absorption factor available in table 5.1.

For the range of D/D_0 values available, it is possible to use a simple linear fit to get the evolution of c . The linear fit will then use only 2 free parameters, a and b , as written in Equation 5.7. This gives us the results showed in Figure 5.14. Figure 5.14b confirms that using only a linear fit to extract c is enough as the evolution of the rate that can be obtained superimposes well on the simulation points.

$$c \left(\frac{D}{D_0} \right) = a \frac{D}{D_0} + b \quad (5.7)$$

$$F^{ABS} = F_0^{ABS} \left(a + \frac{b D_0}{D} \right)^2 \quad (5.8)$$

$$\Delta F^{ABS} = F^{ABS} \left[\frac{\Delta F_0^{ABS}}{F_0^{ABS}} + 2 \frac{\Delta a + \Delta b \frac{D_0}{D}}{a + \frac{b D_0}{D}} \right] \quad (5.9)$$

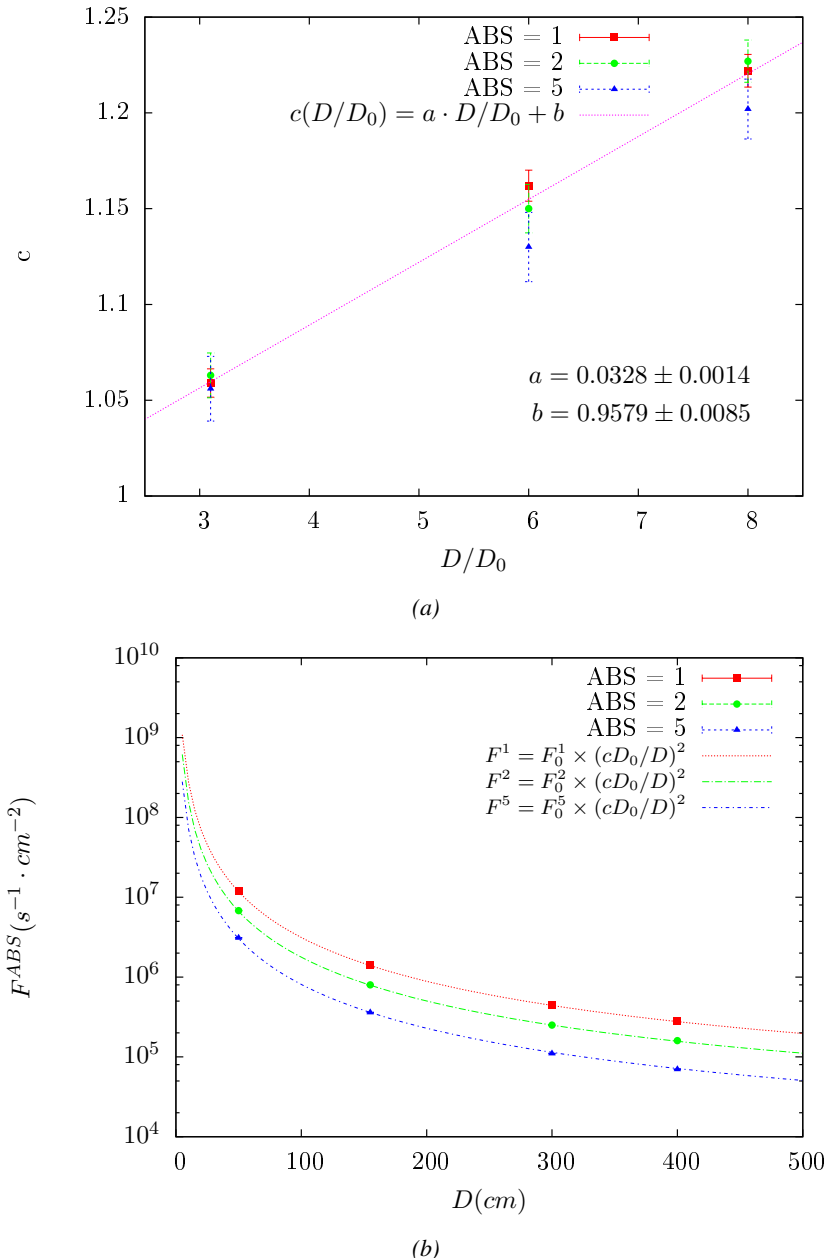


Figure 5.14: Figure 5.14a shows the linear approximation fit done via formulae 5.7 on data from table 5.2. Figure 5.14b shows a comparison of this model with the simulated flux using a and b given in figure 5.14a in formulae 5.4 and the reference value $D_0 = 50$ cm and the associated flux for each absorption factor F_0^{ABS} from table 5.1

In the case of the 2014 GIF tests, the RPC plane is located at a distance $D = 206$ cm to the source. Moreover, to estimate the strength of the flux in 2014, it is necessary to consider the nuclear decay through time associated to the Cesium source whose half-life is well known ($t_{1/2} = (30.05 \pm 0.08)$ y). The very first source activity measurement has been done on the 5th of March 1997 while the GIF

2794 In the case of the 2014 GIF tests, the RPC plane is located at a distance $D = 206$ cm to the source.

2795 Moreover, to estimate the strength of the flux in 2014, it is necessary to consider the nuclear decay

2796 through time associated to the Cesium source whose half-life is well known ($t_{1/2} = (30.05 \pm 0.08)$ y).

2797 The very first source activity measurement has been done on the 5th of March 1997 while the GIF

2798 tests where done in between the 20th and the 31th of August 2014, i.e. at a time $t = (17.47 \pm 0.02)$ y
 2799 resulting in an attenuation of the activity from 740 GBq in 1997 to 494 GBq in 2014. All the needed
 2800 information to extrapolate the flux through our detector in 2014 has now been assembled, leading
 2801 to the Table 5.3. It is interesting to note that for a common RPC sensitivity to γ of 2×10^{-3} , the
 2802 order of magnitude of the estimated hit rate per unit area is of the order of the kHz for the fully
 2803 opened source. Moreover, taking profit of the two working absorbers, it will be possible to scan
 2804 background rates at 0 Hz, ~ 300 Hz as well as ~ 600 Hz. Without source, a good estimate of the
 2805 intrinsic performance will be available. Then at 300 Hz, the goal will be to show that the detectors
 2806 fulfill the performance certification of CMS RPCs. Then a first idea of the performance of the
 2807 detectors at higher background will be provided with absorption factors 2 (~ 600 Hz) and 1 (no
 2808 absorption). *[Here I will also put a reference to the plot showing the estimated background rate at
 2809 the level of RE3/1 in the case of HL-LHC but this one being in another chapter, I will do it later.]*

Nominal ABS	Photon flux F [cm $^{-2}$ s $^{-1}$]			Hit rate/unit area [Hzcm $^{-2}$] at $D^{2014} = 206$ cm
	at $D_0^{1997} = 50$ cm	at $D^{1997} = 206$ cm	at $D^{2014} = 206$ cm	
1	$0.12 \times 10^8 \pm 0.2\%$	$0.84 \times 10^6 \pm 0.3\%$	$0.56 \times 10^6 \pm 0.3\%$	1129 ± 32
2	$0.68 \times 10^7 \pm 0.3\%$	$0.48 \times 10^6 \pm 0.3\%$	$0.32 \times 10^6 \pm 0.3\%$	640 ± 19
5	$0.31 \times 10^7 \pm 0.4\%$	$0.22 \times 10^6 \pm 0.3\%$	$0.15 \times 10^6 \pm 0.3\%$	292 ± 9

Table 5.3: The data at D_0 in 1997 is taken from [86]. In a second step, using Equations 5.8 and 5.9, the flux at D can be estimated in 1997. Then, taking into account the attenuation of the source activity, the flux at D can be estimated at the time of the tests in GIF in 2014. Finally, assuming a sensitivity of the RPC to γ $s = 2 \times 10^{-3}$, an estimation of the hit rate per unit area is obtained.

2810 5.2.4.2 Dose measurements

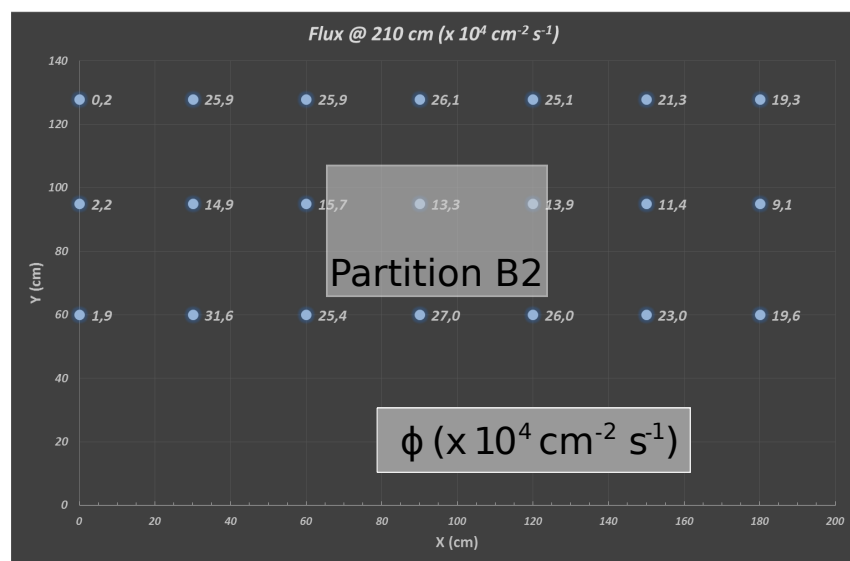


Figure 5.15: Dose measurements has been done in a plane corresponding to the tents front side. This plan is 1900 mm away from the source. As explained in the first chapter, a lens-shaped lead filter provides a uniform photon flux in the vertical plan orthogonal to the beam direction. If the second line of measured fluxes is not taken into account because of lower values due to experimental equipments in the way between the source and the tent, the uniformity of the flux is well showed by the results.

2811 **5.2.5 Results and discussions**

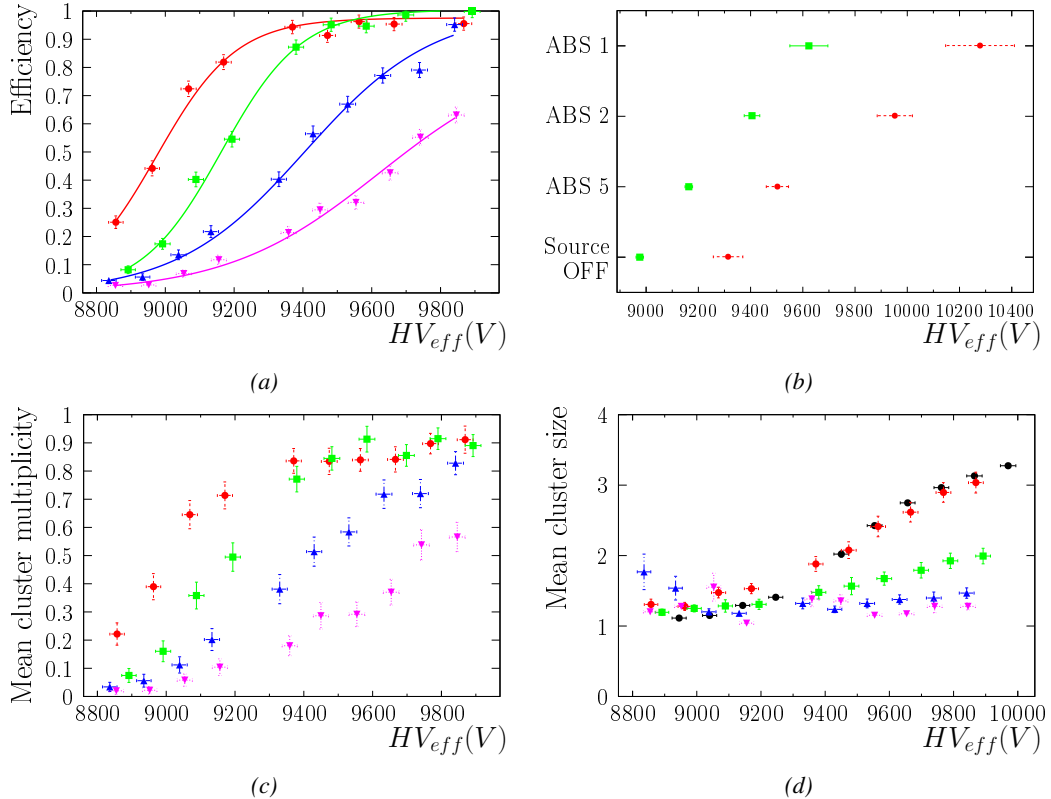


Figure 5.16

2812 **5.3 Longevity tests at GIF++**

2813 Longevity studies imply a monitoring of the performance of the detectors probed using a high inten-
 2814 sity muon beam in a irradiated environment by periodically measuring their rate capability, the dark
 2815 current running through them and the bulk resistivity of the Bakelite composing their electrodes.
 2816 GIF++, with its very intense ^{137}Cs source, provides the perfect environment to perform such kind
 2817 of tests. Assuming a maximum acceleration factor of 3, it is expected to accumulate the equivalent
 2818 charge in 1.7 years.

2819 As the maximum background is found in the endcap, the choice naturally was made to focus the
 2820 GIF++ longevity studies on endcap chambers. Most of the RPC system was installed in 2007. Nev-
 2821 ertheless, the large chambers in the fourth endcap (RE4/2 and RE4/3) have been installed during
 2822 LS1 in 2014. The Bakelite of these two different productions having different properties, four spare
 2823 chambers of the present system were selected, two RE2,3/2 spares and two RE4/2 spares. Having
 2824 two chambers of each type allows to always keep one of them non irradiated as reference, the per-
 2825 formance evolution of the irradiated chamber being then compared through time to the performance
 2826 of the non irradiated one.

2827 The performance of the detectors under different level of irradiation is measured periodically dur-

ing dedicated test beam periods using the H4 muon beam. In between these test beam periods, the two RE2,3/2 and RE4/2 chambers selected for this study are irradiated by the ^{137}Cs source in order to accumulate charge and the gamma background is monitored, as well as the currents. The two remaining chambers are kept non-irradiated as reference detectors. Due to the limited gas flow in GIF++, the RE4 chamber remained non-irradiated until end of November 2016 where a new mass flow controller has been installed allowing for bigger volumes of gas to flow in the system.

Figures 5.17 and 5.18 give us for different test beam periods, and thus for increasing integrated charge through time, a comparison of the maximum efficiency, obtained using a sigmoid-like function, and of the working point of both irradiated and non irradiated chambers [55]. No aging is yet to see from this data, the shifts in γ rate per unit area in between irradiated and non irradiated detectors and RE2 and RE4 types being easily explained by a difference of sensitivity due to the various Bakelite resistivities of the HPL electrodes used for the electrode production.

Collecting performance data at each test beam period allows us to extrapolate the maximum efficiency for a background hit rate of $300\text{ s}^{-1}\text{cm}^{-2}$ corresponding to the expected HL-LHC conditions. Aging effects could emerge from a loss of efficiency with increasing integrated charge over time, thus Figure 5.19 helps us understand such degradation of the performance of irradiated detectors in comparison with non irradiated ones. The final answer for an eventual loss of efficiency is given in Figure 5.20 by comparing for both irradiated and non irradiated detectors the efficiency sigmoids before and after the longevity study. Moreover, to complete the performance information, the Bakelite resistivity is regularly measured thanks to Ag scans (Figure 5.21) and the noise rate is monitored weekly during irradiation periods (Figure 5.22). At the end of 2016, no signs of aging were observed and further investigation is needed to get closer to the final integrated charge requirements proposed for the longevity study of the present CMS RPC sub-system.

2851

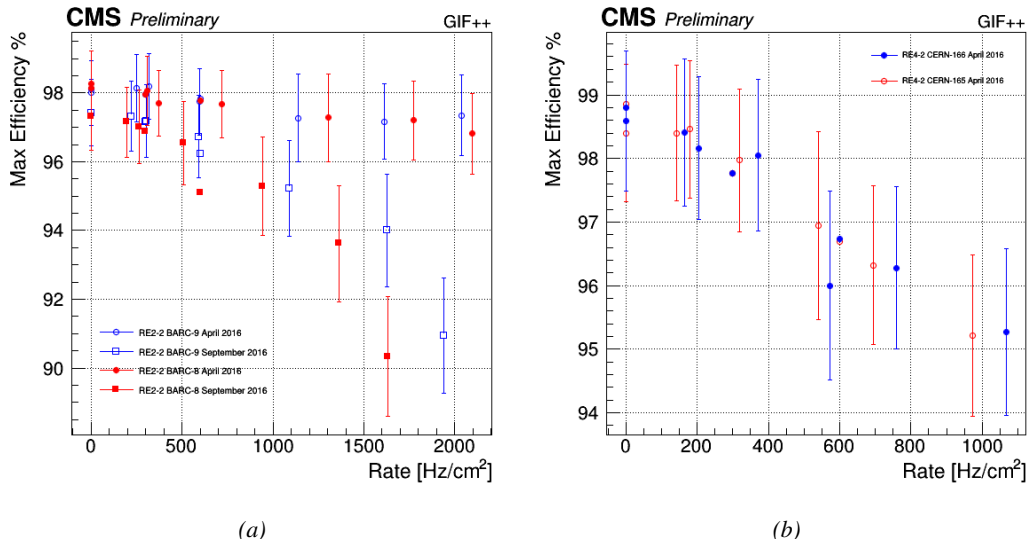


Figure 5.17: Evolution of the maximum efficiency for RE2 (5.17a) and RE4 (5.17b) chambers with increasing extrapolated γ rate per unit area at working point. Both irradiated (blue) and non irradiated (red) chambers are shown.

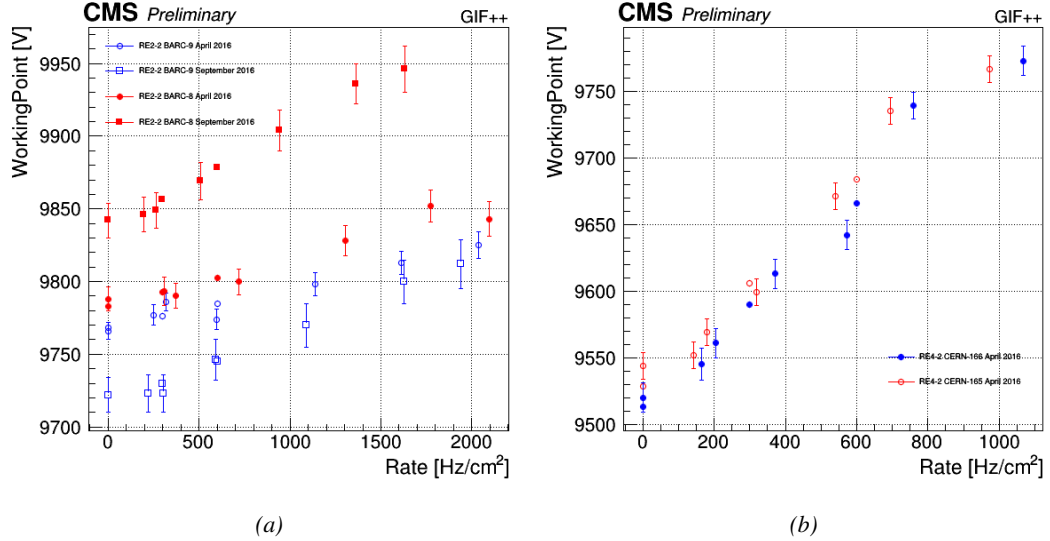


Figure 5.18: Evolution of the working point for RE2 (5.18a) and RE4 (5.18b) with increasing extrapolated γ rate per unit area at working point. Both irradiated (blue) and non irradiated (red) chambers are shown.

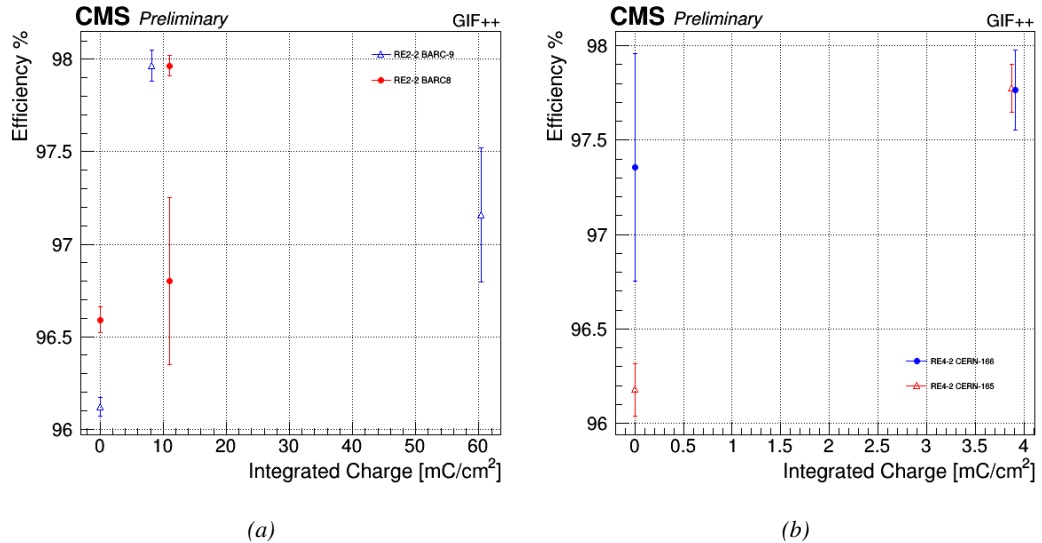


Figure 5.19: Evolution of the maximum efficiency at HL-LHC conditions, i.e. a background hit rate per unit area of 300 Hz/cm², with increasing integrated charge for RE2 (5.19a) and RE4 (5.19b) detectors. Both irradiated (blue) and non irradiated (red) chambers are shown. The integrated charge for non irradiated detectors is recorded during test beam periods and stays small with respect to the charge accumulated in irradiated chambers.

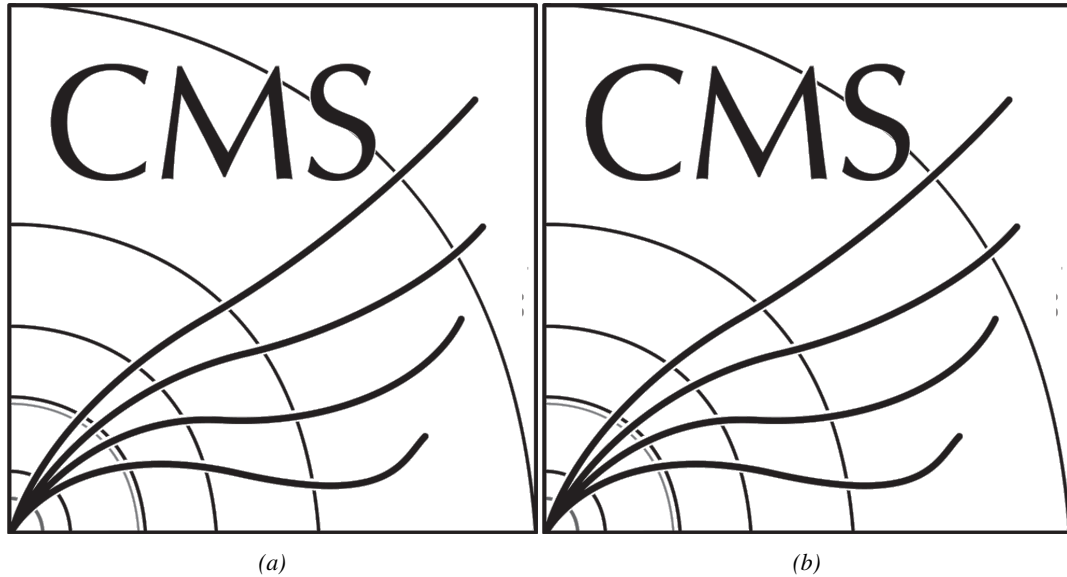


Figure 5.20: Comparison of the efficiency sigmoid before (triangles) and after (circles) irradiation for RE2 (5.20a) and RE4 (5.20b) detectors. Both irradiated (blue) and non irradiated (red) chambers are shown.

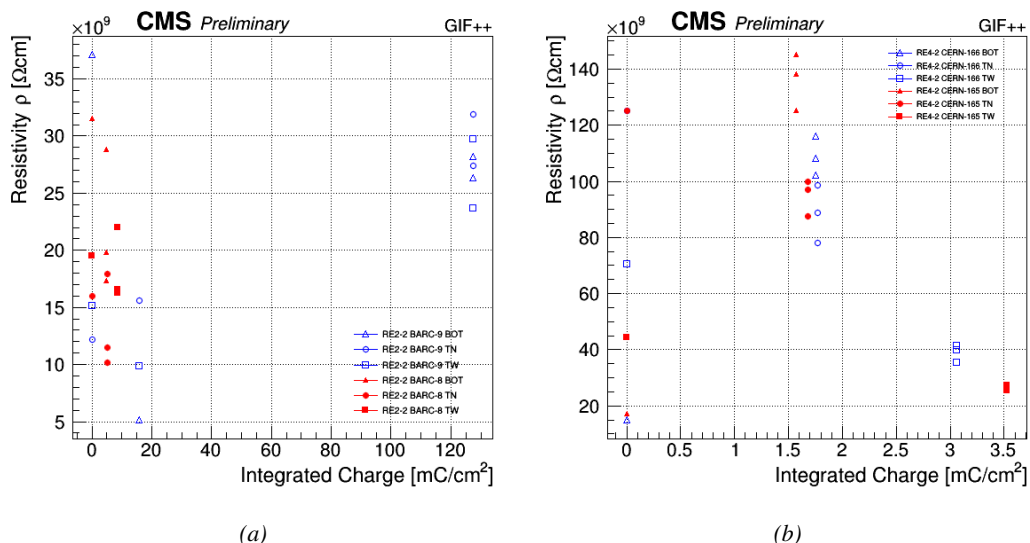


Figure 5.21: Evolution of the Bakelite resistivity for RE2 (5.21a) and RE4 (5.21b) detectors. Both irradiated (blue) and non irradiated (red) chambers are shown.

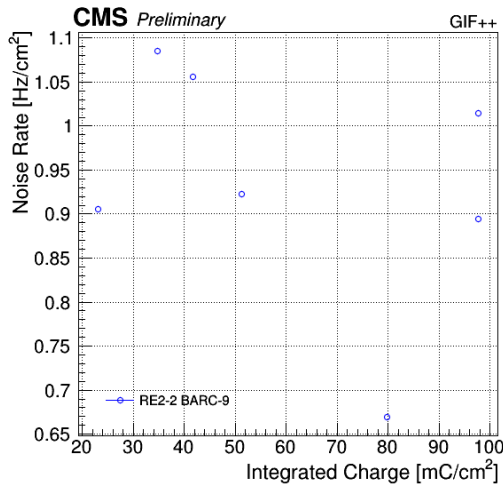


Figure 5.22: Evolution of the noise rate per unit area for the irradiated chamber RE2-2-BARC-9 only.

2852 5.3.1 Description of the Data Acquisition

2853 For the longevity studies, four spare chambers of the present system are used. Two spare RPCs of
 2854 the RE2,3 stations as well as two spare RPCs from the new RE4 stations have been mounted in a
 2855 Trolley. Six RE4 gaps are also placed in the trolley. The trolley is placed inside the GIF++ in the
 2856 upstream region of the bunker, taking the cesium source as a reference. The trolley is oriented for
 2857 the detection surface of the chambers to be orthogonal to the beam line. The system can be moved
 2858 along the orthogonal plane in order to have the beam in all η -partitions. For the aging the trolley is
 2859 moved outside the beam line and is placed in a distance of 5.2 m to the source, which irradiates the
 2860 bunker using an attenuation filter of 2.2 which corresponds to a fluence of 10^7 gamma/cm².

2861 During GIF++ operation, the data collected can be divided into different categories as several
 2862 parameters are monitored in addition to the usual RPC performance data. On one hand, to know
 2863 the performance of a chamber, it is need to measure its efficiency and to know the background
 2864 conditions in which it is operated. To do this, the hit signals from the chamber are recorded and
 2865 stored in a ROOT file via a DAQ software. On the other hand, it is also very important to monitor
 2866 parameters such as environmental pressure and temperature, gas temperature and humidity, RPC
 2867 HV, LV, and currents, or even source and beam status. This is done through the GIF++ web DCS
 2868 that stores this information in a database.

2869 Two different types of tests are conducted on RPCs via the DAQ. Indeed, the performance of the
 2870 detectors is measured periodically during dedicated test beam periods using the H4 muon beam. In
 2871 between these test beam periods, when the beam is not available, the chambers are irradiated by the
 2872 ^{137}Cs in order to accumulate deposited charge and the gamma background is measured.

2873 RPCs under test are connected through LVDS cables to V1190A TDC modules manufactured by
 2874 CAEN. These modules, located in the rack area outside of the bunker, get the logic signals sent by
 2875 the chambers and save them into their buffers. Due to the limited size of the buffers, the collected
 2876 data is regularly erased and replaced. A trigger signal is needed for the TDC modules to send the
 2877 useful data to the DAQ computer via a V1718 CAEN USB communication module.

2878 In the case of performance test, the trigger signal used for data acquisition is generated by the

2879 coincidence of three scintillators. A first one is placed upstream outside of the bunker, a second one
 2880 is placed downstream outside of the bunker, while a third one is placed in front of the trolley, close by
 2881 the chambers. Every time a trigger is sent to the TDCs, i.e. every time a muon is detected, knowing
 2882 the time delay in between the trigger and the RPC signals, signals located in the right time window
 2883 are extracted from the buffers and saved for later analysis. Signals are taken in a time window of
 2884 400 ns centered on the muon peak (here we could show a time spectrum). On the other hand, in the
 2885 case of background rate measurement, the trigger signal needs to be "random" not to measure muons
 2886 but to look at gamma background. A trigger pulse is continuously generated at a rate of 300 Hz using
 2887 a dual timer. To integrate an as great as possible time, all signals contained within a time window of
 2888 10us prior to the random trigger signal are extracted form the buffers and saved for further analysis
 2889 (here another time spectrum to illustrate could be useful, maybe even place both spectrum together
 2890 as a single Figure).

2891 The signals sent to the TDCs correspond to hit collections in the RPCs. When a particle hits
 2892 a RPC, it induce a signal in the pickup strips of the RPC readout. If this signal is higher than the
 2893 detection threshold, a LVDS signal is sent to the TDCs. The data is then organised into 4 branches
 2894 keeping track of the event number, the hit multiplicity for the whole setup, and the time and channel
 2895 profile of the hits in the TDCs.

2896 **5.3.2 RPC current, environmental and operation parameter monitoring**

2897 In order to take into account the variation of pressure and temperature between different data taking
 2898 periods the applied voltage is corrected following the relationship :

$$2899 HV_{eff} = HV_{app} \times \left(0.2 + 0.8 \cdot \frac{P_0}{P} \times \frac{T}{T_0} \right) \quad (5.10)$$

where T_0 (=293 K) and P_0 (=990 mbar) are the reference values.

2900 **5.3.3 Measurement procedure**

2901 Insert a short description of the online tools (DAQ, DCS, DQM).

2902 Insert a short description of the offline tools : tracking and efficiency algorithm.

2903 Identify long term aging effects we are monitoring the rates per strip.

2904 **5.3.4 Longevity studies results**

6

2905

2906

Conclusions and outlooks

2907 **6.1 Conclusions**

2908 **6.2 Outlooks**

A

2909

2910

A data acquisition software for CAEN VME TDCs

2911

2912 Certifying detectors in the perspective of HL-LHC required to develop tools for the GIF++ expe-
2913 riment. Among them was the C++ Data Acquisition (DAQ) software that allows to make the com-
2914 munications in between a computer and TDC modules in order to retrieve the RPC data [88]. In this
2915 appendix, details about this software, as of how the software was written, how it functions and how
2916 it can be exported to another similar setup, will be given.

2917 A.1 GIF++ DAQ file tree

2918 GIF++ DAQ source code is fully available on github at [https://github.com/afagot/GIF_](https://github.com/afagot/GIF_DAQ)
2919 DAQ. The software requires 3 non-optional dependencies:

- 2920 • CAEN USB Driver, to mount the VME hardware,
2921 • CAEN VME Library, to communicate with the VME hardware, and
2922 • ROOT, to organize the collected data into a TTree.

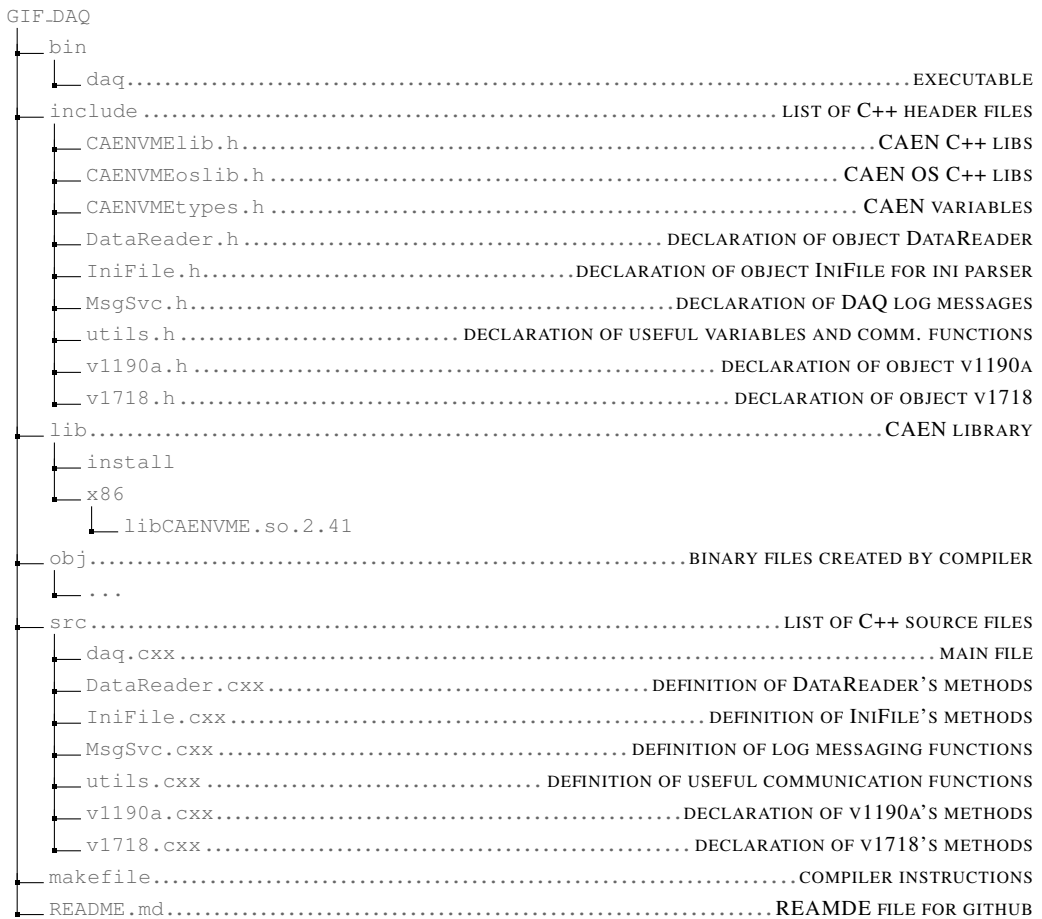
2923 The CAEN VME library will not be packaged by distributions and will need to be installed man-
2924 ually. To compile the GIF++ DAQ project via a terminal, from the DAQ folder use the command:

2925

```
2926     make
```

2927 The source code tree is provided below along with comments to give an overview of the files' con-
2928 tent. The different objects created for this project (`v1718`, `v1190a`, `IniFile` & `DataReader`) will be
2929 described in details in the following sections.

2930



2931 A.2 Usage of the DAQ

2932 GIF++ DAQ, as used in GIF++, is not a standalone software. Indeed, the system being more complexe,
 2933 the DAQ only is a sub-layer of the software architecture developped to control and monitor
 2934 the RPCs that are placed into the bunker for performance study in an irradiated environment. The top
 2935 layer of GIF++ is a Web Detector Control System (webDCS) application. The DAQ is only called
 2936 by the webDCS when data needs to be acquired. The webDCS operates the DAQ through command
 2937 line. To start the DAQ, the webDCS calls:

2938

2939 bin/daq /path/to/the/log/file/in/the/output/data/folder

2940 where /path/to/the/log/file/in/the/output/data/folder is the only argument required. This
 2941 log file is important for the webDCS as this file contains all the content of the communication of the
 2942 webDCS and the different systems monitored by the webDCS. Its content is constantly displayed
 2943 during data taking for the users to be able to follow the operations. The communication messages
 2944 are normally sent to the webDCS log file via the functions declared in file MsgSvc.h, typically
 2945 MSG_INFO(string message).

2946

2947 A.3 Description of the readout setup

2948 The CMS RPC setup at GIF++ counts 5 V1190A Time-to-Digital Converter (TDC) manufactured
 2949 by CAEN [89]. V1190A are VME units accepting 128 independent Multi-Hit/Multi-Event TDC
 2950 channels whose signals are treated by 4 100 ps high performance TDC chips developed by CERN
 2951 / ECP-MIC Division. The communication between the computer and the TDCs to transfer data is
 2952 done via a V1718 VME master module also manufactured by CAEN and operated from a USB
 2953 port [90]. These VME modules are all hosted into a 6U VME 6021 powered crate manufactured by
 2954 W-Ie-Ne-R than can accommodate up to 21 VME bus cards [91]. These 3 components of the DAQ
 2955 setup are shown in Figure A.1.

2956

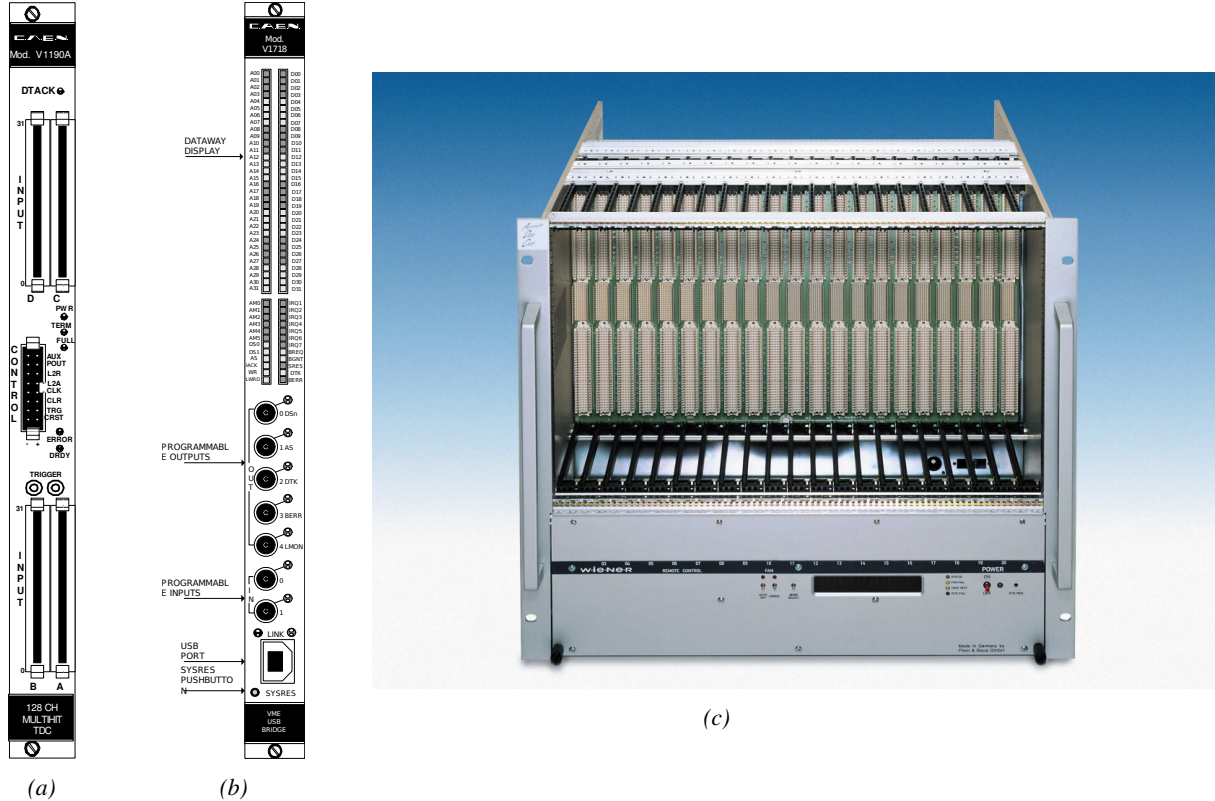


Figure A.1: (A.1a) View of the front panel of a V1190A TDC module [89]. (A.1b) View of the front panel of a VI718 Bridge module [90]. (A.1c) View of the front panel of a 6U 6021 VME crate [91].

2957

A.4 Data read-out

2958 To efficiently perform a data readout algorithm, C++ objects to handle the VME modules (TDCs
 2959 and VME bridge) have been created along with objects to store data and read the configuration file

2960 that comes as an input of the DAQ software.

2961

2962 A.4.1 V1190A TDCs

2963 The DAQ used at GIF takes profit of the *Trigger Matching Mode* offered by V1190A modules.
 2964 This setting is enabled through the method `v1190a::SetTrigMatching (int ntdcs)` where `ntdcs`
 2965 is the total number of TDCs in the setup this setting needs to be enabled for (Source Code A.1). A
 2966 trigger matching is performed in between a trigger time tag, a trigger signal sent into the TRIGGER
 2967 input of the TDC visible on Figure A.1a, and the channel time measurements, signals recorded from
 2968 the detectors under test in our case. Control over this data acquisition mode, explained through
 2969 Figure A.2, is offered via 4 programmable parameters:

- 2970 • **match window:** the matching between a trigger and a hit is done within a programmable time
 2971 window. This is set via the method

2972 `void v1190a::SetTrigWindowWidth(Uint windowHeight, int ntdcs)`

- 2973 • **window offset:** temporal distance between the trigger tag and the start of the trigger matching
 2974 window. This is set via the method

2975 `void v1190a::SetTrigWindowWidth(Uint windowHeight, int ntdcs)`

- 2976 • **extra search margin:** an extended time window is used to ensure that all matching hits are
 2977 found. This is set via the method

2978 `void v1190a::SetTrigSearchMargin(Uint searchMargin, int ntdcs)`

- 2979 • **reject margin:** older hits are automatically rejected to prevent buffer overflows and to speed
 2980 up the search time. This is set via the method

2981 `void v1190a::SetTrigRejectionMargin(Uint rejectMargin, int ntdcs)`

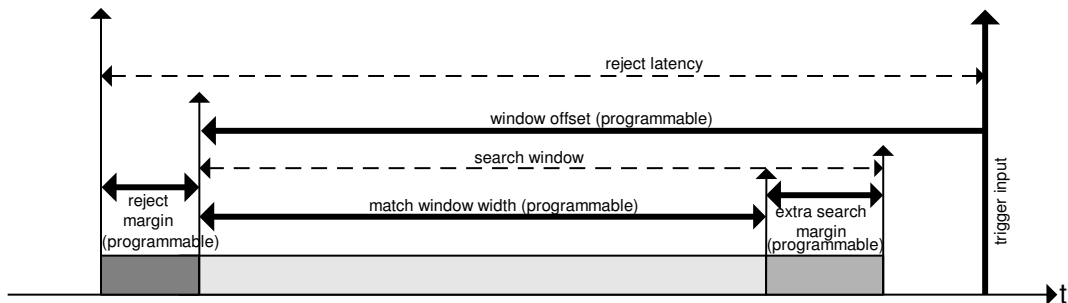


Figure A.2: Module V1190A Trigger Matching Mode timing diagram [89].

2982 Each of these 4 parameters are given in number of clocks, 1 clock being 25 ns long. It is easy to
 2983 understand at this level that there are 3 possible functioning settings:

- 2984 • **1:** the match window is entirely contained after the trigger signal,

- 2985 • **2:** the match window overlaps the trigger signal, or

- 2986 • **3:** the match window is entirely contained before the trigger signal as displayed on Figure A.2.

2987 In both the first and second cases, the sum of the window width and of the offset can be set to
2988 a maximum of 40 clocks, which corresponds to 1 μ s. Evidently, the offset can be negative, allowing
2989 for a longer match window, with the constraint of having the window ending at most 1 μ s after the
2990 trigger signal. In the third case, the maximum negative offset allowed is of 2048 clocks (12 bit) cor-
2991 responding to 51.2 μ s, the match window being strictly smaller than the offset. In the case of GIF++,
2992 the choice has been made to use this last setting by delaying the trigger signal. During the studies
2993 performed in GIF++, both the efficiency of the RPCs, probed using a muon beam, and the noise or
2994 gamma background rate are monitored. The extra search and reject margins are left unused.
2995 To probe the efficiency of RPC detectors, the trigger time tag is provided by the coïncidence of
2996 scintillators when a bunch of muons passes through GIF++ area is used to trigger the data acquisi-
2997 tion. For this measurement, it is useful to reduce the match window width only to contain the muon
2998 information. Indeed, the delay in between a trigger signal and the detection of the corresponding
2999 muon in the RPC being very contant (typically a few tens of ns due to jitter and cable length), the
3000 muon signals are very localised in time. Thus, due to a delay of approximalety 325 ns in between
3001 the muons and the trigger, the settings where chosen to have a window width of 24 clocks (600 ns)
3002 centered on the muon peak thanks to a negative offset of 29 clocks (725 ns).
3003 On the otherhand, monitoring the rates don't require for the DAQ to look at a specific time window.
3004 It is important to integrate enough time to have a robust measurement of the rate as the number of
3005 hits per time unit. The triggerring signal is provided by a pulse generator at a frequency of 300 Hz
3006 to ensure that the data taking occurs in a random way, with respect to beam physics, to probe only
3007 the irradiation spectrum on the detectors. The match window is set to 400 clocks (10 μ s) and the
3008 negative offset to 401 clocks as it needs to exceed the value of the match window.

```

3009
class v1190a
{
    private :
        long             Handle;
        vector<Data32>   Address;
        CVDataWidth      DataWidth;
        CVAddressModifier AddressModifier;

    public:

        v1190a(long handle, IniFile *inifile, int ntdcs);
        ~v1190a();
        Data16 write_op_reg(Data32 address, int code, string error);
        Data16 read_op_reg(Data32 address, string error);
        void Reset(int ntdcs);
        void Clear(int ntdcs);
        void TestWR(Data16 value,int ntdcs);
        void CheckTDCStatus(int ntdcs);
        void CheckCommunication(int ntdcs);
        void SetTDCTestMode(Data16 mode,int ntdcs);
        void SetTrigMatching(int ntdcs);
        void SetTrigTimeSubtraction(Data16 mode,int ntdcs);
        void SetTrigWindowWidth(Uint windowHeight,int ntdcs);
        void SetTrigWindowOffset(Uint windowOffset,int ntdcs);
        void SetTrigSearchMargin(Uint searchMargin,int ntdcs);
        void SetTrigRejectionMargin(Uint rejectMargin,int ntdcs);
        void GetTrigConfiguration(int ntdcs);
        void SetTrigConfiguration(IniFile *inifile,int ntdcs);
        void SetTDCDetectionMode(Data16 mode,int ntdcs);
        void SetTDCResolution(Data16 lsb,int ntdcs);
        void SetTDCDeadTime(Data16 time,int ntdcs);
        void SetTDCHeadTrailer(Data16 mode,int ntdcs);
        void SetTDCEventSize(Data16 size,int ntdcs);
        void SwitchChannels(IniFile *inifile,int ntdcs);
        void SetIRQ(Data32 level, Data32 count,int ntdcs);
        void SetBlockTransferMode(Data16 mode,int ntdcs);
        void Set(IniFile *inifile,int ntdcs);
        void CheckStatus(CVErrorCodes status) const;
        int ReadBlockD32(Uint tdc, const Data16 address,
                         Data32 *data, const Uint words, bool ignore_berr);
        Uint Read(RAWData *DataList,int ntdcs);
};

3010

```

3011 *Source Code A.1: Description of C++ object v1190a.*

3012 The v1190a object, defined in the DAQ software as in Source Code A.1, offers the possibility to
 3013 concatenate all TDCs in the readout setup into a single object containing a list of hardware addresses
 3014 (addresses to access the TDCs' buffer through the VME crate) and each constructor and method acts
 3015 on the list of TDCs.

3016

3017 A.4.2 DataReader

3018 Enabled thanks to v1190a::SetBlockTransferMode(Data16 mode, int ntdcs), the data transfer
 3019 is done via Block Transfer (BLT). Using BLT allows to tranfer a fixed number of events called a
 3020 *block*. This is used together with an Almost Full Level (AFL) of the TDCs' output buffers, defined

3021 through `v1190a::SetIRQ(Data32 level, Data32 count, int ntdcs)`. This AFL gives the maxi-
 3022 mum amount of 32735 words (16 bits, corresponding to the depth of a TDC output buffer) that can
 3023 written in a buffer before an Interrupt Request (IRQ) is generated and seen by the VME Bridge,
 3024 stopping the data acquisition to transfer the content of each TDC buffers before resuming. For each
 3025 trigger, 6 words or more are written into the TDC buffer:

- 3026 • a **global header** providing information of the event number since the beginning of the data
 acquisition,
- 3028 • a **TDC header**,
- 3029 • the **TDC data** (*if any*), 1 for each hit recorded during the event, providing the channel and the
 time stamp associated to the hit,
- 3031 • a **TDC error** providing error flags,
- 3032 • a **TDC trailer**,
- 3033 • a **global trigger time tag** that provides the absolute trigger time relatively to the last reset,
 and
- 3035 • a **global trailer** providing the total word count in the event.

3036 As previously described in Section ??, CMS RPC FEEs provide us with 100 ns long LVDS out-
 3037 put signals that are injected into the TDCs' input. Any avalanche signal that gives a signal above the
 3038 FEEs threshold is thus recorded by the TDCs as a hit within the match window. Each hit is assigned
 3039 to a specific TDC channel with a time stamp, with a precision of 100 ps. The reference time, $t_0 = 0$,
 3040 is provided by the beginning of the match window. Thus for each trigger, coming from a scintillator
 3041 coïncidence or the pulse generator, a list of hits is stored into the TDCs' buffers and will then be
 3042 transferred into a ROOT Tree.

3043 When the BLT is used, it is easy to understand that the maximum number of words that have
 3044 been set as ALF will not be a finite number of events or, at least, the number of events that would
 3045 be recorded into the TDC buffers will not be a multiple of the block size. In the last BLT cycle to
 3046 tranfer data, the number of events to transfer will most probably be lower than the block size. In that
 3047 case, the TDC can add fillers at the end of the block but this option requires to send more data to the
 3048 computer and is thus a little slower. Another solution is to finish the transfer after the last event by
 3049 sending a bus error that states that the BLT reached the last event in the pile. This method has been
 3050 chosen in GIF++.

3052 Due to irradiation, an event in GIF++ can count up to 300 words per TDC. A limit of 4096 words
 3053 (12 bits) has been set to generate IRQ which represent from 14 to almost 700 events depending on
 3054 the average of hits collected per event. Then the block size has been set to 100 events with enabled
 3055 bus errors. When an AFL is reached for one of the TDCs, the VME bridge stops the acquisition by
 3056 sending a BUSY signal.

3058

```

3059     The data is then transferred one TDC at a time into a structure called RAWData (Source Code A.2).
3060
3061 struct RAWData{
3062     vector<int>           *EventList;
3063     vector<int>           *NHitsList;
3064     vector<int>           *QFlagList;
3065     vector<vector<int> >   *Channellist;
3066     vector<vector<float> > *TimeStampList;
3067 };

```

3062 *Source Code A.2: Description of data holding C++ structure `RAWData`.*

3063 In order to organize the data transfer and the data storage, an object called `DataReader` was
3064 created (Source Code A.3). On one hand, it has `v1718` and `v1190a` objects as private members for
3065 communication purposes, such as VME modules settings via the configuration file `*iniFile` or data
3066 read-out through `v1190a::Read()` and on the other hand, it contains the structure `RAWData` that allows
3067 to organise the data in vectors reproducing the tree structure of a ROOT file.

```

3068 class DataReader
3069 {
3070     private:
3071     bool      StopFlag;
3072     IniFile *iniFile;
3073     Data32   MaxTriggers;
3074     v1718   *VME;
3075     int       nTDCs;
3076     v1190a  *TDCs;
3077     RAWData TDCData;
3078
3079     public:
3080     DataReader();
3081     virtual ~DataReader();
3082     void     SetIniFile(string inifilename);
3083     void     SetMaxTriggers();
3084     Data32 GetMaxTriggers();
3085     void     SetVME();
3086     void     SetTDC();
3087     int      GetQFlag(UInt it);
3088     void     Init(string inifilename);
3089     void     FlushBuffer();
3090     void     Update();
3091     string GetFileName();
3092     void     WriteRunRegistry(string filename);
3093     void     Run();
3094 };

```

3070 *Source Code A.3: Description of C++ object `DataReader`.*

3071 Each event is transferred from `TDCData` and saved into branches of a ROOT `TTree` as 3 integers
3072 that represent the event ID (`EventCount`), the number of hits read from the TDCs (`nHits`), and the
3073 quality flag that provides information for any problem in the data transfer (`qflag`), and 2 lists of
3074 `nHits` elements containing the fired TDC channels (`TDCCh`) and their respective time stamps (`TDCTS`),
3075 as presented in Source Code A.4. The ROOT file file is named using information contained into
3076 the configuration file, presented in section A.5.2. The needed information is extracted using method
3077 `DataReader::GetFileName()` and allow to build the output filename format `ScanXXXXXX_HVX_DAQ.root`

3078 where ScanXXXXXX is a 6 digit number representing the scan number into GIFT++ database and HVX
 3079 the HV step within the scan that can be more than a single digit. An example of ROOT data file is
 3080 provided with Figure A.3.

```
3081
RAWData TDCData;
TFile *outputFile = new TFile(outputFileName.c_str(),"recreate");
TTree *RAWDataTree = new TTree("RAWData","RAWData");

int EventCount = -9;
int nHits = -8;
int qflag = -7;
vector<int> TDCCh;
vector<float> TDCTS;

RAWDataTree->Branch("EventNumber",&EventCount, "EventNumber/I");
RAWDataTree->Branch("number_of_hits",&nHits,"number_of_hits/I");
RAWDataTree->Branch("Quality_flag",&qflag,"Quality_flag/I");
RAWDataTree->Branch("TDC_channel",&TDCCh);
RAWDataTree->Branch("TDC_TimeStamp",&TDCTS);

3082
//...
//Here read the TDC data using v1190a::Read() and place it into
//TDCData for as long as you didn't collect the requested amount
//of data.
//...

for(Uint i=0; i<TDCData.EventList->size(); i++){
    EventCount = TDCData.EventList->at(i);
    nHits = TDCData.NHitsList->at(i);
    qflag = TDCData.QFlagList->at(i);
    TDCCh = TDCData.ChannelList->at(i);
    TDCTS = TDCData.TimeStampList->at(i);
    RAWDataTree->Fill();
}
```

Source Code A.4: Highlight of the data transfer and organisation within DataReader::Run() after the data
 3083 has been collected into TDCData.

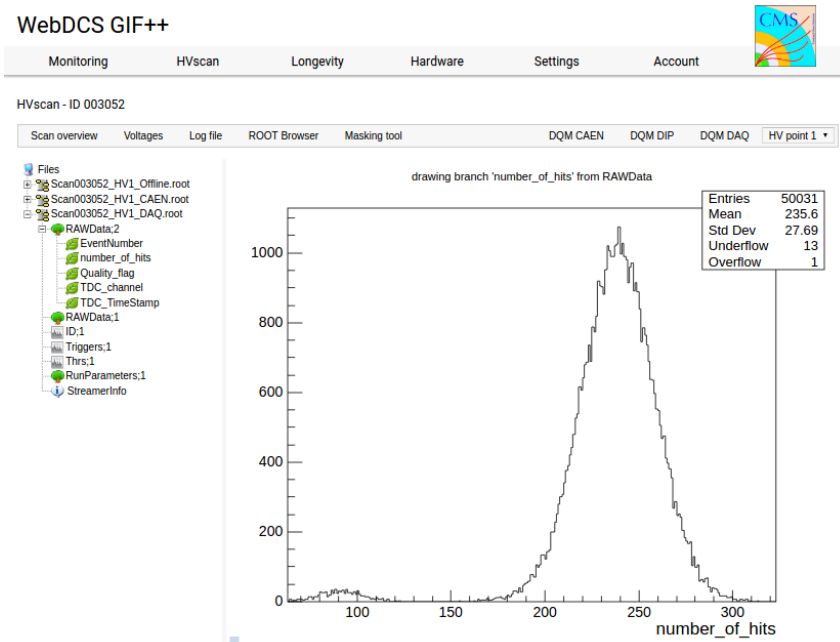


Figure A.3: Structure of the ROOT output file generated by the DAQ. The 5 branches (EventNumber, number_of_hits, Quality_flag, TDC_channel and TDC_TimeStamp) are visible on the left panel of the ROOT browser. On the right panel is visible the histogram corresponding to the variable nHits. In this specific example, there were approximately 50k events recorded to measure the gamma irradiation rate on the detectors. Each event is stored as a single entry in the TTree.

3084 A.4.3 Data quality flag

3085 Among the parameters that are recorded for each event, the quality flag, defined in Source Code A.5,
 3086 is determined on the fly by checking the data recorded by every single TDC. From method `v1190a::Read()`,
 3087 it can be understood that the content of each TDC buffer is readout one TDC at a time. Entries are
 3088 created in the data list for the first TDC and then, when the second buffer is readout, events corre-
 3089 sponding to entries that have already been created to store data for the previous TDC are added to
 3090 the existing list element. On the contrary, when an event entry has not been yet created in the data
 3091 list, a new entry is created.

```
3092    typedef enum _QualityFlag {
  3093     GOOD      = 1,
    CORRUPTED = 0
 } QualityFlag;
```

3094 *Source Code A.5: Definition of the quality flag `enum`.*

3095 It is possible that each TDC buffer contains a different number of events. In cases where the first
 3096 element in the buffer list is an event for corresponds to a new entry, the difference in between the
 3097 entry from the buffer and the last entry in the data list is recorded and checked. If it is greater than 1,
 3098 what should never be the case, the quality flag is set to CORRUPTED for this TDC and an empty entry
 3099 is created in the place of the missing ones. Missing entries are believe to be the result of a bad hold

3100 on the TDC buffers at the moment of the readout. Indeed, the software hold is effective only on 1
 3101 TDC at a time and no solution as been found yet to completely block the writting in the buffers when
 3102 an IRQ is received.

3103 At the end of each BLT cycle, the ID of the last entry stored for each TDC buffer is not recorded.
 3104 When starting the next cycle, if the first entry in the pile corresponds to an event already existing
 3105 in the list, the readout will start from this list element and will not be able to check the difference
 3106 in between this entry's ID and the one of the last entry that was recorded for this TDC buffer in
 3107 the previous cycle. In the case events were missing, the flag stays at its initial value of 0, which is
 3108 similar to CORRUPTED and it is assumed that then this TDC will not contribute to `number_of_hits`,
 3109 `TDC_channel` or `TDC_TimeStamp`.

3110 Finally, since there will be 1 `RAWData` entry per TDC for each event (meaning `nTDCs` entries,
 3111 referring to `DataReader` private attribute), the individual flags of each TDC will be added together.
 3112 The final format is an integer composed `nTDCs` digits where each digit is the flag of a specific TDC.
 3113 This is constructed using powers of 10 like follows:

```
3114 TDC 0: QFlag = 100 × _QualityFlag
3115 TDC 1: QFlag = 101 × _QualityFlag
3116 ...
3117 TDC N: QFlag = 10N × _QualityFlag
```

3118 and the final flag to be with N digits:

```
3119 QFlag = n....3210
```

3120 each digit being 1 or 0. Below is given an example with a 4 TDCs setup.

3121 If all TDCs were good : `QFlag = 1111`,

3122 but if TDC 2 was corrupted : `QFlag = 1011`.

3123 When data taking is over and the data contained in the dynamical `RAWData` structure is transferred
 3124 to the ROOT file, all the 0s are changed into 2s by calling the method `DataReader::GetQFlag()`.
 3125 This will help translating the flag without knowing the number of TDCs beforehand. Indeed, a flag
 3126 111 could be due to a 3 TDC setup with 3 good individual TDC flags or to a more than 3 TDC setup
 3127 with TDCs those ID is greater than 2 being CORRUPTED, thus giving a 0.

3128 The quality flag has been introduced quite late, in October 2017 only, to the list of GIFT++ DAQ
 3129 parameters to be recorded into the output ROOT file. Before this addition, the missing data, corrupting
 3130 the quality for the offline analysis, was contributing to artificially fill data with lower multiplicity.
 3131 Looking at `TBranch number_of_hits` provides an information about the data of the full GIFT++
 3132 setup. When a TDC is not able to transfer data for a specific event, the effect is a reduction of the
 3133 total number of hits recorded in the full setup, this is what can be seen from Figure A.4. After offline
 3134 reconstruction detector by detector, the effect of missing events can be seen in the artificially filled
 3135 bin at multiplicity 0 shown in Figure A.5. Nonetheless, for data with high irradiation levels, as it is
 3136 the case for Figure A.5a, discarding the fake multiplicity 0 data can be done easily during the offline
 3137 analysis. At lower radiation, the missing events contribution becomes more problematic as the multi-
 3138 tiplicity distribution overlaps the multiplicity 0 and that in the same time the proportion of missing

3139 events decreases. Attempts to fit the distribution with a Poisson or skew distribution function were
3140 not conclusive and this very problem has been at the origin of the quality flag that allows to give a
3141 non ambiguous information about each event quality.

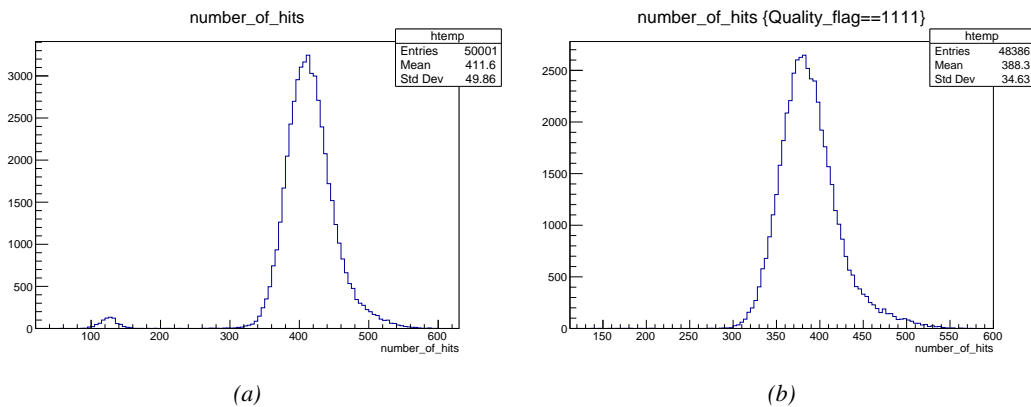


Figure A.4: The effect of the quality flag is explained by presenting the content of `TBranch number_of_hits` of a data file without `Quality_flag` in Figure A.4a and the content of the same `TBranch` for data corresponding to a `Quality_flag` where all TDCs were labelled as `GOOD` in Figure A.4b taken with similar conditions. It can be noted that the number of entries in Figure A.4b is slightly lower than in Figure A.4a due to the excluded events.

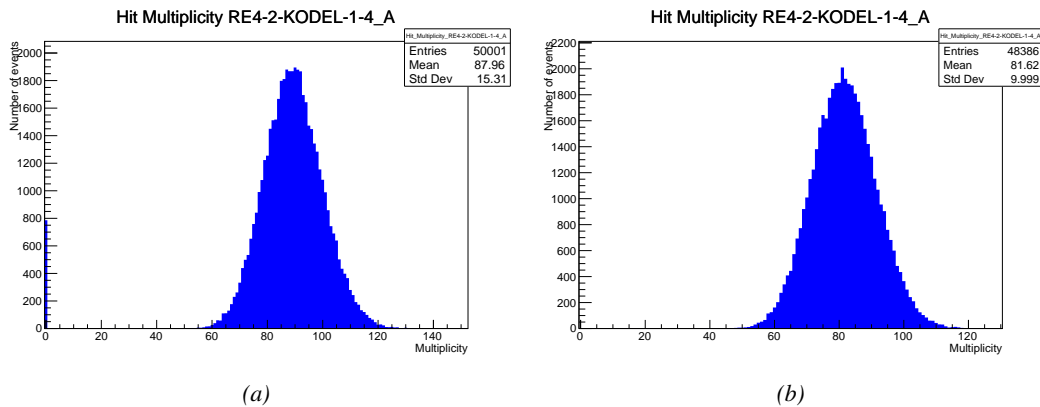


Figure A.5: Using the same data as previously showed in Figure A.4, the effect of the quality flag is explained by presenting the reconstructed hit multiplicity of a data file without `Quality_flag` in Figure A.5a and the reconstructed content of the same RPC partition for data corresponding to a `Quality_flag` where all TDCs were labelled as `GOOD` in Figure A.5b taken with similar conditions. The artificial high content of bin 0 is completely suppressed.

A.5 Communications

To ensure data readout and dialog in between the machine and the TDCs or in between the webDCS and the DAQ, different communication solutions were used. First of all, it is important to have a

3146 module to allow the communication in between the TDCs and the computer from which the DAQ
 3147 operates. When this communication is effective, shifters using the webDCS to control data taking
 3148 can thus send instructions to the DAQ.

3149

3150 A.5.1 V1718 USB Bridge

3151 In the previous section, the data transfer has been discussed. The importance of the `v1718` object
 3152 (Source Code A.6), used as private member of `DataReader`, was not explicated. VME master
 3153 modules are used for communication purposes as they host the USB port that connects the pow-
 3154 ered crate buffer to the computer where the DAQ is installed. From the source code point of view,
 3155 this object is used to control the communication status, by reading the returned error codes with
 3156 `v1718::CheckStatus()`, or to check for IRQs coming from the TDCs through `v1718::CheckIRQ()`.
 3157 Finally, to ensure that triggers are blocked at the hardware level, a NIM pulse is sent out of one of the
 3158 5 programmable outputs (`v1718::SendBUSY()`) to the VETO of the coincidence module where the
 3159 trigger signals originate from. As long as this signal is ON, no trigger can reach the TDCs anymore.
 3160

```
3161
  class v1718{
    private:
      int Handle;
      Data32 Data;           // Data
      CVIRQLevels Level;    // Interrupt level
      CVAddressModifier AM;   // Addressing Mode
      CVDataWidth dataSize;  // Data Format
      Data32 BaseAddress;    // Base Address

    public:
      v1718(IniFile *inifile);
      ~v1718();
      long GetHandle(void) const;
      int GetData(Data16 data);
      Data16 GetData(void);
      int SetLevel(CVIRQLevels level);
      CVIRQLevels GetLevel(void);
      int SetAM(CVAddressModifier am);
      CVAddressModifier GetAM(void);
      int SetDatasize(CVDataWidth datasize);
      CVDataWidth GetDataSize(void);
      int SetBaseAddress(Data16 baseaddress);
      Data16 GetBaseAddress(void);
      void CheckStatus(CVErrorCodes status) const;
      void CheckIRQ();
      void SetPulsers();
      void SendBUSY(BusyLevel level);
  };

```

3162 *Source Code A.6: Description of C++ object v1718.*

3163 A.5.2 Configuration file

3164 The DAQ software takes as input a configuration file written using INI standard [92]. This file is
 3165 partly filled with the information provided by the shifters when starting data acquisition using the
 3166 webDCS, as shown by Figure A.6. This information is written in section [`General`] and will later

3167 be stored in the ROOT file that contains the DAQ data as can be seen from Figure A.3. Indeed,
 3168 another `TTree` called `RunParameters` as well as the 2 histograms `ID`, containing the scan number,
 3169 start and stop time stamps, and `Triggers`, containing the number of triggers requested by the shifter,
 3170 are available in the data files. Moreover, `ScanID` and `HV` are then used to construct the file name
 3171 thanks to the method `DataReader::GetFileName()`.

Chamber	RE2-2-NPD-BARC-8	RE4-2-CERN-106	RE2-3-NPD-BARC-9	RE4-2-CERN-105	RE4-2-KODEL-1-4	Max triggers
HV _{eff} 1	8600	8500	8600	8500	6500	
HV _{eff} 2	8700	8600	8700	8600	6600	
HV _{eff} 3	8800	8700	8800	8700	6700	
HV _{eff} 4	8900	8800	8900	8800	6800	
HV _{eff} 5	9000	8900	9000	8900	6900	
HV _{eff} 6	9100	9000	9100	9000	7000	
HV _{eff} 7	9200	9100	9200	9100	7100	
HV _{eff} 8	9300	9200	9300	9200	7200	
HV _{eff} 9	9400	9300	9400	9300	7300	
HV _{eff} 10	9500	9400	9500	9400	7400	

Figure A.6: WebDCS DAQ scan page. On this page, shifters need to choose the type of scan (Rate, Efficiency or Noise Reference scan), the gamma source configuration at the moment of data taking, the beam configuration, and the trigger mode. These information will be stored in the DAQ ROOT output. Are also given the minimal measurement time and waiting time after ramping up of the detectors is over before starting the data acquisition. Then, the list of HV points to scan and the number of triggers for each run of the scan are given in the table underneath.

3172 The rest of the information is written beforehand in the configuration file template, as explicated
 3173 in Source Code A.7, and contains the hardware addresses to the different VME modules in the
 3174 setup as well as settings for the TDCs. As the TDC settings available in the configuration file are not
 3175 supposed to be modified, an improvement would be to remove them from the configuration file and
 3176 to hardcode them inside of the DAQ code itself or to place them into a different INI file that would
 3177 host only the TDC settings to lower the probability for a bad manipulation of the configuration file
 3178 that can be modified from one of webDCS' menus.

3179

```
[General]
TdcS=4
ScanID=$scanid
HV=$HV
RunType=$runtype
MaxTriggers=$maxtriggers
Beam=$beam
[VMEInterface]
Type=V1718
BaseAddress=0xFF0000
Name=VmeInterface
[TDC0]
Type=V1190A
BaseAddress=0x00000000
Name=Tdc0
StatusA00-15=1
StatusA16-31=1
StatusB00-15=1
StatusB16-31=1
StatusC00-15=1
StatusC16-31=1
StatusD00-15=1
StatusD16-31=1
[TDC1]
Type=V1190A
BaseAddress=0x11110000
Name=Tdc1
StatusA00-15=1
StatusA16-31=1
StatusB00-15=1
StatusB16-31=1
StatusC00-15=1
StatusC16-31=1
StatusD00-15=1
StatusD16-31=1
[TDC2]
Type=V1190A
BaseAddress=0x22220000
Name=Tdc2
StatusA00-15=1
StatusA16-31=1
StatusB00-15=1
StatusB16-31=1
StatusC00-15=1
StatusC16-31=1
StatusD00-15=1
StatusD16-31=1
[TDC3]
Type=V1190A
BaseAddress=0x44440000
Name=Tdc3
StatusA00-15=1
StatusA16-31=1
StatusB00-15=1
StatusB16-31=1
StatusC00-15=1
StatusC16-31=1
StatusD00-15=1
StatusD16-31=1
[TDCSettings]
TriggerExtraSearchMargin=0
TriggerRejectMargin=0
TriggerTimeSubtraction=0b1
TdcDetectionMode=0b01
TdcResolution=0b10
TdcDeadTime=0b00
TdcHeadTrailer=0b1
TdcEventSize=0b1001
TdcTestMode=0b0
BLTMode=1
```

3180

Source Code A.7: INI configuration file template for 4 TDCs. In section [General], the number of TDCs is explicitated and information about the ongoing run is given. Then, there are sections for each and every VME modules. There buffer addresses are given and for the TDCs, the list of channels to enable is given. Finally, in section [TDCSettings], a part of the TDC settings are given.

3182 In order to retrieve the information of the configuration file, the object `IniFile` has been developed
 3183 to provide an INI parser, presented in Source Code A.8. It contains private methods returning a
 3184 boolean to check the type of line written in the file, whether a comment, a group header or a key line
 3185 (`IniFile::CheckIfComment()`, `IniFile::CheckIfGroup()` and `IniFile::CheckIfToken()`). The
 3186 key may sometimes be referred to as *token* in the source code. Moreover, the private element
 3187 `FileData` is a map of `const string` to `string` that allows to store the data contained inside the
 3188 configuration file via the public method `IniFile::GetFileData()` following the formatting (see
 3189 method `IniFile::Read()`):

```
3190
  3191     string group, token, value;
  // Get the field values for the 3 strings.
  // Then concatenate group and token together as a single string
  // with a dot separation.
  token = group + "." + token;
  FileData[token] = value;
```

3192 More methods have been written to translate the different keys into the right variable format
 3193 when used by the DAQ. For example, to get a `float` value out of the configuration file data, knowing
 3194 the group and the key needed, the method `IniFile::floatType()` can be used. It takes 3 arguments
 3195 being the group name and key name (both `string`), and a default `float` value used as exception in
 3196 the case the expected combination of group and key cannot be found in the configuration file. This
 3197 default value is then used and the DAQ continues on working after sending an alert in the log file for
 3198 further debugging.

```

3199 typedef map< const string, string > IniFileData;
3200
class IniFile{
    private:
        bool          CheckIfComment (string line);
        bool          CheckIfGroup(string line, string& group);
        bool          CheckIfToken(string line, string& key, string& value);
        string         FileName;
        IniFileData   FileData;
        int           Error;

    public:
        IniFile();
        IniFile(string filename);
        virtual      ~IniFile();

        // Basic file operations
        void          SetFileName(string filename);
3200      int           Read();
        int           Write();
        IniFileData GetFileData();

        // Data readout methods
        Data32         addressType (string groupname, string keyname, Data32
→      defaultvalue);
        long          intType     (string groupname, string keyname, long
→      defaultvalue);
        long long    longType    (string groupname, string keyname, long long
→      defaultvalue );
        string         stringType  (string groupname, string keyname, string
→      defaultvalue );
        float         floatType   (string groupname, string keyname, float
→      defaultvalue );

        // Error methods
        string         GetErrorMsg();
    };

```

3201 *Source Code A.8: Description of C++ object `IniFile` used as a parser for INI file format.*

3202 A.5.3 WebDCS/DAQ intercommunication

3203 When shifters send instructions to the DAQ via the configuration file, it is the webDCS itself that
 3204 gives the start command to the DAQ and then the 2 softwares use inter-process communication
 3205 through file to synchronise themselves. This communication file is represented by the variable **const**
 3206 **string** __runstatuspath.

3207 On one side, the webDCS sends commands or status that are readout by the DAQ:

- 3208 ● INIT, status sent when launching a scan and read via function `CtrlRunStatus(...)`,
- 3209 ● START, command to start data taking and read via function `CheckSTART()`,
- 3210 ● STOP, command to stop data taking at the end of the scan and read via function `CheckSTOP()`,
 3211 and
- 3212 ● KILL, command to kill data taking sent by user and read via function `CheckKILL()`

3213 and on the other, the DAQ sends status that are controled by the webDCS:

- 3214 ● `DAQ_RDY`, sent with `SendDAQReady()` to signify that the DAQ is ready to receive commands
3215 from the webDCS,
- 3216 ● `RUNNING`, sent with `SendDAQRunning()` to signify that the DAQ is taking data,
- 3217 ● `DAQ_ERR`, sent with `SendDAQError()` to signify that the DAQ didn't receive the expected com-
3218 mand from the webDCS or that the launch command didn't have the right number of argu-
3219 ments,
- 3220 ● `RD_ERR`, sent when the DAQ wasn't able to read the communication file, and
- 3221 ● `WR_ERR`, sent when the DAQ wasn't able to write into the communication file.

3222 **A.5.4 Example of inter-process communication cycle**

3223 Under normal conditions, the webDCS and the DAQ processes exchange commands and status via
3224 the file hosted at the address `__runstatuspath`, as explained in subsection A.5.3. An example of
3225 cycle is given in Table A.1. In this example, the steps 3 to 5 are repeated as long as the webDCS tells
3226 the DAQ to take data. A data taking cycle is the equivalent as what is called a *Scan* in GIFT++ jargon,
3227 referring to a set a runs with several HV steps. Each repetition of steps 3 to 5 is then equivalent to a
3228 single *Run*.

3229 At any moment during the data taking, for any reason, the shifter can decide that the data taking
3230 needs to be stopped before it reached the end of the scheduled cycle. Thus at any moment on the
3231 cycle, the content of the inter-process communication file will be changed to `KILL` and the DAQ will
3232 shut down right away. The DAQ checks for `KILL` signals every 5s after the TDCs configuration is
3233 over. So far, the function `CheckKILL()` has been used only inside of the data taking loop of method
3234 `DataReader::Run()` and thus, if the shifter decides to KILL the data taking during the TDC con-
3235 figuration phase or the HV ramping in between 2 HV steps, the DAQ will not be stopped smoothly
3236 and a *force kill* command will be sent to stop the DAQ process that is still awake on the computer.
3237 Improvements can be brought on this part of the software to make sure that the DAQ can safely
3238 shutdown at any moment.

3241 **A.6 Software export**

3242 In section A.2 was discussed the fact that the DAQ as written in its last version is not a standalone
3243 software. It is possible to make it a standalone program that could be adapted to any VME setup
3244 using V1190A and V1718 modules by creating a GUI for the software or by printing the log mes-
3245 sages that are normally printed in the webDCS through the log file, directly into the terminal. This
3246 method was used by the DAQ up to version 3.0 moment where the webDCS was completed. Also, it
3247 is possible to check branches of DAQ v2.X to have example of communication through a terminal.

3248
3249 DAQ v2.X is nonetheless limited in it's possibilities and requires a lot of offline manual interven-
3250 tions from the users. Indeed, there is no communication of the software with the detectors' power
3251 supply system that would allow for a user a predefine a list of voltages to operate the detectors at

step	actions of webDCS	status of DAQ	<code>__runstatuspath</code>
1	launch DAQ ramp voltages ramping over wait for currents stabilization	readout of IniFile configuration of TDCs	INIT
2		configuration done send DAQ ready wait for START signal	DAQ_RDY
3	waiting time over send START		START
4	wait for run to end monitor DAQ run status	data taking ongoing check for KILL signal	RUNNING
5		run over send DAQ_RDY wait for next DCS signal	DAQ_RDY
6	ramp voltages ramping over wait for currents stabilization		DAQ_RDY
3	waiting time over send START		START
4	wait for run to end monitor DAQ run status	update IniFile information data taking ongoing check for KILL signal	RUNNING
5		run over send DAQ_RDY wait for next DCS signal	DAQ_RDY
7	send command STOP	DAQ shuts down	STOP

Table A.1: Inter-process communication cycles in between the webDCS and the DAQ through file string signals.

3252 and loop over to take data without any further manual intervention. In v2.X, the data is taken for a
3253 single detector setting and at the end of each run, the softwares asks the user if he intends on taking
3254 more runs. If so, the software invites the user to set the operating voltages accordingly to what is
3255 necessary and to manual update the configuration file in consequence. This working mode can be a
3256 very first approach before an evolution and has been successfully used by colleagues from different
3257 collaborations.

3258
3259 For a more robust operation, it is recommended to develop a GUI or a web application to inter-
3260 face the DAQ. Moreover, to limit the amount of manual interventions, and thus the probability to
3261 make mistakes, it is also recommended to add an extra feature into the DAQ by installing the HV
3262 Wrapper library provided by CAEN of which an example of use in a similar DAQ software devel-
3263 opped by a master student of UGent, and called TinyDAQ, is provided on UGent's github. Then, this
3264 HV Wrapper will help you communicating with and give instructions to a CAEN HV powered crate
3265 and can be added into the DAQ at the same level where the communication with the user was made
3266 in DAQ v2.X. In case you are using another kind of power system for your detectors, it is stringly
3267 adviced to use HV modules or crates that can be remotely controled via a using C++ libraries.
3268

B

3269

3270

Details on the offline analysis package

3271 The data collected in GIF++ thanks to the DAQ described in Appendix A is difficult to interpret by
3272 a human user that doesn't have a clear idea of the raw data architecture of the ROOT data files. In
3273 order to render the data human readable, a C++ offline analysis tool was designed to provide users
3274 with detector by detector histograms that give a clear overview of the parameters monitored during
3275 the data acquisition [93]. In this appendix, details about this software in the context of GIF++, as of
3276 how the software was written and how it functions will be given.

3277 B.1 GIF++ Offline Analysis file tree

3278 GIF++ Offline Analysis source code is fully available on github at https://github.com/aafagot/GIF_OfflineAnalysis. The software requires ROOT as non-optionnal dependency
3279 as it takes ROOT files in input and write an output ROOT file containing histograms. To compile the
3280 GIF++ Offline Analysis project is compiled with cmake. To compile, first a build/ directory must
3281 be created to compile from there:

```
3283 mkdir build
3284 cd build
3285 cmake ..
3286 make
3287 make install
```

3285 To clean the directory and create a new build directory, the bash script cleandir.sh can be used:

```
3286
3287 ./cleandir.sh
```

3288 The source code tree is provided below along with comments to give an overview of the files' con-
3289 tent. The different objects created for this project (`Infrastructure`, `Trolley`, `RPC`, `Mapping`, `RPCHit`,
3290 `RPCCluster` and `Inifile`) will be described in details in the following sections.

3291

```

GIF_OfflineAnalysis
├── bin
│   └── offlineanalysis ..... EXECUTABLE
├── build..... CMAKE COMPILATION DIRECTORY
└── ...
    ├── include..... LIST OF C++ HEADER FILES
    │   ├── Cluster.h..... DECLARATION OF OBJECT RPCCLUSTER
    │   ├── Current.h..... DECLARATION OF GETCURRENT ANALYSIS MACRO
    │   ├── GIFTrolley.h..... DECLARATION OF OBJECT TROLLEY
    │   ├── Infrastructure.h..... DECLARATION OF OBJECT INFRASTRUCTURE
    │   ├── IniFile.h..... DECLARATION OF OBJECT INI FILE FORINI PARSER
    │   ├── Mapping.h..... DECLARATION OF OBJECT MAPPING
    │   ├── MsgSvc.h..... DECLARATION OF OFFLINE LOG MESSAGES
    │   ├── OfflineAnalysis.h..... DECLARATION OF DATA ANALYSIS MACRO
    │   ├── RPCTracker.h..... DECLARATION OF OBJECT RPC
    │   ├── RPCHit.h..... DECLARATION OF OBJECT RPCHIT
    │   ├── types.h..... DEFINITION OF USEFUL VARIABLE TYPES
    │   └── utils.h..... DECLARATION OF USEFUL FUNCTIONS
    ├── obj..... BINARY FILES CREATED BY COMPILER
    └── ...
        ├── src..... LIST OF C++ SOURCE FILES
        │   ├── Cluster.cc..... DEFINITION OF OBJECT RPCCLUSTER
        │   ├── Current.cc..... DEFINITION OF GETCURRENT ANALYSIS MACRO
        │   ├── GIFTrolley.cc..... DEFINITION OF OBJECT TROLLEY
        │   ├── Infrastructure.cc..... DEFINITION OF OBJECT INFRASTRUCTURE
        │   ├── IniFile.cc..... DEFINITION OF OBJECT INI FILE FORINI PARSER
        │   ├── main.cc..... MAIN FILE
        │   ├── Mapping.cc..... DEFINITION OF OBJECT MAPPING
        │   ├── MsgSvc.cc..... DECLARATION OF OFFLINE LOG MESSAGES
        │   ├── OfflineAnalysis.cc..... DECLARATION OF DATA ANALYSIS MACRO
        │   ├── RPCTracker.cc..... DECLARATION OF OBJECT RPC
        │   ├── RPCHit.cc..... DECLARATION OF OBJECT RPCHIT
        │   └── utils.cc..... DEFINITION OF USEFUL FUNCTIONS
        ├── cleandir.sh..... BASH SCRIPT TO CLEAN BUILD DIRECTORY
        ├── CMakeLists.txt..... SET OF INSTRUCTIONS FOR CMAKE
        ├── config.h.in..... DEFINITION OF VERSION NUMBER
        └── README.md..... README FILE FOR GITHUB

```

3292

B.2 Usage of the Offline Analysis

3293

In order to use the Offline Analysis tool, it is necessary to know the Scan number and the HV Step of the run that needs to be analysed. This information needs to be written in the following format:

3295

3296

```
Scan00XXXX_HVY
```

3297

where XXXX is the scan ID and Y is the high voltage step (in case of a high voltage scan, data will be taken for several HV steps). This format corresponds to the base name of data files in the database

3298

3299 of the GIF++ webDCS. Usually, the offline analysis tool is automatically called by the webDCS at
 3300 the end of data taking or by a user from the webDCS panel if an update of the tool was brought.
 3301 Nonetheless, an expert can locally launch the analysis for tests on the GIF++ computer, or a user can
 3302 get the code on its local machine from github and download data from the webDCS for its own anal-
 3303 ysis. To launch the code, the following command can be used from the `GIF_OfflineAnalysis` folder:

3304
 3305 `bin/offlineanalysis /path/to/Scan00XXXX_HVY`

3306 where, `/path/to/Scan00XXXX_HVY` refers to the local data files. Then, the offline tool will by itself
 3307 take care of finding all available ROOT data files present in the folder, as listed below:

- 3308
 - 3309 ● `Scan00XXXX_HVY_DAQ.root` containing the TDC data as described in Appendix ?? (events, hit
 and timestamp lists), and
 - 3310 ● `Scan00XXXX_HVY_CAEN.root` containing the CAEN mainframe data recorded by the monitor-
 ing tool webDCS during data taking (HVs and currents of every HV channels). This file is
 created independently of the DAQ.

3313 **B.2.1 Output of the offline tool**

3314 **B.2.1.1 ROOT file**

3315 The analysis gives in output ROOT datafiles that are saved into the data folder and called using the
 3316 naming convention `Scan00XXXX_HVY_Offline.root`. Inside those, a list of `TH1` histograms can be
 3317 found. Its size will vary as a function of the number of detectors in the setup as each set of histograms
 3318 is produced detector by detector. For each partition of each chamber, can be found:

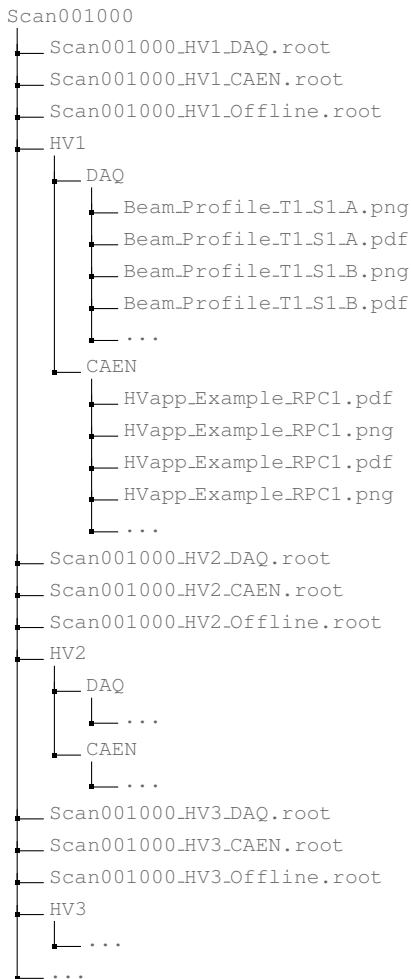
- 3319
 - 3320 ● `Time_Profile_Tt_Sc_p` shows the time profile of all recorded events (number of events per
 time bin),
 - 3321 ● `Hit_Profile_Tt_Sc_p` shows the hit profile of all recorded events (number of events per chan-
 nel),
 - 3323 ● `Hit_Multiplicity_Tt_Sc_p` shows the hit multiplicity (number of hits per event) of all recorded
 events (number of occurrences per multiplicity bin),
 - 3325 ● `Strip_Mean_Noise_Tt_Sc_p` shows noise/gamma rate per unit area for each strip in a se-
 lected time range. After filters are applied on `Time_Profile_Tt_Sc_p`, the filtered version
 of `Hit_Profile_Tt_Sc_p` is normalised to the total integrated time and active detection area
 of a single channel,
 - 3329 ● `Strip_Activity_Tt_Sc_p` shows noise/gamma activity for each strip (normalised version of
 previous histogram - strip activity = strip rate / average partition rate),
 - 3331 ● `Strip_Homogeneity_Tt_Sc_p` shows the *homogeneity* of a given partition ($\text{homogeneity} = \exp(-\text{strip rates standard deviation(strip rates in partition/average partition rate)})$),
 - 3333 ● `mask_Strip_Mean_Noise_Tt_Sc_p` shows noise/gamma rate per unit area for each masked
 strip in a selected time range. Offline, the user can control the noise/gamma rate and decide to
 mask the strips that are judged to be noisy or dead. This is done via the *Masking Tool* provided
 by the webDCS,

- 3337 ● `mask_Strip_Activity_Tt_Sc_p` shows noise/gamma activity per unit area for each masked
3338 strip with respect to the average rate of active strips,
- 3339 ● `NoiseCSize_H_Tt_Sc_p` shows noise/gamma cluster size, a cluster being constructed out of
3340 adjacent strips giving a signal at the *same time* (hits within a time window of 25 ns),
- 3341 ● `NoiseCMult_H_Tt_Sc_p` shows noise/gamma cluster multiplicity (number of reconstructed
3342 clusters per event),
- 3343 ● `Chip_Mean_Noise_Tt_Sc_p` shows the same information than `Strip_Mean_Noise_Tt_Scp` us-
3344 ing a different binning (1 chip corresponds to 8 strips),
- 3345 ● `Chip_Activity_Tt_Sc_p` shows the same information than `Strip_Activity_Tt_Scp` using
3346 chip binning,
- 3347 ● `Chip_Homogeneity_Tt_Sc_p` shows the homogeneity of a given partition using chip binning,
- 3348 ● `Beam_Profile_Tt_Sc_p` shows the estimated beam profile when taking efficiency scan. This
3349 is obtained by filtering `Time_Profile_Tt_Sc_p` to only consider the muon peak where the
3350 noise/gamma background has been subtracted. The resulting hit profile corresponds to the
3351 beam profile on the detector channels,
- 3352 ● `L0_Efficiency_Tt_Sc_p` shows the level 0 efficiency that was estimated **without** muon track-
3353 ing,
- 3354 ● `MuonCSize_H_Tt_Sc_p` shows the level 0 muon cluster size that was estimated **without** muon
3355 tracking, and
- 3356 ● `MuonCMult_H_Tt_Sc_p` shows the level 0 muon cluster multiplicity that was estimated **without**
3357 muon tracking.

3358 In the histogram labels, t stands for the trolley number (1 or 3), c for the chamber slot label in
3359 trolley t and p for the partition label (A, B, C or D depending on the chamber layout) as explained
3360 in Chapter 5.3.

3361 In the context of GIF++, an extra script called by the webDCS is called to extract the histograms
3362 from the ROOT files. The histograms are then stored in PNG and PDF formats into the correspond-
3363 ing folder (a single folder per HV step, so per ROOT file). the goal is to then display the histograms
3364 on the Data Quality Monitoring (DQM) page of the webDCS in order for the users to control the
3365 quality of the data taking at the end of data taking. An example of histogram organisation is given
3366 below:

3368



3369 *Here can put some screens from the webDCS to show the DQM and the plots available to users.*
 3370

3371 **B.2.1.2 CSV files**

3372 Moreover, up to 3 CSV files can be created depending on which ones of the 3 input files were in the
 3373 data folder:

- 3374 • `Offline-Corrupted.csv` , is used to keep track of the amount of data that was corrupted and
 3375 removed from old data format files that don't contain any data quality flag.
- 3376 • `Offline-Current.csv` , contains the summary of the currents and voltages applied on each
 3377 RPC HV channel.
- 3378 • `Offline-L0-EffC1.csv` , is used to write the efficiencies, cluster size and cluster multiplicity
 3379 of efficiency runs. Note that `L0` refers here to *Level 0* and means that the results of efficiency and
 3380 clusterization are a first approximation calculated without performing any muon tracking in

3381 between the different detectors. This offline tool provides the user with a preliminar calculation
 3382 of the efficiency and of the muon event parameters. Another analysis software especially
 3383 dedicated to muon tracking is called on selected data to retrieve the results of efficiency and
 3384 muon clusterization using a tracking algorithm to discriminate noise or gamma from muons
 3385 as muons are the only particles that pass through the full setup, leaving hits than can be used
 3386 to reconstruct their tracks.

- 3387 • `Offline-Rate.csv`, is used to write the noise or gamma rates measured in the detector readout
 3388 partitions.

3389 Note that these 4 CSV files are created along with their *headers* (`Offline-[...]-Header.csv`
 3390 containing the names of each data columns) and are automatically merged together when the offline
 3391 analysis tool is called from the webDCS, contrary to the case where the tool is runned locally from
 3392 the terminal as the merging bash script is then not called. Thus, the resulting files, used to make
 3393 official plots, are:

- 3394 • `Corrupted.csv`,
 3395 • `Current.csv`,
 3396 • `L0-EffCl.csv`.
 3397 • `Rate.csv`.

3398 B.3 Analysis inputs and information handling

3399 The usage of the Offline Analysis tool as well as its output have been presented in the previous section.
 3400 It is now important to dig further and start looking at the source code and the inputs necessary
 3401 for the tool to work. Indeed, other than the raw ROOT data files that are analysed, more information
 3402 needs to be imported inside of the program to perform the analysis such as the description of the
 3403 setup inside of GIFT++ at the time of data taking (number of trolleys, of RPCs, dimensions of the
 3404 detectors, etc...) or the mapping that links the TDC channels to the coresponding RPC channels in
 3405 order to translate the TDC information into human readable data. 2 files are used to transmit all this
 3406 information:
 3407

- 3408 • `Dimensions.ini`, that provides the necessary setup and RPC information, and
 3409 • `ChannelsMapping.csv`, that gives the link between the TDC and RPC channels as well as the
 3410 *mask* for each channel (masked or not?).

3411 B.3.1 Dimensions file and InFile parser

3412 This input file, present in every data folder, allows the analysis tool to know of the number of active
 3413 trolleys, the number of active RPCs in those trolleys, and the details about each RPCs such as
 3414 the number of RPC gaps, the number of pseudo-rapidity partitions (for CMS-like prototypes), the
 3415 number of strips per partion or the dimensions. To do so, there are 3 types of groups in the INI file
 3416 architecture. A first general group, appearing only once at the head of the document, gives information
 3417 about the number of active trolleys as well as their IDs, as presented in Source Code B.1. For

3418 each active trolley, a group similar to Source Code B.2 can be found containing information about
 3419 the number of active detectors in the trolley and their IDs. Each trolley group as a `Tt` name format,
 3420 where `t` is the trolley ID. Finally, for each detector stored in slots of an active trolley, there is a group
 3421 providing information about their names and dimensions, as shown in Source Code B.3. Each slot
 3422 group as a `TtSs` name format, where `s` is the slot ID of trolley `t` where the active RPC is hosted.

```
3423 [General]
3424 nTrolleys=2
3425 TrolleysID=13
```

3425 *Source Code B.1: Example of `[General]` group as might be found in `Dimensions.ini`. In Gif++, only 2 trolleys are available to hold RPCs and place them inside of the bunker for irradiation. The IDs of the trolleys are written in a single string as "13" and then read character by character by the program.*

```
3426 [T1]
3427 nSlots=4
      SlotsID=1234
```

3427 *Source Code B.2: Example of trolley group as might be found in `Dimensions.ini`. In this example, the file tells that there are 4 detectors placed in the holding slots of the trolley `T1` and that their IDs, written as a single string variable, are 1, 2, 3 and 4.*

```
3428 [T1S1]
      Name=RE2-2-NPD-BARC-8
      Partitions=3
      Gaps=3
      Gap1=BOT
      Gap2=TN
      Gap3=TW
      AreaGap1=11694.25
      AreaGap2=6432
      AreaGap3=4582.82
      Strips=32
      ActiveArea-A=157.8
      ActiveArea-B=121.69
      ActiveArea-C=93.03
```

3429 *Source Code B.3: Example of slot group as might be found in `Dimensions.ini`. In this example, the file provides information about a detector named `RE2-2-NPD-BARC-8`, having 3 pseudo-rapidity readout partitions and stored in slot `S1` of trolley `T1`. This is a CMS RE2-2 type of detector. This information will then be used for example to compute the rate per unit area calculation.*

3430 This information is readout and stored in a C++ object called `IniFile`, that parses the information
 3431 in the INI input file and stores it into a local buffer for later use. This INI parser is the exact same
 3432 one that was previously developed for the Gif++ DAQ and described in Appendix A.5.2.

3433 B.3.2 TDC to RPC link file and Mapping

3434 The same way the INI dimension file information is stored using `map`, the channel mapping and mask
 3435 information is stored and accessed through `map`. First of all, the mapping CSV file is organised into
 3436 3 columns separated by tabulations (and not by commas, as expected for CSV files as it is easier using
 3437 streams to read tab or space separated data using C++):

3438

3439 RPC_channel TDC_channel mask

3440 using as formatting for each field:

3441

3442 TSCCC	TCCC	M
------------------	------	---

3443 TSCCC is a 5-digit integer where τ is the trolley ID, s the slot ID in which the RPC is held insite
 3444 the trolley τ and ccc is the RPC channel number, or *strip* number, that can take values up to
 3445 3-digits depending on the detector,

3446 TCCC is a 4 digit integer where τ is the TDC ID, ccc is the TDC channel number that can take values
 3447 in between 0 and 127, and

3448 M is a 1-digit integer indicating if the channel should be considered ($M = 1$) or discarded ($M = 0$)
 3449 during analysis.

3450 This mapping and masking information is readout and stored thanks to the object `Mapping`, pre-
 3451 sented in Source Code B.4. Similarly to `IniFile` objects, this class has private methods. The first
 3452 one, `Mapping::CheckIfNewLine()` is used to find the newline character '`\n`' or return character
 3453 '`\r`' (depending on which kind of operating system interacted with the file). This is used for the
 3454 simple reason that the masking information has been introduced only during the year 2017 but the
 3455 channel mapping files exist since 2015 and the very beginning of data taking at GIF++. This means
 3456 that in the older data folders, before the upgrade, the channel mapping file only had 2 columns, the
 3457 RPC channel and the TDC channel. For compatibility reasons, this method helps controling the
 3458 character following the readout of the 2 first fields of a line. In case any end of line character is
 3459 found, no mask information is present in the file and the default $M = 1$ is used. On the contrary, if
 3460 the next character was a tabulation or a space, the mask information is present.

3461 Once the 3 fields have been readout, the second private method `Mapping::CheckIfTDCCh()` is
 3462 used to control that the TDC channel is an existing TDC channel. Finally, the information is stored
 3463 into 3 different maps (`Link`, `ReverseLink` and `Mask`) thanks to the public method `Mapping::Read()`.
 3464 `Link` allows to get the RPC channel by knowing the TDC channel while `ReverseLink` does the op-
 3465 posite by returning the TDC channel by knowing the RPC channel. Finally, `Mask` returns the mask
 3466 associated to a given RPC channel.

```

3467 typedef map<Uint,Uint> MappingData;

3468 class Mapping {
3469     private:
3470         bool          CheckIfNewLine(char next);
3471         bool          CheckIfTDCCh(Uint channel);
3472         string        FileName;
3473         MappingData  Link;
3474         MappingData  ReverseLink;
3475         MappingData  Mask;
3476         int           Error;
3477
3478     public:
3479         Mapping();
3480         Mapping(string baseName);
3481         ~Mapping();
3482
3483         void SetFileName(const string filename);
3484         int  Read();
3485         Uint GetLink(Uint tdcchannel);
3486         Uint GetReverse(Uint rpcchannel);
3487         Uint GetMask(Uint rpcchannel);
3488     };

```

3469 *Source Code B.4: Description of C++ object Mapping used as a parser for the channel mapping and mask file.*

3470 B.4 Description of GIF++ setup within the Offline Analysis tool

3471 In the previous section, the tool input files have been discussed. The dimension file information is
 3472 stored in a map hosted by the `IniFile` object. But this information is then used to create a series of
 3473 new objects that helps defining the GIF++ infrastructure directly into the Offline Analysis. Indeed,
 3474 from the `RPC`, to the more general `Infrastructure`, every element of the GIF++ infrastrucutre is
 3475 recreated for each data analysis based on the information provided in input. All this information
 3476 about the infrastructure will be used to assign each hit signal to a specific strip channel of a specific
 3477 detector, and having a specific active area. This way, rate per unit area calculation is possible.
 3478

3479 B.4.1 RPC objects

3480 `RPC` objects have been developped to represent physical active detectors in GIF++ at the moment
 3481 of data taking. Thus, there are as many `RPC` objects created during the analysis than there were
 3482 active `RPC`s tested during a run. Each `RPC` hosts the information present in the corresponding INI
 3483 slot group, as shown in B.3, and organises it using a similar architecture. This can be seen from
 3484 *Source Code B.5*.

3485 To make the object more compact, the lists of gap labels, of gap active areas and strip active
 3486 areas are stored into `vector` dynamical containers. `RPC` objects are always contructed thanks to the
 3487 dimension file information stored into the `IniFILE` and their ID, using the format `TtSs`. Using the
 3488 `RPC` ID, the constructor calls the methods of `IniFILE` to initialise the `RPC`. The other constructors
 3489 are not used but exist in case of need. Finally, some getters have been written to access the different
 3490 private parameters storing the detector information.

```

3491
class RPC{
    private:
        string      name;           //RPC name as in webDCS database
        Uint        nGaps;          //Number of gaps in the RPC
        Uint        nPartitions;    //Number of partitions in the RPC
        Uint        nStrips;         //Number of strips per partition
        vector<string> gaps;       //List of gap labels (BOT, TOP, etc...)
        vector<float>  gapGeo;        //List of gap active areas
        vector<float>  stripGeo;      //List of strip active areas

    public:
        RPC();
        RPC(string ID, IniFile* geofile);
        RPC(const RPC& other);
        ~RPC();
        RPC& operator=(const RPC& other);

        string GetName();
        Uint GetNGaps();
        Uint GetNPartitions();
        Uint GetNStrips();
        string GetGap(Uint g);
        float GetGapGeo(Uint g);
        float GetStripGeo(Uint p);
};

3492

```

3493 *Source Code B.5: Description of C++ objects RPC that describe each active detectors used during data taking.*

3494 B.4.2 Trolley objects

3495 Trolley objects have been developped to represent physical active trolleys in GIFT++ at the moment
 3496 of data taking. Thus, there are as many trolley objects created during the analysis than there were
 3497 active trolleys hosting tested RPCs during a run. Each Trolley hosts the information present in the
 3498 corresponding INI trolley group, as shown in B.2, and organises it using a similar architecture. In
 3499 addition to the information hosted in the INI file, these object have a dynamical container of RPC
 3500 objects, representing the active detectors the active trolley was hosting at the time of data taking.
 3501 This can been seen from Source Code B.6.

3502 Trolley objects are always contructed thanks to the dimension file information stored into the
 3503 IniFILE and their ID, using the format Tt. Using the Trolley ID, the constructor calls the methods
 3504 of IniFILE to initialise the Trolley. Retrieving the information of the RPC IDs via SlotsID, a new
 3505 RPC is constructed and added to the container RPCs for each character in the ID string. The other
 3506 constructors are not used but exist in case of need. Finally, some getters have been written to access
 3507 the different private parameters storing the trolley and detectors information.

```

3508
class Trolley{
    private:
        Uint          nSlots; //Number of active RPCs in the considered trolley
        string        SlotsID; //Active RPC IDs written into a string
        vector<RPC*> RPCs;   //List of active RPCs

    public:
        //Constructors, destructor and operator =
        Trolley();
        Trolley(string ID, IniFile* geofile);
        Trolley(const Trolley& other);
        ~Trolley();
        Trolley& operator=(const Trolley& other);

        //Get GIFTrolley members
        Uint  GetNSlots();
        string GetSlotsID();
        Uint   GetSlotID(Uint s);

        //Manage RPC list
        RPC*  GetRPC(Uint r);
        void  DeleteRPC(Uint r);

        //Methods to get members of RPC objects stored in RPCs
        string GetName(Uint r);
        Uint   GetNGaps(Uint r);
        Uint   GetNPartitions(Uint r);
        Uint   GetNStrips(Uint r);
        string GetGap(Uint r, Uint g);
        float  GetGapGeo(Uint r, Uint g);
        float  GetStripGeo(Uint r, Uint p);
    };

```

Source Code B.6: Description of C++ objects `Trolley` that describe each active trolley used during data taking.

3511 B.4.3 Infrastructure object

3512 The `Infrastructure` object has been developped to represent the GIFT++ bunker area dedicated to
 3513 CMS RPC experiments. With this very specific object, all the information about the CMS RPC
 3514 setup within GIFT++ at the moment of data taking is stored. It hosts the information present in the
 3515 corresponding INI general group, as shown in B.1, and organises it using a similar architecture. In
 3516 addition to the information hosted in the INI file, this object have a dynamical container of `Trolley`
 3517 objects, representing the active tolleys in GIFT++ area. This can be seen from Source Code B.7.

3518 The `Infrastructure` object is always contructed thanks to the dimension file information stored
 3519 into the `IniFILE`. Retrieving the information of the trolley IDs via `TrolleysID`, a new `Trolley` is
 3520 constructed and added to the container `Trolleys` for each character in the ID `string`. By extension,
 3521 it is easy to understand that the process described in Section B.4.2 for the construction of RPCs
 3522 takes place when a trolley is constructed. The other constructors are not used but exist in case of
 3523 need. Finally, some getters have been written to access the different private parameters storing the
 3524 infrastructure, tolleys and detectors information.

```

3525
class Infrastructure {
    private:
        Uint             nTrolleys;   //Number of active Trolleys in the run
        string          TrolleysID;  //Active trolley IDs written into a string
        vector<Trolley*> Trolleys;  //List of active Trolleys (struct)

    public:
        //Constructors and destructor
        Infrastructure();
        Infrastructure(IniFile* geofile);
        Infrastructure(const Infrastructure& other);
        ~Infrastructure();
        Infrastructure& operator=(const Infrastructure& other);

        //Get Infrastructure members
        Uint  GetNTrolleys();
        string GetTrolleysID();
        Uint   GetTrolleyID(Uint t);

3526
        //Manage Trolleys
        Trolley* GetTrolley(Uint t);
        void     DeleteTrolley(Uint t);

        //Methods to get members of GIFTrolley objects stored in Trolleys
        Uint  GetNSlots(Uint t);
        string GetSlotsID(Uint t);
        Uint   GetSlotID(Uint t, Uint s);
        RPC*  GetRPC(Uint t, Uint r);

        //Methods to get members of RPC objects stored in RPCs
        string GetName(Uint t, Uint r);
        Uint   GetNGaps(Uint t, Uint r);
        Uint   GetNPartitions(Uint t, Uint r);
        Uint   GetNStrips(Uint t, Uint r);
        string GetGap(Uint t, Uint r, Uint g);
        float  GetGapGeo(Uint t, Uint r, Uint g);
        float  GetStripGeo(Uint t, Uint r, Uint p);
    };

```

Source Code B.7: Description of C++ object Infrastructure that contains the full information about CMS RPC experiment in GIF++.

3528 B.5 Handeling of data

3529 As discussed in Appendix A.4.2, the raw data as a `TTree` architecture where every entry is related to
 3530 a trigger signal provided by a muon or a random pulse, whether the goal of the data taking was to
 3531 measure the performance of the detector or the noise/gamma background respectively. Each of these
 3532 entries, referred also as events, contain a more or less full list of hits in the TDC channels to which
 3533 the detectors are connected. To this list of hits corresponds a list of time stamps, marking the arrival
 3534 of the hits within the TDC channel.

3535 The infrastructure of the CMS RPC experiment within `GIF++` being defined, combining the
 3536 information about the raw data with the information provided by both the mapping/mask file and the
 3537 dimension file allows to build new physical objects that will help in computing efficiency or rates.

B.5.1 RPC hits

3539 The raw data stored in the ROOT file as output of the GIFT++ DAQ, is readout by the analysis tool
3540 using the structure `RAWData` presented in Source Code B.9 that differs from the structure presented
3541 in Appendix A.4.2 as it is not meant to hold all of the data contained in the ROOT file. In this sense,
3542 this structure is in the case of the offline analysis tool not a dynamical object and will only be storing
3543 a single event contained in a single entry of the `TTree`.

```

3544
class RPCHit {
    private:
        Uint Channel;           //RPC channel according to mapping (5 digits)
        Uint Trolley;          //0, 1 or 3 (1st digit of the RPC channel)
        Uint Station;           //Slot where is held the RPC in Trolley (2nd digit)
        Uint Strip;             //Physical RPC strip where the hit occurred (last 3
    → digits)
        Uint Partition;         //Readout partition along eta segmentation
        float TimeStamp;        //Time stamp of the arrival in TDC

    public:
        //Constructors, destructor & operator =
        RPCHit();
        RPCHit(Uint channel, float time, Infrastructure* Infra);
        RPCHit(const RPCHit& other);
        ~RPCHit();
        RPCHit& operator=(const RPCHit& other);

        //Get RPCHit members
        Uint GetChannel();
        Uint GetTrolley();
        Uint GetStation();
        Uint GetStrip();
        Uint GetPartition();
        float GetTime();
};

typedef vector<RPCHit> HitList;
typedef struct GIFHitList { HitList rpc[NTROLLEYS][NSLOTS][NPARTITIONS]; }
→ GIFHitList;

bool SortHitbyStrip(RPCHit h1, RPCHit h2);
bool SortHitbyTime(RPCHit h1, RPCHit h2);

```

Source Code B.8: Description of C++ object `RPCHit`.

```
3547 struct RAWData{  
    int iEvent; //Event i  
    int TDCNHits; //Number of hits in event i  
    int QFlag; //Quality flag list (1 flag digit per TDC)  
    vector<UInt> *TDCCh; //List of channels giving hits per event  
    vector<float> *TDCTS; //List of the corresponding time stamps  
};
```

Source Code B.9: Description of C++ structure RAWData.

3549 Each member of the structure is then linked to the corresponding branch of the ROOT data tree,
3550 as shown in the example of Source Code B.10, and using the method `GetEntry(int i)` of the ROOT
3551 class `TTree` will update the state of the members of `RAWData`.

```

3552   TTree* dataTree = (TTree*)dataFile.Get("RAWData");
3553   RAWData data;
3554
3555   dataTree->SetBranchAddress("EventNumber", &data.iEvent);
3556   dataTree->SetBranchAddress("number_of_hits", &data.TDCNHits);
3557   dataTree->SetBranchAddress("Quality_flag", &data.QFlag);
3558   dataTree->SetBranchAddress("TDC_channel", &data.TDCCh);
3559   dataTree->SetBranchAddress("TDC_TimeStamp", &data.TDCTS);

```

3554 *Source Code B.10: Example of link in between RAWData and TTree.*

3555 The data is then analysed entry by entry and to each element of the TDC channel list, a `RPCHit` is
 3556 constructed by linking each TDC channel to the corresponding RPC channel thanks to the `Mapping`
 3557 object. The information carried by the RPC channel format allows to easily retrieve the trolley and
 3558 slot from which the hit was recorded (see section B.3.2). Using these 2 values, the readout partition
 3559 can be found by knowing the strip channel and comparing it with the number of partitions and strips
 3560 per partition stored into the `Infrastructure` object.

3561 Thus `RPCHit` objects are then stored into 3D dynamical list called `GIFHitList` (Source Code B.9)
 3562 where the 3 dimensions refer to the 3 layers of the readout in `GIF++` : in the bunker there are *trolleys*
 3563 (τ) holding detectors in *slots* (s) and each detector readout is divided into 1 or more pseudo-rapidity
 3564 *partitions* (p). Using these 3 information allows to assign an address to each readout partition and
 3565 this address will point to a specific hit list.

3566

3567 **B.5.2 Clusters of hits**

3568 All the hits contained in the ROOT file have been sorted into the different hit lists through the
 3569 `GIFHitList`. At this point, it is possible to start looking for clusters. A cluster is a group of adjacent
 3570 strips getting hits within a time window of 25 ns. These strips are then assumed to be part of the same
 3571 physical avalanche signal generated by a muon passing through the chamber or by the interaction of
 3572 a gamma stopping into the electrodes of the RPCs.

3573 To keep the cluster information, `RPCCluster` objects have been defined as shown in Source
 3574 Code B.11. Using the information of each individual `RPCHit` taken out of the hit list, it stores
 3575 the cluster size (number of adjacent strips composing the cluster), the first and last hit, the center for
 3576 spatial reconstruction and finally the start and stop time stamps as well as te time spread in between
 3577 the first and last hit.

```

3578
class RPCCluster{
    private:
        Uint ClusterSize; //Size of cluster #ID
        Uint FirstStrip; //First strip of cluster #ID
        Uint LastStrip; //Last strip of cluster #ID
        float Center; //Center of cluster #ID ((first+last)/2)
        float StartStamp; //Time stamp of the earliest hit of cluster #ID
        float StopStamp; //Time stamp of the latest hit of cluster #ID
        float TimeSpread; //Time difference between earliest and latest hits
                           //of cluster #ID

    public:
        //Constructors, destructor & operator =
        RPCCluster();
        RPCCluster(HitList List, Uint cID, Uint cSize, Uint first, Uint firstID);
        RPCCluster(const RPCCluster& other);
        ~RPCCluster();
        RPCCluster& operator=(const RPCCluster& other);

        //Get Cluster members
        Uint GetID();
        Uint GetSize();
        Uint GetFirstStrip();
        Uint GetLastStrip();
        float GetCenter();
        float GetStart();
        float GetStop();
        float GetSpread();
};

typedef vector<RPCCluster> ClusterList;

//Other functions to build cluster lists out of hit lists
void BuildClusters(HitList &cluster, ClusterList &clusterList);
void Clusterization(HitList &hits, TH1 *hcSize, TH1 *hcMult);

```

Source Code B.11: Description of C++ object cluster.

To investigate the hit list of a given detector partition, the function `Clusterization()` defined in `include/Cluster.h` needs the hits in the list to be time sorted. This is achieved by calling function `sort()` of library `<algorithm>` using the comparator `SortHitbyTime(RPCHit h1, RPCHit h2)` defined in `include/RPCHit.h` that returns `true` if the time stamp of hit `h1` is lower than that of `h2`. A first isolation of strips is made only based on time information. All the hits within the 25 ns window are taken separately from the rest. Then, this sub-list of hits is sorted this time by ascending strip number, using this time the comparator `SortHitbyStrip(RPCHit h1, RPCHit h2)`. Finally, the groups of adjacent strips are used to construct `RPCCluster` objects that are then stored in a temporary list of clusters that is at the end of the process used to know how many clusters were reconstructed and to fill their sizes into an histogram that will allows to know the mean size of muon or gamma clusters.

3593 B.6 DAQ data Analysis

All the ingredients to analyse GIF++ data have been defined. This section will focus on the different part of the analysis performed on the data, from determining the type of data the tool is dealing with

3596 to calculating the rate in each detector or reconstructing muon or gamma clusters.

3597 B.6.1 Determination of the run type

3598 In GIF++, both the performance of the detectors in detecting muons in an irradiated environment and
 3599 the gamma background can be independantly measured. These corresponds to different run types
 3600 and thus, to different TDC settings giving different data to look at.

3601

3602 In the case of performance measurements, the trigger for data taking is provided by the coïncidence
 3603 of several scintillators when muons from the beam passing through the area are detected. Data
 3604 is collected in a 600 ns wide window around the arrival of muons in the RPCs. The expected time
 3605 distribution of hits is shown in Figure B.1a. The muon peak is clearly visible in the center of the
 3606 distribution and is to be extracted from the gamma background that composes the flat part of the
 3607 distribution.

3608 On the other hand, gamma background or noise measurements are focussed on the non muon
 3609 related physics and the trigger needs to be independant from the muons to give a good measurement
 3610 of the gamma/noise distribution as seen by the detectors. The trigger is then provided by a pulse
 3611 generator at a frequency of 300 Hz whose pulse is not likely to be on time with a muon. In order
 3612 to increase the integrated time without increasing the acquisition time too much, the width of the
 3613 acquisition windows are increased to 10 μ s. The time distribution of the hits is expected to be flat, as
 3614 shown by Figure B.1b.

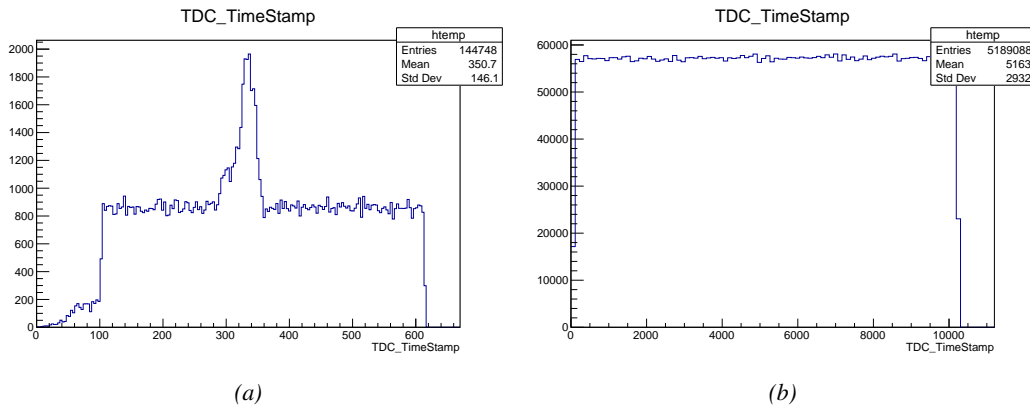


Figure B.1: Example of expected hit time distributions in the cases of efficiency (Figure B.1a) and noise/gamma rate per unit area (Figure B.1b) measurements as extracted from the raw ROOT files. The unit along the x-axis corresponds to ns. The fact that "the" muon peak is not well defined in Figure B.1a is due to the contribution of all the RPCs being tested at the same time that don't necessarily have the same signal arrival time. Each individual peak can have an offset with the ones of other detectors. The inconsistency in the first 100 ns of both time distributions is an artefact of the TDCs and are systematically rejected during the analysis.

3615 The ROOT files include a TTree called RunParameters containing, among other things, the in-
 3616 formation related to the type of run. The run type can then be accessed as described by Source
 3617 Code B.12 and the function IsEfficiencyRun() is then used to determine if the run file is an effi-
 3618 ciency run or, on the contrary, another type of run (noise or gamma measurement).

```

3619     TTree* RunParameters = (TTree*)dataFile.Get("RunParameters");
3620     TString* RunType = new TString();
3621     RunParameters->SetBranchAddress("RunType", &RunType);
3622     RunParameters->GetEntry(0);

```

3621 *Source Code B.12: Access to the run type contained in TTree* RunParameters.*

3622 Finally, the data files will have a slightly different content whether it was collected before or after
 3623 October 2017 and the upgrade of the DAQ software that brought a new information into the ROOT
 3624 output. This is discussed in Appendix A.4.3 and implies that the analysis will differ a little depending
 3625 on the data format. Indeed, as no information on the data quality is stored, in older data files, the cor-
 3626 rections for missing events has to be done at the end of the analysis. The information about the type
 3627 of data format is stored in the variable **bool** `isNewFormat` by checking the list of branches contained
 3628 in the data tree via the methods `TTree::GetListOfBranches()` and `TCollection::Contains()`.

3629 **B.6.2 Beam time window calculation for efficiency runs**

3630 Knowing the run type is important first of all to know the width of the acquisition window to be used
 3631 for the rate calculation and finally to be able to seek for muons. Indeed, the peak that appears in the
 3632 time distribution for each detectors is then fitted to extract the most probable time window in which
 3633 the tool should look for muon hits. The data outside of this time window is then used to evaluate the
 3634 noise or gamma background the detector was subjected to during the data taking. Computing the
 3635 position of the peak is done calling the function `SetBeamWindow()` defined in file `src/RPCHit.cc` that
 3636 loops a first time on the data. The data is first sorted in a 3D array of 1D histograms (`GIFH1Array`, see
 3637 `include/types.h`). Then the location of the highest bin is determined using `TH1::GetMaximumBin()`
 3638 and is used to define a window in which a gaussian fit will be applied to compute the peak width.
 3639 This window is a 80 ns defined by Formula B.1 around the central bin.

$$t_{center}(ns) = bin \times width_{bin}(ns) \quad (\text{B.1a})$$

$$[t_{low}; t_{high}] = [t_{center} - 40; t_{center} + 40] \quad (\text{B.1b})$$

3640 Before the fit is performed, the average number of noise/gamma hits per bin is evaluated using
 3641 the data outside of the fit window. Excluding the first 100 ns, the average number of hits per bin
 3642 due to the noise or gamma is defined by Formula B.2 after extracting the amount of hits in the time
 3643 windows $[100; t_{low}]$ and $[t_{high}; 600]$ thanks to the method `TH1::Integral()`. This average number
 3644 of hits is then subtracted to every bin of the 1D histogram, in order to *clean* it from the noise or
 3645 gamma contribution as much as possible to improve the fit quality. Bins where $\langle n_{hits} \rangle$ is greater
 3646 than the actual bin content are set to 0.

$$\Delta t_{noise}(ns) = 600 \overbrace{-t_{high} + t_{low}}^{-80ns} - 100 = 420ns \quad (\text{B.2a})$$

$$\langle n_{hits} \rangle = width_{bin}(ns) \times \frac{\sum_{t=100}^{t_{low}} + \sum_{t=t_{high}}^{600}}{\Delta t_{noise}(ns)} \quad (\text{B.2b})$$

3647 Finally, the fit parameters are extracted and saved for each detector in 3D arrays of **float**
 3648 (`muonPeak`, see `include/types.h`), a first one for the mean arrival time of the muons, `PeakTime`,

3649 and a second one for the width of the peak, `PeakWidth`. The width is defined as 6σ of the gaussian
 3650 fit. The same settings are applied to every partitions of the same detector. To determine which one
 3651 of the detector's partitions is directly illuminated by the beam, the peak height of each partition is
 3652 compared and the highest one is then used to define the peak settings.

3653 **B.6.3 Data loop and histogram filling**

3654 3D arrays of histogram are created to store the data and display it on the DQM of GIF++ webDCS
 3655 for the use of shifters. These histograms, presented in section B.2.1.1, are filled while looping on
 3656 the data. Before starting the analysis loop, it is necessary to control the entry quality for the new
 3657 file formats featuring `QFlag`. If the `QFlag` value for this entry shows that 1 TDC or more have a
 3658 `CORRUPTED` flag, then this event is discarded. The loss of statistics is low enough to be neglected.
 3659 `QFlag` is controled using the function `IsCorruptedEvent()` defined in `src/utils.cc`. As explained
 3660 in Appendix A.4.3, each digit of this integer represent a TDC flag that can be 1 or 2. Each 2 is
 3661 the sign of a `CORRUPTED` state. Then, the data is accessed entry by entry in the ROOT `TTree` using
 3662 `RAWData` and each hit in the hit list is assigned to a detector channel and saved in the corresponding
 3663 histograms. In the first part of the analysis, in which the loop over the ROOT file's content is
 3664 performed, the different steps are:

3665 **1- RPC channel assignment and control:** a check is done on the RPC channel extracted thanks
 3666 to the mapping via the method `Mapping::GetLink()`. If the channel is not initialised and is 0, or if
 3667 the TDC channel was greater than 5127, the hit is discarded. This means there was a problem in the
 3668 mapping. Often a mapping problem leads to the crash of the offline tool.

3669 **2- Creation of a `RPCHit` object:** to easily get the trolley, slot and partition in which the hit has
 3670 been assigned, this object is particularly helpful.

3671 **3- General histograms are filled:** the hit is filled into the time distribution and the general hit
 3672 distribution histograms, and if the arrival time is within the first 100 ns, it is discarded and nothing
 3673 else happens and the loop proceeds with the next hit in the list.

3674 **4- Multiplicity counter:** the hit multiplicity counter of the corresponding detectors incremented.

3675 **5-a- Efficiency runs - Is the hit within the peak window? :** if the peak is contained in the peak
 3676 window previously defined in section B.6.2, the hit is filled into the beam hit profile histogram of
 3677 the corresponding chamber, added into the list of muon hits and increments the counter of *in time*
 3678 hits. The term *in time* here refers to the hits that are likely to be muons by arriving in the expected
 3679 time window. If the hit is outside of the peak window, it is filled into the noise profile histogram
 3680 of the corresponding detector, added into the list of noise/gamma hits and increments the counter of
 3681 noise/gamma hits.

3682 **5-b- Noise/gamma rate runs - Noise histograms are filled:** the hit is filled into the noise profile
 3683 histogram of the corresponding detector, added into the list of noise/gamma hits and increments the
 3684 counter of noise/gamma hits.

3686 After the loop on the hit list of the entry is over, the next step is to clusterize the 3D lists filled
 3687 in the previous steps. A 3D loop is then started over the active trolley, slot and RPC partitions to
 3688 access these objects. Each `NoiseHitList` and `MuonHitList`, in case of efficiency run, are clusterized
 3689 as described in section B.5.2. There corresponding cluster size and multiplicity histograms are filled
 3690 at the end of the clustering process. Then, the efficiency histogram is filled in case of efficiency run.
 3691 The selection is simply made by checking whether the RPC detected signals in the peak window
 3692 during this event. Nevertheless, it is useful to highlight that at this level, it is not possible yet to
 3693 discriminate in between a muon hit and noise or gamma hit. Thus, `MuonCSize_H`, `MuonCMult_H`
 3694 and `Efficiency0_H` are subjected to noise and gamma contamination. This contamination will be
 3695 estimated and corrected at the moment the results will be written into output CSV files. Finally, the
 3696 loop ends on the filling of the general hit multiplicity histogram.

3697 **B.6.4 Results calculation**

3698 As mentioned in section B.2.1, the analysis of DAQ data provides the user with 3 CSV files and
 3699 a ROOT file associated to each and every ROOT data file. The fourth CSV file is provided by the
 3700 extraction of the CEAN main frame data monitored during data taking and will be discussed later.
 3701 After looping on the data in the previous part of the analysis macro, the output files are created and a
 3702 3D loop on each RPC readout partitions is started to extract the histograms parameters and compute
 3703 the final results.

3704

3705 **B.6.4.1 Rate normalisation**

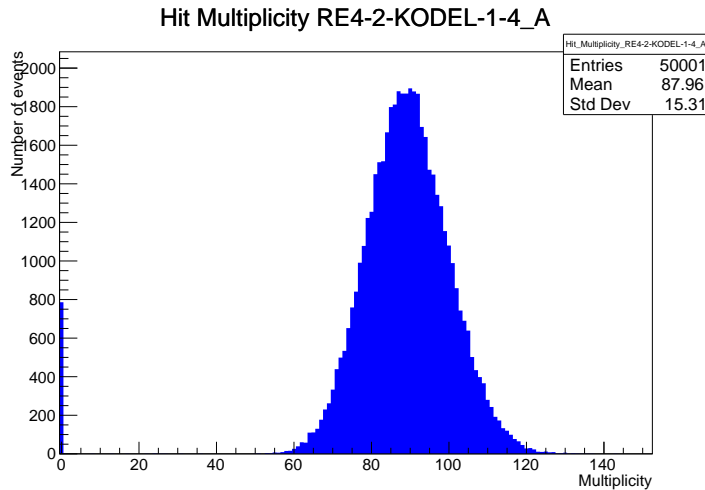


Figure B.2: The effect of the quality flag is explained by presenting the reconstructed hit multiplicity of a data file without `Quality_flag`. The artificial high content of bin 0 is the effect of corrupted data.

3706 To analyse old data format files, not containing any quality flag, it is needed to estimate the amount
 3707 of corrupted data via a fit as the corrupted data will always fill events with a fake "0 multiplicity".
 3708 Indeed, as no hits were stored in the DAQ ROOT files, these events artificially contribute to fill
 3709 the bin corresponding to a null multiplicity, as shown in Figure B.2. In the case the mean of the

3710 hit multiplicity distribution is high, the contribution of the corrupted data can easily be evaluated
 3711 for later correction by comparing the level of the bin at multiplicity 0 and of a skew fit curve that
 3712 should indicate a value consistent with 0. A skew fit has been chosen over a Poisson fit as it was
 3713 giving better results for lower mean multiplicity values. Nevertheless, for low irradiation cases,
 3714 as explained in Appendix A.4.3, the hit multiplicity distribution mean is, on the contrary, rather
 3715 small and the probability to record events without hits can't be considered small anymore, leading
 3716 to a difficult and non-reliable estimation of the corruption. As can be seen in Source Code B.13,
 3717 conditions have been applied to prevent bad fits and wrong corruption estimation in cases where :

3718 • The difference in between the data for multiplicity 1 and the corresponding fit value should be
 3719 lower than 1% of the total amount of data : $\frac{|n_{m=1} - sk(1)|}{N_{tot}} < 0.01$ where $n_{m=1}$ is the number
 3720 of entries with multiplicity 1, $sk(1)$ the value of the skew fit, as defined by Formula 5.3, for
 3721 multiplicity 1 and N_{tot} the total number of entries.

3722 • The amount of data contained in the multiplicity 0 bin should not exceed 40% : $\frac{n_{m=0}}{N_{tot}} \leq 0.4$
 3723 where $n_{m=0}$ is the number of entries with multiplicity 0. This number has been determined
 3724 to be the maximum to be able to separate the excess of data due to corruption from the hit
 3725 multiplicity distribution.

3726 Those 2 conditions need to be fulfilled to estimate the corruption of old data format files. If the
 3727 fit was successful, the level of corruption is written in `Offline-Corrupted.csv` and the number of
 3728 corrupted entries, refered as the integer `nEmptyEvent`, is subtracted from the total number of entries
 3729 when the rate normalisation factor is computed as explicit in Source Code B.13. Note that for new
 3730 data format files, the number of corrupted entries being set to 0, the definition of `rate_norm` stays
 3731 valid.

```

3732   if(!isNewFormat){
      TF1* GaussFit = new TF1("gaussfit","[0]*exp(-0.5*((x-[1])/[2])**2)",0,Xmax);
      GaussFit->SetParameter(0,100);
      GaussFit->SetParameter(1,10);
      GaussFit->SetParameter(2,1);
      HitMultiplicity_H.rpc[T][S][p]->Fit(GaussFit,"LIQR","");
      HitMultiplicity_H.rpc[T][S][p]->Fit(GaussFit,"LIQR","");
      TF1* SkewFit = new TF1("skewfit","[0]*exp(-0.5*((x-[1])/[2])**2) / (1 +
→      exp(-[3]*(x-[4])))",0,Xmax);
      SkewFit->SetParameter(0,GaussFit->GetParameter(0));
      SkewFit->SetParameter(1,GaussFit->GetParameter(1));
      SkewFit->SetParameter(2,GaussFit->GetParameter(2));
      SkewFit->SetParameter(3,1);
      SkewFit->SetParameter(4,1);
      HitMultiplicity_H.rpc[T][S][p]->Fit(SkewFit,"LIQR","");
      HitMultiplicity_H.rpc[T][S][p]->Fit(SkewFit,"LIQR","");
      double fitValue = SkewFit->Eval(1,0,0,0);
      double dataValue = (double)HitMultiplicity_H.rpc[T][S][p]->GetBinContent(2);
      double difference = TMath::Abs(dataValue - fitValue);
      double fitTOdataVSentries_ratio = difference / (double)nEntries;
      bool isFitGOOD = fitTOdataVSentries_ratio < 0.01;

3733   double nSinglehit = (double)HitMultiplicity_H.rpc[T][S][p]->GetBinContent(1);
   double lowMultRatio = nSinglehit / (double)nEntries;
   bool isMultLOW = lowMultRatio > 0.4;

   if(isFitGOOD && !isMultLOW){
      nEmptyEvent = HitMultiplicity_H.rpc[T][S][p]->GetBinContent(1);
      nPhysics = (int)SkewFit->Eval(0,0,0,0);
      if(nPhysics < nEmptyEvent)
         nEmptyEvent = nEmptyEvent-nPhysics;
   }
}

double corrupt_ratio = 100.*(double)nEmptyEvent / (double)nEntries;
outputCorrCSV << corrupt_ratio << '\t';

float rate_norm = 0.;
float stripArea = GIFIInfra->GetStripGeo(tr,sl,p);

if(IsEfficiencyRun(RunType)){
   float noiseWindow = BMTDCWINDOW - TIMEREJECT - 2*PeakWidth.rpc[T][S][p];
   rate_norm = (nEntries-nEmptyEvent)*noiseWindow*1e-9*stripArea;
} else
   rate_norm = (nEntries-nEmptyEvent)*RDMNOISEWDW*1e-9*stripArea;

```

Source Code B.13: Definition of the rate normalisation variable. It takes into account the number of non corrupted entries and the time window used for noise calculation, to estimate the total integrated time, and the strip active area to express the result as rate per unit area.

3735 B.6.4.2 Rate and activity

3736 At this point, the strip rate histograms, StripNoiseProfile_H.rpc[T][S][p], only contain an in-
 3737 formation about the total number of noise or rate hits each channel received during the data taking.
 3738 As described in Source Code B.14, a loop on the strip channels will be used to normalise the content
 3739 of the rate distribution histogram for each detector partitions. The initial number of hits recorded for
 3740 a given bin will be extracted and 2 values will be computed:

- 3741 ● the strip rate, defined as the number of hits recorded in the bin normalised like described in
 3742 the previous section, using the variable `rate_norm`, and

- 3743 ● the strip activity, defined as the number of hits recorded in the bin normalised to the average
 3744 number of hits per bin contained in the partition histogram, using the variable `averageNhit`.
 3745 This value provides an information on the homogeneity of the detector response to the gamma
 3746 background or of the detector noise. An activity of 1 corresponds to an average response.
 3747 Above 1, the channel is more active than the average and bellow 1, the channel is less active.

```

int nNoise = StripNoiseProfile_H.rpc[T][S][p]->GetEntries();
float averageNhit = (nNoise>0) ? (float)(nNoise/nStripsPart) : 1.;

for(Uint st = 1; st <= nStripsPart; st++) {
    float stripRate =
        StripNoiseProfile_H.rpc[T][S][p]->GetBinContent(st)/rate_norm;
    float stripAct =
        StripNoiseProfile_H.rpc[T][S][p]->GetBinContent(st)/averageNhit;

    StripNoiseProfile_H.rpc[T][S][p]->SetBinContent(st,stripRate);
    StripActivity_H.rpc[T][S][p]->SetBinContent(st,stripAct);
}

```

3749 *Source Code B.14: Description of the loop that allows to set the content of each strip rate and strip activity
 channel for each detector partition.*

3750 On each detector partitions, which are readout by a single FEE, all the channels are not processed
 3751 by the same chip. Each chip can give a different noise response and thus, histograms using a chip
 3752 binning are used to investigate chip related noise behaviours. The average values of the strip rate
 3753 or activity grouped into a given chip are extracted using the using the function `GetChipBin()` and
 3754 stored in dedicated histograms as described in Source Codes B.15 and B.16 respectively.

```

3755 float GetChipBin(TH1* H, Uint chip){
    Uint start = 1 + chip*NSTRIPSCHIP;
    int nActive = NSTRIPSCHIP;
    float mean = 0.;

    for(Uint b = start; b <= (chip+1)*NSTRIPSCHIP; b++) {
        float value = H->GetBinContent(b);
        mean += value;
        if(value == 0.) nActive--;
    }

    if(nActive != 0) mean /= (float)nActive;
    else mean = 0.;

    return mean;
}

```

3757 *Source Code B.15: Function used to compute the content of a bin for an histogram using chip binning.*

```

3758     for(UInt ch = 0; ch < (nStripsPart/NSTRIPSCHIP); ch++) {
      ChipMeanNoiseProf_H.rpc[T][S][p]->
          SetBinContent(ch+1,GetChipBin(StripNoiseProfile_H.rpc[T][S][p],ch));
      ChipActivity_H.rpc[T][S][p]->
          SetBinContent(ch+1,GetChipBin(StripActivity_H.rpc[T][S][p],ch));
}

```

Source Code B.16: Description of the loop that allows to set the content of each chip rate and chip activity bins for each detector partition knowing the information contained in the corresponding strip distribution histograms.

The activity variable is used to evaluate the homogeneity of the detector response to background or of the detector noise. The homogeneity h_p of each detector partition can be evaluated using the formula $h_p = \exp(-\sigma_p^R / \langle R \rangle_p)$, where $\langle R \rangle_p$ is the partition mean rate and σ_p^R is the rate standard deviation calculated over the partition channels. The more homogeneously the rates are distributed and the smaller will σ_p^R be, and the closer to 1 will h_p get. On the contrary, if the standard deviation of the channel's rates is large, h_p will rapidly get to 0. This value is saved into histograms as shown in Source Code B.17 and could in the future be used to monitor through time, once extracted, the evolution of every partition homogeneity. This could be of great help to understand the apparition of eventual hot spots due to ageing of the chambers subjected to high radiation levels. The monitored homogeneity information could then be combined with a monitoring of the activity of each individual channel in order to have a finer information. Monitoring tools have been suggested and need to be developed for this purpose.

```

3772     float MeanPartSDev = GetTH1StdDev(StripNoiseProfile_H.rpc[T][S][p]);
     float strip_homog = (MeanPartRate==0)
        ? 0.
        : exp(-MeanPartSDev/MeanPartRate);
     StripHomogeneity_H.rpc[T][S][p]->Fill("exp -#left(#frac{\#sigma_{Strip
        \rightarrow Rate}}{\#mu_{Strip Rate}}\#right)",strip_homog);
     StripHomogeneity_H.rpc[T][S][p]->GetYaxis()->SetRangeUser(0.,1.);

3773     float ChipStDevMean = GetTH1StdDev(ChipMeanNoiseProf_H.rpc[T][S][p]);
     float chip_homog = (MeanPartRate==0)
        ? 0.
        : exp(-ChipStDevMean/MeanPartRate);
     ChipHomogeneity_H.rpc[T][S][p]->Fill("exp -#left(#frac{\#sigma_{Chip
        \rightarrow Rate}}{\#mu_{Chip Rate}}\#right)",chip_homog);
     ChipHomogeneity_H.rpc[T][S][p]->GetYaxis()->SetRangeUser(0.,1.);

```

Source Code B.17: Storage of the homogeneity into dedicated histograms.

3775 B.6.4.3 Strip masking tool

The offline tool is automatically called at the end of each data taking to analyse the data and offer the shifter DQM histograms to control the data quality. After the histograms have been published online in the DQM page, the shifter can decide to mask noisy or dead channels that will contribute to bias the final rate calculation by editing the mask column of `ChannelsMapping.csv` as can be seen in Figure B.3.

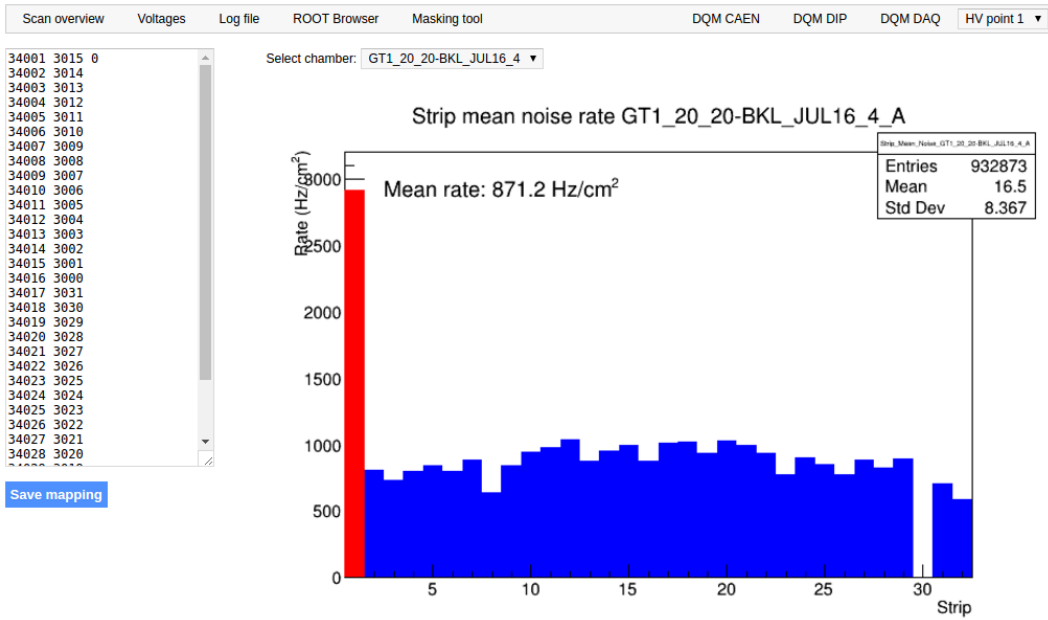


Figure B.3: Display of the masking tool page on the webDCS. The window on the left allows the shifter to edit ChannelsMapping.csv. To mask a channel, it only is needed to set the 3rd field corresponding to the strip to mask to 0. It is not necessary for older mapping file formats to add a 1 for each strip that is not masked as the code is versatile and the default behaviour is to consider missing mask fields as active strips. The effect of the mask is directly visible for noisy channels as the corresponding bin turns red. The global effect of masking strips will be an update of the rate value showed on the histogram that will take into consideration the rejected channels.

3781 From the code point of view, the function `GetTH1Mean()` is used to retrieve the mean rate par-
 3782 tition by partition after the rates have been calculated strip by strip and filled into the histograms
 3783 `StripNoiseProfile_H.rpc[T][S][p]`, as described through Source Code B.18.

3784 Once the mask for each rejected channel has been updated, the shifter can manually run the of-
 3785 fline tool again to update the DQM plots, now including the masked strips, as well the rate results
 3786 written in the output CSV file `Offline-Rate.csv`. If not done during the shifts, the strip masking
 3787 procedure needs to be carefully done by the person in charge of data analysis on the scans that were
 3788 selected to produce the final results.

```

3789
float GetTH1Mean(TH1* H) {
    int nBins = H->GetNbinsX();
    int nActive = nBins;
    float mean = 0.;

    for(int b = 1; b <= nBins; b++) {
        float value = H->GetBinContent(b);
        mean += value;
        if(value == 0.) nActive--;
    }

    if(nActive != 0) mean /= (float)nActive;
    else mean = 0.;

    return mean;
}

```

Source Code B.18: The function `GetTH1Mean()` is used to return the mean along the y-axis of TH1 histograms containing rate information. In order to take into account masked strips whose rate is set to 0, the function looks for masked channels and decrement the number of active channels for each null value found.

3792 B.6.4.4 Output CSV files filling

3793 All the histograms have been filled. Parameters will then be extracted from them to compute the
 3794 final results that will later be used to produce plots. Once the results have been computed, the very
 3795 last step of the offline macro is to write these values into the corresponding CSV outputs. Aside of
 3796 the file `Offline-Corrupted.csv`, 2 CSV files are being written by the macro `offlineAnalysis()`,
 3797 `Offline-Rates.csv` and `Offline-L0-EffCl.csv` that respectively contain information about noise
 3798 or gamma rates, cluster size and multiplicity, and about level 0 reconstruction of the detector effi-
 3799 ciency, muon cluster size and multiplicity. Details on the computation and file writing are respec-
 3800 tively given in Sources Codes B.19 and B.20.

3801 **Noise/gamma background variables** are computed and written in the output file for each detector
 3802 partitions. A detector average of the hit and cluster rate is also provided, as shown through Sources
 3803 Code B.19. The variables that are written for each partition are:

- 3804 • The mean partition hit rate per unit area, `MeanPartRate`, that is extracted from the histogram
 3805 `StripNoiseProfile_H` as the mean value along the y-axis, as described in section B.6.4.3. No
 3806 error is recorded for the hit rate as this is considered a single measurement. No statistical error
 3807 can be associated to it and the systematics are unknown.
- 3808 • The mean cluster size, `cSizePart`, is extracted from the histogram `NoiseCSize_H` and it's
 3809 statistical error, `cSizePartErr`, is taken to be 2σ of the total distribution.
- 3810 • The mean cluster multiplicity per trigger, `cMultPart`, is extracted from the histogram `NoiseCMult_H`
 3811 and it's statistical error, `cMultPartErr`, is taken to be 2σ of the total distribution. It is impor-
 3812 tant to point to the fact that this variable gives an information that is dependent on the buffer
 3813 window width used for each trigger for the calculation.
- 3814 • The mean cluster rate per unit area, `ClustPartRate`, is defined as the mean hit rate normalised

3815 to the mean cluster size and it's statistical error, `ClustPartRateErr`, is then obtained using the
 3816 relative statistical error on the mean cluster size.

```

for (UInt tr = 0; tr < GIFInfra->GetNTrolleys(); tr++){
  UInt T = GIFInfra->GetTrolleyID(tr);

  for (UInt sl = 0; sl < GIFInfra->GetNSlots(tr); sl++){
    UInt S = GIFInfra->GetSlotID(tr,sl) - 1;

    float MeanNoiseRate = 0.;
    float ClusterRate = 0.;
    float ClusterSDev = 0.;

    for (UInt p = 0; p < GIFInfra->GetNPartitions(tr,sl); p++){
      float MeanPartRate = GetTH1Mean(StripNoiseProfile_H.rpc[T][S][p]);
      float cSizePart = NoiseCSIZE_H.rpc[T][S][p]->GetMean();
      float cSizePartErr = (NoiseCSIZE_H.rpc[T][S][p]->GetEntries()==0)
        ? 0.
        : 2*NoiseCSIZE_H.rpc[T][S][p]->GetStdDev() /
          sqrt(NoiseCSIZE_H.rpc[T][S][p]->GetEntries());
      float cMultPart = NoiseCMult_H.rpc[T][S][p]->GetMean();
      float cMultPartErr = (NoiseCMult_H.rpc[T][S][p]->GetEntries()==0)
        ? 0.
        : 2*NoiseCMult_H.rpc[T][S][p]->GetStdDev() /
          sqrt(NoiseCMult_H.rpc[T][S][p]->GetEntries());
      float ClustPartRate = (cSizePart==0) ? 0.
        : MeanPartRate/cSizePart;
      float ClustPartRateErr = (cSizePart==0) ? 0.
        : ClustPartRate * cSizePartErr/cSizePart;

      outputRateCSV << MeanPartRate << '\t'
        << cSizePart << '\t' << cSizePartErr << '\t'
        << cMultPart << '\t' << cMultPartErr << '\t'
        << ClustPartRate << '\t' << ClustPartRateErr << '\t';

      RPCarea += stripArea * nStripsPart;
      MeanNoiseRate += MeanPartRate * stripArea * nStripsPart;
      ClusterRate += ClustPartRate * stripArea * nStripsPart;
      ClusterSDev += (cSizePart==0)
        ? 0.
        : ClusterRate*cSizePartErr/cSizePart;
    }

    MeanNoiseRate /= RPCarea;
    ClusterRate /= RPCarea;
    ClusterSDev /= RPCarea;

    outputRateCSV << MeanNoiseRate << '\t'
      << ClusterRate << '\t' << ClusterSDev << '\t';
  }
}

```

Source Code B.19: Description of rate result calculation and writing into the CSV output `Offline-Rate.csv`. Are saved into the file for each detector, the mean partition rate, cluster size and cluster mutiplicity, along with their errors, for each partition and as well as a detector average.

3819 **Muon performance variables** are computed and written in the output file for each detector parti-
 3820 tions as shown through Sources Code B.20. The variables that are written for each partition are:

- 3821 ● The muon efficiency, `eff`, extracted from the histogram `Efficiency0_H`. It is reminded that
3822 this offline tool doesn't include any tracking algorithm to identify muons from the beam and
3823 only relies on the hits arriving in the time window corresponding to the beam time. The con-
3824 tent of the efficiency histogram is thus biased by the noise/gamma background contribution
3825 into this window and is thus corrected by estimating the muon data content in the peak re-
3826 gion knowing the noise/gamma content in the rate calculation region. Both time windows
3827 being different, the choice was made to normalise the noise/gamma background calculation
3828 window to it's equivalent beam window in order to have comparable values using the variable
3829 `windowRatio`. Finally, to estimate the data ratio in the peak region, the variable `DataRatio`
3830 is defined as the ratio in between the estimated mean cluster multiplicity of the muons in the
3831 peak region, `MuonCM`, and of the total mean cluster multiplicity in the peak region, `PeakCM`.
3832 `MuonCM` is itself defined as the difference in between the total mean cluster multiplicity in the
3833 peak region and the normalised mean noise/gamma cluster multiplicity calculated outside of
3834 the peak region. The statistical error related to the efficiency, `eff_err`, is computed using a
3835 binomial distribution, as the efficiency measure the probability of "success" and "failure" to
3836 detect muons.
- 3837 ● The mean muon cluster size, `MuonCS`, is calculated using the total mean cluster size and multi-
3838 plicity in the peak region, respectively extracted from histograms `MuonCSize_H` and `MuonCMult_H`,
3839 the noise/gamma background mean cluster size and normalised multiplicity, extracted from
3840 `NoiseCSize_H` and `NoiseCMult_H`, and of the estimated muon cluster multiplicity `MuonCM` pre-
3841 viously explicated. The associated statistical error, `MuonCM_err`, is calculated using the propa-
3842 gation of errors of the mentioned variables.
- 3843 ● The mean muon cluster multiplicity in the peak region, `MuonCM`, explicated above whose sta-
3844 tistical error, `MuonCM_err`, is the sum of statistical error associated to the total mean clus-
3845 ter multiplicity in the peak reagion, `PeakCM_err`, and of the mean noise/gamma cluster size,
3846 `NoiseCM_err`.

3847 In addition to these 2 CSV files, the histograms are saved in ROOT file `Scan00XXXX_HVY_Offline.root`
3848 as explained in section B.2.1.1.

3849

```

for (UInt tr = 0; tr < GIFInfra->GetNTrolleys(); tr++) {
    UInt T = GIFInfra->GetTrolleyID(tr);
    for (UInt sl = 0; sl < GIFInfra->GetNSlots(tr); sl++) {
        UInt S = GIFInfra->GetSlotID(tr,sl) - 1;
        for (UInt p = 0; p < GIFInfra->GetNPartitions(tr,sl); p++) {
            float noiseWindow =
                BMTDCWINDOW - TIMEREJECT - 2*PeakWidth.rpc[T][S][p];
            float peakWindow = 2*PeakWidth.rpc[T][S][p];
            float windowRatio = peakWindow/noiseWindow;

            float PeakCM = MuonCMult_H.rpc[T][S][p]->GetMean();
            float PeakCS = MuonCSize_H.rpc[T][S][p]->GetMean();
            float NoiseCM = NoiseCMult_H.rpc[T][S][p]->GetMean() *windowRatio;
            float NoiseCS = NoiseCSize_H.rpc[T][S][p]->GetMean();
            float MuonCM = (PeakCM<NoiseCM) ? 0. : PeakCM-NoiseCM;
            float MuonCS = (MuonCM==0 || PeakCM*PeakCS<NoiseCM*NoiseCS)
                ? 0.
                : (PeakCM*PeakCS-NoiseCM*NoiseCS) / MuonCM;
            float PeakCM_err = (MuonCMult_H.rpc[T][S][p]->GetEntries()==0.)
                ? 0.
                : 2*MuonCMult_H.rpc[T][S][p]->GetStdDev() /
                    sqrt(MuonCMult_H.rpc[T][S][p]->GetEntries());
            float PeakCS_err = (MuonCSize_H.rpc[T][S][p]->GetEntries()==0.)
                ? 0.
                : 2*MuonCSize_H.rpc[T][S][p]->GetStdDev() /
                    sqrt(MuonCSize_H.rpc[T][S][p]->GetEntries());
            float NoiseCM_err = (NoiseCMult_H.rpc[T][S][p]->GetEntries()==0.)
                ? 0.
                : windowRatio*2*NoiseCMult_H.rpc[T][S][p]->GetStdDev() /
                    sqrt(NoiseCMult_H.rpc[T][S][p]->GetEntries());
            float NoiseCS_err = (NoiseCSize_H.rpc[T][S][p]->GetEntries()==0.)
                ? 0.
                : 2*NoiseCSize_H.rpc[T][S][p]->GetStdDev() /
                    sqrt(NoiseCSize_H.rpc[T][S][p]->GetEntries());
            float MuonCM_err = (MuonCM==0) ? 0. : PeakCM_err+NoiseCM_err;
            float MuonCS_err = (MuonCS==0 || MuonCM==0) ? 0.
                : (PeakCS*PeakCM_err + PeakCM*PeakCS_err +
                    NoiseCS*NoiseCM_err + NoiseCM*NoiseCS_err +
                    MuonCS*MuonCM_err) / MuonCM;

            float DataRatio = MuonCM/PeakCM;
            float DataRatio_err = (MuonCM==0) ? 0.
                : DataRatio*(MuonCM_err/MuonCM + PeakCM_err/PeakCM);
            float eff = DataRatio*Efficiency0_H.rpc[T][S][p]->GetMean();
            float eff_err = DataRatio*2*Efficiency0_H.rpc[T][S][p]->GetStdDev() /
                sqrt(Efficiency0_H.rpc[T][S][p]->GetEntries()) +
                Efficiency0_H.rpc[T][S][p]->GetMean()*DataRatio_err;

            outputEffCSV << eff << '\t' << eff_err << '\t'
                << MuonCS << '\t' << MuonCS_err << '\t'
                << MuonCM << '\t' << MuonCM_err << '\t';
        }
    }
}

```

3850

3851

3851

Source Code B.20: Description of efficiency result calculation and writing into the CSV output Offline-L0-EffCl.csv. Are saved into the file for each detector, the efficiency, corrected taking into account the background in the peak window of the time profile, muon cluster size and muon cluster multiplicity, along with their errors, for each partition and as well as a detector average.

3852 B.7 Current data Analysis

3853 Detectors under test at GIF++ are connected both to a CAEN HV power supply and to a CAEN
3854 ADC that reads the currents inside of the RPC gaps bypassing the supply cable. During data tak-
3855 ing, the webDCS records into a ROOT file called `Scan00XXXX_HVY_CAEN.root` histograms with the
3856 monitored parameters of both CAEN devices. Are recorded for each RPC channels (in most cases,
3857 a channel corresponds to an RPC gap):

- 3858 • the effective voltage, HV_{eff} , set by the webDCS using the PT correction on the CAEN power
3859 supply,
- 3860 • the applied voltage, HV_{app} , monitored by the CAEN power supply, and the statistical error
3861 related to the variations of this value through time to follow the variation of the environmental
3862 parameters defined as the RMS of the histogram divided by the square root of the number of
3863 recorded points,
- 3864 • the monitored current, I_{mon} , monitored by the CAEN power supply, and the statistical error
3865 related to the variations of this value through time to follow the variation of the environmental
3866 parameters defined as the RMS of the histogram divided by the square root of the number of
3867 recorded points,
- 3868 • the corresponding current density, J_{mon} , defined as the monitored current per unit area,
3869 $J_{mon} = I_{mon}/A$, where A is the active area of the corresponding gap,
- 3870 • the ADC current, I_{ADC} , recorded through the CAEN ADC module that monitors the dark
3871 current in the gap itself. First of all, the resolution of such a module is better than that of
3872 CAEN power supplies and moreover, the current is not read-out through the HV supply line
3873 but directly at the chamber level giving the real current inside of the detector. The statistical
3874 error is defined as the RMS of the histogram distribution divided by the square root of the
3875 number of recorded points.

3876 Once extracted through a loop over the element of GIF++ infrastructure via the C++ macro
3877 `GetCurrent()`, these parameters, organised in 9 columns per detector HV supply line, are written in
3878 the output CSV file `Offline-Current.csv`. The macro can be found in the file `Current.cc`.

References

- 3880 [1] T. Massam et al. “Experimental observation of antideuteron production”. In: *Il Nuovo Cimento A* 63 (1965), pp. 10–14.
- 3881
- 3882 [2] UA1 Collaboration. “Experimental observation of isolated large transverse energy electrons with associated missing energy at $s = 540 \text{ GeV}$ ”. In: *Physics Letters B* 122 (1983), pp. 103–116.
- 3883
- 3884
- 3885 [3] UA2 Collaboration. “Observation of single isolated electrons of high transverse momentum in events with missing transverse energy at the CERN pp collider”. In: *Physics Letters B* 122 (1983), pp. 476–485.
- 3886
- 3887
- 3888 [4] UA1 Collaboration. “Experimental observation of lepton pairs of invariant mass around $95 \text{ GeV}/c^2$ at the CERN SPS collider”. In: *Physics Letters B* 126 (1983), pp. 398–410.
- 3889
- 3890 [5] UA2 Collaboration. “Evidence for $Z_0 \rightarrow e^+e^-$ at the CERN pp collider”. In: *Physics Letters B* 129 (1983), pp. 130–140.
- 3891
- 3892 [6] ALEPH Collaboration. “Determination of the number of light neutrino species”. In: *Physics Letters B* 231 (1989), pp. 519–529.
- 3893
- 3894 [7] CERN, ed. (1985).
- 3895 [8] CERN, ed. (1986).
- 3896 [9] CERN, ed. (1994).
- 3897 [10] CERN, ed. (1998).
- 3898 [11] CERN, ed. (1999).
- 3899 [12] CERN. Geneva. LHC Experiments Committee. *Letter of Intent for A Large Ion Collider Experiment [ALICE]*, note = CERN-LHCC-93-016. Tech. rep. ALICE Collaboration, 1993.
- 3900
- 3901 [13] CERN. Geneva. LHC Experiments Committee. *ATLAS : technical proposal for a general-purpose pp experiment at the Large Hadron Collider at CERN*, note = CERN-LHCC-94-43. Tech. rep. ATLAS Collaboration, 1994.
- 3902
- 3903
- 3904 [14] CERN. Geneva. LHC Experiments Committee. *CMS : letter of intent by the CMS Collaboration for a general purpose detector at LHC*, note = CERN-LHCC-92-003. Tech. rep. CMS Collaboration, 1992.
- 3905
- 3906
- 3907 [15] CERN. Geneva. LHC Experiments Committee. *LHCb : letter of intent*. Tech. rep. CERN-LHCC-95-5. LHCb Collaboration, 1995.
- 3908
- 3909 [16] L. Evans and P. Bryant. “LHC Machine”. In: *JINST* 3 (2008). S08001.
- 3910 [17] CMS Collaboration ATLAS Collaboration. “Combined Measurement of the Higgs Boson Mass in pp Collisions at $\sqrt{s} = 7$ and 8 TeV with the ATLAS and CMS Experiments”. In: *Physical Review Letters* 114 (2015). 191803.
- 3911
- 3912
- 3913 [18] LHCb Collaboration. “Observation of $J/\psi p$ Resonances Consistent with Pentaquark States in $\Lambda_b^0 \rightarrow J/\psi K^- p$ Decays”. In: *Physical Review Letters* 115 (2015). 072001.
- 3914

- 3915 [19] LHCb Collaboration. “Observation of $J/\psi\phi$ Structures Consistent with Exotic States from
 3916 Amplitude Analysis of $B^+ \rightarrow J/\psi\phi K^+$ Decays”. In: *Physical Review Letters* 118 (2017).
 3917 022003.
- 3918 [20] CERN. Geneva. *High-Luminosity Large Hadron Collider (HL-LHC) Technical Design Report V. 0.1*. Tech. rep. CERN-2017-007-M. 2017.
- 3919 [21] CERN. Geneva. LHC Experiments Committee. *The CMS muon project : Technical Design Report*. Tech. rep. CERN-LHCC-97-032. CMS Collaboration, 1997.
- 3920 [22] CERN. Geneva. LHC Experiments Committee. *CMS, the Compact Muon Solenoid : technical proposal*. Tech. rep. CERN-2015-005. 2015.
- 3921 [23] CERN. Geneva. LHC Experiments Committee. *The Phase-2 Upgrade of the CMS Muon Detectors*. Tech. rep. CERN-LHCC-2017-012, CMS-TDR-016. CMS Collaboration, 2017.
- 3922 [24] CERN. Geneva. LHC Experiments Committee. *High-Luminosity Large Hadron Collider (HL-LHC) Preliminary Design Report*. Tech. rep. CERN-LHCC-94-38. CMS Collaboration, 1994.
- 3923 [25] CERN. Geneva. LHC Experiments Committee. *The Phase-2 Upgrade of the CMS Level-1 Trigger - Interim Report to the LHCC*. Tech. rep. CERN-LHCC-2017-013, CMS-TDR-017. CMS Collaboration, 2017.
- 3924 [26] CERN. Geneva. LHC Experiments Committee. *Technical Proposal for the Phase-II Upgrade of the CMS Detector*. Tech. rep. CERN-LHCC-2015-010, CMS-TDR-15-02. CMS Collaboration, 2015.
- 3925 [27] A. Gelmi. *CMS iRPC at HL-LHC: background study*. 2018. URL: https://indico.cern.ch/event/732794/contributions/3021836/attachments/1657792/2654574/iRPC_bkg_study_Upgrade29_05_18.pdf.
- 3926 [28] F.Sauli. “GEM: A new concept for electron amplification in gas detectors”. In: *Nucl. Instr. Meth. Phys. Res.* 386 (1997), pp. 531–534.
- 3927 [29] CERN. Geneva. LHC Experiments Committee. *CMS Technical Design Report for the Muon Endcap GEM Upgrade*. Tech. rep. CERN-LHCC-2015-012, CMS-TDR-013. CMS Collaboration, 2015.
- 3928 [30] The CMS collaboration. “The performance of the CMS muon detector in proton-proton collisions at $\sqrt{s} = 7$ TeV at the LHC”. In: *JINST* 8 (2013). P11002.
- 3929 [31] P.Bortignon. “Design and performance of the upgrade of the CMS L1 muon trigger”. In: *Nucl. Instr. Meth. Phys. Res.* 824 (2016), pp. 256–257.
- 3930 [32] The European Parliament and the Council of the European Union. “Regulation (EU) No 517/2014 of 16 April 2014 on fluorinated greenhouse gases and repealing Regulation (EC) No 842/2006”. In: *Official Journal of the European Union* 150 (2014), pp. 195–230.
- 3931 [33] R. Santonico and R. Cardarelli. “Development of resistive plate counters”. In: *Nucl. Instr. Meth. Phys. Res.* 187 (1981), pp. 377–380.
- 3932 [34] Yu.N. Pestov and G.V. Fedotovich. *A picosecond time-of-flight spectrometer for the VEPP-2M based on local-discharge spark counter*. Tech. rep. SLAC-TRANS-0184. SLAC, 1978.
- 3933 [35] W.W. Ash, ed. *Spark Counter With A Localized Discharge*. Vol. SLAC-R-250. 1982, pp. 127–131.
- 3934 [36] I. Crotty et al. “The non-spark mode and high rate operation of resistive parallel plate chambers”. In: *NIMA* 337 (1993), pp. 370–381.

BIBLIOGRAPHY

- [37] I. Crotty et al. "Further studies of avalanche mode operation of resistive parallel plate chambers". In: *NIMA* 346 (1994), pp. 107–113.
- [38] R. Cardarelli et al. "Avalanche and streamer mode operation of resistive plate chambers". In: *NIMA* 382 (1996), pp. 470–474.
- [39] R. Cardarelli et al. "Performance of a resistive plate chamber operating with pure CF_3Br ". In: *NIMA* 333 (1993), pp. 399–403.
- [40] M. Abbrescia et al. "Performance of a Resistive Plate Chamber operated in avalanche mode under ^{137}Cs irradiation". In: *NIMA* 392 (1997), pp. 155–160.
- [41] M. Abbrescia et al. "Properties of C2H2F4-based gas mixture for avalanche mode operation of resistive plate chambers". In: *NIMA* 398 (1997), pp. 173–179.
- [42] P. Camarri et al. "Streamer suppression with SF6 in RPCs operated in avalanche mode". In: *NIMA* 414 (1998), pp. 317–324.
- [43] E. Cerron Zeballos et al. "Effect of adding SF6 to the gas mixture in a multigap resistive plate chamber". In: *NIMA* 419 (1998), pp. 475–478.
- [44] E. Cerron Zeballos et al. "A new type of resistive plate chamber: The multigap RPC". In: *NIMA* 374 (1996), pp. 132–135.
- [45] M.C.S. Williams. "The development of the multigap resistive plate chamber". In: *Nucl. Phys. B* 61 (1998), pp. 250–257.
- [46] H. Czyrkowski et al. "New developments on resistive plate chambers for high rate operation". In: *NIMA* 419 (1998), pp. 490–496.
- [47] CERN. Geneva. LHC Experiments Committee. *ATLAS muon spectrometer: Technical design report*. Tech. rep. CERN-LHCC-97-22. ATLAS Collaboration, 1997.
- [48] CERN. Geneva. LHC Experiments Committee. *ALICE Time-Of-Flight system (TOF) : Technical Design Report*. Tech. rep. CERN-LHCC-2000-012. ALICE Collaboration, 2000.
- [49] The CALICE collaboration. "First results of the CALICE SDHCAL technological prototype". In: *JINST* 11 (2016).
- [50] PoS, ed. *Density Imaging of Volcanoes with Atmospheric Muons using GRPCs*. International Europhysics Conference on High Energy Physics - HEP 2011. 2011.
- [51] C. Lippmann. "Detector Physics of Resistive Plate Chambers". PhD thesis. Johann Wolfgang Goethe-Universität, 2003.
- [52] W. Riegler. "Induced signals in resistive plate chambers". In: *NIMA* 491 (2002), pp. 258–271.
- [53] M. Abbrescia et al. "Effect of the linseed oil surface treatment on the performance of resistive plate chambers". In: *NIMA* 394 (1997), pp. 13–20.
- [54] G.Battistoni et al. "Sensitivity of streamer mode to single ionization electrons". In: *NIMA* 235 (1985), pp. 91–97.
- [55] M. Abbrescia et al. "Cosmic ray tests of double-gap resistive plate chambers for the CMS experiment". In: *NIMA* 550 (2005), pp. 116–126.
- [56] JINST, ed. *Performance of the Resistive Plate Chambers in the CMS experiment*. The 9th International Conference on Positioin Sensitive Detectors. 2012.
- [57] PoS, ed. *The CMS RPC detector performance during Run-II data taking*. The European Physical Society Conference on High Energy Physics (EPS-HEP2017). 2018.
- [58] Honeywell International Inc. *Solstice(R) ze Refrigerant (HFO-1234ze): The Environmental Alternative to Traditional Refrigerants*. Tech. rep. FPR-003/2015-01. 2015.

- 4001 [59] E. Cerron Zeballos et al. “A comparison of the wide gap and narrow gap resistive plate
4002 chamber”. In: *NIMA* 373 (1996), pp. 35–42.
- 4003 [60] ALICE Collaboration. “A study of the multigap RPC at the gamma irradiation facility at
4004 CERN”. In: *NIMA* 490 (2002), pp. 58–70.
- 4005 [61] B. Bonner et al. “A multigap resistive plate chamber prototype for time-of-flight for the STAR
4006 experiment at RHIC”. In: *NIMA* 478 (2002), pp. 176–179.
- 4007 [62] S. Yang et al. “Test of high time resolution MRPC with different readout modes for the
4008 BESIII upgrade”. In: *NIMA* 763 (2014), pp. 190–196.
- 4009 [63] A. Akindinovg et al. “RPC with low-resistive phosphate glass electrodes as a candidate for
4010 the CBM TOF”. In: *NIMA* 572 (2007), pp. 676–681.
- 4011 [64] JINST, ed. *Development of the MRPC for the TOF system of the MultiPurpose Detector*.
4012 RPC2016: XII Workshop on Resistive Plate Chambers and Related Detectors. 2016.
- 4013 [65] M.C.S. Williams. “Particle identification using time of flight”. In: *Journal of Physics G* 39
4014 (2012).
- 4015 [66] A. Alici et al. “Aging and rate effects of the Multigap RPC studied at the Gamma Irradiation
4016 Facility at CERN”. In: *NIMA* 579 (2007), pp. 979–988.
- 4017 [67] M. Abbrescia et al. “The simulation of resistive plate chambers in avalanche mode: charge
4018 spectra and efficiency”. In: *NIMA* 431 (1999), pp. 413–427.
- 4019 [68] C. Patrignani et al. (Particle Data Group). “Review of Particle Physics”. In: *Chin. Phys. C*
4020 C40 (2016), p. 100001.
- 4021 [69] JINST, ed. *Description and simulation of physics of Resistive Plate Chambers*. RPC2016:
4022 XII Workshop on Resistive Plate Chambers and Related Detectors. 2016.
- 4023 [70] V. Français. “Description and simulation of the physics of Resistive Plate Chambers”. PhD
4024 thesis. LPC - Laboratoire de Physique Corpusculaire - Clermont-Ferrand, 2017.
- 4025 [71] H. Bethe. “Zur Theorie des Durchgangs schneller Korpuskularstrahlen durch Materie”. In:
4026 *Annalen der Physik* 397 (1930), pp. 325–400.
- 4027 [72] International Commission on Radiation Units and Measurements. *Stopping Powers for Elec-*
4028 *trons and Positions*. Tech. rep. Report 37. 1984.
- 4029 [73] International Commission on Radiation Units and Measurements. *Stopping Power and Ranges*
4030 *for Protons and Alpha Particles*. Tech. rep. Report 49. 1994.
- 4031 [74] H. Bichsel. “A method to improve tracking and particle identification in TPCs and silicon
4032 detectors”. In: *NIMA* 562 (2006), pp. 154–197.
- 4033 [75] W. W. M. Allison and J. H. Cobb. “Relativistic charged particle identification by energy loss”.
4034 In: *Annual Review of Nuclear and Particle Science* 30 (1980), 253–298.
- 4035 [76] International Commission on Radiation Units and Measurements. *Average energy to produce*
4036 *an ion pair*. Tech. rep. Report 31. 1994.
- 4037 [77] I.B. Smirnov. “Modeling of ionization produced by fast charged particles in gases”. In: *NIMA*
4038 554 (2005), pp. 474–493.
- 4039 [78] <https://doi.org/10.1088/1742-6596/587/1/012035>.
- 4040 [79] W. Riegler et al. “Detector physics and simulation of resistive plate chambers”. In: *NIMA* 500
4041 (2003), pp. 144–162.
- 4042 [80] I.B. Smirnov. *HEED++ simulation program*. 2010. URL: \href{http://ismirnov.
4043 web . cern . ch / ismirnov / heed } {http : / / ismirnov . web . cern . ch /
4044 ismirnov/heed}.

BIBLIOGRAPHY

- 4045 [81] S.F. Biagi. “Monte Carlo simulation of electron drift and diffusion in counting gases under
4046 the influence of electric and magnetic fields”. In: *NIMA* 421 (1999), pp. 234–240.
- 4047 [82] W. H. Furry. “On Fluctuation Phenomena in the Passage of High Energy Electrons through
4048 Lead”. In: *Phys. Rev.* 52 (1937), pp. 569–581.
- 4049 [83] H. Genz. “Single electron detection in proportional gas counters”. In: *Nucl. Instr. and Meth.*
4050 112 (1973), pp. 83–90.
- 4051 [84] M. Abbrescia et al. “Study of long-term performance of CMS RPC under irradiation at the
4052 CERN GIF”. In: *NIMA* 533 (2004), pp. 102–106.
- 4053 [85] H.C. Kim et al. “Quantitative aging study with intense irradiation tests for the CMS forward
4054 RPCs”. In: *NIMA* 602 (2009), pp. 771–774.
- 4055 [86] S. Agosteo et al. “A facility for the test of large-area muon chambers at high rates”. In: *NIMA*
4056 452 (2000), pp. 94–104.
- 4057 [87] PoS, ed. *CERN GIF ++ : A new irradiation facility to test large-area particle detectors for*
4058 *the high-luminosity LHC program*. Vol. TIPP2014. 2014, pp. 102–109.
- 4059 [88] A. Fagot. *GIF++ DAQ v4.0*. 2017. URL: https://github.com/afagot/GIF_DAQ.
- 4060 [89] CAEN. *Mod. V1190-VX1190 A/B, 128/64 Ch Multihit TDC*. 14th ed. 2016.
- 4061 [90] CAEN. *Mod. V1718 VME USB Bridge*. 9th ed. 2009.
- 4062 [91] W-Ie-Ne-R. *VME 6021-23 VXI*. 5th ed. 2016.
- 4063 [92] Wikipedia. *INI file*. 2017. URL: https://en.wikipedia.org/wiki/INI_file.
- 4064 [93] S. Carrillo A. Fagot. *GIF++ Offline Analysis v6*. 2017. URL: https://github.com/afagot/GIF_OfflineAnalysis.
- 4065